Numerical Study of Morphing Helicopter Rotors

Rinaldo Steininger

Submitted in fulfilment of the requirements for the degree of Doctor of Philosophy

James Watt School of Engineering
College of Science and Engineering
University of Glasgow

May 2025

Abstract

This thesis shows high-fidelity numerical simulations for combined fluid, structural and servo-systems of a helicopter, to make predictions and validations of helicopter rotor on-blade-actuators. This aero-servo-elastic approach forms the main novelty of this thesis. The physics of the active rotor blade aerodynamics and structural dynamics are simulated, and the resulting knowledge can then be implemented in comprehensive rotor suites. Assessing the physics is important for the introduction of new rotor concepts, something which low- and mid-order methods can not do. The Helicopter Multi-Block 3 (HMB3) simulation suite developed at Unversity of Glasgow was expanded to include the servo system in the aeroelastic models. The software does not include a rigid body model for the rotor hub. Both hub and blade structural dynamics are simulated in the commercial FEM solver MSC NASTRAN.

Expanding the flight envelope with higher top-speeds, while avoiding retreating blade stall, has been a challenge since the inception of helicopters. A promising innovation is the variable twist rotor blade, which through intrinsic actuation, can optimise the twist for the given flight condition and exploit aeroelasticity to modify the rotor blade path for vibration control and possibly higher trim-able thrust. This thesis only considers twist actuators, due to their benefits in weight, simplicity and airworthiness over other actuation methods. However, the aero-servo-elastic modelling can be applied to any rotor blades with piezoceramic actuators, such as active flaps or Gurney flaps, if the actuator is sufficiently resolved in the structural model.

The aeroelastic method is validated against the Helicopter Validation and Acoustic Baseline rotor (HVAB). Performance metrics, structural deformations and flow physics are compared and confirm the accuracy of the method. Additionally, rotor blade structural models of 1D-beam and 2D/3D-finite elements are modelled and compared, including a mesh study. Finite elements allow the modelling of on-blade actuators, instead of simplifying the problem to only include their effects in simulations. The structural models of the Smart Twisting Active Rotor (STAR) are compared to experimentally obtained data, for validation of the methods used in this thesis. This also includes a study of the actuator modelling via a thermal analogy method, where the voltage on a piezoelectric material is equated to temperature in a thermally expanding material.

Using the developed aero-servo-elastic method, improvements in the forward flight vibration metric could be predicted for the STAR rotor blade in two flight conditions. The largest vibration improvement was observed at high-speed level flight. In this condition, increased passive blade twist has a large vibration penalty. In a level flight at maximum thrust, experiencing blade-vortex interactions (BVI), the active twist was shown to improve the moment trim, leading to conclusions of higher thrust capacity in this relatively high-speed flight case. The observed effects on the rotor lift-to-drag ratios were negligible.

For the STAR, a 1D beam model and a mixed 2D/3D finite element model were compared. The beam model overpredicts the blade mode frequencies of the measured rotor blades, because the sectional properties of the received dataset were slightly overpredicted. A modified set of properties, yielding more accurate mode frequencies is also presented. The finite element model, built from available geometric and material data, was within 10% of the measured frequencies. The strong 3-dimensional structural coupling of the finite element model is showcased, which could not be observed in the beam model. A small blade-untwisting under centrifugal force is found for the finite element model. The actuator effectiveness degrates under centrifugal tension and this mechanism is discussed. A hovering simulation of the rotor, with a loosely coupled fluid-structure simulation shows the differences between the models. It concludes, that especially for blades with torsion actuators, 3D finite element model approaches are necessary to obtain correct results.

List of Publications

In Journals

Steininger R., Barakos, G., “Simulation of Active Twist Rotor Blades using a Thermal Analogy Method in HMB3”. *Aeronautical Journal*, **Submitted 04/12/2024**.

Steininger R., Barakos, G., “Aeroelastic Fluid Dynamics Assessment of Performance and Vibration on Active Twisting Rotors”. *Aerospace, Science and Technology*, **151**, 109317, 2024. ISSN 1270-9638, https://doi.org/10.1016/j.ast.2024.109317

van der Wall, B. G., Lim, J. W., Riemenschneider, J., Kalow, S., Wilke, G. A., D. Douglas, J. B., Bailly, J., Delrieux, Y., Cafarelli, I., Tanabe, Y., Sugawara, H., Jung, S. N., Hong, S. H., Kim, D.-H., Kang, H. J., Barakos, G., and Steininger, R., “New Smart Twisting Active Rotor (STAR): Pretest predictions”. *CEAS Aeronautical Journal*, **15**, 721–750 (2024). https://doi.org/10.1007/s13272-024-00731-z

Conferences and Workshops

S. H. Chang, S. H. Hong, S. N. Jung, D.-H. Kim, F. Becker, S. Kalow, and R. Steininger, “Experimental-cum-numerical evaluation of structural properties and vibrational spectra of new smart twisting active rotor blades”. *50th European Rotorcraft Forum, ERF 2024*, Marseille, France, September 2024.

Steininger, R. and Barakos, G., “Structural Modelling of Active Twist Rotor Blades using Thermal Analogy”. *UK Vertical Lift Network 9th Annual Technical Workshop*, May 2024, Cheshire, United Kingdom.

Wilke, G. A., van der Wall, B. G., Tanabe, Y., Sugawara, H., Kim, D.-H., Kang, H. J., Hong, S. H., Bailly, J., Barakos, G. N., Steininger, R., Lim, J. W. “Vortex-Induced Stall on an Actively Twisted Highly Loaded Model Rotor Blade”. In: *Dillmann, A., Heller, G., Krämer, E., Wagner, C., Weiss, J. (eds) New Results in Numerical and Experimental Fluid Mechanics XIV. STAB/DGLR Symposium 2022. Notes on Numerical Fluid Mechanics and Multidisciplinary De-*

sign, **154**, 2024. Springer, Cham. https://doi.org/10.1007/978-3-031-40482-5_59

Steininger, R. and Barakos, G., “Simulation of Active Twist Rotor Blades using a Thermal Analogy Method in HMB3”. *49th European Rotorcraft Forum, ERF 49* 5–7 September 2023, Buckeburg, Germany

Steininger, R. and Barakos, G., “Active Twist and Passive Rotors in Hover and Level Flight”. *Vertical Flight Society, Forum 79*, 16–18 May 2023, West Palm Beach, FL, USA.

Steininger, R. and Barakos, G., “Active Twist and Passive Rotors in Hover and Level Flight”. *UK Vertical Lift Network 8th Annual Technical Workshop*, May 2023, Cheshire, United Kingdom.

Steininger, R., Barakos, G. and Woodgate, M., “Numerical Analysis of HVAB and STAR Rotor Blades using HMB3”. *Proceedings of the 2022 SciTech AIAA Forum*, 23–27 January 2023, National Harbor, MD, USA.

van der Wall, B. G., Lim, J. W., Riemenschneider, J., Kalow, S., Wilke, G. A., D. Douglas, J. B., Bailly, J., Delrieux, Y., Cafarelli, I., Tanabe, Y., Sugawara, H., Jung, S. N., Hong, S. H., Kim, D.-H., Kang, H. J., Barakos, G., and Steininger, R., “Smart Twisting Active Rotor (STAR) — Pre-test predictions”. *Proceedings of the 48th European Rotorcraft Forum*, 6–8 September 2022, Winterthur, Switzerland.

Steininger, R. and Barakos, G., “Simulation of Rotors with Active Twist”. *UK Vertical Lift Network 7th Annual Technical Workshop*, May 2022, Cheshire, United Kingdom.

Steininger, R. and Barakos, G., “Active Twist Rotor Blades and the STAR project”. *UK Vertical Lift Network 6th Annual Technical Workshop*, May 2021, online only.

Technical Notes

Steininger, R., “Structural Modelling and Thermal Analogy in MSC NASTRAN”, *unpublished*, 2024. 112 pages.

Contents

List of Tables

List of Figures

Acknowledgements

First of all, I am truly appreciative to my first supervisor Prof. George Barakos for his guidance over all these years, starting from my undergraduate study. His patience, encouragement, technical knowledge and the passion he inspired in me have been instrumental in my growth and the completion of this thesis. I also extend my gratitude to my second supervisor Dr. Mark Woodgate, who was always there to help me find the answers to my many questions on the fluid solver, aero-structural coupling and our HPC system.

I am grateful to Richard Markiewicz and Neil Taylor of DSTL for sharing their technical knowledge of real-world rotor blades and their efforts to oversee the progress and publications of this project. The financial support from DSTL under contract number DSTLX-10000129255, which also enabled our participation in the STAR project, is gratefully acknowledged.

I wish to thank all members of the CFD lab, who were always there to provide techical and mental support through all these years, specially, my closest colleagues Thomas, Tao, Murray, Geng and Andrea. Without your help, this achievement would not have been possible, and I hope I was able to support you in return.

I am also thankful for the assistance and cooperation from Gunther Wilke, Steffen Kalow, Berend van der Wall and the many other participants of the STAR project.

Finally, I am profoundly grateful to my love Judit, who endured the challenges of our time apart and supported me during my years in Scotland. I also want to thank my parents and my family for their unconditional love, even when I had so little time to visit them.

Declaration

I certify that the thesis presented here for examination for a PhD degree of the University of Glasgow is solely my own work other than where I have clearly indicated that it is the work of others (in which case the extent of any work carried out jointly by me and any other person is clearly identified in it) and that the thesis has not been edited by a third party beyond what is permitted by the University's PGR Code of Practice.

The copyright of this thesis rests with the author. No quotation from it is permitted without full acknowledgement.

I declare that the thesis does not include work forming part of a thesis presented successfully for another degree.

I declare that this thesis has been produced in accordance with the University of Glasgow's Code of Good Practice in Research.

I acknowledge that if any issues are raised regarding good research practice based on review of the thesis, the examination may be postponed pending the outcome of any investigation of the issues.

May 2025

....

Rinaldo Steininger

2238057

Nomenclature

Latin symbols

a	lift curve slope or speed of sound
A	area $[m^2]$
AR	rotor blade aspect ratio, $\frac{R}{c_{ref}}$
c	chord $[m]$
C_D	drag coefficient, $\frac{D}{\frac{1}{2}\rho V_\infty^2 S}$
C_L	lift coefficient, $\frac{L}{\frac{1}{2}\rho V_\infty^2 S}$
C_M	pitching moment coefficient, $\frac{M}{\frac{1}{2}\rho V_\infty^2 cS}$
C_{Mx}	non-dimensional rotor rolling moment coefficient (US), $\frac{M_x}{\rho_{ref}(V_{inf})^2\pi(AR)^3}$
C_{My}	non-dimensional rotor pitching moment coefficient (US), $\frac{M_y}{\rho_{ref}(V_{inf})^2\pi(AR)^3}$
C_{Mz}	non-dimensional rotor torque (US), $\frac{M_z}{\rho_{ref}(V_{inf})^2\pi(AR)^3}$
C_P	pressure coefficient, $\frac{p-p_\infty}{\frac{1}{2}\rho(\Omega r)^2}$
C_q	blade section torque coefficient, $\frac{dQ/dr}{\frac{1}{2}\rho c_{ref}R(\Omega r)^2}$
C_Q	torque coefficient (US), $\frac{Q}{\rho(\Omega R)^2\pi R^3}$
C_t	blade section thrust coefficient, $\frac{dT/dr}{\frac{1}{2}\rho c_{ref}(\Omega r)^2}$
C_T	thrust coefficient (US), $\frac{T}{\rho(\Omega R)^2\pi R^2}$
D	drag force $[kgm/s^2]$
E	energy per unit mass $[m^2/s^2]$ or Young's modulus $[kg/(ms^2)]$
f	frequency $[1/s]$
$\mathbf{F}$	flux vector in x direction
F_i	Force in direction i $[kgm/s^2]$
FoM	figure of merit, $\frac{C_T^{3/2}}{\sqrt{2}C_Q}$
G	shear modulus $[kg/(ms^2)]$
$\mathbf{G}$	flux vector in y direction
$\mathbf{H}$	flux vector in z direction
H_{out}	source-sink model distance of outflow region from rotor disk plane
I_c, I_f	chordwise/flapwise moment of area $[m^4]$
J	torsion constant $[m^4]$

k	turbulent kinetic energy per unit mass $[m^2/s^2]$
L	lift Force $[kgm/s^2]$ or length $[m]$
M	Mach number or mass per unit length $[kg/m]$
M_x	rotor disk rolling moment $[kgm^2/s^2]$
M_y	rotor disk pitching moment $[kgm^2/s^2]$
M^2C_d	blade section drag coefficient (rotor disk in-plane force), $\frac{D}{\frac{1}{2}\rho a^2 c}$
M^2C_l	blade section lift coefficient (rotor disk normal force), $\frac{L}{\frac{1}{2}\rho a^2 c}$
M^2C_m	blade section pitching moment coefficient, $\frac{M_y}{\frac{1}{2}\rho a^2 c^2}$
$\mathbf{n}$	unit normal vector
N_B	number of blades
p	pressure $[kg/(ms^2)]$
P	Rotor power $[kgm^2/s^3]$, ΩQ
q	heat flux vector $[kg/s^3]$
Q	rotor torque $[kgm^2/s^2]$ or Q-criterion
r	radial position along blade span $[m]$
$\mathbf{r}$	vector of structural interpolation point coordinates $[m]$
R	rotor radius $[m]$ or specific gas constant $[m^2/(s^2K)]$
$\mathbf{R}$	flow residual vector
Re	Reynolds number, $\frac{V_\infty c_{ref}\rho}{\mu}$
R_{et}	turbulent eddy viscosity ratio, $\frac{\mu_t}{\mu}$
$\mathbf{S}$	source term vector
$\{T\}$	Strain vector
S_{ij}	strain rate tensor
t	time $[s]$ or thickness $[m]$
t^*	non-dimensional time
T	rotor thrust $[kgm/s^2]$ or time $[s]$ or temperature $[K]$ or oscillation period, $\frac{2\pi}{\omega}$
$\{T\}$	Stress vector
T_s	Sutherland Temperature $[K]$
U	velocity $[m/s]$
$U = (u,v,w)^T$	Cartesian velocity vector $[m/s]$
$\mathbf{v}$	arbitrary vector
V	velocity $[m/s]$ or cell volume $[m^3]$
$\mathbf{W}$	vector of conserved variables
y^+	non-dimensional wall distance, $\frac{yu_\tau}{\upsilon}$
x,y,z	spacial coordinates in Cartesian system $[m]$
$x = (x,y,z)^T$	fluid position vector $[m]$

Greek symbols

α	angle of incidence $[deg]$
α_A	rotor disk aerodynamic angle
α_s	rotor shaft angle
β_0	rotor coning angle $[deg]$
β_{1c}	rotor longitudinal flapping angle $[deg]$
β_{1s}	rotor lateral flapping angle $[deg]$
γ	shear rate $[1/s]$ or turbulence intermittency factor or specific heat ratio or rotor Lock number
δ_{ij}	Kronecker delta
ε	turbulent energy dissipation rate
Θ	Temperature $[^\circ C]$ or $[K]$
θ_0	rotor collective angle $[deg]$
θ_{75}	rotor pitch angle at 75% radius $[deg]$
θ_{1c}	rotor lateral cyclic angle $[deg]$
θ_{1s}	rotor longitudinal cyclic angle $[deg]$
θ_{tw}	blade linear twist rate $[deg/R]$
λ	rotor tip speed ratio, $\frac{M_\infty}{M_{tip}}$
μ	dynamic Viscosity $[kg/(ms)]$, $\frac{\tau}{\gamma}$ or rotor advance ratio, $\lambda \cos \alpha_a$
μ_t	turbulent eddy viscosity $[kg/(ms)]$
ρ	density $[kg/m^3]$
σ	nominal rotor solidity, $\sigma_N = N_b/(\pi R/c_{ref})$
τ	shear stress $[kg/(ms^2)]$
τ_{ij}	viscous shear stress tensor
τ_{ij}^R	Reynolds shear stress Tensor
υ	kinematic viscosity $[m^2/s]$
υ_t	turbulent kinematic viscosity $[m^2/s]$
ϕ	phase angle $[deg]$ or voltage $[V]$ or mode shape $[m]$
ψ	azimuthal position $[deg]$
ω	specific dissipation rate of turbulent kinetic energy $[1/s]$ or frequency $[1/s]$
Ω	rotor rotational speed $[rad/s]$

Acronyms

AIAA	American Institute of Aeronautics and Astronautics
ARES	Aeroelastic Rotor Experimental System (test bed)
ATR	(NASA/US Army/MIT) Active Twist Rotor
CFD	Computational Fluid Dynamics
CSD	Computational Solid Dynamics

CVT	Constant Volume Tetrahedron (Deformation Method)
DLR	German Aerospace Center
DNW	German-Dutch Wind Tunnels
DNW-LLF	DNW-Large Low-Speed Facility
HHC	Higher-Harmonic Control
HMB3	Helicopter Multi Block 3
HVAB	(AIAA) Hover Validation and Acoustic Baseline [Rotor]
IBC	Individual Blade Control
IDEPFC	InterDigitated Electrode Piezoelectric Fibre Composite
IGE	In Ground Effect
IDWM	Inverse Distance Weighting Method
ISA	International Standard Atmosphere
JAXA	Japan Aerospace Exploration Agency
KARI	Korea Aerospace Research Institute
Konkuk	Konkuk University, South Korea
MIT	Massachusetts Institute of Technology
NASA	National Aeronautics and Space Administration
OGE	Out of Ground Effect
ONERA	French Aerospace Lab
RHTF	(NASA Langley) Rotorcraft Hover Test Facility
SMA	Shape Memory Alloy
STAR	Smart Twist Active Rotor
TDT	(NASA Langley) Transonic Dynamics Tunnel
VFS	Vertical Flight Society

Subscripts

e	equivalent
i, j, k	indices
imp	implicit
pp	peak-to-peak
ref	reference value
rms	root-mean-square
tip	tip value
v	viscous term
∞	freestream value

Superscripts

i	inviscid

T	transpose
v	viscous
n	generic iterator

Chapter 1

Introduction

1.1 Motivation and Background

Helicopters are versatile aircraft, useful for military and civilian operations. They have vertical take-off and landing capability and can hover with moderate power requirements. Designing their main rotor and rotor blades is a complex engineering task, because of unsteady flow conditions and trade-offs between aerodynamics and structural requirements. There is a need to expand the envelope of helicopter rotors to increase performance, reliability, and decrease their environmental impact through emissions and noise. Especially, due to commitments of the aerospace industry to reduce pollution, reduced blade drag is needed to lower emissions and through smart control of vibrations, the noise profile can be shaped and reduced.

1.1.1 Rotor Aerodynamics

The hovering rotor produces a pressure differential at the disk, which accelerates air downwards, resulting in a net thrust force of $T = \iint \Delta p dA$. Based on momentum theory, this results in a contracting wake, which is approximately half of the rotor disk area. The simplest case, considering uniform inflow is illustrated in Figure 1.1. In reality, the induced velocity distribution is not uniform, the wake contracts slightly less and there is a tiny amount of rotation added to the wake.

The derivations of the hover momentum theory and blade element momentum theory can be found in any textbook on helicopter aerodynamics, for example [1, 2]. Terms and coefficients relating to rotor performance were also explained in the nomenclature and in Section 1.2.2. Notably, the hover figure of merit (FoM) only compares the lifting efficiency to the rotor's ideal induced lift profile. It is dependent on the blade solidity σ and rotor disk loading T/A, and therefore caution must be taken when comparing different rotors.

In forward flight, the rotor blades experience high Mach numbers on the advancing side, while the retreating blade needs high incidence to compensate for the low dynamic pressure.

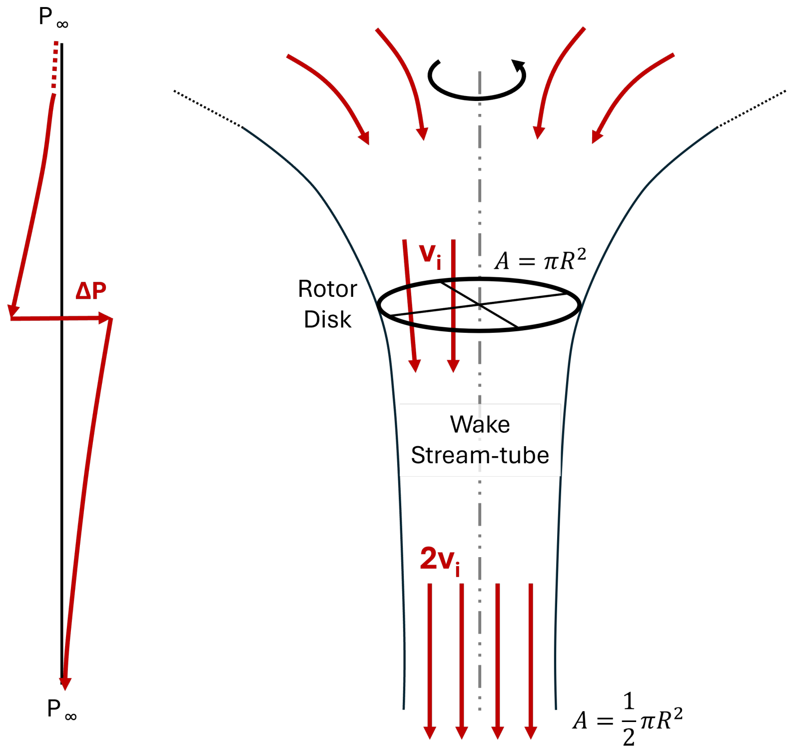

Figure 1.1: Simplified view of the pressure change and airflow velocity of a rotor in hover.

This is illustrated in Figure 1.2. With an increasing advance ratio, the region of reversed flow experienced on the retreating side increases. This complex non-uniform lift distribution requires cyclic controls, and is affected by blade aeroelasticity. To achieve trim in level flight, the rolling moments from the thrust distribution at the advancing and retreating sides must cancel out. This requires a differential in blade pitch, called the lateral cyclic angle $\theta_{1,s}$. In the illustration, the rotor disk is presented with free stream flow in the plane. If the rotor shaft angle, does not correspond to the flight direction, the effective advance ratio $\mu = \lambda \cos \alpha_A$ is a factor of the tip speed ratio $\lambda = V_{tip}/V_\infty$, where the angle is the effective offset between inflow velocity and disk plane, illustrated in Figure 1.3.

At the very outboard of the rotor blades, the tip vortex induces some downwash, reducing the local lift. This is called tip relief, it mildly reduces the effective angle of attack locally. A similar phenomenon can also be exploited at sections of rapidly changing chord-length, producing a so-called notch vortex. The rotor blades are exposed to the wake and tip vortices of other blades, resulting in a complex aerodynamic problem. The unsteady periodic forces on the slender blades make blade structural design an important consideration, as it affects performance, vibration and service life.

The operational envelope of a helicopter is partially limited by the power plant output or the weight penalty of stronger transmissions. The main rotor power is a limiting factor of the load-carrying capacity, as it is crucial during hover, take-off and landing. The primary contribution to this is the lift-induced power in hover, but due to practical constraints, a helicopter rotor is

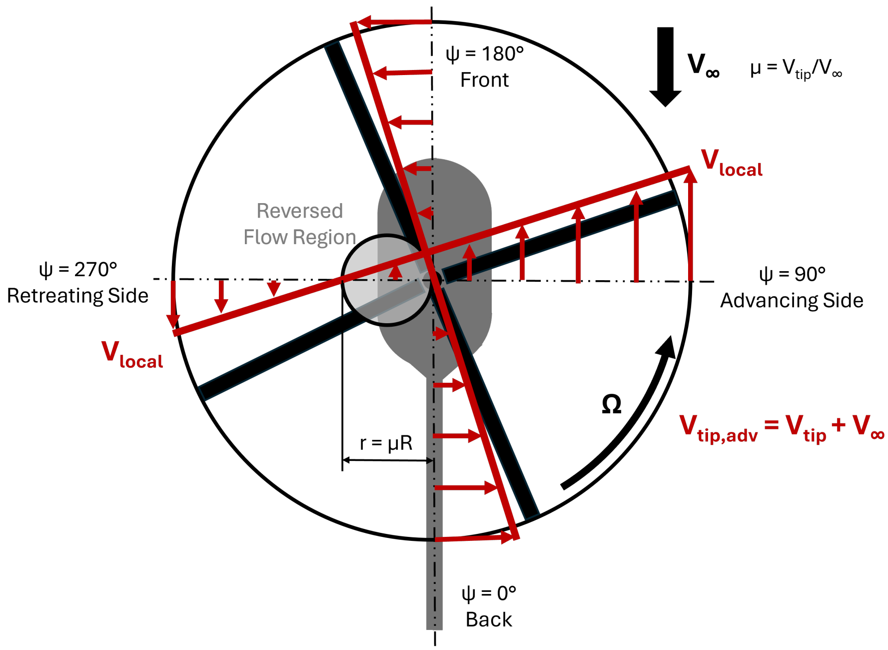

Figure 1.2: The rotor blade velocities are shown relative to the inflowing air, as seen from above in a case of high-speed forward flight. The advance ratio μ equals the tip speed ratio λ in this case where freestream is in-plane with the rotor disk.

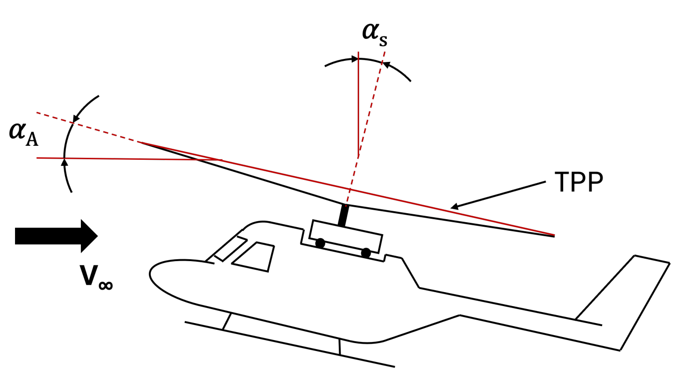

Figure 1.3: Illustration of the rotor shaft angle α_s, and the effective aerodynamic angle of the tip path plane (TPP) α_A in manoeuvring flight. If the coning is equal on the front and rear of the rotor, the two angles are effectively equal.

limited in its blade radius. Longer rotor blades need sufficient solidity to bear the increasing centrifugal stresses, which in turn increase the blade and hub assembly weight. Longer and heavier blades must also be stiffer, to respond to cyclic pitch inputs, and to avoid excessive bending. Lift capability can be increased by varying the chord length and switching to aerofoils with higher $C_{L,max}$, but this brings other trade-offs such as increased torque or control loads. A short review of some rotor blade planforms is presented in Section 2.2.

Blade element momentum theory (BEMT) predicts the most efficient hovering rotor as one, which has a uniform downwash velocity over the whole rotor disk area. In other terms, the blade sectional lift is theoretically constant: $\theta(r)r = \text{const}$. This can be achieved with the hyperbolic θ_{tip}/R blade twist distribution since the angle of attack must compensate for the lack of dynamic pressure close to the blade root [3]. While such high twist rates are common for propellers, there are practical problems in helicopter applications. It is well documented that high blade twist is undesirable in forward flight, as it is a source of vibration. This was also experimentally confirmed in the unpublished report by DSTL (Defence Science Technology Laboratory) [4]. Furthermore, the high angle of attack inboard leads to increased retreating side stall, as the maximum lift angle of the aerofoil is surpassed. The advancing side tip will also be pitched negatively to achieve trim, which reduces efficiency and increases vibration. Non-linear twist distributions require more complex moulds, and are more costly to design and build. Linear twist distributions can approximate the hyperbolic function reasonably well in the outboard half of the rotor blade, and mainly differ in the root cut-out region, where the rotor hub and hinges take up space. Johnson's [5] wind tunnel tests of linearly twisted rotor blades found that the coefficient of thrust was constant if the blade pitch at 75% R was constant. Therefore, the rotor collective of such blades is usually defined as zero, where the chord line of this spanwise station lies in the principal rotor disk plane.

Beyond the maximum endurance advance ratio, the parasitic drag becomes significant, and the airfoil on the advancing side will reach the drag-divergence Mach number M_{dd}. Rotor blades, especially with thick aerofoil sections outboard of 75% span, suffer from compressibility effects at high advance ratios. The parasitic power P_p is a result of many contributions including friction and pressure drag on the airframe and rotor hub. It is proportionate to the forward flight speed as $P_p \propto V_\infty^3$. Therefore, the gross weight plays a smaller role in fast forward flight than in hover as seen in Figure 1.4.

The aerodynamic phenomena of rotor flow have large ranges of time and spatial scales. The near-blade flow has significant time-variations, and is vortical. While the strong tip vortex is preserved and slowly breaks down, the vortex sheet, which is shed along the length of the blade diffuses earlier. In the far field, the tip vortices at the sides of the rotors roll-up into a large scale, low frequency structure. The far field phenomena are most relevant to rotor performance predictions in cases of low advance ratio.

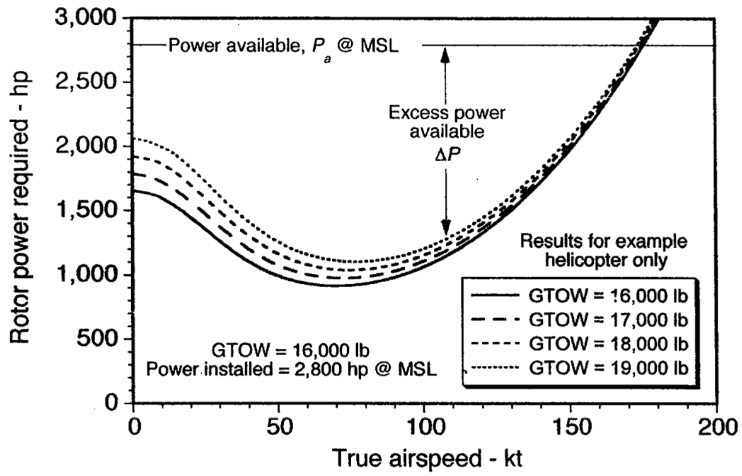

Figure 1.4: Example Helicopter power requirement from hover to high-speed flight for different gross take-off weights (GTOW) [6, p. 228].

1.1.2 Vibration Control in Helicopter Applications

The rotor of a helicopter is the main cause of vibration due to the unsteady loading. The vibratory loads are then passed from the rotor blades, through the hub, the main shaft, the gearbox and engine to the airframe. At every point where the loads are transferred, some vibration reduction measures can be taken. Vibrations are detrimental to the operation of the helicopter. They cause large discomfort to the pilot and passengers, which can be especially crucial for air ambulances and other rescue operations. Vibrations also exacerbate mechanical wear on helicopter components. The rotor blades, which are a significant cost factor to the helicopter, directly experience significant steady and unsteady loading. Therefore, they are usually mounted in a way, which allows them to rotate around a hinge point or similar semi-rigid assembly, to reduce the blade stresses. The collective and cyclic controls are passed onto the rotor blades via the pitch-links. The forces required to overcome the blade pitching moment C_M and torsional inertia I_{rot} are called the control loads. Large pitching moments in the local blade reference frame increase the control loads, which causes additional mechanical wear and creates a need for heavy force amplifiers. Unsteady blade loads are also partially transmitted through the rotor shaft and bearings into the gearbox and engine and to the airframe. The service life of parts is reduced and the operating cost increases with vibrations [7]. Vibration reduction is also integral when delicate electronics or sensors are integrated into the airframe, especially on the rotor hub, to extend service life and to avoid erroneous noise in the measurements.

Number of Rotor Blades

An important early design consideration is the number of rotor blades used. To illustrate this, consider the sum of all blades' periodic loadings on a rotor hub. Equations 1.1 to 1.7 show a rigorous derivation of [1, pp. 291–293]. The forces can be expressed by their harmonics via a Fourier series. The complex forcing term A_n contains magnitude and phase information ($A_n = |A_n|\angle\phi_n$) for multiples of the rotational frequency n. For an N_b-bladed rotor with equal spacing, the added phase for each blade is $\phi_k = (k-1)\phi$, where $\phi = 2\pi/N_b$. Summing the harmonic loading on the rotor as a function of azimuth ψ in terms of cosine or natural logarithm:

$$F(\psi) = \sum_{n=0}^{\infty}\sum_{k=1}^{N_b} A_n \cos\left(n\left(\psi + (k-1)\phi\right)\right) \tag{1.1}$$

$$= \sum_{n=0}^{\infty}\sum_{k=1}^{N_b} A_n \frac{e^{in(\psi+(k-1)\phi)} + e^{-in(\psi+(k-1)\phi)}}{2}. \tag{1.2}$$

Evaluating the finite geometric series via the substitution $\sum_{k=1}^{N_b} r^{(k-1)} = \sum_{k=0}^{N_b-1} r^k = \frac{r^{N_b}-1}{r-1}$ and substituting for ϕ results in:

$$\begin{aligned} F(\psi) =& \frac{1}{2}\sum_{n=0}^{\infty} A_n e^{in\psi}\left[\frac{\left(e^{in2\pi/N_b}\right)^{N_b}-1}{e^{in2\pi/N_b}-1}\right] + \\ & \frac{1}{2}\sum_{n=0}^{\infty} A_n e^{-in\psi}\left[\frac{\left(e^{-in2\pi/N_b}\right)^{N_b}-1}{e^{-in2\pi/N_b}-1}\right]. \end{aligned} \tag{1.3}$$

This generic forcing function is undefined as $e^{in2\pi/N_b} = 1$ and $e^{-in2\pi/N_b} = 1$ for any harmonic $n = mN_b$, where $m \in \mathbb{Z}$ and zero otherwise. Therefore L'Hopital's rule is applied, to find the forcing function when n approaches mN_b:

$$\begin{aligned} F(\psi) = \frac{1}{2}\lim_{n\to mN_b}\sum_{n=0}^{\infty} A_n \Bigg[& e^{in\psi}\frac{\frac{\partial}{\partial n}\left(\left(e^{in2\pi/N_b}\right)^{N_b}-1\right)}{\frac{\partial}{\partial n}\left(e^{in2\pi/N_b}-1\right)} \\ & + e^{-in\psi}\frac{\frac{\partial}{\partial n}\left(\left(e^{-in2\pi/N_b}\right)^{N_b}-1\right)}{\frac{\partial}{\partial n}\left(e^{-in2\pi/N_b}-1\right)}\Bigg]. \end{aligned} \tag{1.4}$$

Simplifying the expression and considering only the set of positive integers $n \in \mathbb{N}^+$, which results in $e^{in2\pi} = 1$ and $e^{-in2\pi} = 1$:

$$F(\psi) = \frac{1}{2}\lim_{n\to mN_b}\sum_{n=0}^{\infty} A_n\left[e^{in\psi}\frac{2i\pi e^{in2\pi}}{\frac{2i\pi e^{in2\pi}}{N_b}} + e^{-in\psi}\frac{-2i\pi e^{-in2\pi}}{\frac{-2i\pi e^{-in2\pi}}{N_b}}\right]. \tag{1.5}$$

$$F(\psi) = \lim_{n\to mN_b}\sum_{n=0}^{\infty} A_n \frac{\left[e^{in\psi}N_b + e^{-in\psi}N_b\right]}{2}. \tag{1.6}$$

We find, that the real part of the forcing function is $e^{in\psi}N_b$ for $n = mN_b$ and zero otherwise, and expressing the logarithms as cosine, this results in the total forcing:

$$F(\psi) = \begin{cases} \sum_{m=0}^{\infty} \left(A_{mN_b} \cos(mN_b \psi)\right), & \text{if } m \in \mathbb{Z}^+. \\ 0, & \text{otherwise.} \end{cases} \tag{1.7}$$

Assuming the harmonic forces A_n are all unity without phase offset, we can see that for an N_b-bladed rotor, only integer multiple harmonics of N_b are transferred through the rotor. An example of this is shown in Figure 1.5. If the same analysis is repeated for harmonic blade forcing of induced moments $F_M(\psi) = \sum_{n=0}^{\infty} \sum_{k=1}^{N_b} A_n \cos(n(\psi + (k-1)\phi)) r \sin(n(\psi + (k-1)\phi))$, we find that harmonics which are $N_b \pm 1$ are transferred. Hinged rotors also transfer less of the blade moments to the hub, as they are usually allowed to flap freely, and lag with some damping. Hingeless rotor hubs, or otherwise semi-rigid assemblies transfer more of the moments into the hub.

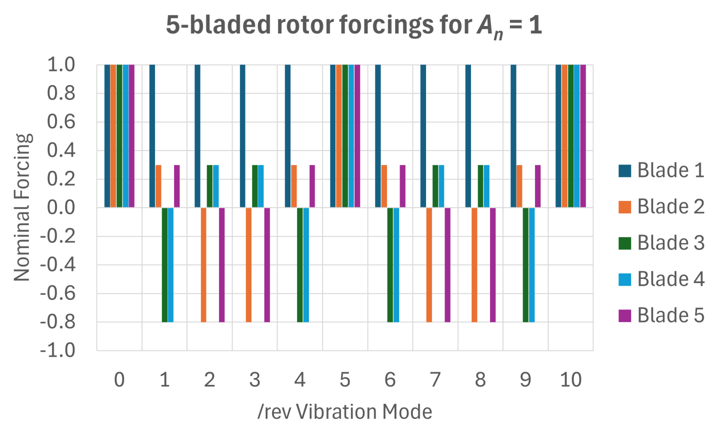

Figure 1.5: Example forcing components for a 5-bladed rotor, considering the simplified case where $A_n = 1$. Only at frequency multiples of $N_B = 5$, the vibration components do not cancel out. 0/rev is a static loading.

In reality, these amplitudes are not of the same phase and usually decaying at increasing harmonics. Nonetheless, higher blade numbers are preferable for vibration reduction, as most of the low-frequency, high-amplitude harmonics are diminished by opposing blade forces. This is especially true for the pitching and rolling moment contributions, as demonstrated in Figure 1.6, where at high forward speed, the moment contributions escalate for the example 4-bladed rotor. However, high numbers of rotor blades also need increasingly complex and large rotor hub assemblies. Currently, the most popular choice for newly introduced medium-sized utility helicopters is 5-bladed; 7-bladed helicopters are viable when high lifting capability is required.

Vibration and noise are also generated at a wide range of frequencies, which do not fall on a multiple of the rotor frequency. The draggy rotor hub in particular creates large amounts of turbulence, which can be ingested by the tail rotor. Even more significant are the trailing tip vortices of the rotor blades, which might impinge on the boom, fin and rotor at the tail. Hovering in ground effect (HIGE) causes the turbulent air to be recirculated back through the

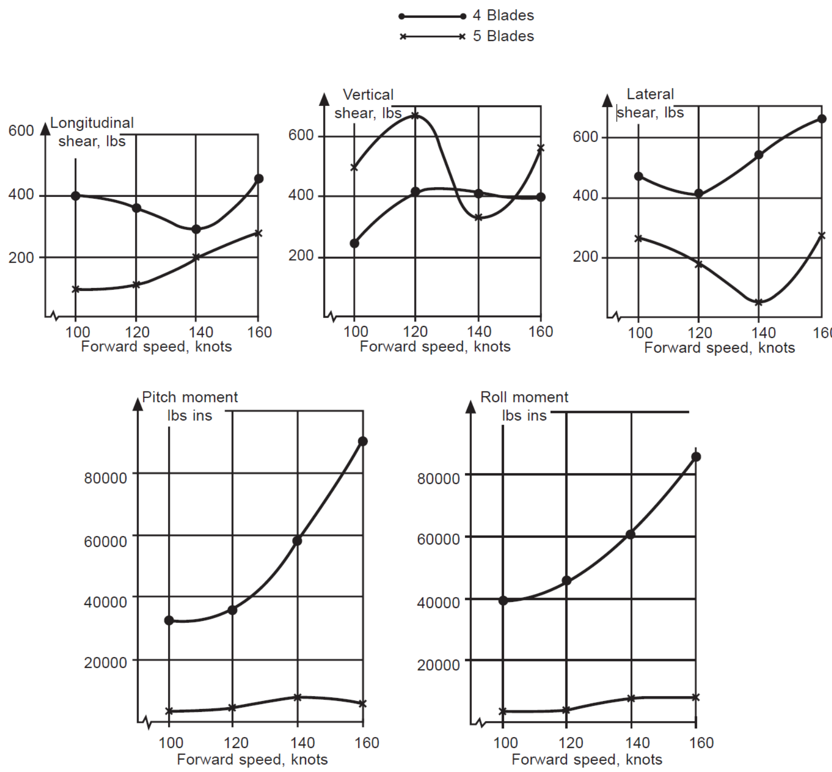

Figure 1.6: Typical vibratory loads experienced by 4 and 5 blade variations of a typical medium-weight helicopter using a semi-rigid hub, considering real loading where A_n is complex. From [1][p. 294]

rotor disk, which in the worst case can cause terminal structural resonance. Flying at a high side-slip angle can cause fluid-structure cross-coupling with tail boom bending. Often, clear aerodynamic separation points are needed on the lower edges of the airframe and boom, to avoid uncontrolled flow separations of the rotor downwash. This undesired side-loading induced by this phenomenon is comparable to the flow over a cylinder, besides the additional cyclic pressure waves and impinging vortices.

On-Rotor Vibration Reduction

Blade structural design is another important engineering task for vibration avoidance. Around the target rotational speed, the structural resonance frequencies of the rotor blades should not coincide with the multiples of the blade passing frequencies. Specifically, frequencies, which are amplified by the blade number, as expressed in Equation 1.7 are critical but can be difficult to avoid. Stiffening the blade skin, spar and trailing edge increases the structural frequencies but comes with increased weight. Care must be taken when the blade structural axes (neutral axis, elastic axis, centre of gravity line) are modified since cross-coupling between modes can have large unintended consequences or introduce blade torsion. Flutter, stall flutter, and pitch-lag coupling can all produce significant vibrations in helicopter applications and should be avoided. Typically, articulated rotors use lag dampers mounted between the rotor blades and hub. The lag dampers avoid excessive chordwise rotating hinge motion, to improve aerodynam-

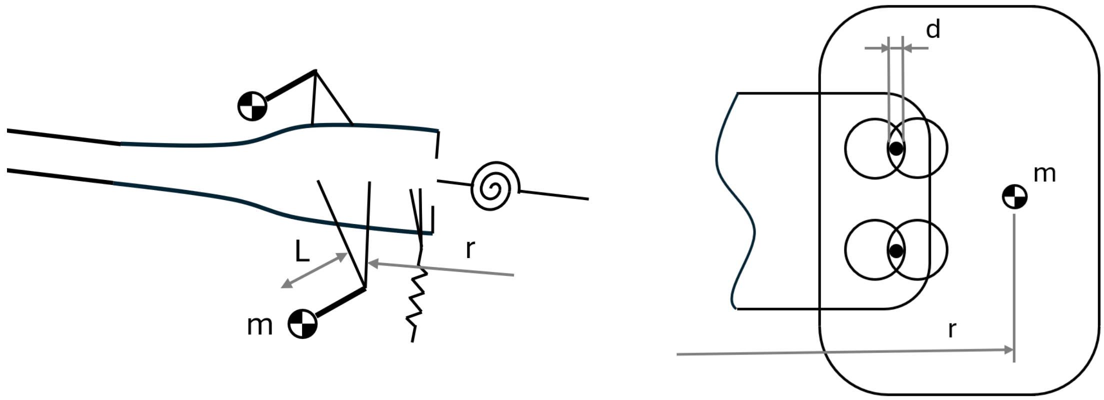

(a) Pendulum absorbers (b) Bifilar absorber

Figure 1.7: Illustrations of two types of rotor head vibration absorbers.

ics in high-speed flight and to stabilise the spin-up when centrifugal forces are low. Lag dampers are often made of an elastic rubber-like material, adding a spring component. Magnetorheological dampers can adapt the damping properties to the flight condition. Rotor blades must also be manufactured with the smallest possible differences in each set, as uneven blade-tracking can cause unforeseen aerodynamic and structural problems, inducing vibration. Usually, blade tuning masses are inserted at a mid-span and tip location. The same applies to other spinning components such as in the drivetrain to some extent.

Multiple types of vibration absorbers exist on the rotor head, and they are often combined to limit vibrations where they are generated. These are usually based on mass-spring systems, where the spring part can come from the centrifugal force under changing angles. Such absorbers are often bulky and increase the rotor hub drag and mass. A commonly seen type is the pendulum absorber, attached to or near the rotor blade root. It involves a mass on a lever arm, which responds to the periodic blade flapping, as a product of the rolling and pitching moments trim. For 4-bladed rotors, these masses are often tuned according to $3\times$ or $5\times$ the rotational speed. Bifilar absorbers are tuning masses, which can move in circular patterns — in the rotor plane — to counteract in-plane forces and variations of the rotor torque. Another mechanism is the flexispring absorber of Figure 1.8 (a), which sits in the centre of the rotor hub. A long coiled spring connects the large, tuned mass of its housing to the hub and shaft. This mainly absorbs torque variations for the tuned frequency, but can also reduce in-plane vibrations [1, pp. 290–318]. Such systems however, required regular maintenance and their effectiveness is limited during maneuvering flight. Similar to bifilar and flexispring absorbers, a variable off-centred spinning mass can also be attached to the rotor head shaft [8].

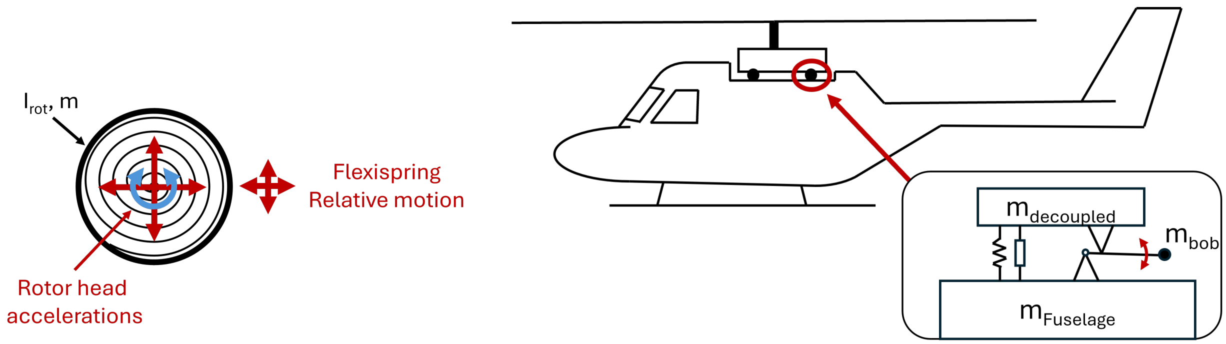

(a) Flexispring absorber (b) DAVI system

Figure 1.8: Illustrations of the flexispring rotor head absorber and the DAVI (Dynamic Anti-Resonant Vibration Isolator) between fuselage and gearbox, engine and rotor.

Gearbox and Engine Mounting

With the rotor shaft connected to the gearbox and engine, it is vital to decouple the assembly from the airframe. Simple elastomer or spring-based systems, coupled with the mass of the engine, gearbox and rotor can be employed. This method, however, suffers from large static deflections during manoeuvres with higher accelerations and has limited potential to reduce vibrations. These issues can be overcome through smart arrangements of springs and dampers, or by allowing the whole upper structure to hinge around a forward mounting point. A mechanism called Dynamic Anti-Resonant Vibration Isolator (DAVI), employs a swinging mass counterweight on a lever arm in addition to springs. It is shown in Figure1.8 (b). The bob mass m_{bob} is accelerated in the opposite direction of the overhead mass at a multiple rate. Once again, these mechanisms must be tuned to attenuate a specific frequency, such as the blade passing frequency, to be most effective [1, pp. 290–318].

Airframe Vibration Reduction

Through finite element analysis and experiments, the structural modes of the airframe need to be identified. Just as with rotor blades, structural modes near the strongest forcing frequencies of the rotor must be avoided. Through stiffening and weakening structures, and adjusting the position of on-board systems, vibration in critical areas, such as the cockpit may be reduced. Heavy subsystems of the airframe can also be elastically mounted, as mass-spring vibration absorbers. One example is the battery of the Sikorski Sea King on a leaf-spring assembly (Figure 1.9). Absorbers such as these can also be mounted in specific positions, such as at the nose, under the cockpit or near the pylon, where packaging permits.

The Active Control of Structural Response (ACRS) system uses multiple actuators inducing vibrations into the airframe to exploit destructive wave-overlapping. Accelerometers measure the airframe vibrations and through a control loop, the actuators respond. As with other vibration control systems, they add mass and maintenance requirements to the helicopter. Active control

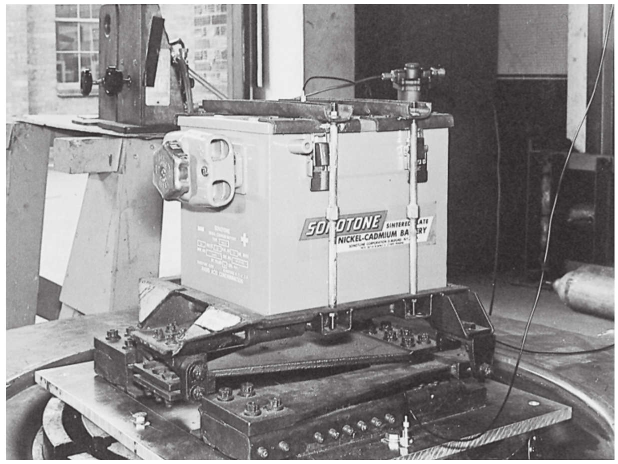

Figure 1.9: The battery on a spring-tuned mass vibration absorber, from [1].

systems also require a source of power for piezoelectrics or to pressurise hydraulic fluid [1, pp. 290–318].

On-Blade Vibration Reduction

The possibilities to reduce vibration with passive blade designs are relatively limited, and blades are preferably optimised for aerodynamic efficiency and load capacity. Nonetheless, some design choices affect the vibration characteristics, mainly due to Blade-Vortex Interactions (BVIs). Highly twisted rotor blades produce only a small amount of downwash near the blade tips. In low weight flight with correspondingly low collective angles, tip-vortex ingestion and highly unsteady, vibratory aerodynamic loads can occur. Similarly, a high blade twist increases vibration at high forward flight speeds, partially through the negative tip loading on the advancing side. Care must be taken to account for the interactions with tip vortices and previous blade shear layers to avoid vibration in the relevant flight conditions and maneuvres.

On the other hand, many active on-blade control mechanisms exist, with the goal to improve aerodynamic performance, and to reduce noise and vibration through similar means [9]. Examples of this are: active morphing trailing edges, active flaps, active Gurney flaps, active pitch links, active twist and other active aerodynamic parts, such as slats or integrated jets. Higher-harmonic control (HHC) systems on the rotor head, which usually use piezoelectric or hydraulic actuators have been developed since the 1990s. A more comprehensive review of the development on higher-harmonic and independent blade control (IBC) is represented in Section 2.3. Such methods have the potential to apply an input to the blade at multiples of the blade rotating frequency, compared to the 1/rev of ordinary helicopter swashplates. Also, active pitch link systems such as IBC (Individual Blade Control) have been flight tested [10]. For example, this higher harmonic control fitted on the BO-105 reduced vibrations by 60%, and power savings of 6% in fast forward flight were observed at low actuation amplitudes of less than 0.67°.

The active twist method is considered in this dissertation due to its potential advantages over the other technologies. Active twist actuators are stressed members, which can be integrated into the blade skin, adding little parasitic weight. There are no exposed moving parts, which makes them suitable for dusty environments, like brown-out conditions, without added maintenance. The blade returns to its passive shape when the voltage supply is disabled, ensuring airworthiness even during failure. Because the blade is deformed over its radius, high actuation energy is required, however, aeroelastic coupling can be exploited to tailor the blade eigenfrequency to the desired actuation frequency. The skin-integrated nature of such actuators also makes repairs more difficult, so these systems should be designed for a similar lifetime as the passive blade.

1.2 Objectives of this Research

The main novelties targeted for this research are to:

- employ combined high-fidelity simulation and coupling methods for aero-servo-elastics,
- quantify the effect of twist on vibration and performance for a simple planform rotor,
- evaluate the benefits of embedded active twist systems through numerical simulation.

1.2.1 Employing Novel Simulation Methods for Aero-servo-elastic Rotors

The rotor blade flow velocity and effective angle of attack vary around the azimuth and span. In forward flight, the advancing side of the rotor disk experiences high Mach numbers, which requires intelligent tip design and moderate blade twist to avoid the formation of shockwaves with the consequent rise in drag, possible shock-induced flow separation, and formation of strong tip vortices. The blade tip should not be pitched negatively at this point. The retreating side, however, experiences a much reduced dynamic pressure and the whole blade needs to be pitched up to balance the rolling moment of the advancing side. In addition, the corresponding inboard section will experience locally reversed inflow and in many flight conditions, the tip vortex will hit or near-miss following rotor blades. Such blade-tip vortex interactions (BVI) add to the difficulty of predicting the rotor flow field and forces. Due to the issue with the rolling moment, the front and back of the rotor disk are loaded more to achieve the target thrust. The flow field also causes the rotor blades to elastically deform and vibrate, which are hinged at the shaft hub. This greatly reduces the vibration transfer onto the airframe and structural stress on the blade root. Predicting the blade structural response and the effect of vibrations and blade tracking on aerodynamics form part of the difficulty in rotorcraft simulations.

The tools used for simulations of fixed-wing aircraft have been considered mature, partially as dynamic aeroelasticity and vortex interactions are rare, or at least avoided by design. However, in rotorcraft there is a continued need for better predicting capability. Comprehensive rotor codes are commonly used and effective in predicting the aeroelastic rotor system, often also considering the airframe. They are continually improved to match the physics of reality and have been adapted to simulate higher-harmonic rotor blade control technologies, usually by either assuming a rigid blade rotation or by applying moments to the beam structural models. Aerodynamic models are often created from a mix of analytical and empirical models and struggle with complex vortex interactions and previously untested flow conditions. With steady improvements in computing power, CFD (Computational Fluid Dynamics) is increasingly used to predict and validate rotor designs and technologies. CFD can capture the physics involved in complex, novel problems, for which no suitable comprehensive models exist. With the introduction of on-blade active elements, accurately predicting the servo-elastic response and coupling this with aerodynamics becomes crucial. The modern materials used in on-blade actuators introduce problems of modelling time-dependent hysteresis behaviour and evaluating stresses. Accurate prediction is required to prove the airworthiness of these systems, and to stoke interest in further flight tests and full-scale demonstrators. While there has been work on aeroelastic coupling in CFD tool-boxes and research into actuator-dynamics modelling, the research conducted in this report intends to bridge the gap to create a full aero-servo-elastic simulation to predict the active twist rotor of the ongoing STAR (II) research project.

1.2.2 Evaluation of Active Twist in Rotorcraft Performance and Design

With aerodynamic propulsion devices, the power required to produce a set amount of thrust partially depends on the induced velocity of the air travelling through the propulsive device. The corresponding contribution is called induced power. From blade element momentum theory (BEMT), an ideal hovering rotor has uniform inflow. The induced power factor κ_i represents the contribution of inflow profile variation on the rotor power for a given thrust setting. For an inflow that varies with the radius according to the power law, $\lambda(r) = \lambda_{tip} * (r/R)^n$ the induced power in US-convention is expressed in Equation 1.8 [6, pp. 68, 127].

$$\begin{aligned} C_{P,i} &= \frac{\kappa_i C_T^{3/2}}{\sqrt{2}} \\ \kappa_i &= \frac{2(n+1)^{3/2}}{3n+2} \end{aligned} \tag{1.8}$$

A factor $n = 0$ describes results of the uniform downwash as $\kappa_i = 1$, so the rotor operates with the ideal efficiency for the given thrust. From this, we can define a metric of efficiency for a rotor in hover, called figure of merit (FM/FoM). The figure of merit is the ratio of actual rotor power, compared to the ideal rotor power without induced drag, and is defined for a given thrust coefficient [6, p. 70]:

$$FoM = \frac{P_{ideal}}{P_{actual}} = \frac{C_{T,actual}^{3/2}}{\sqrt{2}C_{P,actual}} \tag{1.9}$$

Knowing that the dynamic pressure depends on the square of the local section radius, an efficient hovering rotor must have a high angle of attack at the root and reduce it in the outboard direction. This is usually achieved by manufacturing the rotor blade with a linear pre-twist. A hovering rotor ideally has twist levels beyond $-20°/\mathrm{R}$, but highly twisted blades are known to cause large vibrations in forward flight.

Active, on-blade twist promises many benefits for rotorcraft. While hover requires a high twist angle, a lower one is preferable to avoid stalling the inboard section on the retreating blade in forward flight. A higher-harmonic actuation can be used to specifically manipulate blade flapping and vortex tracking [11]. This potentially enables power, noise, and/or vibration reductions in high-speed flight and noise and vibration reductions in descending flight. By manipulating the blade tracking, a sufficiently actuated blade has the potential to replace the swashplate system through changes in effective inflow angles.

To evaluate the vibration characteristics and the efficiency of a rotor in forward flight, a vibration intrusion index and an equivalent lift-to-drag ratio are defined. The lift-to-drag equivalent ratio $L/D_e = \frac{C_L}{-C_X + C_Q/\mu}$ equates the torque to the created rotor propulsive force. With negative rotor shaft tilt (α_s), such as for a rotor at high speed, creates a net propulsive force (wind axis upstream). At 0° shaft angle, translational drag is created in addition to the rotor torque.

The vibration index (VI), described in Equation 1.10 was created based on an Intrusion Index (II), which measures harmonic vibrations experienced throughout the aircraft [12]. It is calculated from the N_b/rev and $2N_b$/rev harmonic components of the aerodynamic forces $F_{x,i}, F_{y,i}, F_{z,i}$, roll and pitching moments $M_{x,i}, M_{y,i}$ of the full rotor head. Here, i represents the harmonic of a 4-bladed rotor:

$$VI = \sum_{i=4,8} \left[\frac{\sqrt{(0.5F_{x,i})^2 + (0.67F_{y,i})^2 + (F_{z,i})^2}}{W_0} + \frac{\sqrt{(M_{x,i})^2 + (M_{y,i})^2}}{RW_0} \right], \tag{1.10}$$

where $W_0 = 3600\,\mathrm{N}$ represents the nominal model scale weight and $R = 2\,\mathrm{m}$ is the rotor radius of the STAR, which is evaluated in Section 5.3. The same index is also described in reference [13].

Chapter 2

Literature Survey

A literature review is performed to study the current state-of-the-art in the area of active rotor design and to determine the aims and objectives of the present research. The literature survey was conducted by searching scientific databases such as SCOPUS, Science Direct, Aerospace Research Central and the NASA Technical Reports Server, using keywords related to each subtopic in the literature survey. Additionally, conference proceedings of the Vertical Flight Society (VFS, formerly AHS) and European Rotorcraft Forum (ERF) were consulted. The survey is focused on evaluating active twist and morphing rotor blades using numerical methods and begins with a historical overview of higher harmonic inputs to helicopter rotors using active swashplate systems or active flaps and Gurneys.

An overview of past experimental works on active twist rotors is presented next. Subsections cover the ATR-I, STAR, STAR-II and other experimental research efforts. These subsections include the blade geometry and structural properties, the implementation of the active twist system and a summary of wind tunnel test conditions and results, followed by a synthesis.

The literature review also covers numerical studies on active twisting rotors, focusing on performance improvements, and vibration and noise reductions. Current methods of on-blade twist actuation are then explained. Following this, the AIAA HVAB rotor test was selected to validate the aeroelastic methodology of this work and is therefore presented in detail.

Past work on the coupling between structural models, piezoelectric actuators and fluid dynamics solvers is shown in Section 2.5.2 and also discussed in the relevant methodology Section 3.2.2.

2.1 Mechanism of the Survey

As a starting point, combinations of keywords have been generated to find research papers on the topic of active morphing helicopter rotors on the databases of Elsevier SCOPUS, the American Institute of Aeronautics and Astronautics (AIAA), Clarivate Web of Science, and the Vertical Flight Society (VFS). Table 2.1 presents the findings, where the terms in brackets were required for some databases to filter only relevant results.

After removing the duplicates and sorting by relevance, the literature review was continued during the study period with background reading on related topics. Works from the proceedings of the above-mentioned conferences and Journals were regularly visited during the research to follow the state-of-the-art.

Table 2.1: Keywords and the number of results for the literature research on active twist related topics. Numbers in brackets show findings after duplicates were removed.

	SCOPUS	**Web of Science**	**VFS**
(helicopter rotor) morphing	33 (17)	–	20 (6)
(helicopter rotor) (active blade) piezo	38 (17)	59 (6)	19 (2)
(helicopter rotor) active camber	25 (14)	11 (1)	1 (0)
(helicopter rotor) active twist	193 (unsorted)	38 (24)	27 (21)
(helicopter rotor) (active) actuated blade	112 (27)	55 (14)	
(helicopter rotor) variable twist	100 (uns.)	126 (uns.)	

2.2 Passive Rotor and Tip Design

A full review of passive rotor blade and rotor blade tip design is outside of the scope of this work, though a comprehensive review is given by Brocklehurst [14], concluding that there is not yet a consensus on the ideal rotor blade shape, partially due to differing helicopter mission requirements and historic developments. The main planforms in the US are shear-swept and swept-tapered blades, in Europe, state-of-the-art uses parabolic, anhedral tips and forward-backwards sweep, while the UK has its unique BERP planform.

While early rotorcraft used wooden or sheet metal rotor blades with symmetric aerofoils such as NACA 0012, modern helicopters use composite materials and specially designed helicopter aerofoils. The strength and anisotropy of fibre-reinforced materials made way for lighter and stronger rotor blades and research to tailor the aeroelastic response for target flight conditions.

The easiest blades to manufacture are flat-tipped, which increases pressure drag and Blade Vortex Interactions (BVI). For high advance ratio flight, such a tip must be swept back, tapered or use a thinner section to avoid shock formation. Alternatively, modern planforms such as the British Experimental Rotor Programme (BERP, Figure 2.2) or PUMA blade with an increased near-tip chord or the Advanced Chinook Rotor Blade (ACBR) with its smooth dihedral-anhedral are in service or under development.

As shown in Figure 2.1 (a), the Composite Main Rotor Blade (CMRB) of the AH-64 Apache, from the Affordable Apache Rotor Program (AARP), used a rectangular planform with a 20° swept and tapered tip and has a $12^\circ/R$ twist. It was designed using mid-fidelity analysis methods

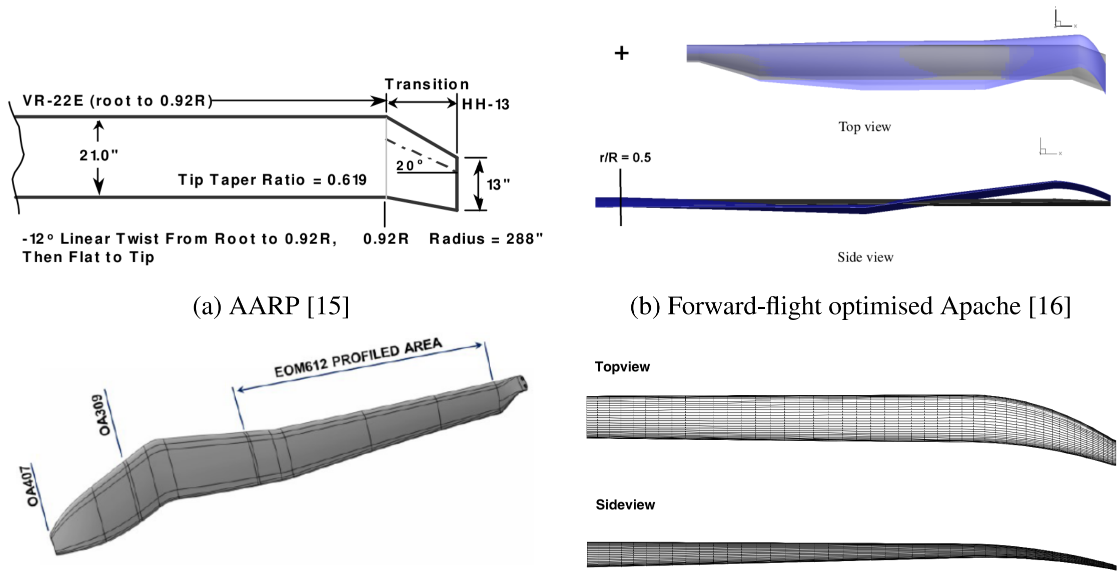

(a) AARP [15]

(b) Forward-flight optimised Apache [16]

(c) PROTEGE [17]

(d) Forward-flight optimised [18]

Figure 2.1: Modern, optimised rotor planforms.

and engineering judgement [15]. Thomas Fitzgibbon [16] investigated the aerodynamic optimisation of rotor planforms in hover and forward flight using CFD/CSD. The AH-64 rotor blade was optimised using an adjoint method, and a harmonic balance method for the temporal model, to reduce the computational cost. The structural models were of the 1D beam type, where properties were scaled with chord size. 3D-FE models were also used. The resulting blade shape of the forward-flight optimisations is shown in Figure 2.1 (b). It is anhedral-dihedral, with tapered, parabolicly swept tips and showed shaft power and vibration reduction compared to the baseline blade in HMB3. The work also presented a review of rotor optimisation methods used in academia and industry.

The Blue-Edge blade, a development from the ERATO blade used a forward-backward swept tip with taper, which resulted in reduced hover noise emissions without losses in forward flight and with reduced vibrations [19]. A combined hover and forward flight optimisation saw a further improvement toward the PROTEGE planform, with an increased chord at the 70%R span. This was determined as beneficial to high lift capacity in the research of BERP [17]. The planform is forward-backwards swept with a taper, without increasing control loads. Imiela of DLR [18] concluded rotor optimisation to be highly multi-modal and require a global optimisation scheme, after employing three different optimiser algorithms on high-fidelity CFD coupled with structural dynamics. A failure-or-crash surrogate model was added to the previously investigated surrogate model. This, with a mixed fidelity approach, showed the potential to decrease computational effort, while also showing the robustness of the result [20]. Both works optimised a rectangular blade and found the optimum for moderate twist ($10°$–$14°/R$), backwards swept, tip anhedral, tapered blades. The parameterisation was restricted, not allowing for more complex planforms. Optimisation efforts as such are still ongoing with parameterised planforms and

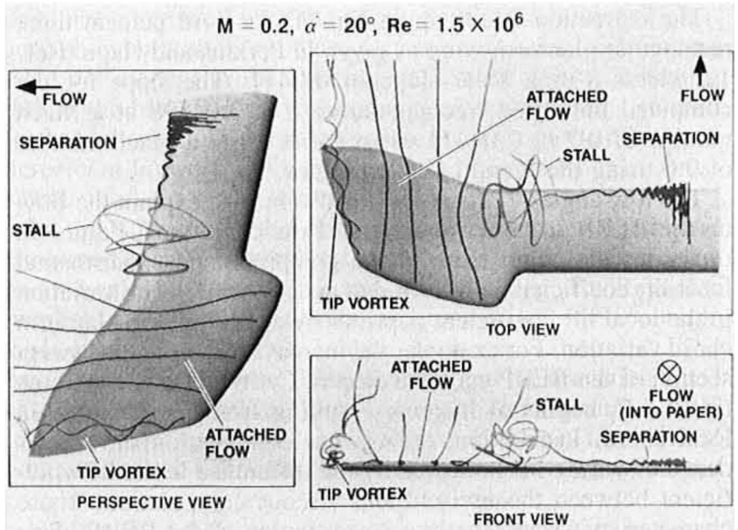

Figure 2.2: BERP III at high angle of attack with the "unstallable" tip due to tip-relief [22].

constraints [21].

The BERP planform creates a conventional tip vortex and a notch effect, which provide tip relief to achieve an "unstallable" tip, negating the disadvantages of low-thickness aerofoils as seen in Figure 2.2. This, combined with the outboard increasing sweep allows for usage in high advancing Mach number, while the tip does not stall on the retreating side [22]. Proving this high advance ratio envelope is the helicopter speed record of the Westland Lynx helicopter using BERP III rotor blades, with a peak Mach number of 0.977 on the advancing tip [23]. The forward offset outboard the notch also keeps the aerodynamic centre close to the feathering axis. The BERP blade uses a high-lifting aerofoil in the region of 70-85%R, with the inboard aerofoils countering the pitching moment [24]. The blade tip is also highly loaded compared to parabolic or anhedral rotor tip shapes. This allows for a higher tip-loading and a stronger tip vortex convection, affecting BVI.

While there is no clear trend for future rotor blade planforms, high-fidelity CFD/CSD is increasingly considered for optimisation studies. Rectangular planforms with sweep, taper and anhedral are a popular choice for optimisation studies because of their constrained design space and therefore computational effort. Many studies do not consider the effect of surface deformation on the blade structural properties yet, where coupling with 3D-FEM promises a further increase in fidelity.

2.3 Higher-Harmonic Control Input to Rotors

Conventional helicopters utilise a swashplate system around the rotor shaft, which transfers the quasi-steady control stick input of the pilot into the aerodynamic, rotating frame. The swashplate is made of two rings, where a control input lifts the lower, non-rotating ring at the azimuthal station where increased blade pitch is required. Spherical bearings transport this displacement

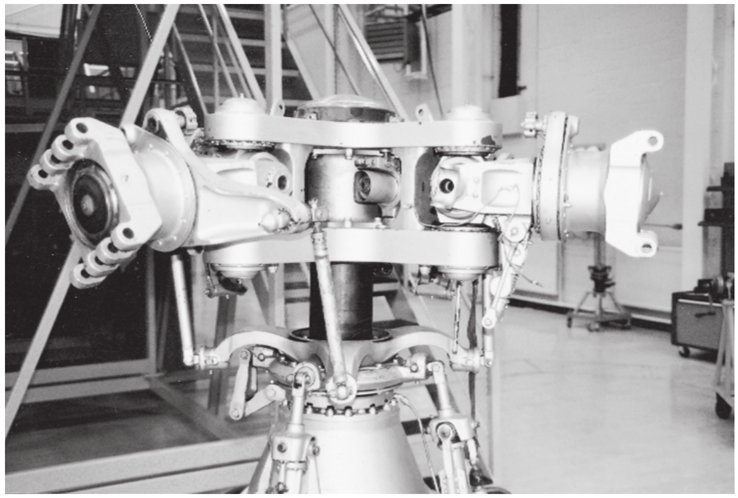

Figure 2.3: Westland Wessex rotor hub [1, p. 5]. The image shows the pitch links between the blade root attachments and the swashplate. The swashplate is actuated by links in the non-rotating system, visible at the bottom.

into the rotating part of the swashplate, which is connected to the rotor blades via pitch links. An example is shown in Figure 2.3. Substantial loads are transferred through this system, and it is critical to the operation of the helicopter. Lifting the full ring produces an overall increase in the blade pitch (collective control angle), whereas tilting the disk gives lateral and longitudinal cyclic control. The latter changes the blade pitch at the rotational frequency, at a phase and amplitude determined by the stick input.

Higher-harmonic control (HHC) is a concept, where the blade aerodynamics and kinematics are influenced at multiples of the rotational speed. The most obvious and simple approach is the actuation of the pitch links through a periodic variation of the blade collective at the swashplate. Such higher harmonic control systems have been studied since the 1990s and promise vibration and noise improvements through their targeted effect on these higher frequency blade dynamics. Additionally, such systems may be leveraged for performance and efficiency gains. Friedmann [25] showed the difficulty of achieving multiple actuation objectives with a single active system on a rotor. A focus on vibration reduction partially prohibits gains in noise reduction or performance.

This method of periodic changing collective has been demonstrated as an effective method to cancel vibratory load components on the rotor hub [26]. Cheng *et al.* [27] used a reduced fidelity analysis to show possible helicopter power reductions in high-load scenarios using HHC. This system could also be extended to Individual Blade Control (IBC), with either an increasingly complex swashplate system, or without swashplates as demonstrated by Kessler [28]. Instead of a single hydraulic actuator, which moves the swashplate, IBC requires one actuator per blade or per harmonic, depending on the implementation. Individual blade actuators may for example be attached to the the spinning pitch links of the rotor blades. Another such system is using multiple stacked swashplates (DLR META) to achieve higher-harmonic IBC [29]. Both methods add more complexity below the rotor hub and need powerful actuators, which in the former case must be rotationally decoupled from the airframe. These methods have been shown effective at reducing the BVI noise and vibrations [30], but HHC and IBC are also power inefficient, as the full blade is actuated [25]. As mentioned earlier, IBC was also successfully demonstrated, with over 85 flight hours, reporting either large vibration and control loads reductions or some rotor power reductions [10]. A review paper by Kessler [31] outlined the need for individual blade control over HHC, especially for helicopters with four or more blades. It also presented a background on helicopter vibration control and noise reduction.

In the HART and HART-II [32, 33] international research collaborations, 40% Mach-scaled BO-105 rotors with IBC were tested in hover and forward flight. Extensive pre-test numerical prediction work was also compared to the experimental findings. In the HART-II project a large variety of measurements were taken, including performance data, flow data via particle-induced velocimetry (PIV), acoustic noise measurements, and much more. A large array of over 50 journal publications exist for this well-documented project. In a DLR and Konkuk University collaboration, Jung *et al.* [34] presented blade tomography data and applied this to finite element modelling, similar to how this was repeated in the STAR project [35]. The experiences from the HART and HART-II prediction, testing and post-processing were then carried over to the STAR project, which is described in Section 2.4.4.

Another issue with swashplate-actuation methods is the high stress on the pitch control system, and potentially fatal consequences in failure scenarios. Higher-harmonic actuation of trailing edge flaps and Gurney micro flaps can partially alleviate these problems. An advantage over whole-blade IBC is the lower actuation power requirement. The emergence of "smart" piezoelectric materials enabled active trailing edge flaps without hydraulic systems and allowed for multiple spanwise sections for localised control. However, a weakness of piezoelectric mechanism-based flaps is their reliability, as the space inside the blade is very limited, and the weight is far outboard. Milott and Friedmann [36] used comprehensive numerical analysis to show how higher harmonic flap actuation can provide similar vibration benefits as IBC at a fraction of the required power. A CFD analysis of actively flapped rotors by Dehaeze *et al.* [37] found the performance improvements in hover and forward flight limited to below 1%, while there were vibration benefits. The Smart Material Actuated Rotor Technology (SMART) research collaboration by Boeing, NASA, US Army, Air Force, DARPA, MIT, UCLA and University of Maryland [38, 39], was a full-scale active flap rotor for wind-tunnel testing. High-speed in-plane noise could be reduced by 5 dB through 3/rev, significant vibration reductions up to 80% were shown and in high-speed flight, around 2% L/D improvement was seen near the 90° phase. Another similar approach is the continuous morphing trailing edge, which uses piezoelectric skin composites similar to the active twist approach. Mistry and Gandhi [40, 41] have built a blade with a hybrid actuator approach, featuring an active trailing edge which effectively increased camber and pitch. It was designed using a combination of beam, shell and brick elements in the ANSYS v14 structural solver, and the actuation is created by spanwise extension or tension of the open skin profile.

Woodgate *et al.* [42] introduced active Gurney flaps into the HMB CFD solver framework, but highlighted the need for experimental validation data. These flaps create additional circulation, which improves lift. Pastrikakis *et al.* [43, 44] concluded that the active Gurney flap on a hovering W3-Sokol blade could not increase the maximum hovering figure of merit, but improved the efficiency at high collective angles. A 3.3% power reduction in forward flight due to a decrease in retreating blade stall could also be demonstrated [45, 46]. Implementation in experimental rotors is however difficult due to the small aerofoil thickness near the trailing edge, which makes it difficult to fit robust mechanisms. The surface discontinuities by such devices also bring aerodynamic drawbacks.

One more proposed option was discontinuous active blade tips [47–49], where a short section of the rotor blade is rotated around the pitching axis. A spanwise piezoactuator beam would bend up and down, to create the blade tip motion. The beam exploits a similar feature of the active twist, by using extension torsion coupling. Multiple opposing torsion pairs are used, to achieve a beam-bending via a torsion-bending coupling mechanism. In a model-scale test rotor, comparable tip authority was found to active twist blades at a fraction of the voltage, however, also only a fraction of the blade experiences the changed flow. This type of actuation also suffers from having exposed moving parts, which may potentially become stuck at unfavourable angles, and surface discontinuities which reduce the aerodynamic efficiency. Similarly, Amoozgar *et al.* [50] suggested a moving mass, which achieved active twist as a product of the centrifugal force experienced in motion. The work demonstrates the importance of the mass distribution on the expected rotor blade twist deformation.

A variety of other on-blade flow control methods have been conceptualised, such as synthetic jets, surface suction or blowing and plasma actuators. These methods, however, are only effective in limited regions of the rotor blade, and the reliability of these systems, especially in air particulate-heavy environments, such as sandstorms, is still a large concern.

More overviews of the various smart material and blade actuation concepts are also presented in the review papers [25, 51–53] among others.

Blade-integrated torsion actuators are considered in this study, due to their advantages over other higher harmonic control concepts. For example, without seams, thin ducts or moving exposed parts they have resistance to airborne sand, snow and other particulate. Also icing before take-off or in mid-flight is no concern. The actuators cannot become stuck in positions, which would cause aerodynamic or structural problems. In the case of an electrical failure, the piezoelectrics deactivate and return to the passive blade shape. These advantages are critical for both civilian and military adoption of this technology. A downside of the active twist method is the relatively high power requirement, as a large amount of strain-work is needed to torsionally twist the full rotor blade structure. However, with intelligent structural design, blade elastic resonance can be exploited, to reduce the actuator power at its design frequency.

For the development and certification of such devices, accurate simulation tools are needed. Often, structural optimisation methods are employed to maximise the control authority for a given energy input, which can create unconventional structural properties. High-fidelity aero-servo-elastically coupled tools are needed to quantify the safety of such novel rotor blades. Specially, where structural resonances are exploited, safety must be demonstrated in all possible flight conditions. To correctly simulate these difficulties and inherent couplings between in-plane and out-of-plane structural deformations, the HMB3 aeroelastic Navier-Stokes fluid solver is coupled to the commercial finite-element structural solver MSC NASTRAN. In this work, conventional 1D beam-models are compared to a 3D FE-model to determine which tools are suitable for accurate simulations of rotor blades with blade-integrated piezoelectric actuators.

2.4 Experiments on the Effect of Active Twist on Rotors

Validation data for active twist rotors is rare, and Table 2.2 presents active twist rotor experiments identified in this survey. The Active Twist Rotor (ATR) show the potential of active twist to reduce vibrations, and the STAR hover experiments emphasised the possibility of higher-harmonic twist to affect blade flapping and vortex convection. Additionally, the practical feasibility of an Advanced Materials Rotor (AMR) and a full-scale Active Low Vibration Rotor (ALVR) have been proven [54–56], however only a single blade each has been manufactured. The ATR, AMR and ALVR employed Active Fibre Composites (AFC), while the more modern STAR rotors use Macro Fibre Composite layers, which are described in Section 2.6.

Table 2.2: Active twist aerodynamic experiments in literature, static actuation amplitude is shown as peak-to-peak.

Name	**Radius** [m]	**Static actuation**	**Tests**
Smart Rotor	0.9	$\approx 0.5^\circ$	Hover [57], Forward [58]
ATR	1.4	1°	Hover [59], Forward [60–62]
AMR	1.5	2°	Hover, Structural [54,55]
ALVB	9.1	0.02°	Structural [56]
STAR-I	2.0	4°	Hover [11,63]
STAR-II	2.0	4.1°	Hover, Forward flight (planned 2025)

2.4.1 Smart Material Rotor by Chen and Chopra

In the early and mid-1990s, Chen and Chopra built and tested composite beams and model-scale rotors with piezoelectric fibres. As expected, the peak torsion response was achieved when actuators were mounted in a $\pm 45^\circ$ orientation to the elastic axis. Torsional stiffness has been identified as a main obstacle to high actuator amplitudes. Increasing the distance between the thin actuator patches improved the torsion response. The small torsion amplitudes require rotor blades to be mostly covered in actuator material. On the experimental blade dummies,

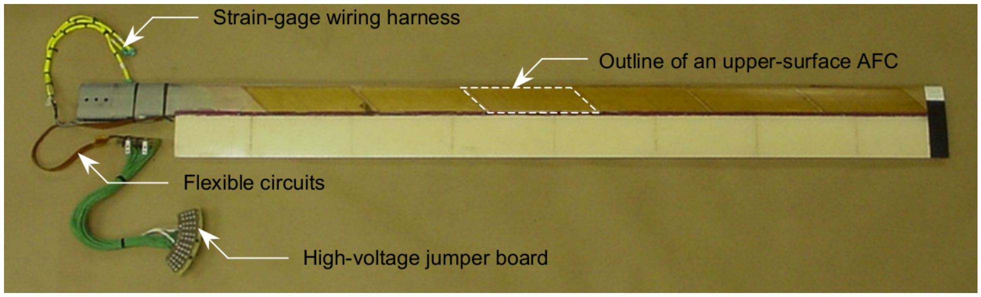

Figure 2.4: ATR-I rotor blade [60].

centrifugal stiffening, and the aerodynamic forces reduced the tip torsion amplitude by more than 80% [57]. The rotor was tested in the 11 × 7.5 ft section of the Glenn L. Martin wind tunnel at the University of Maryland. The rotor collective was fixed to 2°, and the rolling moment was trimmed to zero. For an advance ratio of 0.22, a NACA0012-based rotor of 0.91 m radius with single-layer actuators achieved 0.5° to 0.6° of peak-to-peak tip torsion depending on actuation phase and frequency (1/rev to 5/rev). A similar rotor with double-layer actuators managed up to 4.6° at the highest voltage for 3/rev 225° phase actuation, due to a structural resonance and reduced aerodynamic blocking force. In all actuation conditions of the low thrust forward flight, rotor torque has increased from the baseline rotor. Increasing n/rev was also shown to augment the rotor thrust. Some actuation frequency and phase combinations managed to significantly reduce rotor oscillatory pitching and/or rolling moments, such as 1/rev between 90° and 135° [58]. Additional results for low and high-advance ratios have been published in [64]. While the rotor experiments give hints on the performance improvements of actively twisted rotors, the simple construction of the rotor blade, the small rotor scale and the low thrust coefficient make it difficult to draw conclusions for full-size applications.

2.4.2 Active Twist Rotor (ATR)

A joint research program by NASA Langley/Army Research Laboratory and MIT numerically and experimentally investigated an Active Twist Rotor (ATR) built using active fibre composites (AFC). An early publication on the design and manufacture was presented in 1997 [65].

ATR-I Blade Geometry The ATR-I rotor was 4-bladed, with rectangular NACA0012 rotor blades. The blade radius was 55 in, with a nominal chord of 4.24 in. The blades were linearly pre-twisted by $-10°$. The root cut-out was located at 6.87 in and the trailing edge fairing starts at 12.5 in from the rotational centre [60,66]. The nominal rotor speed is given as 688 rpm, which equates to a tip speed of 100.65 m/s, or tip Mach number of 0.60 in the heavy gas atmosphere of R134a [60].

Active Twist System The active twist system was built from AFC plies inside the D-Spar. They were positioned above and below the rotor pitch axis and aligned at a 45° angle with

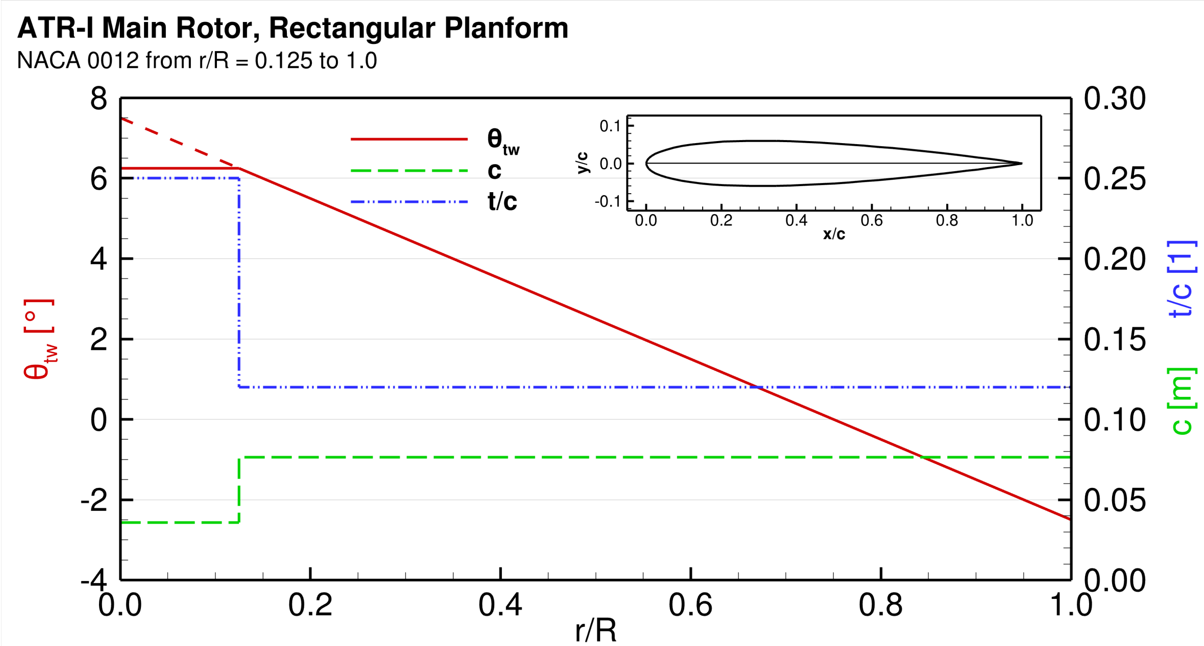

Figure 2.5: Twist, chord, thickness of the ATR-I experimental rotor blade.

the axis for maximal torsion. Five out of the 24 AFC actuators were damaged during high-voltage bench testing. Therefore the operating voltages were halved from the design voltage of $\pm 2000V$ [60]. Measurements with projection moire-interferometry showed a static peak-to-peak twist of 1.1° possible for 2000 V_{pp}. Another actuator failed during hover testing, even after reducing the voltage [60]. In non-rotating blade testing, at the first torsional mode at 85 Hz, the peak-to-peak response using $V_{PP} = 400$ V was measured as 3.5° [60]. The actuators were controlled in an open loop setting with harmonic voltage input synchronised with azimuth and described phase. The blades were instrumented with one chordwise, 6 torsional and 3 flapwise strain gauges.

Structural Properties The ATR rotor blade consisted of a D-spar section with a ballast weight at the front and a trailing edge fairing. The blade body was filled with low-density foam. The flap-lag hinge was on the main blade pitch-axis, at 3 in from the rotational centre. Multiple publications give the structural data for the sections of the rotor blade in the active ply region between r/R=0.31 and r/R=0.97.

Table 2.3 shows the blade mass per unit span, the centre of gravity and elastic axis offsets aft of the quarter chord (in units of chord length), the spanwise and torsional stiffnesses, the flap and lag stiffnesses, and the torsional mass moment of inertia reported in the literature. The values in the papers were obtained using cross-sectional analysis. Two sets of data appear, where one set describes the original blade layup design. The properties published in the master's thesis by Shin in 1999 [67] represent the "final" proposed blade design for whirl testing, however, an additional ply of E-Glass 90°/0° was applied to the leading edge to comply with fatigue limits

Table 2.3: Properties of the ATR-I blade main section outboard of 30%R.

Property	**Cesnik, 1999** [66]	**Wilbur, 2000** [60]	**Shin, 1999(final)** [67]	**Shin, 2001(modified)** [68]	**Shin, 2005** [62]
Mass/Length [kg/m]	1.4	0.7	0.696	—	0.6998
CoG offset [%chord]	-0.1%	—	-0.1%	-7.1%	-7.1%
EA offset [%chord]	5.8%	—	5.8%	9.4%	9.4%
EA [N]	1.637×10^6	1.637×10^6	1.637×10^6	1.787×10^1	1.787×10^6
GJ [N]	3.622×10^1	3.620×10^1	3.622×10^1	3.143×10^1	3.143×10^1
EI_{flap} [Nm^2]	4.023×10^1	4.023×10^1	4.023×10^1	4.416×10^1	4.419×10^1
EI_{lag} [Nm^2]	1.094×10^3	1.095×10^3	1.094×10^3	1.153×10^3	1.153×10^3
I_{xx} [kgm]	3.307×10^{-4}	3.309×10^{-4}	3.307×10^{-4}	3.810×10^{-4}	3.810×10^{-4}
Lock Number	4.55	—	4.55	9.0	—

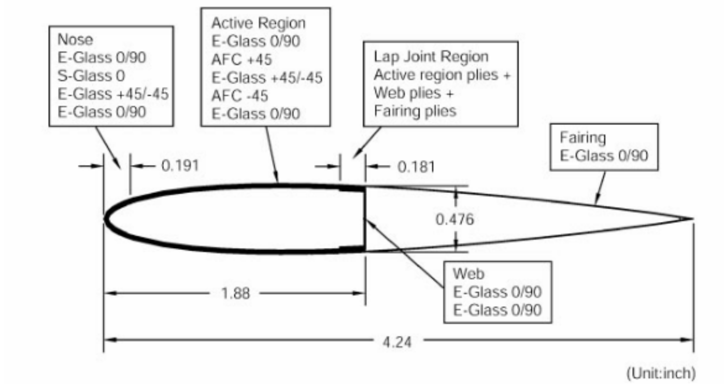

Figure 2.6: ATR-I rotor layup cross section [62].

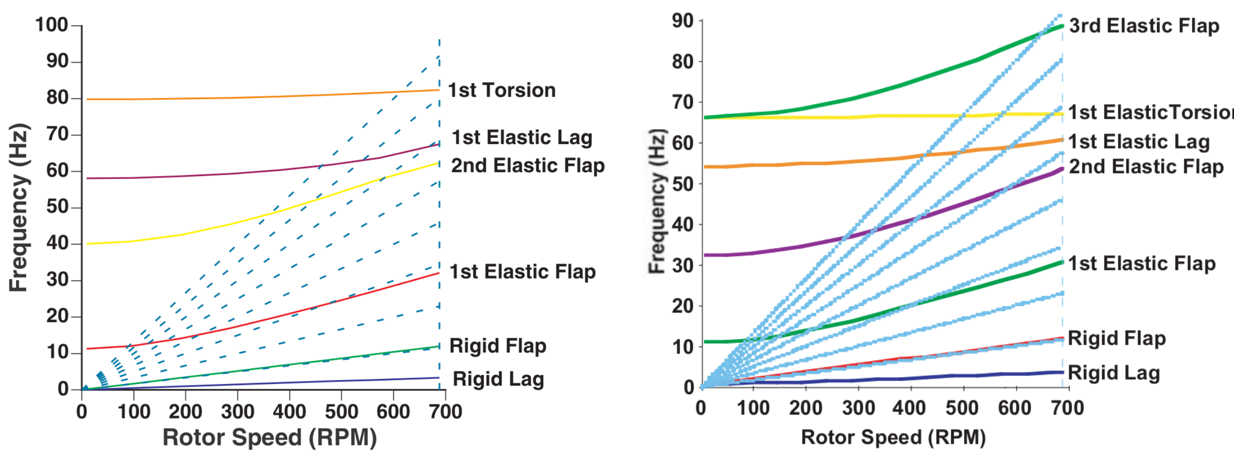

(a) Cesnik, 2001 [69] (b) Shin, 2003 [59]

Figure 2.7: Structural eigenmode fan-plots for ATR-I rotor of different iterations, in vacuum.

for wind tunnel testing [68].

The rotor blade layup is shown in Figure 2.6. The structural properties of the E-Glass, S-Glass, AFC packs and further details on the ATR-I blade properties were also given in the appendix of the theses by Shin [67][pp. 141–145], [68][pp. 151–152], the paper of Cesnik *et al.* [69] and in [70]. To predict the dynamic torsional amplitude of the experiment, a structural damping term needed to be included in the simulation work [66].

The ATR rotor eigenmodes were obtained numerically, and two sets of fan-plots were published, as seen in Figure 2.7. Subfigure (a) shows the fan-plot obtained from the "proposed" blade design, which is stiffer in torsion and has much smaller offsets of the centre of gravity and elastic axis from the quarter chord line. Plot (a) shows the same frequencies for the rigid modes and the first elastic flap, but higher frequency for the remaining given modes.

The rotational frequencies for the first two flap modes and the first torsion mode were obtained in the wind tunnel at nominal rotational speed and atmospheric air conditions. The frequencies in the experiment were found as the actuator frequencies with peak torsional responses. The non-rotating frequency of the first torsion mode was measured at 86 Hz, while the rotating

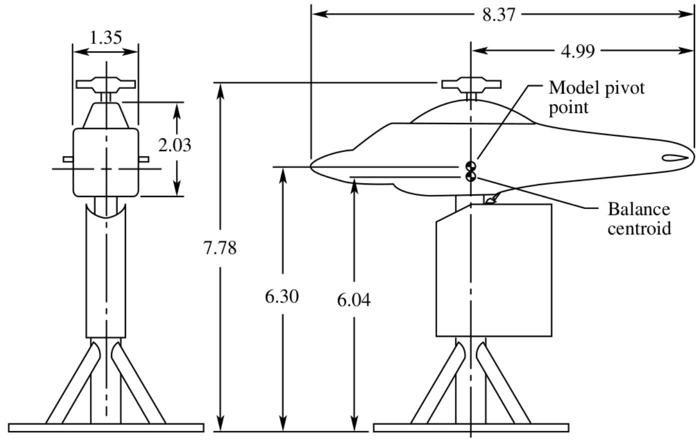

Figure 2.8: ARES test bed and fuselage fairing geometry. Measurements in feet. [60].

mode peak was measured at 81 Hz, even though centrifugal stiffening should cause an increase in the value. CAMRAD II predicted the moments at the strain gages at all conditions and it was found that gas density and rotor speed had the largest impact on the mode frequencies [60, 66].

ATR-I Rotor Test Bed The test bed for the ATR-I was the Aeroelastic Rotor Experimental System (ARES) helicopter test bed. The rotor shaft fairing was covered by a generic helicopter fuselage, shown in Figure 2.8. The test bed can monitor individual blade loads and position, pitch link loads for torsion and the full rotor forces, moments, speed and control angles. The wind-tunnel tests were conducted in the NASA Langley Transonic Dynamics Tunnel (TDT). The TDT allows the use of air and heavier gases. The lower speed of sound of around 160 m/s at ISA conditions [71] of R134a gas allows lower rotational speeds at model size, which gives more accurate time scales for rotor blade actuation. The reduced centrifugal loads also facilitate lower-stiffness glass fibre models with higher actuation capability. Due to the size of the TDT, the rotor hover tests were conducted in ground effect [60], limiting performance measurements.

ATR-I Wind-Tunnel Test Conditions The ATR-I rotor was tested in hover and in forward flight at advance ratios between 0.14 and 0.367. The nominal conditions are shown in Table 2.4 In hover, the rotor was tested in atmospheric air at 0°, 4°, 8° and 12° collective angles and with 500 V or 1000 V of actuator voltage. In R134a, the rotor was tested at 0°, 4°, 8° at 57.8 kPa and 8° collective for pressures from 38.3 kPa to 58.5 kPa [60]. Forward flight tests with open and closed loop controllers were conducted in the heavy gas environment of the TDT [59].

Shin [62] gives four test conditions for the closed-loop controller vibration testing at μ =0.14, 0.2, 0.267 and 0.333 at $C_T^{US} = 0.0066$. The rotor was trimmed to achieve a first flapping harmonic of less than 0.1°. The shaft angle was fixed to $-6°$ for the highest advance ratio. The same trim conditions were used in the open loop test [72].

Table 2.4: ATR-I Rotor Test Parameters [72].

Parameter	ATR-I
Nominal rotor speed	688 RPM
Nominal gas density	$0.0047\,\mathrm{sl/ft^3}$
Tip Mach number	0.6
Thrust for 1g flight	225 lbs

ATR-I Wind-Tunnel Test Results In hover, strain gauge readings of the hovering ATR rotor have been presented for an actuation frequency sweep. The first two non-rotating flap-bending modes were identified and matched the predictions of CAMRAD-II [68]. However, no performance measurements could be made, likely due to the ground effect and recirculation associated with the test setup. Projection Moire-Interferometry was used to obtain torsion amplitudes under excitation [73].

Mainly vibration results were published about the active twist results on the ATR-I in forward flight. A 3/rev actuation achieved the largest decrease in 4/rev fixed system loads, 65% at a low advance ratio and 95% at a high advance ratio (Figure 2.9). Rotating system loads could also be reduced. 4/rev actuation resulted in reduced rotating system loads except for a fivefold increase in pitch link force, which nullified the fixed vibration reductions. Blade torsion loads were increased at the harmonic frequencies of the actuation. The tip twist deformations for 3/rev, 4/rev and 5/rev at 200° phase were given for a $\mu = 0.2$, $\alpha_s = -1.0°$ cases and for ranges of $-1.4°$ to $1.5°$ delta from the baseline measurement in the blade front and retreating sections. The change in blade flap deflections with active twist is also provided in [72].

Further work [61] showed amplitude and phase changes of all measured fixed and rotating 4/rev force and moment components for the low advance ratio condition, including 3/rev to 5/rev actuation. These plots are shown for all advance ratios for 3/rev actuation. The actuator power required is shown to be linearly dependent on the actuation frequency and was up to 0.9% of the maximum rotor power at 5/rev.

The ATR has been tested in forward flight with a closed-loop controller. It managed to reduce 1/rev and 4/rev vibratory loads throughout the test range and proved much more effective than higher-harmonic pitch control of the same blade. With 1/rev actuation, blade tracking irregularities and BVI effects could also be reduced [62], showing another benefit of active twist blades.

The test facility provided hard, reverberating walls, so sound power could only escape via up- and downstream faces. The sound recordings were split into low frequency (loading, thickness noise) spectrum from 0.5 BPF to 6.5 BPF and BVI spectrum from 6.5 BPF to 40.5 BPF. The measurement errors were determined to be 0.7 and 0.5 dB SPL for the spectra. The sound pressure levels of the three upstream microphones were averaged and then averaged with the single usable downstream microphone, to weigh the front and back of the rotor equally. BVI

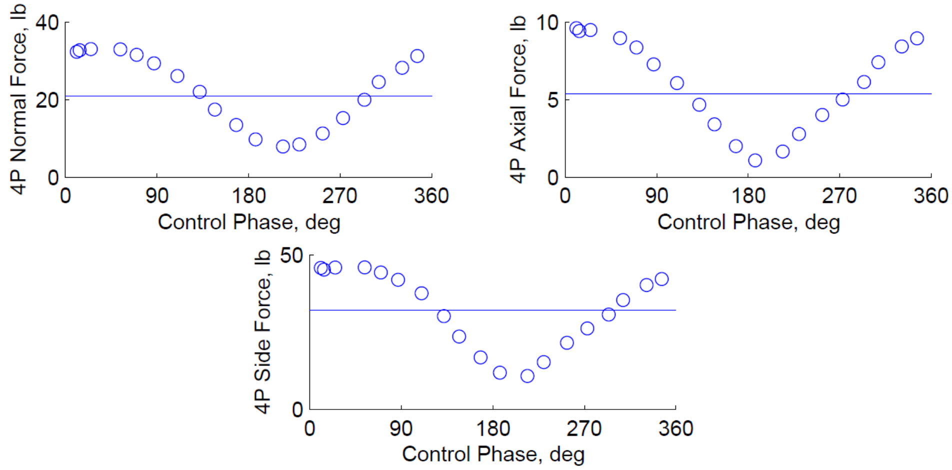

Figure 2.9: ATR-I hub forces at $\mu = 0.14$, $\alpha_s = -1.0°$, $C_L^{US} = 0.0066$, for 3/rev actuation of ± 1000 V actuation for all control phases [72].

noise reductions of up to 2.8 dB were obtained in varied advance ratios (0.14–0.27) and shaft angle ($-2°$–$8°$) settings. 3/rev to 5/rev actuation achieved similar results. The 5/rev active twist however came with a large low-frequency noise penalty, while 3/rev only had a small penalty [74].

2.4.3 Advanced Materials Rotor (AMR), Active Low Vibration Rotor (ALVR)

Starting from 1995, piezoelectric smart material applications have been studied for use in helicopter rotors at the Massachusetts Institute of Technology (MIT), with support from Boeing and NASA. A 1/6th-scale CH-47D rotor blade with internal torsion actuation was built by the Boeing Corporation to be compared with a passive and a trailing edge flap blade. Despite expectations, the piezoelectric skin-actuators proved as more cost-efficient and easier to implement than the flap, while providing 4° of peak-to-peak twist in the target actuation frequency, near the first torsion mode eigenfrequency. The rotor blades were hover tested, however, no performance data has been made available [54]. Wickramasinghe and Hagood [55] tested AFC actuator fibres and patches for their durability during actuation and simulated flight conditions. The material was found to withstand 20 million actuator cycles at 3000 V_{pp} without performance degradation and 10 million cycles in a simulated mixed actuation and mechanical fatigue test. However, upon closer inspection, burns and cracks were found at the fibre edges. Following this, a full-scale CH-47 LVR (Low Vibration Rotor) blade was produced, containing three layers of AFC in upper and lower surface each, which was called the Active Low Vibration Rotor (ALVR). The goal was to achieve 4° peak-to-peak torsion deformation while retaining 70% of the torsion strength. However, only 0.02° could be achieved at the maximum static voltages. The first torsion mode of the rotor blade was near 5/rev, so the 4/rev actuation could achieve the torsion target of 2° peak-to-peak in a bench test. Because of high actuator temperatures, the test was not extended beyond that point [56]. No aerodynamic test data has been published for any of the advanced material rotors. However, it was concluded, that skin-embedded actuators proved to be the most robust and cost-effective means of achieving a higher-harmonic input using piezoelectric materials. The skin-actuators are load-bearing structures and kept the rotor blade weight within 1% of the reference design, while alternative blades with fitted flap mechanisms were heavier outboard.

2.4.4 Smart Twisting Active Rotor (STAR)

The AcTOR (Active Twist Optimized Rotor) of DLR was the 4-bladed model scale test rotor designed and built in 2009–2013 for aerodynamic testing. It was sometimes referred to as Active Twist Blade (ATB) [75, 76]. It came as a result of the international FRIENDCOPTER (Integration of Technologies in Support of a Passenger and Environmentally Friendly Helicopter) effort, which considered active twisting rotor blades [77,78]. As other project partners joined the effort, it was re-named to STAR [11, 12].

A model main rotor with piezoceramic macro-fibre composite (MFC) on-blade actuators was produced in a collaboration of DLR, US Army, NASA, ONERA, JAXA, KARI and Konkuk University. It was the spiritual successor of the HART and HART II programs, which used a geometrically similar rotor model. In 2013 a hover test was conducted in a whirl tower hall of DLR. A test in forward flight could not be conducted because the on-blade actuators developed short circuits due to micro-cracks forming inside the piezoelectric material, which reduced their performance [11, 63]. The University of Glasgow joined the prediction efforts of the STAR follow-up project, which is sometimes referred to as STAR-II. The improved design features an upgraded rotor hub and control system, and new rotor blades. The new rotor blades use the same geometry but offer increased instrumentation and differ in structural properties. The manufacturing of the updated rotor blades finished in September 2020.

STAR Blade Geometry The STAR project rotor was based on a scaled Bo-105 rotor. The main parameters can be seen in Table 2.5. The current iteration of the STAR rotor blades has the same design geometry outboard of the blade root as the blades used in the early STAR experiments [12].

All blades were designed with a nominal twist of $-8°/\mathrm{R}$, a chord length of 12.1 cm and a radius of 2 m from the shaft axis as seen in Figure 2.10. The STAR I blades were closer to $-10.3°/\mathrm{R}$ to $-11.3°/\mathrm{R}$, while the STAR-II blades matched the linear twist rate [13]. The nominal speed is 1041 rpm ($\Omega = 109\,\mathrm{rad/s}$). The blade is a constant chord rectangular planform with the reference pitch axis at the quarter chord and a zero-twist location at 75% of the Radius.

The aerofoil for the STAR rotor is a modified NACA 23012 section with a trailing edge tab 1.0 mm thick and 5.4 mm long (Figure 2.11). Its 12%c thickness increases the chance of locally supersonic flow near the blade tip, with unfavourable behaviour at high-thrust settings and high advance ratios. The radially uniform design made it possible to manufacture all model rotor

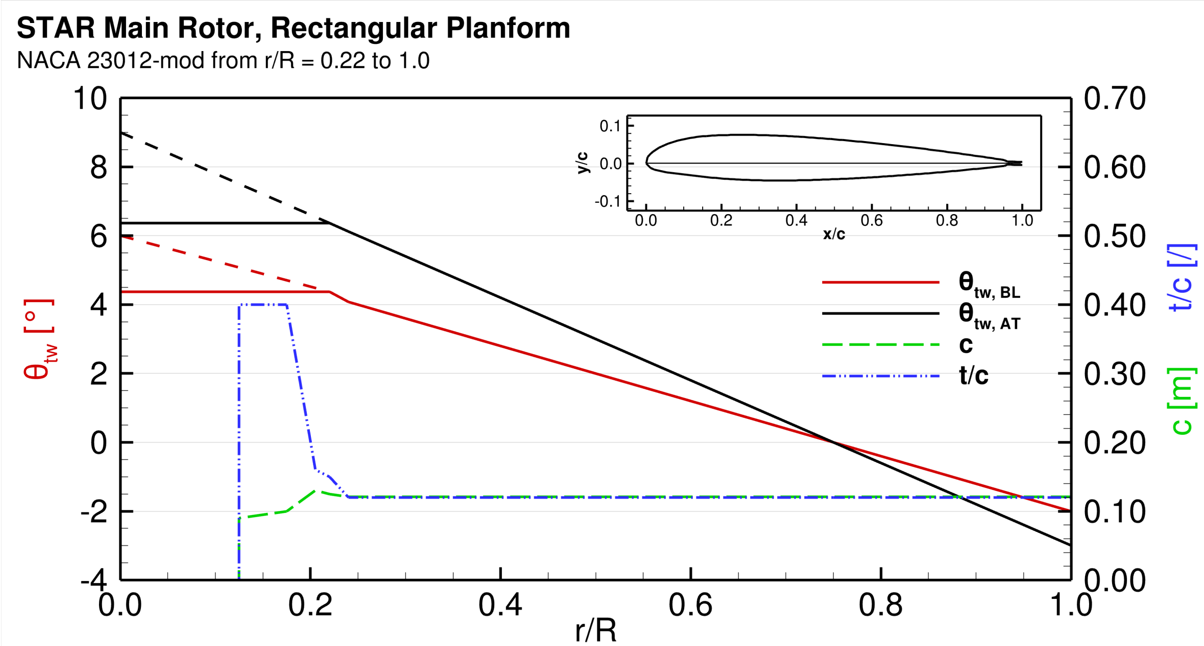

Figure 2.10: Twist, chord, thickness of the STAR experimental rotor blade. The twist for the baseline rotor blade is denoted by BL; AT (active twist) is the twist level used for some numerical comparisons in Chapter 5 only.

blades in tight tolerances. For practical purposes, the thickness also allowed for uncompromised pressure transducer placements far outboard. The maximum camber of 1.8% produces an overall pitch-down moment, which is relatively constant in the useful range of angles of attack, at full-scale Reynolds numbers.

Table 2.5: Rotor parameters of the STAR and HART experiments and the BO-105.

Parameter	**STAR**	**HART II**	**Bo-105** [79]
N_b	4	4	4
R [m]	2.0	2.0	4.905
c [m]	0.121	0.121	0.299
Ω [rad/s]	109.0	109	44.4
θ_{tw} [deg/R]	-8	-8	-8
σ	0.077	0.077	0.0769

Active Twist System In the STAR [12] project, initialised in 2009, a model main rotor with piezoceramic macro-fibre composite (MFC) on-blade actuators was produced. The MFC actuators were found to support a voltage range of -500 V to 1100 V, after they were originally designed for -700 V to 1300 V. The limitation was due to cracks forming and increasing in number during the lifetime, which threatened to cause short circuits. This, over time, reduced the effect of the actuators. Therefore, the STAR I experimental rotor has only been tested in hover, using 0/rev to 3/rev actuation [63] and up to 6/rev on the whirl tower. The actuation supports sinusoidal higher harmonic inputs, and a static offset is used due to a positive voltage

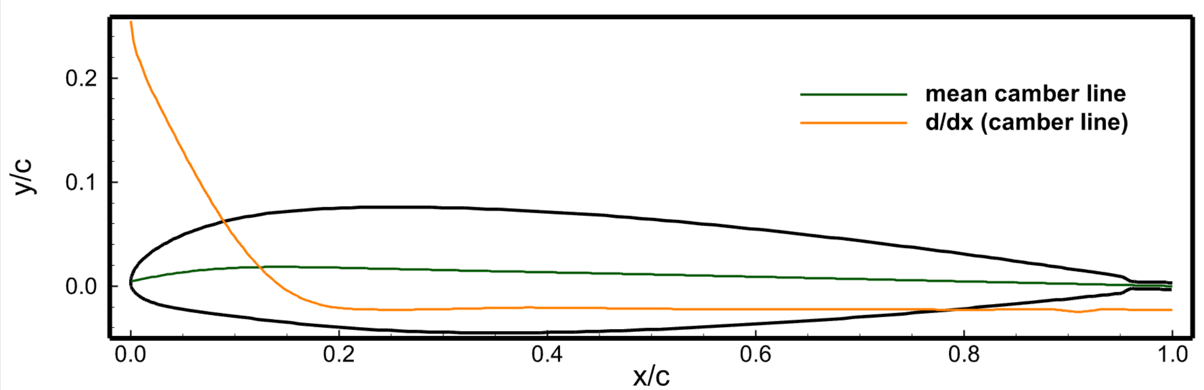

Figure 2.11: Shape, mean camber line and mean camber line slope of the NACA 23012 modified aerofoil of the STAR rotor.

bias of the MFC actuators. At the offset voltage of 300 V, 1.55 Nm of pitch down moment at the end of the blade cantilever was measured. The maximum moment achievable was 4.18 Nm. Low-voltage, multi-layer actuators were also tested following this, finding higher torsion amplitudes [80].

The updated STAR rotors also use MFC actuators, and the manufacturing is documented in [81]. The active twist system runs on a +400 V offset with ±800 V (80% of maximum) range. The achievable peak-to-peak tip twist ranged from 4.04° to 4.4° for the blade set. The mean moment produced is 5.20 Nm/kV.

On-blade Instrumentation Each STAR-II blade is equipped with 30 patches of skin actuators, 9 torsion gauges, 9 flap strain gauges, 14 lead-lag strain gauges and a tip sensor. Unsteady pressure sensors are distributed among the five manufactured blades, with 20 each on the leading edges and at three radial sections of blade Alpha (77.3% R, 87.5% R, 97.5% R) and two sections of blade Beta (67.2% R, 87.5% R). These five sections contain 17 and 11 unsteady pressure sensors on the upper surface and lower surfaces respectively.

All blades are equipped with SPR markers similar to the STAR I test. The rotor hub includes electronic slip rings and active twist amplifiers. It is mounted on the DNW sting support used in the SKAT/META past projects of DLR. The control unit was developed by KARI and relies on an FPGA solution to eliminate time delays stemming from process scheduling on the host computer. The data-acquisition system recorded signals from 320 rotating sensors and 45 non-rotating inputs at a rate of 1024 samples per revolution and is triggered by the rotor phase.

Structural Properties While the HART and HART-II rotor blades were hingeless with an inbuilt 2.5° pre-cone, the STAR and STAR-II have been fully articulated. The lag stiffness of the HART-II was measured to be 3013 Nm/rad on average, which was replicated via an elastomeric lag-spring-damper at the STAR rotor hinges. The modelling of the structural properties and the hinges of the STAR-II rotor are detailed in Section 5.

All five STAR-I rotor blades were measured, and the elastic axis positions were found near 10% for two blades and around 18% chord behind the leading edge for the other three. This was attributed to the first two blades being fully instrumented including the cables, which add to mass and stiffness. The prototype STAR-II blade featured a very forward elastic axis position of 8% chord. Because of the added trailing edge spar, to avoid the cross-coupled trailing edge stresses, the flap bending stiffness was increased to 170% of the old blades, at 320 Nm^2 when measured over the full blade range [81, 82].

Both STAR blades were analysed with x-ray computer tomography to ensure similarity between the blades and to create accurate analytical models of the blade structure, especially considering the mass distribution [35, 83]. The weight of the new rotor blade was found to be 3 kg, of which 0.5 kg were the blade's internal cable mass, and another 0.5 kg was later added by the cable connector box for the actuators and sensors. The average blade elastic axis position of the aerofoil sections of the new rotor blades (not the prototype blade), was found at 20% chord behind the leading edge [35].

Wind-Tunnel Test Conditions All forward flying rotor tests are planned to be held at the DNW-LLF (German-Dutch Wind tunnels – large low-speed facility) in Marknesse, the Netherlands. The 8 m x 6 m open jet section enables measurement techniques such as LLS (Laser Light Sheet) to measure blade and vortex positions, SPR (Stereo Pattern Recognition) for all blade deflections, and mounting of microphones in a fixed array and on a traverse. The microphone array and traverse cannot be used simultaneously. The array is the quicker-to-execute method but covers a smaller region. The microphone traverse is important to capture the downward noise radiation in the flight-path angle sweep study, where BVIs are expected. LLS is planned to be used in the high load and high advance ratio cases to visualise the stall and tip vortex at the retreating side.

Blade weight and rotor hub drag are not included in the measurements as they are subtracted from the wind tunnel measurements. The wind tunnel does not introduce any wall effects, but the shaft angle is adjusted inside the tunnel to compensate for the changed rotor inflow/downwash angle. The proposed high-load test cases were found to surpass the capabilities of the rotor test bed, so the condition was changed to 50% rotor and freestream speed, at the previous thrust coefficient.

STAR-I Wind-Tunnel Test Results The 1/rev test of the STAR-I showed a significant 1%R change in blade tip flapping but had little impact on the tip vortex convection velocity. 2/rev and 3/rev actuation increased the tip vortex miss distance to 1.4%R and 2%R respectively. The higher frequency actuation showed a larger impact on the initial swirl velocity, corresponding to the change in tip angle of attack and a large impact on vortex tracking. A forward flight test in the DNW-LLF did not go ahead because the on-blade actuators developed short circuits due to micro-cracks forming inside the piezoelectric material, which reduced their performance [11, 63]. Results of the ongoing STAR-II project tests are presented in the relevant chapters of this thesis.

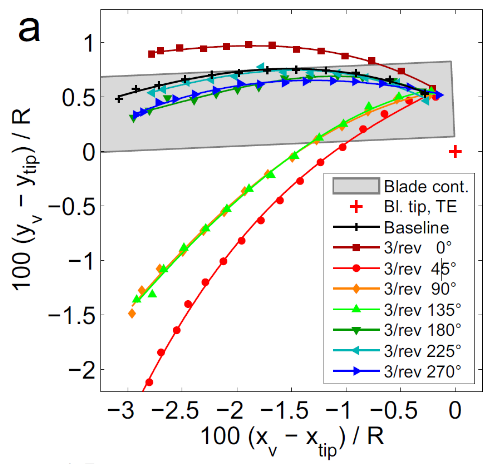

Figure 2.12: Blade tip vortex trajectories for the un-actuated baseline case, compared with 3/rev actuations at varying control phase angle [63].

2.4.5 Conclusions from Active Twist Experiments

None of the experimental works have complete data sets available for the structural models, structural responses and aerodynamic validation data for multiple cases. Only very limited information and results are publicly available for the AMR and ALVR. For the ATR, only rudimentary cross-sectional data for the aerodynamic blade section has been published. Performance data from the experiment has only been published for a single forward flight test case and many other results are only expressed as strain gauge readings. Some structural response data from the wind tunnel experiments are available, usually in the form of strain gauge responses to actuator input frequency sweeps. Noise measurements are available, but they were taken in the reverberating wind tunnel, which would be difficult to model in the simulation. The STAR-I has a comparable amount of published data to the ATR. No forward flight test or representative hover has been conducted due to the actuator failure. However, by joining the STAR-II prediction efforts, a large amount of information has been made available to accurately model such an active twisting blade. DLR kindly supplied the project partners with detailed cross-sectional structural properties, measurements of the blade and hinge stiffnesses, blade resonant frequency fan-plots, x-ray tomography data, structural layups and material properties. Therefore, this dissertation demonstrates most of the work on the STAR-II. Some whirl-tower measurements have been made available by the time of publishing, and wind-tunnel tests are planned in the coming years.

While earlier active twist prototypes, including the full-scale blades, used active fibre composites (AFC), the STAR blades employed a newer and more effective macro-fibre composite

(MFC). This type of actuator is easier to apply, as it can be attached similarly to other pre-preg materials. The ATR and STAR-I demonstrate the need to keep rotor blades sufficiently stiff in flap- and chordwise bending to protect the integrity of the actuators. The high maximum actuation voltages from the manufacturer spec sheet may need to be reduced for applications in rotor blades. The piezoceramics are introduced as load-bearing elements to avoid excess weight, whereby they experience the additional stress and strain of the centrifugal and bending forces, not accounted for by the manufacturer.

2.5 Numerical simulations of Active Twist Rotors

This section first presents the numerical prediction work, related to the previously mentioned experimental rotors, and other active twist concepts. Some of the prediction and design optimisation work of the rotors was already mentioned in the experimental section. The second part is focused on the numerical methods for aeroelastically coupling, with a focus on rotor flows and active twist predictions.

2.5.1 Works related to the Experimental Rotors

Active Twist Rotor (ATR) In 2004, Cesnik *et al.* [84] demonstrated numerical simulations using coupled wake models and 1D elastic beams to model the active twist rotor ATR, UH-60 and Bo-105, showing the twist response amplitude at varying actuation frequency.

A parametric study by Wilbur and Sekula [85] showed the effect of sweep and taper on active twist response. Sweep reduced the active twist effectiveness by up to 60%. The blade properties were simplified to a 1D beam model and loads were applied from the CAMRAD-II comprehensive code. Active twist was modelled by opposing torsion moments at two beam stations.

The ATR project was followed with proposed designs using Macro Fibre Composites (MFC) as actuator material, such as the Advanced Active Rotor Blade (AATR). Park *et al.* [86] showed a higher control amplitude at lower voltage for both the new MFC design and the original ATR design with MFC replacing the AFC, using numerical cross-sectional analysis.

The PhD thesis of Mok [87] is a purely numerical study on the design optimisation of active twisting rotors. The finite element cross-sectional solver VABS (Variational Asymptotic Beam Sectional) from the University of Michigan was integrated into the inner loop of a structural optimisation algorithm, developed in that work. Using constraints on the structural properties such as elastic axis position, mass/length, and maximum strain, the sizing of the cross-sectional was optimised for active twist control authority. For this, automated meshing of these cross-sections was implemented. Using the optimisation algorithm, an improved design for the original ATR (ATR-I) cross-section was found, which could achieve 20% more static twist deformation while staying within the constraints. The main optimisation was to extend the surface area of the active fibre composite from 40% of the chord to 80%, at a small weight penalty and a small increase in torsional stiffness. More detailed structural properties of the ATR can be found in the thesis [87, p. 55-56].

The work also described a proposed ATR-A rotor, similar to the earlier mentioned AATR. It used AFC actuators but was geometrically similar to the AH-64D Apache rotor. The blade planform was rectangular with a swept tip of increased chord and used VR-18 aerofoils. The rotor hub was changed to fully-articulated, from the hingeless rotor of the AH-64D. The ATR-A cross-section at multiple blade stations was optimised. The results were fed into an outer loop, where the CAMRAD-II helicopter suite was used to evaluate the aerodynamic loads. Inner iterations of this structural optimisation algorithm then considered the loads to evaluate the stress and strain constraints. Finally, different materials have been compared to produce an optimised design of this ATR-A, which could reasonably manufactured. In this process, the effect of the materials on the structural properties and the twist authority of this D-spar rotor blade were characterised, such as higher stiffness foam filler causing a large backward shift of the elastic axis. The thesis concluded, recommending the production and testing of this model scale ATR-A rotor, however, there are no follow-up publications on this specific design.

Fogarty *et al.* [88] simulated the NASA/Army/MIT ATR-I using the CFD solver OVERFLOW2 coupled with CAMRAD-II. The latter software calculated the structural response using a beam model approach. At a level flight condition of $\mu = 0.17$, noise predictions were made and subsequently compared with 3/rev to 5/rev of active twist. $1000V_{pp}$ of input voltage predicted between 1.02° and 3.02° of twist, depending on phase and frequency. Up to 4.5 dB of peak noise reduction was predicted and up to 11 dB reduction in lower noise regions. It was predicted that the harmonic active twist changes the blade flapping response by less than one unit of blade chord thickness.

In a study by Kumar and Cesnik [89] optimisation methods were used on blade cross-section simulations, to maximise the active twist amplitudes at the 3–5/rev frequencies. The spar location, the nose mass, and the composite layers of the skin and spar were optimised for the ATR blade, using either gradient-based or neural network-based algorithms. The US Army RCAS (Rotorcraft Comprehensive Analysis Software) tool was used to estimate the aerodynamic prestressing and resulting structural frequencies of a blade design. The cross-sectional data was calculated with VABS. Composite layups and cross-sections, which could increase the twist actuation by more than double were found, effectively reducing the number of composite layers. However, the remaining blade stiffness and internal stresses were not demonstrated in the study.

The experimental test data of the ATR in the TDT was compared to CFD-CSD coupled simulations by Massey, Kreshok and Sekula [90, 91]. The blade cross-sections obtained from VABS were used in the panel method of CAMRAD-II for aeroelastic coupling. A delta-airloads approach as described in [92,93] — and explained in more detail in Section 3.2.2 of this work —

was used to coupled CFD airloads from unstructured CFD code FUN3D. The Spalart-Allmaras (SA) single-equation turbulence model was used in the unstructured solver, to fully resolve the boundary layers of the rotor, test bed and wind-tunnel section. The active twist was applied via point moments at the beginning and end locations of the actuator regions. While this method matched well with the experiment in most conditions, some limitations of the structural model were pointed to, especially related to the chordwise bending moment. Significant reductions in the rotor head vibration components of 44–81% were confirmed in the simulation (59–87%), at 3/rev 220° phase, ±500V amplitude actuation in the slow forward flight condition $\mu = 0.125$. Some phase differences were attributed to the hysteresis of the fibre actuator.

Smart Active Twisting Rotor (STAR) The STAR research consortium [12] published numerical predictions in anticipation of wind tunnel tests of a 40% scaled BO-105 rotor with macro fibre composite twist actuators. CFD/CSD simulations and comprehensive codes predicted a 1–2 count improvement in figure of merit at 1100 V 0/rev (static) actuation, corresponding to roughly 5.7 Nm of blade-tip pitch-down torque. Higher deformation would be necessary for hover efficiency improvements. In descent, 3/rev actuation promised the largest reduction in BVI-noise (2–5 dB SPL) and 2/rev actuation either managed a slight power decrease or a 47% vibration reduction in high-speed level flight.

Hoffmann, Keimer and Riemenschneider [94] modelled the 3D structure of the STAR blade using ANSYS software. The model featured one extruded cross-section including spar, weight, skin and actuator for the main section, and one without weight and actuators for the tip section. From this model, and experimental measurements a simplified 1D finite element beam model was created. The mass distributions of cross-sections were compared to x-ray computer tomography scans of the blade. However, one of the takeaways from the study was that more complex volumetric models would be needed for pure-prediction efforts, as experimental corrections had to be applied in this case.

As part of the FRIENDCOPTER European research collaboration, an active twist variant of a model-scale BO-105 rotor was designed. Therefore, the simulated rotor featured a similar shape, internal structure and materials to the later STAR. A finite element structural analysis was conducted using an ANSYS structural solver, on a 2D/3D combined model, pictured in Figure 2.13. A purely structural parameter study for the blade stiffness and active twist effictiveness was conducted, exploiting a thermal analogy approach [95].

Kovalovs *et al.* [96] formulated an optimisation algorithm for the volumetric finite element structural model resembling the FRIENDCOPTER model. A thermal analogy was used on the actuator shell elements to demonstrate blade torsion. Later another structural model of a full-scale BO-105 rotor based on the previously modelled prototype was created. Through a constrained optimisation study, a C-spar blade design which can produce sufficient active twist authority was found. However, the constraints did not consider bending stiffness or internal

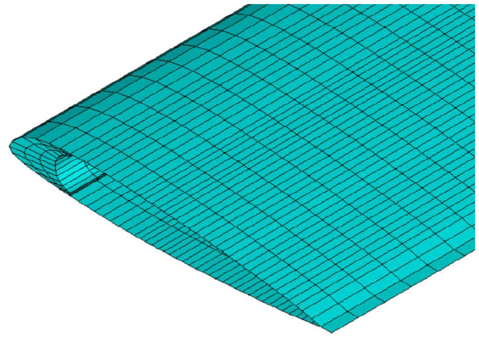

Figure 2.13: Finite element model of the active twist BO-105 model by Glukhikh *et al.* [95].

stresses [97, 98]. In 2018, an optimisation study to increase active twist was conducted on a similar blade, which found D-spar designs more effective than C-spar internal structure [99].

Blind, numerical predictions on the follow-up STAR-II rotor were first published in [13,100]. Results of both comprehensive analysis and aeroelastic CFD codes are compared for a variety of rotor conditions. The active twist authority was found to be too small to achieve measurable hover efficiency improvements. This is due to the voltage bias of the actuators being mounted favouring the untwisting direction. In low advance-ratio flight, the highest BVI noise was found near 9° of descent. Large variations were found for 2/rev and 3/rev actuation phase sweeps of 50% and 80% amplitude of active twist. The most promising active twist to reduce BVI sound pressure level seemed to be 2/rev between 90° and 270° phase. In high-speed flight, some scatter between the results was isolated to the structural response of the rotor, affecting the trim angles. An improvement in vibration index or lift-to-drag ratio could be found for most codes for a similar actuation as in the previous case. In the high-load, level flight scenario at halved speed, the correlation between codes was stronger and improvements in both vibration index and rotor power were found for 2/rev actuation at 0°. A high-advance ratio $\mu = 0.7$ flight showed a vibration reduction when using 2/rev 330° actuation. Relatively large differences in predictions were found between the project partners, showing the difficulties in predicting the structural and aerodynamic properties of the complicated STAR. A more detailed analysis of the high-load flight cases was also published in another joint publication [101].

DLR's FLOWER code [102] coupled with the HOST tool of Airbus [103] and JAXA's rFLOW and rMode [104], were demonstrated to simulate the complex, difficult to model conditions of the STAR in DLR's whirl tower [105]. Strong recirculation and vortex ingestion occurred, with periodic oscillations. Due to the non-linearity, the delta-airloads CFD-CSD coupling approach was found not sufficient. It was concluded that simulation of such extreme conditions was possible, but at a high computational cost with 50–100 revolutions required.

Other Rotors Han *et al.* [106] confirmed the potential of skin-embedded actuators to reduce the power requirement for these flight regimes in a numerical study of a UH-60A rotor with a prescribed, higher harmonic twist. A reduced-order model was used to determine the optimal

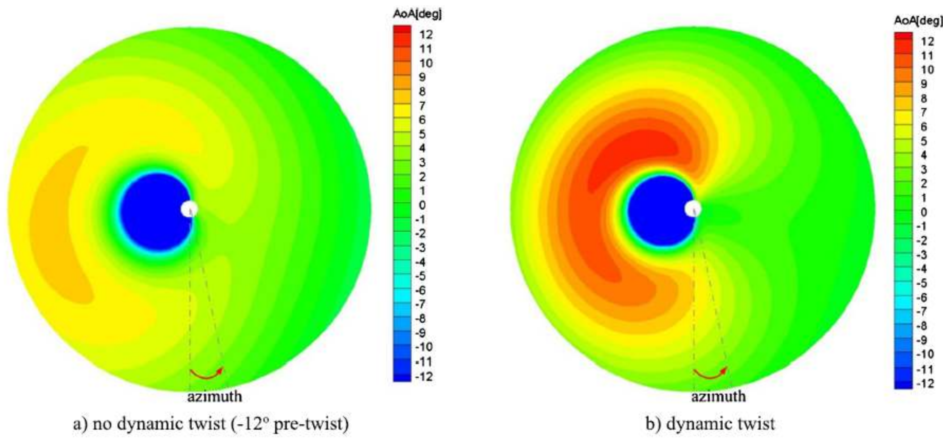

Figure 2.14: Angle of attack distribution at 230 km/h forward flight, comparison between linear pre-twist and ideal active twist for a clockwise rotor, freestream from top to bottom [106].

actuation frequencies, phases and amplitudes of a uniform active twist and selected results were validated using HMB2. The main reduction in power was achieved by the high, constant twist in hover, while small power reductions in forward flight could be found using 2/rev and 3/rev harmonic actuation. The benefits of the active twist were most pronounced in high-load scenarios. However, the ideal higher harmonic and steady-state twist changes for these results are in the range of more than 20°, which is out of reach for the current techniques used.

Thakkar and Ganguli [107, 108] demonstrated a modelling of NACA23012-based active twist blades. Cross-sectional data was calculated and used in coupled aeroelastic simulation using a free-wake-based rotor dynamics code. Vibration reductions over the un-actuated blades of up to 69% were presented in the numerical study. Pawar and Jung [109] used box-beam models to show how tailored actuation of blades can correct tracking issues when blade asymmetries exist, for example coming from partial actuator failures.

Studies on the ideal Active Twist Deployment Schedule A large number of numerical studies exist on the optimal deployment schedules of active twist or other higher harmonic rotor blade actuation methodologies. Some works are presented in [110–114] among others. Usually, comprehensive rotorcraft toolboxes are employed and coupled with optimisation algorithms or closed-loop controllers. Such tools can calculate individual trimmed forward flight cases in minutes, while high-fidelity simulations are too computationally expensive, requiring months' worth of CPU hours and are only suited to confirm the benefits of the best-proposed actuation profiles.

The optimisation of the actuation schedules is beyond the scope of this dissertation. This work focuses on sinusoidal harmonic actuation at multiples of the rotational frequency, for their simplicity and widely reported benefits.

2.5.2 Relevant Numerical Work on Aeroelastic Coupling of Rotors

History of Aeroelastic Coupling in Helicopter Rotor Applications In the 1990s and 2000s, comprehensive rotor codes using lifting line theories with 1D beam structural coupling identified difficulties predicting the vibration, pitch link loads and aerodynamic loads in transonic, negative lift or reversed flow regions. Accurately capturing the force and moment variations is vital to calculate vibration metrics and structural stresses. The blade tip torsion also has a significant impact on the listed metrics, so the aerodynamic pitching moments are therefore crucial. Replacing the simplified aerodynamic tools with CFD, helped predict rotor loads and thereby hub vibrations, especially in difficult conditions, such as high lift, high advance-ratio, and Blade Vortex Interaction (BVI) cases. However, even with the most recent advancements on the side of fluid simulation, 1D beam model approaches have been commonplace in rotorcraft analysis until recently. These models are often part of rotor dynamics and trimming toolboxes, which are integrated with mid-fidelity and high-fidelity CFD solvers. Because of the strong historical integration between the codes, significant effort is needed to open the toolboxes to higher-fidelity structural analyses using 3D finite element approaches.

Many rotor tools use a fluid-structure coupling and trimming algorithm based on the delta-airloads approach. Tung *et al.* [92] was the first to demonstrate this loosely coupled trimming methodology by combining the fidelity of a finite difference solver for the blade tip with an integral rotor code. Once per revolution or similar period, the trim and the loads are updated, with the goal of reaching a convergence. This approach is explained in Section 3.2.2. It was applied to Euler and Navier-Stokes solvers in the early 2000s and has been one of the most popular rotor coupling schemes since [93, 115–117].

In recent years, rotorcraft simulation research at the University of Maryland has been working on the introduction of a 3D structural solver to couple with the helicopter CFD code CREATE-AV HELIOS. The first presented conference paper in 2016 [118] outlined the background and long-term goals of this development and showed first results. The framework is called X3D and was verified to experimental results of the model-scale TRAM proprotor of NASA and US-Army in 2018 [119]. Good correlations were found, with some smaller differences in the structural predictions. The work showed the feasibility of the software to obtain blade and root hub stresses from the coupled software.

In addition to Newton-Raphson-based forward time-stepping, periodic structural deformations could be obtained using a modified harmonic balance method with the X3D finite element solver. This solver is based on the linearised structural equation of motion with a forcing function: $\boldsymbol{M}\ddot{x} + \boldsymbol{C}\dot{x} + \boldsymbol{K}x = \boldsymbol{F}$. A more than $8\times$ speedup compared to the previous, parallelised, time-marching FEM structural solver was demonstrated and applied to a UH-60A forward flight case [120]. A loose coupling similar to delta airloads was used, its implementation is similar as described in [93], which is explained in more detail in Section 3.2.2. The rotor aeroelastic deformations and trimming solution were obtained using a free-wake lifting line method. After validating the method, Patil [121] showed how blade bending stresses could be obtained from FEM in the aeroelastic-coupled and trimmed simulation of an open-source coaxial rotor, modelled after the Sikorsky S-97 Raider. The X3D model of this Metaltail-II rotor blade was made of multiple rigid and deformable parts. The blade and connector meshes exclusively used 27-vertex brick elements, resulting in $\tilde{6}900$ degrees of freedom per blade. The element vertices did not coincide with the aerodynamic mesh, as the structural mesh is much coarser. For the work on the co-axial rotor, the data between Computational Fluid Dynamics (CFD) and Computational Solid Dynamics (CSD) was exchanged by interpolation on the quarter chord line. In this approach, the usually negligible in-plane deformations are lost. Deformations of the blade aerofoil cross-section could therefore not be modelled. Work is ongoing to introduce a 3D exchange method at the University of Maryland [122], which also requires changes to the flow solver.

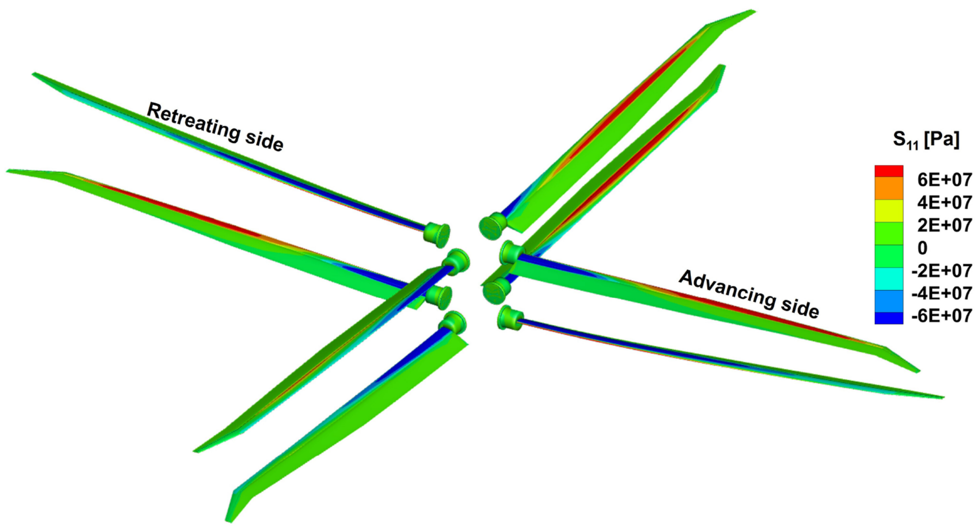

Figure 2.15: Blade-internal stresses obtained from coupled CFD and 3D FE simulation of Metaltail-II coaxial rotor at $\mu = 0.35$ [121].

Other numerical works on aero-structural coupling A conference paper by Sicim and Kaya [123] describe a two-way coupling between structure and aerodynamics using the ANSYS multiphysics toolbox. However, this was not demonstrated.

Benra *et al.* [124] showed the importance of two-way fluid-structure coupling in a numerical study of varying test cases using ANSYS coupled solid dynamics and fluid dynamics solvers.

A number of published works on aero-servo-elastic modelling of floating offshore wind turbines were identified in the review. However, the 'servo' portion usually refers to a PID controller, adjusting rigid rotations of the combined beam-element and rigid-multibody physics packages. Therefore the methods of these studies have been deemed not relevant to the work of this dissertation.

Limitations of 1D Beam-models The limitations of beam structural models are documented in several publications. They are unable to account for in-plane warping of cross-sections, and blade stresses may only be obtained indirectly by replicating the obtained deformations and loading in finite element models. Anisotropic materials, with strain coupling between spanwise and in-plane components, cannot be modelled accurately. It may be an advantage or a disadvantage that the beam elements are defined by their cross-sectional properties at set stations. This reduced spanwise resolution is insufficient for blades, which have large spanwise gradients in any property, such as in highly instrumented experimental blades. The properties are often derived from cross-sectional FE simulations, which is another potential source of inaccuracies. Critical parameters, such as the neutral and elastic axes positions are difficult to obtain within reasonable tolerances, even when using destructive methods on spare blades. The advantages of the beam model approach are its low computational cost, and that the cross-sectional properties can be tweaked relatively easily. However, it is still difficult to tweak beam models of blades with strong cross-coupling between modes, as they arise from spanwise property variations and the effects of the centrifugal force.

Advantages of 3D FE-models At the cost of computational expense and meshing time, the root and aerofoil portions of the rotor blade can be analysed using the 3-D Finite Element Method (FEM). This method allows to directly model on-blade actuators, and better account for spanwise material properties and geometry variations. FEM also allows for the extraction of blade stresses and can even be used to identify corner stresses, e.g. where cut-outs exist. Ideally, the three-dimensional structural models can be directly converted from CAD and manufacturing data, as is the case in this study. With additional data on part positioning, manufacturing variations, and coupon-checked material properties, an almost perfect digital replica can be produced for the simulations. However, if necessary, adjusting an FEM model is different, since sectional properties cannot be edited directly. Material properties can be adjusted, but changes in geometry are time-consuming. Compared to beam-models, it is not trivial to change properties to achieve a target value for neutral axis position, torsional bending stiffness, or similar without influencing other characteristics.

Aerodynamic and Structural Design — A Trade-off Rotor blade structural design is a significant challenge, with aerodynamicists targeting thinner and higher aspect ratio rotor blades. Achieving the required bending and torsional rigidity, the desired neutral axis, elastic axis and centre of gravity locations within a given outer mould line, competes with the goal of decreasing the blade weight. Due to the centrifugal stresses, any additional blade mass also requires additional strength, hence amplifying the problem. Blade structural designs are validated either by FEM models or by sectional analyses. An example of a sectional analysis tool is VABS by Analyswift, and efforts have been made by Purdue University and the US Army to integrate optimisation algorithms for the internal structure of blades [125]. Either global optimisation schemes such as using genetic algorithms, or local gradient-based methods are available. Current approaches to this optimisation iterate between structural design and analysis, similar to the approach of a human designer. It was found, that the aerodynamic loads are relatively insensitive to the structural properties, simplifying the process of finding designs, which fulfil the criterion for stress safety factors.

2.6 Active Twist Technology

Producing rotor blades with integrated torsion actuators has been a topic of research in the last three decades and various technologies and mechanisms have been demonstrated. Chopra gave an in-depth overview of potential on-blade actuation technologies in 2002 [126]. While active flaps use stacked piezoelectric actuators to create the required displacements, the materials used to achieve active twist are layered throughout the rotor blade skin. Such actuators can only provide effective strain in their longitudinal fibre direction, as opposed to the target torsional shear strain. Therefore, an extension-torsion coupling is created by aligning the layers at an angle to the blade spanwise direction. Actuator layers on the upper and lower surface of the blade are required to avoid unwanted bending moments through the extension components of the strain. The upper and lower surface actuators must be arranged parallel in the blade surface reference frame, or anti-parallel when the blade is seen from above. This way, extending or compressing both sets of actuators will create an equal spanwise strain, but constructively add torsion. This simple mechanism is illustrated in Figure 2.16. Such actuators may be biased for either extension or compression, so +45° and -45° layup alignments make them biased to either increase or decrease blade twist at the bias voltage. This is explained in detail by Büeter and Breitbach [127] and also illustrated in [128]. Because of the extension/torsion coupling of the fibre composite active twist mechanism, blade spanwise strain and torsional deflection are not independent. Blades with such actuators have been investigated before using in-house or commercial structural solvers without aerodynamic loads, or as beam-model approximations in rotor comprehensive codes. Therefore, one aim of this thesis is to examine the actuator effectiveness under centrifugal stresses and aerodynamic loads, using high-fidelity aero-servo-elastically coupled tools as the main novelty. It is expected, that these tools will be able to quantify a degradation of actuator effectiveness under centrifugal load in combination with blade bending.

Contemporary piezoceramic composites can be split into two categories: active fibre composites (AFC) and macro fibre composites (MFC). Both materials are built similarly, with interdigitated electrode patterns sandwiching a sheet of piezoelectric material. This can be seen in both Figure 2.17 and Figure 2.18. The most general name for these actuators is InterDigitated Electrode Piezoelectric Fibre Composite (IDEPFC). The interdigitated electrodes generate electric fields in a way, where the field effect strains are aligned in the lengthwise direction of the actuator (d33 effect). This is also the most effective field-effect orientation of piezoelectric

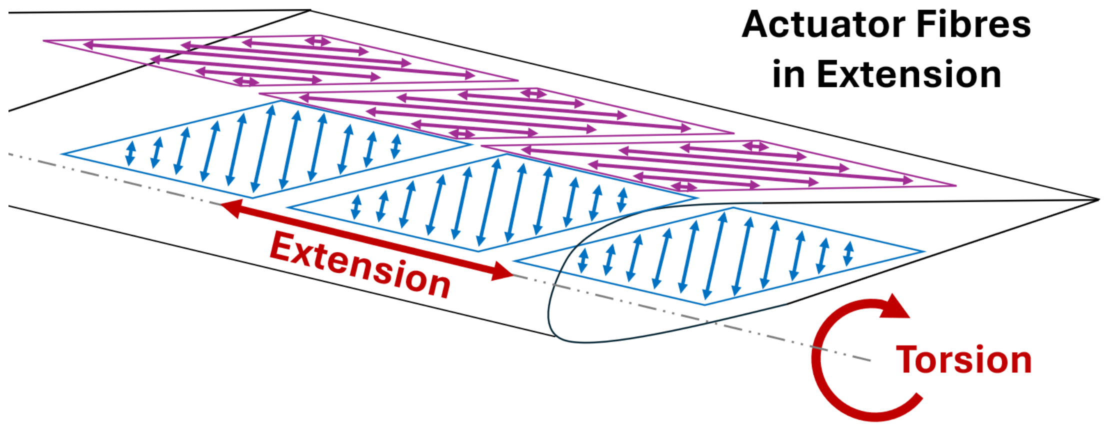

Figure 2.16: Illustration of the active twist mechanism, exploiting tension/torsion cross-coupling. The pictured layup angles produce a nose-up torsion moment if they are actuated to elongate the fibres. This also causes a minor amount of tension stress in the remaining blade components.

materials.

AFC actuators are made of thin piezoceramic fibres laid up in parallel and moulded inside a soft epoxy matrix. This drastically reduces the brittleness coming from monolithic piezoceramics and allows for higher tensile stress in the fibre direction. The actuator can be built within the same thickness as other fibre-reinforced plastics. Bent and Hagood [129], during their work on the AFC, found actuator performance improvements using interdigitated electrodes compared to the uniform top and bottom electrodes.

MFC actuators are made from a sheet of rectangular piezoceramic fibres, separated and bonded by a smaller amount of epoxy, than with cylindrical AFC fibres. This method of actuator creation is also cost-effective and can be scaled to mass production [130]. The technology has been licensed to commercial manufacturer Smart Material Corporation. These MFCs are specified for $-500\,\mathrm{V}$ to $1500\,\mathrm{V}$ input voltage for 10×10^9 cycles and can measure strain or generate electricity from vibrations if no voltage is applied [131].

A different concept to piezoceramic actuators for rotor blade twist is the use of shape memory alloys (SMA) [132]. These systems are unable to provide the rapid actuation which is required for higher-harmonic control, but static twist changes can be achieved, aiding rotor and propeller performance in suitable flight regimes.

Park and Kim [133] modelled a proprotor with blades, featuring a skin made partially of a hybrid, shape memory alloy fibre composite. Cross-section solver VABS and comprehensive suite DYMORE-II were used to create a multibody physics model of the rotor with beam-element proprotor blades. Worst-case aerodynamic loads from DYMORE-II were considered for the optimisation study, where 4° of static tip twist increase were predicted.

A pre-twisted torsion tube as a blade structural member has been simulated by Ameduri and Concilio [134, 135] as part of the SABRE project. The shape change occurs by a low-temperature austenite-martensite transition, which creates a hysteresis in the Young's modulus

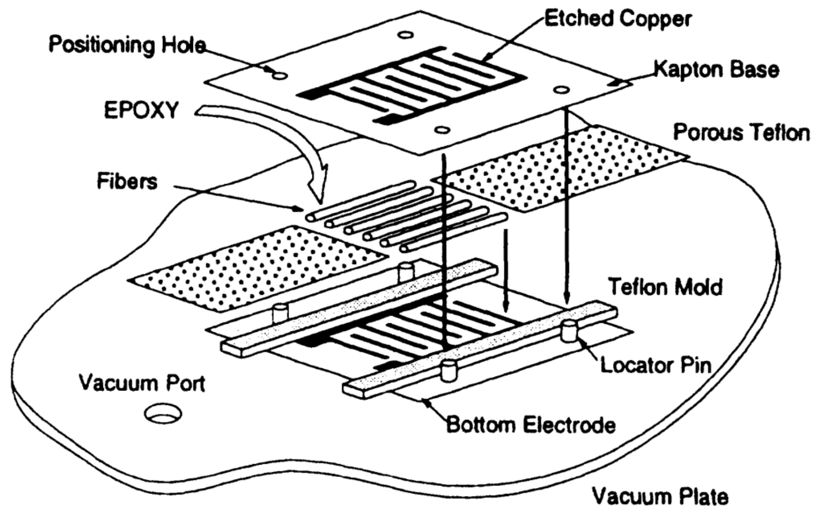

Figure 2.17: Inner Construction of an Active Fibre Composite, from [129].

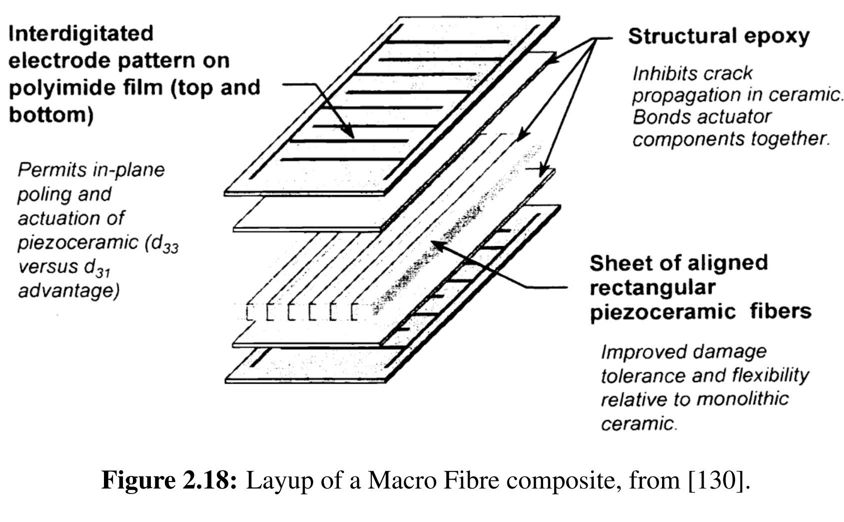

Figure 2.18: Layup of a Macro Fibre composite, from [130].

of the material. Being temperature-based, the tube should safely return to its original twist if heating is turned off. The thermal inertia is too high for higher harmonic actuation, and the heating and cooling are also difficult to implement within a helicopter rotor blade. Because large energy fluxes are required, the technology is only suited for quasi-static twist changes. The work in [135, 136] also featured 3D finite element structural modelling of the blades in MSC NASTRAN, using implicit solver SOL400. Instead of a thermal analogy, the change of the crystalline structure was simulated using the MATSMA entry card of NASTRAN, where stresses, transition temperatures and hysteresis behaviour can be defined. Two boundary conditions (cantilevered and cantilevered with tip support) were simulated, although in the absence of aerodynamic forces or rotor hub modelling.

2.7 Passive rotors simulated in this work

2.7.1 Hover Validation and Acoustic Baseline (HVAB)

The AIAA Hover Validation and Acoustics Baseline (HVAB) rotor was designed to compare the current numerical prediction capabilities of hovering rotors. It is geometrically similar to the PSP rotor but includes more on-blade instrumentation. Compared to the PSP, the HVAB blade was tested in a larger 80×120 ft test section of the NASA Ames NFAC (National Full-scale Aerodynamics Complex). The rotor is 4-bladed with a geometric solidity of $\sigma = 0.1033$. The HVAB blade was not designed for any form of higher harmonic input or on-blade actuators. The nominal rotational speed was 1250.39 rpm ($\Omega = 130.94$ rad/s), but some conditions at lower speeds were tested.

HVAB Blade Geometry The rotor blade radius is 66.50 in, with a cutout at 14% R. The root fairing blends into the blade section at 25.19% R. The main section chord is 5.45 in and tapers to 3.27 in. The 30° swept leading edge at the tip intersects the main leading edge at 95.023% R, however, the transition is rounded off at the leading edge with a 0.5 in sweep break, which is not shown in Figure 2.19. The rotor blade uses RC-series helicopter aerofoils, which are blended as seen in Figure 2.19. The latter part of the aerofoil name designates the thickness in % of chord length. All aerofoils were modified to have a uniform trailing edge thickness of 0.035 in and are embedded in the NASA Technical Memorandum by Overmeyer *et al.* [137]. The rotor blade has a high linear twist rate of $-14^\circ/\mathrm{R}$ with zero pitch defined at 75% R. The design tip-speed was 221.17 m/s. Hover blade SN-004 was equipped with 187 pressure sensors, distributed at 40%, 60%, 67.5%, 75%, 82.5%, 87.5%, 90%, 93% 95.5%, 97.3% and 99% of the rotor radius for sectional load extraction. 11 sensors were built into the upper surface and 6 in the lower surface for each section, and the lower sensors were shifted inboard by 0.45% R. Additionally, strain gauges, temperature sensors and tip LEDs were installed [137].

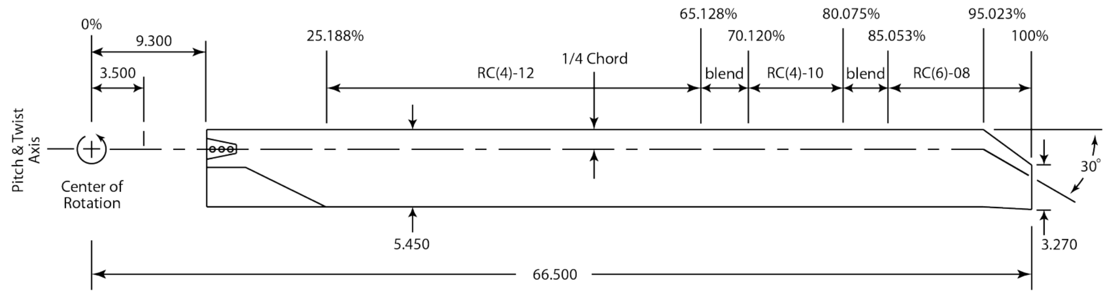

Figure 2.19: HVAB rotor blade planform and aerofoil choices. Measurements in inch. [137].

Structural Properties The structural properties are provided in the untwisted reference frame for sections 17.8–99.8% R. The properties of blades 1–5 were chosen for the structural model of the HVAB rotor in this study. Where more than one set of parameters were given for a spanwise station, the parameters were averaged. Inboard of 17.8%R, the rotor was considered rigid and the most outboard sectional properties were assumed for the blade tip. Because of the duplicate property listings of [137] and the corrections [138], some doubt is cast on the accuracy of the data. The data was likely generated by numerical cross-sectional analysis. The combined flap, lag, and pitch hinge is located at 3.5 in (5.26% R).

Wind-tunnel Test Results The Army Rotor Test Stand (ARTS) used to mount the blades was encompassed by a cylindrical fairing, with an increased diameter about 1 R below the hub. The HVAB hover test results have been published on a NASA-sponsored website [139]. A part of the results, including high-fidelity simulations were presented in May 2023 [140]. Data on the hover performance at three Mach numbers (0.60, 0.65, 0.675) are available. The accuracy of the force and torque measurements were given as ± 0.005 FoM. Some results are available for runs with either the pressure side surface or both surfaces tripped. Thermography snapshots were provided to show the laminar-turbulent transition at several conditions. With shadowgraphy, the tip vortex positions have been published up to 1 rotor revolution of age. The rotor deformations have been measured using photogrammetry.

Chapter 3

Methodology

3.1 Flow Solver Framework HMB3

The Helicopter MultiBlock 3 flow solver framework [141, 142] is used for all fluid dynamics calculations presented in this dissertation. It is primarily a structured flow solver for rotorcraft applications, but also works on unstructured meshes and now contains a meshless point-cloud-based method. It solves the discretised Navier-Stokes flow equations. Various turbulence closing equations are available, starting from single equation ones such as the Spalart-Allmaras (SA) [143] model up to four-equation turbulence models. Also, multiple mesh deformation and interpolation algorithms are available, such as spring-analogy method & inverse distance weighting deformation methods, and sliding planes & overset (chimera) interpolation. In hover and forward flight, HMB3 has three- and four-variable trim algorithms. The HMB3 framework contains an aeroelastic method via blade eigenmodes, or can be coupled to the commercial finite element structural solver MSC NASTRAN. The aeroelastic methods are described in Section 3.2.

Over the last decades, the University of Glasgow HMB3 flow solver framework has been applied to a range of applications, starting from two-dimensional flows such as transition modelling of pitching aerofoils or buffeting predictions with PANS (Partially Averaged Navier-Stokes), to complex 3D flows of eVTOLs, wind-turbines, distributed propulsion systems, rotors, propellers, wings, missiles and stores.

3.1.1 Flow Solver

The HMB3 flow solver discretises the domain into structured meshes, forming control volumes, sometimes also referred to as finite volumes. Structured methods are preferable over unstructured ones for rotorcraft applications for their low numerical diffusion and their computational efficiency. Low diffusion is needed in rotorcraft applications, as tip vortices strongly interact with following lifting surfaces and other helicopter components even after significant time has passed. Numerical diffusion in unstructured solvers causes these tip vortices to diffuse their rotational momentum quicker into the surrounding fluid, making them less suitable. This is more pronounced in flight conditions where strong blade vortex interactions (BVIs) occur, such as hover or descending forward flight. Structured meshes are also sufficiently flexible to model the usually simple rotor blade geometries with great cell quality. The meshes used in this dissertation are detailed in Chapter 4. There is a trend in rotorcraft CFD towards Cartesian, structured background solvers for further computational performance gains. HMB3 does not contain a dedicated Cartesian solver, but as part of the solver, the curvilinear structured grids are transformed into a Cartesian frame of reference to evaluate the gradients. Therefore, the 2×2×2 stencil determinant is a primary measurement of cell quality. It is the ratio of the smallest to the largest Jacobi determinant of the hexahedron's vertices. This value indicates the ease (or difficulty) of transforming the cell in HMB3, which affects the calculation's accuracy. A 2×2×2 determinant of 1 indicates a perfect cube, 0 is a degenerate shape (i.e. there are collinear sides or an hourglass shape), and negative values show inverted volumes (based on node numbering or axes righthandedness) [144, pp. 480–488]. The determinant of the Jacobian matrix of any cuboid's vertex gives the volume of the parallelepiped made of the vertice's connected sides.

3.1.2 Navier-Stokes Equations

The Navier-Stokes equations described fluid flow based on the principal conservation laws of mass momentum and energy for any continuous fluids. The rate of change of density in a control volume must equal the sum of its in and outflow to satisfy the conservation of mass. Formulating the continuity equation in Cartesian coordinates and using Einstein notation yields:

$$\frac{\partial \rho}{\partial t} + \frac{\partial}{\partial x_i}(\rho u_i) = 0. \tag{3.1}$$

Similarly, in Newton's Second Law, the conservation of momentum can be expressed as:

$$\frac{\partial(\rho u_i)}{\partial t} + \frac{\partial(\rho u_i u_j)}{\partial x_j} = \rho f_i - \frac{\partial p}{\partial x_i} + \frac{\partial \tau_{ij}}{\partial x_j}, \tag{3.2}$$

where f_i is a generic body force acceleration. The final conservation law, states that energy and work must not be created or destroyed:

$$\frac{\partial}{\partial t}(\rho E) + \frac{\partial}{\partial x_j}\left(\rho u_j E + P u_j + q_j - u_i \tau_{ij}\right) = S_e. \tag{3.3}$$

The usual notation applies, where i represents the dimension of a quantity, summation of all components is implied and δ_{ij} is the Kronecker delta. The density is ρ, u is the flow velocity, P is the pressure. The energy density E is a sum of the internal energy e and the kinetic energy $u_i u_i/2$. The source terms are S_i for momentum sources and S_e for energy sources. They are non-zero in steady hover simulations to create the rotational flow field. The fundamental formu-

Table 3.1: Properties for international standard atmosphere (ISA) air.

Property	ISA Air
μ_{ref}	$1.7894 \times 10^{-5}\,\mathrm{kg/m/s}$
T_{ref}	$288.16\,\mathrm{K}$
T_S	$110.4\,\mathrm{K}$

lations and derivations of the continuous and discretised Navier-Stokes equations are commonly found in any modern textbook on CFD, such as [145].

The viscous shear stress tensor τ_{ij} for Newtonian fluids is made of the symmetric rate-of-strain tensor and the isotropic compressibility correction:

$$\tau_{ij} = \mu \left[\left(\frac{\partial u_i}{\partial x_j} + \frac{\partial u_j}{\partial x_i}\right) - \frac{2}{3}\delta_{ij}\frac{\partial u_k}{\partial x_k} \right]. \tag{3.4}$$

The shear stress tensor is linearly dependent on the molecular dynamic viscosity of the fluid. Sutherland's law [146] relates this temperature-dependent viscosity to a measured reference viscosity μ_{ref} at reference temperature T_{ref}:

$$\mu = \mu_{ref} \left(\frac{T}{T_{ref}}\right)^{\frac{3}{2}} \left(\frac{T_{ref} + T_S}{T + T_S}\right), \tag{3.5}$$

where the usual notation applies, T is the fluid temperature, T_S is the Sutherland temperature. The reference values for atmospheric air are detailed in Table 3.1.
The heat flux q_i of the energy conservation equation (3.3) is described by Fourier's law:

$$q_i = -k_h \frac{\partial T}{\partial x_i}, \tag{3.6}$$

where the thermal conductivity $k_h = C_P\mu/\mathrm{Pr}$ depends on the temperature via the dynamic viscosity, the isobaric specific heat capacity C_P and the Prantl number. The Prantl Number of around 0.7 gives atmospheric air its similarly sized boundary layers for heat and momentum.

The equation of state for ideal gases is:

$$P = \rho R T, \tag{3.7}$$

with R as the gas constant.

3.1.3 Non-dimensionalisation

The flow solver HMB3 uses non-dimensionalised quantities in its formulation, based on quantities chosen appropriate to the problem. This approach brings the orders of magnitude for numbers to a smaller range, which reduces numerical dissipation via accumulating floating point errors. Additionally, limiting values to a similar order of magnitude in the solver matrix reduces the system's stiffness, for better convergence.

The reference values for rotors are usually chosen as follows:

- L_{ref}, Reference length, chord length
- ρ_{ref}, Reference density, ISA condition air density
- μ_{ref}, Reference dynamic viscosity, ISA condition air viscosity
- u_{ref}, Reference speed, rotor tip speed or freestream reference speed
- T_{ref}, Reference temperature, ISA condition air temperature at ground level

Further quantities such as non-dimensional time can be derived from the above reference quantities to yield the non-dimensional values, marked by superscript *:

$$x_i^* = \frac{x_i}{L_{ref}}, \qquad u_i^* = \frac{u_i}{V_{ref}}, \qquad t^* = \frac{t u_{ref}}{L_{ref}}, \tag{3.8}$$

$$\rho^* = \frac{\rho}{\rho_{ref}}, \qquad \mu^* = \frac{\mu}{\mu_{ref}}, \qquad P^* = \frac{P}{\rho_{ref} V_{ref}^2}, \tag{3.9}$$

$$T^* = \frac{T}{T_{ref}}, \qquad e^* = \frac{e}{V_{ref}^2}. \tag{3.10}$$

For simplicity, the * notation is dropped in the remainder of this chapter, because all values are non-dimensionalised in HMB3. Using the non-dimensionalisation allows to formulate the Navier-Stokes equations in terms of the commonly used ratios:

$$\mathrm{Re} = \frac{\rho_{ref} U_{ref} L_{ref}}{\mu_{ref}}, \tag{3.11}$$

$$\mathrm{Pr} = \frac{\mu_{ref} C_P}{k_h} \tag{3.12}$$

$$\mathrm{Ma} = \frac{u_{ref}}{a_{ref}}, \tag{3.13}$$

where a_{ref} is the speed of sound in the freestream of the simulation medium. The Reynolds number Re is a measure of the ratio between inertial and viscous forces, the Prantl number Pr describes the ratio between heat conduction and convection, and the Mach number Ma is the ratio between flow-speed and the speed of sound in the medium.

3.1.4 Reynolds Averaging of the Navier-Stokes Equations

Direct numerical simulation (DNS) of turbulence using the Navier-Stokes equations is the most computationally expensive method to obtain flow solutions. Grid discretisations are needed, which can resolve even the smallest turbulent eddies on the Kolmogorov scale, coupled with tiny time steps. Based on this scale, cell numbers in the order of $\mathrm{Re}^{9/4}$ are required to accurately resolve such turbulence using direct simulation. This makes it impractical to resolve flow problems on a larger scales, with significantly larger Reynolds numbers. Flows of helicopter rotors exhibit turbulent scales up the order of the rotor radius, together with the aforementioned small-scale eddies in the boundary layers, largely dominated by viscous forces. There are simplifications to the turbulence modelling, which reduce the prohibitive computational cost. For example, Large Eddy Simulation (LES) calculates the smallest turbulent scales using sub-grid methods but fully resolves larger-scale turbulences.

Currently, the most common turbulence modelling approach is the Reynolds-Averaged Navier-Stokes (RANS) method. It is a statistical approach, splitting all turbulence scales from the mean flow. This approach has more unknowns than the number of equations, so usually, empirical turbulence models are used to close the equation system. RANS simulations are robust and computationally efficient, but have limitations, such as high numerical diffusion, and its inability to resolve eddies of all scales. Intermediate approaches exist, such as Detached Eddy Simulation (DES) and Delayed DES (DDES), which use the RANS simplifications for the small-scale turbulence of boundary layers, while resolving larger turbulence scales in the remainder of the domain. DDES has also been successfully demonstrated for the simulation of rotor flows. While these intermediate methods are available, the RANS approach was chosen for this study because of its robustness, past experience and validation in HMB3, and to focus on the aeroelastic modelling. The RANS formulation of the following section can be found in any modern CFD textbook, such as [145, pp. 91–92].

Reynolds Averaging

The formulation of the RANS equations is primarily sourced from splitting the time-dependant flow variables, indicated by ϕ, into an average $\bar{\phi}$ and fluctuating component ϕ' [147]:

$$\phi = \bar{\phi} + \phi' \tag{3.14}$$

However, in compressible flows with fluctuating density, many non-zero terms coupling mass, momentum and energy equations exist. Density weighted averaging (Favre averaging) [148], is employed to simplify the RANS equations for compressible flows:

$$\hat{\phi} = \overline{\rho\phi}/\overline{\rho} \tag{3.15}$$

$$\phi = \overline{\phi} + \phi' = \hat{\phi} + \phi'' \tag{3.16}$$

In the following equations, the overbar for averaged non-flux terms is dropped for simplicity. The averaging step is applied to the Navier-Stokes conservation equations. This results in the RANS equations, which are made of the time-averaged components:

$$\frac{\partial \rho}{\partial t} + \frac{\partial (\rho u_i)}{\partial x_i} = 0 \tag{3.17}$$

$$\frac{\partial \rho u_i}{\partial t} + \frac{\partial (\rho u_i u_j)}{\partial x_i} = \rho f_i - \frac{\partial p}{\partial x_i} + \frac{\partial}{\partial x_j}(\tau_{ij} + \tau_{ij}^R) \tag{3.18}$$

$$\frac{\partial \rho E}{\partial t} + \frac{\partial [U_i(\rho E + p)]}{\partial x_j} - \frac{\partial}{\partial x_j}(U_i(\tau_{ij} + \tau_{ij}^R) - (q_j + q_j^R)) = 0 \tag{3.19}$$

The mass conservation equation remains unchanged after averaging, as it is linearly dependent on the velocities. The continuum equations instead produce extra terms, as the non-linearities create significant contributions containing fluctuation terms. The resulting terms are contained in the Reynolds stresses $\tau_{ij}^R = -\rho\overline{u_i' u_j'}$. This will result in 11 unknowns, ρ, P, u_i (three-variables) and τ_{ij}^R. The Reynolds stress tensor is symmetric and therefore has 6 unknown variables in three dimensions, leading to more unknowns than equations. This is known as the closure problem of the RANS equations.

The Boussinesq hypothesis [149] is a popular method to reduce the number of unknowns. The Reynolds stress tensor is assumed to be proportional to the averaged rate-of-strain tensor:

$$\tau_{ij}^R = -\overline{\rho u_i' u_j'} = 2\mu_t S_{ij} - \frac{2}{3}k\delta_{ij}, \tag{3.20}$$

where μ_t is the turbulent eddy viscosity, a scalar representing the increased viscous effects in turbulent flow regions, k is the specific kinetic energy of the fluctuations and S_{ij} is the rate-of-strain tensor:

$$S_{ij} = \frac{1}{2}\left(\frac{\partial u_i}{\partial x_j} + \frac{\partial u_j}{\partial x_i}\right) \tag{3.21}$$

The Boussinesq hypothesis, is however only correct where the rate-of-strain tensor is isotropic, that means, where eddy viscosity applies equally in all directions. This is not valid in flow conditions where discontinuities occur, such as in shock wave boundary layer interactions, high curvature flows, where large shear layers appear or where eddy turbulence is largely time-dependent.

This now expresses the six variables of τ_{ij}^R as a combination of the previous principal unknowns and the turbulent eddy viscosity μ_t. This brings the number of total unknowns to 6, with

5 equations. A large number of turbulence models exist, which express the eddy viscosity in terms of other turbulence equations to close the system. Popular models are the single equation Spalart-Allmaras turbulence model, which adds a turbulent intensity ν_t, or two-equation models such as the k-ω models. Some three- and four-equation turbulent models are also implemented in the HMB3 flow solver.

The limitations of the Boussinesq hypothesis can however be partially overcome by the k-ω SST model of Menter [150], explained in Section 3.1.4. While it still suffers from the fundamental problems of modelling the eddy viscosity as isotropic, it is known to perform well in boundary layers with adverse pressure gradients and mild flow separation. Other modelling approaches, such as the previously mentioned SAS, DES and DDES, can also be used to overcome some of the Boussinesq hypothesis' limitations, by resolving vorticity in suitable flow areas.

The k-ω SST Turbulence Model

Throughout this work, the $k-\omega$ SST (Shear Stress Transport) turbulence model is used, for its good numerical stability and accuracy for rotor flows, which are not in deep stall. The two-equation $k-\varepsilon$ [151] and $k-\omega$ models [152] form the basis of the SST variation. The eddy viscosity μ_t in the two models depends on the turbulent kinetic energy k and either the turbulence energy dissipation rate ε or the specific turbulence dissipation rate ω, and on k. C_μ is an empirically determined constant, usually, 0.09 is used:

$$\mu_t = \rho C_\mu \frac{k^2}{\varepsilon} \qquad (k-\varepsilon) \tag{3.22}$$

$$\mu_t = \rho \frac{k}{\omega} \qquad (k-\omega). \tag{3.23}$$

The $k-\varepsilon$ model works well to capture turbulence, such as in vortices or shear layers away from the boundary layer, but suffers from poor accuracy in adverse pressure gradients and consequent flow separation. The $k-\omega$ model works well in the regions of adverse pressure gradients, such as in the boundary layer, but is overly sensitive to freestream turbulence, which reduces stability and accuracy for shear layers and vortices away from the boundary layer.

The advantages of both models were combined via blending functions in the $k-\omega$ SST model of Menter [150]. Since the SST model is based on the k-ω scheme, the equations of conservation are only expressed for k and ω:

$$\begin{aligned}
\frac{\partial}{\partial t}(\rho k) + \frac{\partial}{\partial x_j}(\rho u_j k) &= \frac{\partial}{\partial x_j}\left[\left(\mu + \frac{\mu_t}{\sigma_k}\right)\frac{\partial k}{\partial x_j}\right] + P_k - \rho \beta^* \omega k \\
\frac{\partial}{\partial t}(\rho \omega) + \frac{\partial}{\partial x_j}(\rho u_j \omega) &= \frac{\partial}{\partial x_j}\left[\left(\mu + \frac{\mu_t}{\sigma_\omega}\right)\frac{\partial \omega}{\partial x_j}\right] + \rho\left(\frac{\alpha}{\upsilon_t}P_\omega - \frac{\beta}{\beta^* \omega^2}\right) + \rho S_\omega
\end{aligned} \tag{3.24}$$

The SST model, uses a blending function F_1 to smoothly switch between $k-\omega$ [152] in the boundary layer regions and the $k-\varepsilon$ [151] away from the walls. An additional blending function F_2 includes near-wall corrections for this fully turbulent model. These functions and the remaining production terms P_k and P_ω, constants α, β, β^*, and blending coefficients σ_k, σ_ω are detailed in the relevant literature.

The performance of the $k-\omega$ SST model in adverse pressure gradients of boundary layers was further improved by incorporating the Bradshaw assumption. It states, that turbulent kinetic energy and shear stresses are proportional in the boundary layer $\tau \propto \rho k$. This is implemented by clipping the eddy viscosity μ_t to physically realistic values in the relevant regions.

3.1.5 Conservative Vector Form

HMB3 solves the equations in conservative vector form using an arbitrary Lagrangian-Eulerian (ALE) approach. Depending on the selected turbulence model, the Euler or RANS system of equations is made of 5 to 9 equations, and the 7 equation variation of the $k-\omega$ SST is shown here. The five continuity Equations 3.17, 3.18 and 3.19, together with the turbulent model's equations can then be written in non-dimensional vector form of the Navier-Stokes equations, once again following a Cartesian coordinate convention:

$$\frac{\partial \mathbf{W}}{\partial t} + \frac{\partial (\mathbf{F}-\mathbf{F^v})}{\partial x} + \frac{\partial (\mathbf{G}-\mathbf{G^v})}{\partial y} + \frac{\partial (\mathbf{H}-\mathbf{H^v})}{\partial z} = \mathbf{S}, \tag{3.25}$$

$\mathbf{W}$ is the vector of conserved variables, $(\mathbf{F},\mathbf{G},\mathbf{H})$ and $(\mathbf{F^v},\mathbf{G^v},\mathbf{H^v})$ are the convective flux terms split into inviscid and viscous contributions. The source term $\mathbf{S}$ can introduce sources or sinks of mass, momentum, energy, or production terms of turbulent quantities if required. This can be applied to simulate non-inertial reference frames.

The conservative variables $\mathbf{W}$ and the convective flux terms $(\mathbf{F},\mathbf{G},\mathbf{H})$ are written in full as

$$\mathbf{W} = \begin{bmatrix} \rho \\ \rho u \\ \rho v \\ \rho w \\ \rho E \\ \rho k \\ \rho \omega \end{bmatrix}, \quad \mathbf{F} = \begin{bmatrix} \rho u \\ \rho u^2 + P \\ \rho uv \\ \rho uw \\ \rho uH \\ \rho uk \\ \rho u\omega \end{bmatrix}, \quad \mathbf{G} = \begin{bmatrix} \rho v \\ \rho vu \\ \rho v^2 + P \\ \rho vw \\ \rho vH \\ \rho vk \\ \rho v\omega \end{bmatrix}, \quad \mathbf{H} = \begin{bmatrix} \rho w \\ \rho wu \\ \rho wv \\ \rho w^2 + P \\ \rho wH \\ \rho wk \\ \rho w\omega \end{bmatrix}, \tag{3.26}$$

where H is the total enthalpy.

The viscous flux terms $(\mathbf{F^v},\mathbf{G^v},\mathbf{H^v})$ are written in full as

$$\mathbf{F^v} = \frac{1}{\text{Re}} \begin{bmatrix} 0 \\ \tau_{xx} \\ \tau_{xy} \\ \tau_{xz} \\ u\tau_{xx} + v\tau_{xy} + \\ \quad w\tau_{xz} - q_x \\ -\left(\mu + \frac{\mu_t}{\sigma_k}\right)\frac{\partial k}{\partial x} \\ -\left(\mu + \frac{\mu_t}{\sigma_\omega}\right)\frac{\partial \omega}{\partial x} \end{bmatrix}, \quad \mathbf{G^v} = \frac{1}{\text{Re}} \begin{bmatrix} 0 \\ \tau_{xy} \\ \tau_{yy} \\ \tau_{yz} \\ u\tau_{xy} + v\tau_{yy} + \\ \quad w\tau_{yz} - q_y \\ -\left(\mu + \frac{\mu_t}{\sigma_k}\right)\frac{\partial k}{\partial y} \\ -\left(\mu + \frac{\mu_t}{\sigma_\omega}\right)\frac{\partial \omega}{\partial y} \end{bmatrix}, \quad \mathbf{H^v} = \frac{1}{\text{Re}} \begin{bmatrix} 0 \\ \tau_{xz} \\ \tau_{yz} \\ \tau_{zz} \\ u\tau_{xz} + v\tau_{yz} + \\ \quad w\tau_{zz} - q_z \\ -\left(\mu + \frac{\mu_t}{\sigma_k}\right)\frac{\partial k}{\partial z} \\ -\left(\mu + \frac{\mu_t}{\sigma_\omega}\right)\frac{\partial \omega}{\partial z} \end{bmatrix}. \tag{3.27}$$

An example source term including a body force and the turbulence model production terms are:

$$\mathbf{S} = \begin{bmatrix} 0 \\ \rho f_x \\ \rho f_y \\ \rho f_z \\ 0 \\ P_k - \beta^* \rho k \omega \\ \alpha \frac{\omega}{k} P_k - \beta \rho \omega^2 + S_\omega \end{bmatrix}, \tag{3.28}$$

where $P_k = \mu_t S_{ij} S_{ij}$, and S_{ij} is described in Equation 3.21. The terms f_i are a generic body force acceleration, such as the gravitational acceleration g in vector form.

This vector form of the Navier-Stokes equation now has the same number of equations as unknowns, when considering the following ideal gas relations, describing the correlations between the total enthalpy H, total energy E, internal energy e, pressure P, density ρ, and static temperature T:

$$H = E + \frac{P}{\rho}, \tag{3.29}$$

$$E = e + \frac{1}{2} u_i u_i, \tag{3.30}$$

$$P = (\gamma - 1)\rho e, \tag{3.31}$$

$$T = \gamma \text{Ma}_{ref}^2 \frac{P}{\rho}, \tag{3.32}$$

where γ is the specific heat ratio of the fluid. Atmospheric air at ISA sea-level conditions has a ratio of specific heats of $\gamma = 1.4$.

Discretisation in Space

The governing partial differential Equation 3.25 is discretised in space, by expressing it in terms of volume integrals [141]:

$$\frac{d}{dt}\int_{V(t)} \mathbf{W} dV + \int_{\partial V(t)} (\mathbf{F}-\mathbf{F^v}, \mathbf{G}-\mathbf{G^v}, \mathbf{H}-\mathbf{H^v}) \cdot \mathbf{n} dS = \int_{V(t)} \mathbf{S} dV, \tag{3.33}$$

$V(t)$ are the control volumes with $\partial V(t)$ being the boundaries, all dependant on time t. The Arbitrary Lagrangian Eulerian (ALE) formulation is used and the time-dependent mesh velocities are included in the velocity components of the flux terms. $(\mathbf{F}-\mathbf{F^v}, \mathbf{G}-\mathbf{G^v}, \mathbf{H}-\mathbf{H^v})$ are the inviscid and viscous flux vectors as in Equations 3.26 and 3.27. $\mathbf{n}$ is the control volume's surface normal unit vector, pointing outwards. $\mathbf{S}$ is the vector of source terms, which may be non-zero in inertial reference frames, or if external conditions introduce volume forces.

The discretised finite volumes of Equation 3.33 are evaluated using a cell-centred method. The inviscid, convective fluxes are hyperbolic and discretised using Osher's upwind scheme [153] for its stability and accuracy. A 3^{rd}-order MUSCL variable extrapolation [154] is applied to this scheme for improved accuracy. The Albada limiter [155] is used to prevent oscillations around discontinuities, such as shockwaves. The parabolic viscous fluxes are discretised using a 2^{nd}-order central differencing scheme, as this information propagates evenly in all flow directions. This also correlates to the Boussinesq hypothesis' isotropy requirements. The boundary conditions are implemented via ghost cells, extrapolated from the mesh borders.

Evaluating the conserved vector integration for a finite volume creates a residual vector $\mathbf{R}$. It contains the flux and source terms to balance, and also accounts for the finite accuracy of the discretised Navier-Stokes equation [141]:

$$\frac{d}{dt}\left(\mathbf{W}_{i,j,k} V_{i,j,k}\right) + \mathbf{R}_{i,j,k}(\mathbf{W}_{i,j,k}) = 0. \tag{3.34}$$

The cell indices are denoted by i, j, k and $V_{i,j,k}$ are corresponding cell volumes.

Discretisation in Time

The ordinary differential Equation 3.34 is time discretised in either forward or backward differencing schemes. Forward time integration leads to explicit schemes, which are simple to implement, but are unstable if the time-step is too large. HMB3 uses implicit, backward finite differences in time for their stability at large Courant Friedrichs Lewy numbers and time steps, especially in stiff systems. Implicit schemes are more complex to implement and most advantageous for steady calculations, while explicit schemes are more popular when resolving small time scales, such as in Large Eddy Simulation (LES), Detached Eddy Simulation (DES) or Direct Numerical Simulation (DNS).

Steady-State Solver

The implicit time integration, with the future solution and flux terms on both sides of the equation, can be defined as [141]:

$$\frac{\mathbf{W}_{i,j,k}^{n+1} - \mathbf{W}_{i,j,k}^{n}}{\Delta t} = -\frac{1}{V_{i,j,k}} \mathbf{R}_{i,j,k}\left(\mathbf{W}_{i,j,k}^{n+1}\right). \tag{3.35}$$

The steps n and $n+1$ indicate values at time steps t and $t+\delta t$ respectively. To simplify the non-linear implicit scheme, the flux residual is linearised in the time domain by Taylor series expansion [141]:

$$\begin{aligned} \mathbf{R}_{i,j,k}\left(\mathbf{W}^{n+1}\right) &= \mathbf{R}_{i,j,k}\left(\mathbf{W}^{n}\right) + \frac{\partial \mathbf{R}_{i,j,k}}{\partial t}\Delta t + O(\Delta t^2) \\ &\approx \mathbf{R}_{i,j,k}^{n}\left(\mathbf{W}^{n}\right) + \frac{\partial \mathbf{R}_{i,j,k}}{\partial \mathbf{W}_{i,j,k}} \frac{\partial \mathbf{W}_{i,j,k}}{\partial t}\Delta t \\ &\approx \mathbf{R}_{i,j,k}^{n}\left(\mathbf{W}^{n}\right) + \frac{\partial \mathbf{R}_{i,j,k}}{\partial \mathbf{W}_{i,j,k}}\left(\mathbf{W}_{i,j,k}^{n+1} - \mathbf{W}_{i,j,k}^{n}\right), \end{aligned} \tag{3.36}$$

Therefore, Equation 3.35 now follows in its linearised form with **I** as the identity matrix [141]:

$$\left[\frac{V_{i,j,k}}{\Delta t}\mathbf{I} + \frac{\partial \mathbf{R}_{i,j,k}}{\partial \mathbf{W}_{i,j,k}}\right]\Delta \mathbf{W}_{i,j,k} = -\mathbf{R}_{i,j,k}^{n}\left(\mathbf{W}^{n}\right). \tag{3.37}$$

Solving the linear Equation 3.37 directly is difficult due to its large size and stiffness. An iterative Generalised Conjugate Residual (GCR) method is used to invert the large matrices efficiently. The equation system is also pre-conditioned by a Block Incomplete Lower-Upper (BILU) preconditioner. For stability, a small number of explicit steps of Euler formulation are performed after initialising the free stream flow field. The flux Jacobian is reduced to 1^{st}-order accuracy reducing computational time and memory requirements. This makes the Jacobian more diagonally dominant. BILU preconditioning is efficiently parallelised between the processor cores to reduce communication.

Time-Marching Solver

Jameson's dual time stepping method [156] was used for unsteady flow calculations in this work. The implicit equations are solved at each real-time step using inner iterations as steady-state problems in the pseudo-time. This allows exploiting the advantages of the steady-state solver for the unsteady calculations, and to reuse the same algorithms. The previous differential Equation 3.34 is first-order discretised into real-time steps in a similar implicit scheme [141, 156]:

$$\frac{1}{V_{i,j,k}}\mathbf{R}^* = \frac{3\mathbf{W}^{n+1}_{i,j,k} - 4\mathbf{W}^{n}_{i,j,k} + \mathbf{W}^{n-1}_{i,j,k}}{2\Delta t} + \frac{1}{V_{i,j,k}}\mathbf{R}_{i,j,k}(\mathbf{W}^{n+1}_{i,j,k}) = 0. \tag{3.38}$$

Within the real-time step, a pseudo time τ is introduced, with similar characteristics to the steady-state solver of Equation 3.37:

$$\frac{\mathbf{W}^{n+1,m+1}_{i,j,k} - \mathbf{W}^{n+1,m}_{i,j,k}}{\Delta \tau} + \frac{1}{V_{i,j,k}}\mathbf{R}^*_{i,j,k}(\mathbf{W}^{n+1,m+1}_{i,j,k}) = 0, \tag{3.39}$$

where m is the m^{th} pseudo-time step.

3.1.6 Overset Grid Method

While a sliding plane method with dedicated processors for interchange between moving grids is available, this work uses an overset (chimera) [157] approach. With this method, multiple levels of refined meshes can be placed on top of one another, allowing for an easy method to create local refinements in multiblock meshes. This method allows moving rotor blade meshes independently from one another in aeroelastic simulations. Deforming meshes, which contain all blades, are restrictive in terms of available blocking strategies and thereby avoided. This helps to preserve the cell qualities, at the cost of increased interpolation surface area. A benefit of the chimera method for structured grid applications is that local refinements do not need to be carried to the domain boundary, reducing the cell count compared to single-level meshes.

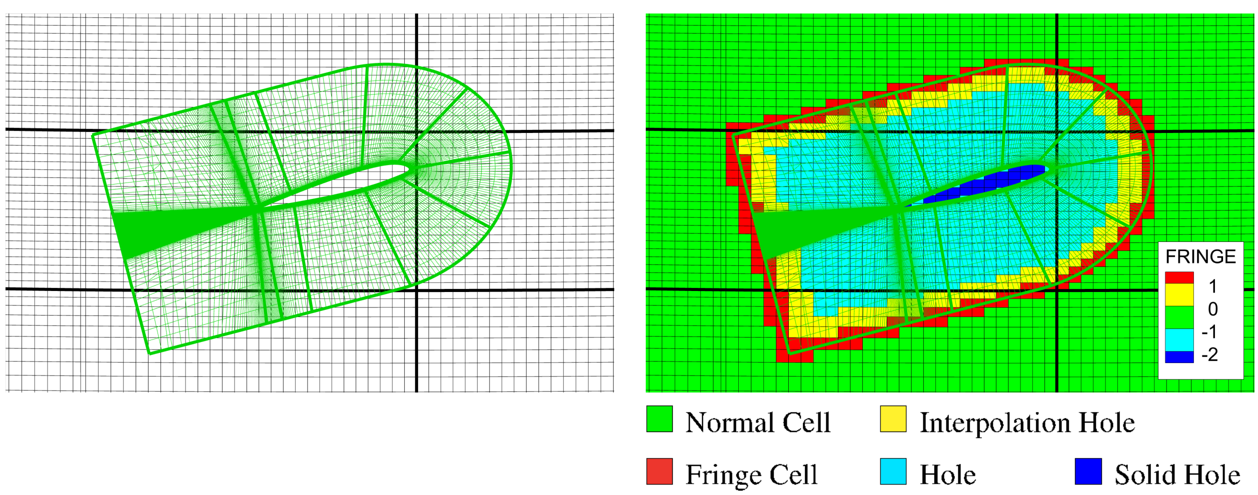

(a) Near-blade and background meshes (b) Cell flags on background mesh

Figure 3.1: The chimera overlapping grids of a rotor blade and its background.

An example of the overlapping chimera grid of a rotor blade, in its refined disk is shown in Figure 3.1. The first image shows the comparable cell resolutions near the boundaries. Figure 3.1 (b) shows the background colours, based on the applied chimera boundary condition. Normal and fringe cells are computed as usual on the background grid. Two layers of interpolation cells are chosen, where information is exchanged between foreground and background. This number of interpolation cell layers is suitable for the stencil of the discretisation scheme of HMB3. The hole cells are not computed on the background, and solid hole cells are ones, which are partially inside of a solid body on the higher-level grid.

For the interpolation, three methods are available: zeroth-order (nearest neighbour), least-squares and inverse-distance. The first is often used for debugging the chimera when large mesh motions exist. The inverse-distance weighting method is used in all simulations of this work, for its flexibility and accuracy. The higher-level mesh does not have specific interpolation cells, and instead, any suitably placed cells are considered. Where mesh motions occur, suitable time-stepping must be chosen, so that hole cells do not become computational cells in a single update. The contained values must first be initialised via interpolation from the foreground grid. Finer background meshes with thinner interpolation layers therefore require adequately small motions and time-steps.

The chimera fringes are calculated from a minimum volume bounding box (MVBB) based on the second moment of the grids' area matrix. A tree algorithm, together with raycasting, is used to categorize the cells. Some additional computations are required for multiple layers of overset cells, to assign the correct levels and boundary conditions. More detail on the chimera method implementation in HMB3 is available in [158].

3.2 Aero-servo-elastic Modelling in HMB3

On-blade actuators for higher-harmonic control have been demonstrated for improved vibration control, noise attenuation and fuel efficiency. Blade-integrated torsion actuators are considered in this study, due to their advantages, for example, their resistance to airborne sand and snow, and in icing conditions. For the development and certification of such devices, accurate simulation tools are needed. Because of the inherent couplings between in-plane and out-of-plane structural deformations, the HMB3 aeroelastic Navier-Stokes fluid solver is coupled to the commercial finite-element structural solver MSC NASTRAN. Conventional 1D beam models are compared to a 3D FE model to determine which tools are suitable for accurate simulations of rotor blades with blade-integrated piezoelectric actuators.

3.2.1 Structural Analysis in NASTRAN

The structural analysis techniques employed in rotor analysis vary due to requirements of accuracy, analysis speed and available data. Often, simplified 1D beams, where properties of structure and mass are applied at set stations, are employed in rotorcraft simulations. These models can integrate an approximation for the hub including the hinges and the pitch links. They are often natively integrated with low- and mid-fidelity aerodynamic tools but can also be coupled to CFD. However, there are limitations to the accuracy of beam structural models. At the cost of computational expense and meshing time, the root and aerofoil portions of the rotor blade can be analysed using the 3-D Finite Element Method (FEM). This method allows direct modelling of on-blade actuators and can represent spanwise variations better. Volumetric FEM also enables the extraction of blade stresses and can model corner stresses where cut-outs exist.

In structural solvers such as NASTRAN, a large number of parameters and different analysis types can be configured. For static deflection problems, linear and non-linear analyses are available. Different types of integration schemes can be selected for the elements. For example, reduced shear, and under-integration models are available, which avoid artificially stiffening high aspect-ratio, thin elements, without introducing zero-energy modes in the solution. Additional functions can be selected to reduce shear locking at large displacements, but this comes at an increased computational cost. These methods and their related functions are further described in the NASTRAN reference manuals [159].

The structural eigenmodes can be extracted from modal analyses. The frequencies and mode shapes can then be compared to other structural models and experimental measurements. The modes can also be used to calculate the blade motions in hover and forward flight, with weak- or strongly coupled aeroelastic algorithms, within some limitations. Besides this, transient response modelling with tables of aerodynamic loads and actuator positions can be used for CFD-CSD coupled simulation. This type of analysis is usually done using weakly coupled schemes, requiring sequential iterations. However, it is simpler to implement and allows for higher structural fidelity and direct actuator modelling. The HMB3 technical note [160] contains a beginner's guide to running cases in MSC NASTRAN and explains common parameters, syntax and input formats.

Linear Static Analysis

For small forces and deformations, at long time scales, a linear static analysis may be appropriate. The preconditions for this are a linear stress-strain response of the structure and no inertial effects. All stresses must be below the yield stress. In NASTRAN, this solution type is called with *SOL 101*, but the same results can also be obtained using *SOL 400* by specifying a *STATICS* type of analysis. The stiffness matrix $\mathbf{K}$ stays constant throughout the analysis, so no iterations are needed. This includes the boundary conditions and the forces of the problem. The relationship between the force vector $\mathbf{P}$, the stiffness matrix and the displacement vector $\mathbf{u}$ is linear:

$$\mathbf{P} = \mathbf{K}\mathbf{u}. \tag{3.40}$$

The displacement vector is obtained by inverting the stiffness matrix. The principle of superposition applies to loads and displacements.

Non-linear Static Analysis

Linear analysis is not suitable when the physical problem contains large structural deflections, non-linear material responses or possible contacts between parts. In non-linear problems, the stiffness matrix $\mathbf{K}$ depends on the loading and displacement vectors, the structural properties, the geometry and the boundary conditions:

$$\mathbf{P} = \mathbf{K}(\mathbf{P}, \mathbf{u})\mathbf{u}. \tag{3.41}$$

The final displacements cannot be solved directly, and iterative schemes are required, where the non-linear material properties are updated, based on the element deformations of the last iteration. Every iteration step also requires the stiffness matrix to be inverted, adding to the computational time. Non-linear static analysis in NASTRAN is executed via *SOL 106* or *SOL 400* when specified via *NLSTATICS* keyword.

Modal Analysis

Eigenmode extraction for modal analysis requires building the stiffness matrix before frequencies and shapes can be extracted. The stiffness matrix of a pre-loaded structure after a static or transient analysis may be used. The pre-loaded stiffness matrix is assumed to be symmetric and therefore orthogonal modes can be extracted, which contain frequencies and mode shapes. This is a suitable simplification, which linearises the structural response. However, the actual stiffness matrix is asymmetric to some extent, as the small angle approximation and centrifugal force introduce some non-linearity. The nonlinearity is not captured in the modal method-based unsteady simulations, however, a large static portion of it is included via the pre-stressing step.

The usage of these modes in CFD-CSD coupling is explained in Section 3.2.2. MSC NASTRAN supports the calculation of the modes in *SOL 106* and *400*, among others. In this work, both Lanczos and Modified Givens methods were used and the differences in mode frequencies and shapes were negligible. The centrifugal stiffening can be added by prepending a subcase of linear-static analysis. *SOL 106* natively accounts for the loading on the mode output when a previous non-linear statics result is taken as the initial solution of the modal type analysis. Similarly, *SOL 400* allows for linear and non-linear static analyses, or any other types of analyses to be chained with the modal analysis, making it also suitable. The implicit *SOL 400* method supports parts with contact and friction boundary conditions, which 106 does not.

Sources of Non-linearity

A common source of non-linearity in structural analysis arises from the material properties. Within the time frame of the analysis, most materials follow a linear, spring-like relation between stress and strain below the yield stress. The stiffness is the Young's modulus. Going beyond this stress, materials undergo plastic deformation, where the molecular and/or crystal structures begin to rearrange. The stress-strain relationship turns non-linear, often increasing strain disproportionately to the stress, until failure. Over long time spans under load, materials such as plastics undergo creep, where the strain is dependent on time and stress, and may undergo hysteresis. Other material non-linearities can come from kinematic hardening or viscoplasticity. Such non-linearities are not considered here, because the materials of rotor blades should never exceed the yield stress for durability.

Geometric non-linearities are problems associated with large displacements. The flap bending angles experienced on rotor blades may require a non-linear analysis. Linear analysis methods based on small angle approximations might not sufficiently capture the non-linear relation between strain and displacements. Other geometric non-linearities like buckling or snap-through are rare in rotorcraft applications, as these conditions are generally avoided. However, some on-blade actuators may exploit snap-through characteristics to avoid constant power draw during deployment.

Non-linearity can also arise from boundary conditions. Forces may change in amplitude, direction and application area, depending on structural deformations. As a rotor flaps and bends, the centrifugal force angle changes with respect to the finite elements. Iterative methods are required to resolve and update the force equilibrium. Other boundary condition non-linearities can arise from parts coming in contact or friction.

Structural Elements

In NASTRAN, structural elements are often denoted with a “C” prefix, while properties of such elements are entered by commands with the “P” prefix. Examples are CBEAM, CPENTA, PBEAM, PSOLID, PCOMP. Types of beam elements can be mixed in the structural analysis, within reason. Where rigid connections need to be made, such as between the hinge point and the surface layer of the blade root, rigid bar elements or similar (RBAR, RBE) can be employed.

A choice of 1D, 2D and 3D elements is available, which can be combined into a single model through clever application of constraints and connection elements. A summary of the element types is given in Table 3.2. While higher-order elements offer to capture the stresses and physics of the problem better, when resolution is sufficient, their modelling becomes increasingly complex and computationally expensive. Beam elements are most suitable for slender elements and are simple to define in terms of geometry, properties and loading. However, they are limited to axial, bending, torsion and shear effects without in-plane deformations. They also cannot account for corner stresses of material discontinuities, as the average stresses are simplified to the whole cross-section. Two-dimensional elements strike a good balance in terms of accuracy and complexity. They are the most suited element to resolve thin parts, where stresses can be assumed linear through the thickness. Replacing such 2D elements with 3D ones would often require an enormous increase in mesh resolution, as at least 3–4 volumetric elements are recommended in the thickness direction, and the element aspect ratios limit the in-plane sizing. 2D elements are also easier in simulation set-up, with a limited set of needed material properties, and these elements are usually aligned with the plane of fibre-reinforced materials.

Table 3.2: Comparison of 1D, 2D, and 3D elements in structural modeling using NASTRAN.

Type	Use Case	Complexity	Notes
1D	Frames, trusses, beams	Very Low	Simple geometry; easy to define cross-section
2D	Thin shells, plates	Moderate	Linear out-of-plane; no 3D aspect ratio issues
3D	Solid bodies, joints	High	Suited for stress analysis; careful meshing required

Beam-Element CBEAM The beam element (CBEAM) includes the properties of cross-sectional area, area moment of inertia in flap and lag, torsional stiffness, mass/length and the locations of the centre of gravity and elastic axis and pre-twist angle at both ends of the beam and at any intermediate stations. Concentrated and distributed loads can be applied to the beam. Non-linear material properties can be applied if necessary. The beam elements are defined as a line between two grid points, and the axial rotation is defined via two planes collinear with the axis. Their axes are explained in Figure 3.2. The beams form the elastic axis (shear centre), and the offsets for the neutral axis (tension centre) and mass axis (centre of gravity) can be provided at any beam location. However, since the structural properties are given with respect to the direction of the beam, large differences between the elastic axis' angle and the beam cross-section will introduce errors. Three-point beams are also available, where a middle point is specified for a beam with quadratic curvature.

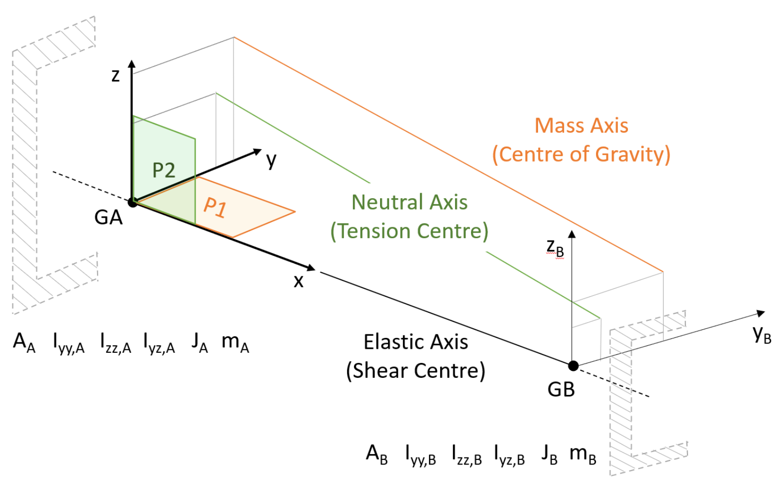

Figure 3.2: NASTRAN two-point CBEAM element axes and properties are shown. Reproduced from MSC NASTRAN Quick Reference Guide [161].

Shell-Elements CTRIA, CQUAD Shell elements are the two-dimensional intermediate between beam- and volume elements. They are highly computationally efficient and have been

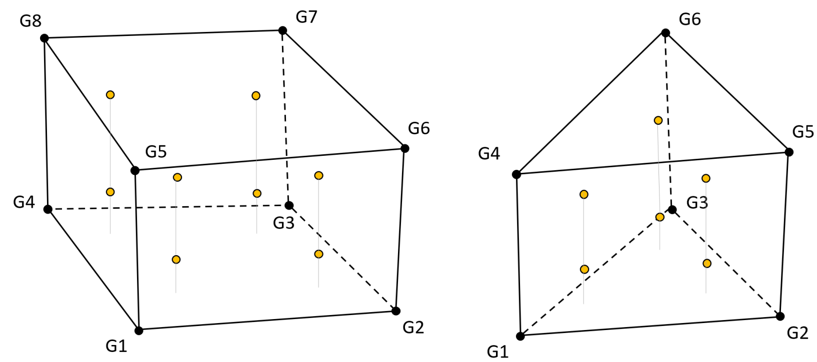

(a) CHEXA(8) element (b) CPENTA(6) element

Figure 3.3: NASTRAN CHEXA(8) and CPENTA(6) elements with the standard Gauss collocation points.

commonly used to represent complex structures such as fuselages or chassis designs. Moreso they are still commonly used during initial design stages. In this dissertation, shell elements have been used for thin parts, where the aspect ratio would otherwise be excessively large for volumetric elements. This speeds up convergence and also avoids introducing artificial stiffness. Shell elements are preferred for parts, whose thickness is less than 3–4 solid elements otherwise.

MSC NASTRAN supports composite layup calculations for these two-dimensional elements, via the *PCOMP* material entry. The layup ordering and orientation for any anisotropic or two-dimensional isotropic layers can be specified. The directions of the properties are defined by the positive surface normal direction from the node ordering and the principal in-plane direction, obtained either via a defined vector or the node numbering. The bulk properties of such a layered composite shell element can be calculated, and displayed natively in MSC NASTRAN, as a combination of four sets of isotropic properties.

Volume-Elements CTETRA, CPYRAM, CPENTA, CHEXA The 3D finite element model is made mostly from volume elements. The elements can be defined with linear edges (two points per edge), or as second-order elements made from three points per edge. The structural and non-structural mass properties are automatically calculated from the element's shape, size and assigned material density. The material properties can be provided as anisotropic or isotropic, including thermal properties. For parts made of composite materials, orthotropic properties can be provided in the preferred local or global reference frame. However, in the version of NASTRAN used here, the bulk properties of composite volume elements must be provided, and cannot be directly calculated from layups. Example hexa and penta elements are shown in Figure 3.3, where the Gaussian collocation points are marked orange.

NASTRAN Integration Schemes

Two integration schemes were considered in this study, and compared in Section 4.2.4. The integration scheme can be changed on a part-per-part basis. The first model is a 2×2×2 standard isoparametric integration scheme. The load and deformation distributions follow the same order as the element edges. Under-integration can be used to solve the problem quicker, however, a loss of accuracy is expected because of the introduction of zero-energy modes. A $2{\times}2{\times}2$ under-integration scheme with reduced shear and bubble-functions is available, which avoids hourglassing and shear locking for high aspect ratio cells. This formulation is also compared in the refinement study. Over-integration is also available in NASTRAN, where the elements may better resolve steep gradients such as in corner stresses at the expense of increased cost. This method, however, can result in elements with unrealistically high stiffnesses and is not needed for the models in this thesis. The formulations of the integration schemes are described in the MSC NASTRAN reference manual [159].

3.2.2 CFD-CSD coupling

In the current, state-of-the-art rotor aeroelasticity, the structure and aerodynamics are not evaluated simultaneously in a shared matrix. Therefore, it is necessary to couple the separate CSD and CFD codes. In terms of coupling frequency, loose and tight coupling exist. Loose coupling evaluates the structure, and sometimes trim, for a given solver-time period, then passes the deformations to CFD to repeat the same period. This is an iterative process, and to obtain convergence, the two separate solvers must also converge to a periodic (or static) solution. The method is not suitable for simulations of maneuvering flight, or other aperiodic conditions. A tight coupling scheme is one, where the structure and aerodynamics are updated at every time step. This method is not limited to periodic flows and can give correct transient results, at increased computational cost. A "strong-strong" coupling variation of this is achieved by coupling CFD and CSD at the sub-time-step level.

Two types of aeroelastic coupling are available in the steady and time-marching formulations of HMB3. In steady simulations, where time effects are ignored, the HMB Middleware is used to weakly couple CFD with the non-linear static structural analysis from MSC NASTRAN (Section 3.2.1). In time-marching simulations, the modal method directly included in HMB3 is employed, where the mode shapes obtained in MSC NASTRAN are superimposed by their respective amplitudes. Some more background information on the history of CFD-CSD coupling in rotorcraft applications was presented in Section 2.5.2.

The comprehensive review by Datta, Nixon and Chopra [117] in 2007 found that loosely and tightly coupled algorithms both could predict the same airloads in periodic flight conditions. Early problems with torsion oscillation of loose coupling schemes were attributed to the discrepancies between the pitching moment predictions of the comprehensive tools and the CFD solutions of the time. The state-of-the-art was described as non-linear beam models in single inertial-frame multibody solvers, connected by joints and rigid elements.

Loose coupling

Many contemporary rotor toolboxes use a fluid-structure coupling and trimming algorithm based on the “delta-airloads” approach. Notable implementations are [115, 116, 162]. Such a loosely coupled trimming methodology was first demonstrated by Tung *et al.* [92], combining the fidelity of a finite difference solver for the blade tip with an integral rotor code. The delta-airloads approach in its simplest form for periodic flow and deformations, is shown in Equation 3.42.

$$F_x^i = F_x^{mid,i} + (F_x^{CFD,i-1} - F_x^{mid,i-1}) \tag{3.42}$$

The parameter x represents the different aerodynamic force and moment components applied to the structure. The coupling approach combines the results of a mid-fidelity aerodynamic solver F_x^{mid} and calculates the error to the CFD solution F_x^{CFD}. The forces applied to the structure for period i are calculated from the error (delta) of the previous period $i-1$. When a periodic state is reached, the final forces and moments F_x^i are equal to the CFD loads. A loose coupling approach without mid-fidelity tools is possible, by calculating deformations purely from the CFD airloads (Figure 3.5). However, this may require more iterations and computational time than delta-airloads. A major advantage of the delta-airloads approach is also that the CFD error prediction is applied to the trim calculation of the mid-fidelity comprehensive code. The delta-airloads method is not currently employed in HMB3, since the framework does not contain a quicker, lower-fidelity solver in addition to the CFD solver.

The hover (OGE) simulations in this work use a steady formulation and hence only the static aerodynamic loading, the angular velocity centrifugal force and the boundary conditions are required for a converged aeroelastic simulation. The 3D coupling interface from the surface cell pressures to the FE-model nodes was implemented and verified as part of this work. Previously implemented algorithms for moving elements were adapted to enable the different methods of active twist application on the blade grid or structure. The HMB3 suite contains a middleware tool for data exchanges with external software packages. An interpolation skeleton file is created for the file-IO data exchange between HMB3 and NASTRAN. This file, written in NASTRAN bulk data format contains a list of points, which designate the outer mould line of the rotor blade CFD mesh. These points are connected to the nearest element on the NASTRAN structural model via rigid bar elements. Due to the convergence sensitivity of NASTRAN, these points are generated in locations where the surface-normal pressure force is mostly collinear with the connecting rigid bar. In the middleware, the forces are calculated and applied to the structural model via a NASTRAN input file. For 1-D beams, the CFD surface solution is sliced at the beam stations and integrated forces and moments are passed onto the beam nodes. In volume FE analyses, this step is modified for a direct three-dimensional force transfer. From the pressures and surface normal vector at every blade surface mesh cell, a force vector is written to the loads file. The force is applied to the nearest point in the interpolation file (0^{th}-order interpolation),

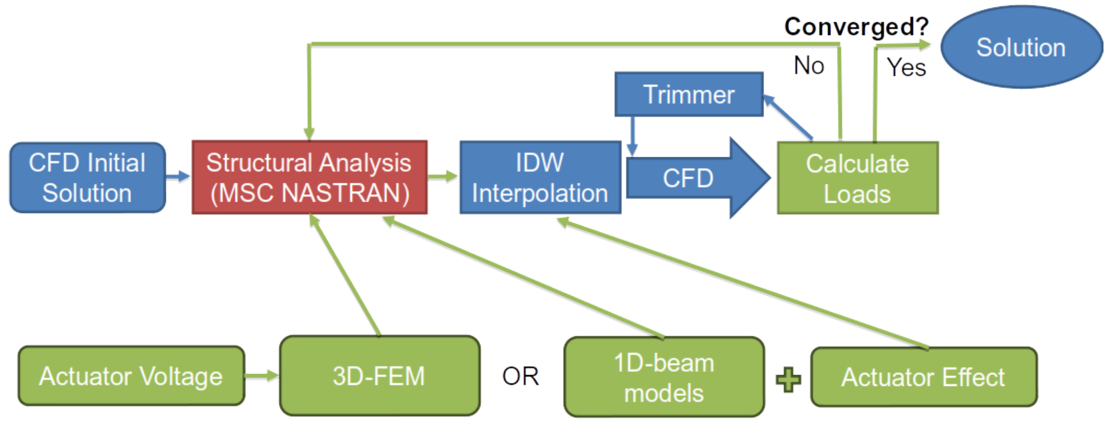

Figure 3.4: Flowchart of the aero-servo-elastic coupling of steady hover simulations in HMB3 with Middleware and MSC NASTRAN.

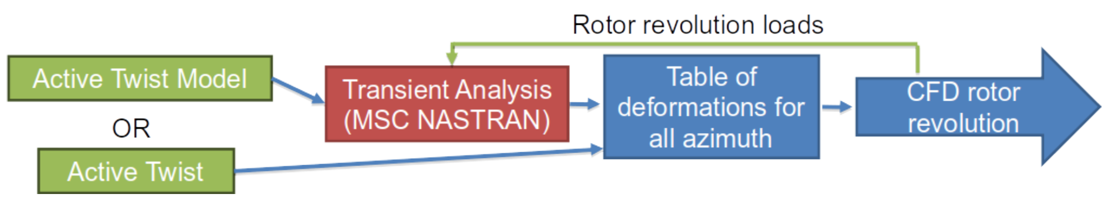

Figure 3.5: Flowchart of the loose aero-servo-elastic coupling for unsteady flows.

with negligible error, due to the high resolution. The displacements for each of the points are also taken directly from the NASTRAN output file. The mesh deformation algorithm, which is used in both loosely and tightly coupled simulations, is described below in Section 3.2.2.

Strong coupling

The strong coupling between structures and fluids can either be done via one structural update per CFD time-step, as a weaker form, or iteratively over multiple inner sub-steps. An illustration of the weaker and tighter strong coupling schemes is shown in Figure 3.6.

In unsteady flow conditions, a tight coupling of CFD and CSD is implemented in HMB3 using a modal method. It is a serial coupling, also known as the Gauss-Seidl method, as opposed to a Jacobi parallel coupling scheme. The transient structural response of the following time step

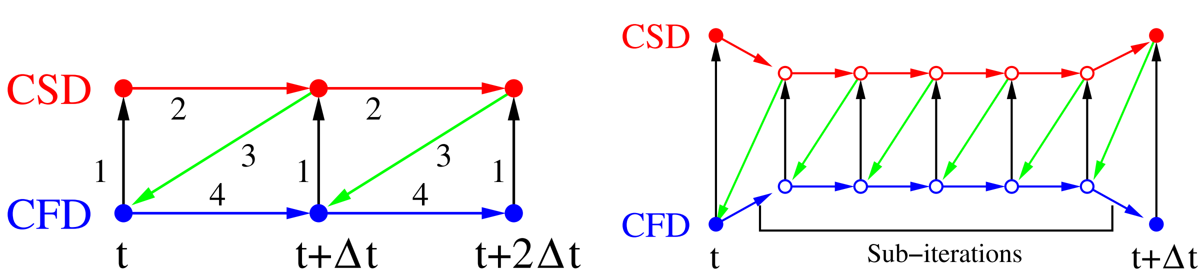

(a) Weak, sequential coupling (Gauss-Seidl)

(b) Tight coupling, Newton method.

Figure 3.6: Strong coupling data exchange sequencing.

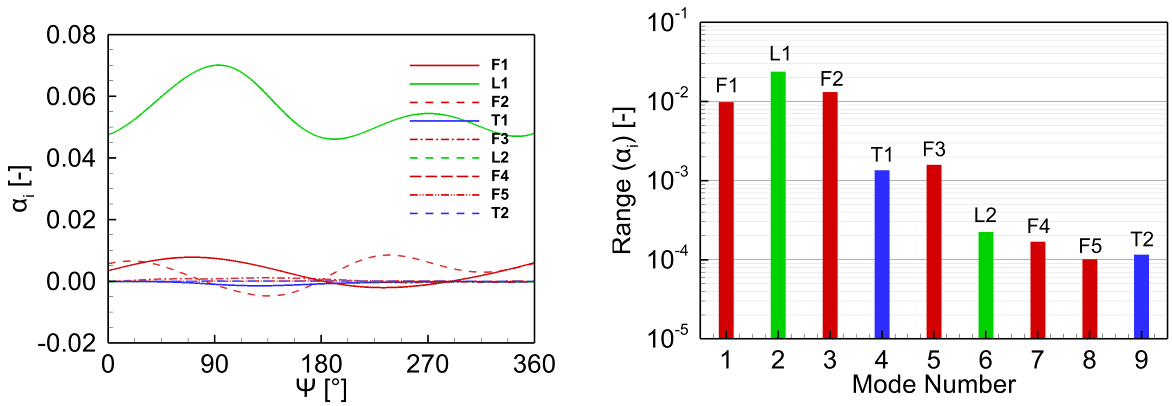

(a) Time history

(b) Range (max-min)

Figure 3.7: Values of the generalised coordinates of the first nine modes of blade 1 in the high-speed forward flight calculation of Section 5.3. The range is defined as the period maximum - minimum.

is evaluated before the CFD-solvers iteration. From MSC NASTRAN, usually, the first 9 structural eigenmodes are obtained. These modes are orthogonal to one another. The mode shapes are dimensional, and the generalised masses are scaled to $m_i = 1$kg, This permits the splitting of the aerodynamic forces $\mathbf{f}$ into the forcing of each individual mode f_i, as the dot product projection between the forcing and mode shape. The blade pressure and viscous forces are directly interpolated from CFD, rather than from integrated slices. Each mode is then evaluated by the general mass-spring-damper equations of motion [163]:

$$\frac{\partial^2 \alpha_i}{\partial t^2} + 2\zeta_i \omega_i \frac{\partial \alpha_i}{\partial t} + {\omega_i}^2 \alpha_i = \int f_i \cdot \phi_i(r)\, d(r)\,. \tag{3.43}$$

ω_i are frequencies per mode and ζ_i are the structural damping coefficients [164]; $\mathbf{r}$ is the list of the point coordinates used for interpolation. ζ_1 is usually applied as the value of the lag damper, while the remaining structural damping is low, simulating friction, work and other structural energy dissipation. The aerodynamic forcing then produces the generalised coordinates α_i, which is sometimes also referred to as the mode amplitude.

The superposition of these individual modes gives the complete deformed rotor blade shape [163]:

$$\phi(\psi, \mathbf{r}) = \phi_0 + \sum_{i=1}^{n_m} \alpha_i(\psi)\phi_i(\mathbf{r})\,, \tag{3.44}$$

where ϕ_0 is the undeformed shape. This approach linearises the deformation, and the number and shape of the supplied modes limit the space of possible deformations. However, the generalised coordinates of high-frequency modes, beyond the 10^{th} mode, are often orders of magnitude smaller than the first non-rigid modes. This is exemplified in Figure 3.7, which gives the time-history and range of generalised coordinates for the baseline high-speed flight case of Section 5.3. The solver implementation of the tight structural coupling using the frozen modes is shown in Figure 3.8.

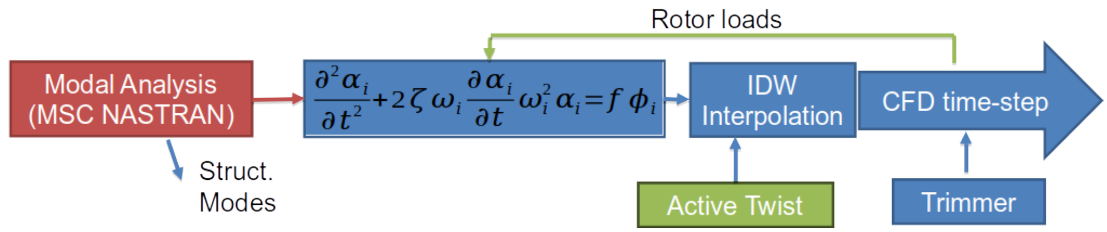

Figure 3.8: Flowchart of the aero-servo-elastic coupling for unsteady flows using frozen modes.

An even stronger coupling method as shown in Figure 3.6 (b) can be achieved by iterating between structural and fluid dynamics steps in sub-steps of the time-stepping. This considers both the fluid-to-structure and the structure-to-fluid coupling terms within the time step, guaranteeing accurate coupling when convergence is achieved. However, for every inner update, the mesh deformation algorithm must be executed. Because of the associated excessive computational cost, the method is not used in this study.

Mesh deformation

The moving least squares method [165] is used for smoothing and interpolation of the deformation from the CSD solution to the CFD grid. The method starts with a weighted least squares formulation for arbitrary points in the deformed solid. From the best match of these points in the deformed blade, a quasi-averaged translation and rotation of the mesh is calculated. This allows for an initial rigid mesh movement, before the surface is deformed, to reduce the likelihood of artifacts and errors in the deformed mesh. The volume grid is then deformed using the Inverse Distance Weighting (IDW) method proposed by Luke *et al.* [166]. IDW is a multi-variate interpolation method that calculates the value at an unknown point with a weighted average of the values of a known set of scattered points. The chimera boundary is also deformed with the volume to preserve cell quality.

Due to the large deformations of rotor blades through hinge rotations, these methods need to be robust for large deformation differences between sections or cells. High-skewness cells can significantly impact the accuracy and convergence of the CFD solver. Specifically, points in the volume mesh, located in the concave of a swept section will have their closest surface points at multiple separate sections of the rotor blade, with different deformations. This problem is mostly circumvented by the described initial mesh rotation and translation step, moving the undeformed mesh to the average deformed position. Additionally, the cell spacing of the CFD mesh is usually expanded at the chimera boundary, which distributes any remaining deformation gradients over larger cells.

3.2.3 Multi-Physics FEM Modelling for Piezoelectric Actuators

There are a number of analysis tools that allow direct simulation of piezoelectric transducers. For example, ANSYS Multiphysics developed by ANSYS Inc, Abaqus FEA developed by SIMULIA and the Structural Dynamics Toolbox by SDTOOLS for MATLAB [167]. In ANSYS both two and three-dimensional solid elements are available. While real piezoelectric materials can show some hysteresis, the constitutive response is usually modelled linearly in such toolboxes. Some piezoelectrics like quartz have negligible hysteresis, while others may reach up to 20% of the maximum displacement. The MacroFiberComposite™ by SMART Material does not list any hysteresis properties [131], and is therefore also modelled linearly in this study.

Piezoelectric Constitutive Equations

Piezoelectricity is the accumulation of electric charge of certain solids under mechanical strain. It is usually generated by the electromechanical interactions on the microscopic level of some crystalline materials. The reverse process, where an external electric field produces a mechanical strain is called the inverse piezoelectric effect. The IEEE Standards on piezoelectricity [168] define the three-dimensional piezoelectric constitutive equations for a linear piezoelectric material as:

$$\begin{Bmatrix} T_{11} \\ T_{22} \\ T_{33} \\ T_{23} \\ T_{31} \\ T_{12} \\ D_1 \\ D_2 \\ D_3 \end{Bmatrix} = \begin{bmatrix} c_{11}^E & c_{12}^E & c_{13}^E & 0 & 0 & 0 & 0 & 0 & -e_{31} \\ c_{12}^E & c_{22}^E & c_{23}^E & 0 & 0 & 0 & 0 & 0 & -e_{32} \\ c_{13}^E & c_{23}^E & c_{33}^E & 0 & 0 & 0 & 0 & 0 & -e_{33} \\ 0 & 0 & 0 & c_{44}^E & 0 & 0 & 0 & -e_{24} & 0 \\ 0 & 0 & 0 & 0 & c_{55}^E & 0 & -e_{15} & 0 & 0 \\ 0 & 0 & 0 & 0 & 0 & c_{66}^E & 0 & 0 & 0 \\ 0 & 0 & 0 & 0 & e_{15} & 0 & \varepsilon_{11}^S & 0 & 0 \\ 0 & 0 & 0 & e_{24} & 0 & 0 & 0 & \varepsilon_{22}^S & 0 \\ e_{31} & e_{32} & e_{33} & 0 & 0 & 0 & 0 & 0 & \varepsilon_{33}^S \end{bmatrix} \begin{Bmatrix} S_{11} \\ S_{22} \\ S_{33} \\ 2S_{23} \\ 2S_{31} \\ 2S_{12} \\ E_1 \\ E_2 \\ E_3 \end{Bmatrix} \tag{3.45}$$

where E_i and D_i are components of the electric field and electric displacement vectors. c^E is the elastic stiffness coefficient matrix in constant electric field conditions, e is the piezoelectric coupling coefficient matrix, ε is the matrix of dielectric permittivities in constant strain conditions, and T_i and S_i are the components of the stress and the normal and shear strain vectors. Assuming this linearity simplifies the actuator model to not include hysteresis, as discussed earlier.

Example units for the electric field are V/m, equal to N/C. The dimensions can be broken down into $MassLengthTime^{-3}Current^{-1}$. When using a matrix notation the equations can be written as:

$$\{T\} = \left[c^E\right]\{S\} - [e]^T\{E\} \tag{3.46}$$

$$\{D\} = [e]\{S\} - \left[\varepsilon^S\right]\{E\}. \tag{3.47}$$

However, there is a widely used alternative and equivalent representation, due to manufacturers usually providing the strain-charge form of the piezoelectric coupling matrix d. For example, Dong and Meng [169] write the constitutive equations in the following form:

$$\{S\} = \left[s^E\right]\{T\} - [d]^T\{E\} \tag{3.48}$$

$$\{D\} = [d]\{T\} - \left[\varepsilon^T\right]\{E\}, \tag{3.49}$$

where the following relationships hold:

$$\left[s^E\right] = \left[c^E\right]^{-1} \tag{3.50}$$

$$[e] = [d]\left[c^E\right] \tag{3.51}$$

$$\left[\varepsilon^S\right] = \left[\varepsilon^T\right] - [d][e]^T. \tag{3.52}$$

Here s^E is the symmetric compliance matrix, and d is the piezoelectric strain-charge coefficient matrix. By convention, the ferroelectric ceramics used in piezoelectric materials are polarized along the z-axis (direction 3) and present a symmetry in their hexagonal crystallographic structure. This in-plane symmetry reduces the number of independent coefficients to describe the piezoelectric behaviour from 21 to 10. Five elastic coefficients, three piezoelectric coupling coefficients, and two dielectric coefficients. Hence [169]:

$$\left[c^E\right] = \begin{bmatrix} c_{11}^E & c_{12}^E & c_{13}^E & 0 & 0 & 0 \\ c_{12}^E & c_{11}^E & c_{13}^E & 0 & 0 & 0 \\ c_{13}^E & c_{13}^E & c_{33}^E & 0 & 0 & 0 \\ 0 & 0 & 0 & c_{44}^E & 0 & 0 \\ 0 & 0 & 0 & 0 & c_{44}^E & 0 \\ 0 & 0 & 0 & 0 & 0 & \frac{c_{11}^E - c_{12}^E}{2} \end{bmatrix}, \tag{3.53}$$

$$[e] = \begin{bmatrix} 0 & 0 & 0 & 0 & e_{15} & 0 \\ 0 & 0 & 0 & e_{15} & 0 & 0 \\ e_{31} & e_{31} & e_{33} & 0 & 0 & 0 \end{bmatrix}, \tag{3.54}$$

$$\left[\varepsilon^S\right] = \begin{bmatrix} \varepsilon_{11}^S & 0 & 0 \\ 0 & \varepsilon_{11}^S & 0 \\ 0 & 0 & \varepsilon_{33}^S \end{bmatrix}, \tag{3.55}$$

Table 3.3: Equivalence between thermal and piezoelectric strain.

Physical Quantity	Piezoelectric Problem	Thermal Analogy
Electrical Field E	Applied to material	Temperature Change $\Delta\Theta$
Induced Strain S^E	$S^E = d^T E$	$S^\Theta = \alpha\Delta\Theta$
Piezo strain coefficient d	Material constants	Thermal expansion coefficient α

while the piezoelectric strain coefficient matrix can be written as [169]:

$$[d] = \begin{bmatrix} 0 & 0 & 0 & 0 & d_{15} & 0 \\ 0 & 0 & 0 & d_{15} & 0 & 0 \\ d_{31} & d_{31} & d_{33} & 0 & 0 & 0 \end{bmatrix}. \tag{3.56}$$

Thermoelastic Constitutive Equation

From classical thermoelasticity theory, the generalized Hooke's law, with thermal effects taken into account, is:

$$\{T\} = \left[c^E\right]\{S\} - \left[c^E\right]\{\alpha\}\Delta\Theta, \tag{3.57}$$

where α is the thermal expansion coefficient vector and $\Delta\Theta$ is a temperature difference, relative to a user-defined reference temperature

3.2.4 Thermal Analogy Method

The thermal analogy method is a simplified modelling technique to describe the reverse piezoelectric effect as an analogous thermal expansion of a material. It leverages the physical similarity between thermal strain and electrically induced strain. This equivalence is demonstrated in Table 3.3. Hysteresis and non-linearity, which complicate the piezoelectric strain coefficients d into functions of displacement, charge and field properties can also be partially recreated if the structural solver supports hysteresis or custom thermal expansion coefficient definition.

The main advantages of the thermal analogy method are its simplicity, software compatibility and computational efficiency. It does not require solving the electro-mechanical coupled PDEs, at the cost of less accuracy compared to elaborate piezoelectric modelling software. This simplicity allows it to be used in common structural FEM solvers, which only offer thermal expansion effects in their toolboxes. Solvers such as NASTRAN, even allow definitions of non-linear thermal expansion coefficients with hysteresis, bringing it closer to full physical modelling. However, the thermal analogy method cannot directly model phenomena, such as charge accumulation, and applying the thermal boundary condition equivalents for non-constant electric fields may require impractical actuator resolution and modelling effort. Furthermore, strain sensing capability is not possible in most structural FEM solvers, as deformations are not transferred back into temperature changes, and so no additional piezoelectric resistance is present.

Taking equation 3.46 and 3.51 the piezoelectric strains can be rewritten as:

$$\{T\} = \left[c^E\right]\{S\} - \left[c^E\right][d]^T\{E\} \tag{3.58}$$

and comparing it to the formulation of thermal strain, equation 3.57.

$$[d]^T\{E\} = \{\alpha\}\Delta\Theta. \tag{3.59}$$

In the general case, the only non-zero terms of $[d]^T$ are d_{15}, d_{24}, d_{31}, d_{32} and d_{33} so, equation 3.59 reduces to:

$$d_{15}\Delta E_1 = \alpha_5\Delta\Theta, \quad d_{24}\Delta E_2 = \alpha_4\Delta\Theta, \quad d_{3i}\Delta E_3 = \alpha_i\Delta\Theta \quad (i = 1,2,3), \tag{3.60}$$

where the electric field $E_i = \phi_i/t$ is the voltage deltas divided by the thickness of the piezoceramic actuator. $\Delta\phi_1$ and $\Delta\phi_2$ are the in-plane voltage differences and $\Delta\phi_3$ the voltage differences between the elecrodes [170].

This can be further simplified, as usually, the in-plane electric fields E_1 and E_2 are negligible. The actuation mechanism usually relies on the d_{3i} effects only, in the reference poling direction, which is applied over the thickness of the actuator. Setting them to zero and $E_3 = \Delta\phi_3/t$ then an exact analogy between piezoelectric strain and thermal strain for linear, ideal piezo actuators is obtained [170]:

$$d_{3i}\frac{\Delta\phi_3}{t} = \alpha_i\Delta\Theta, \quad i = 1,2,3. \tag{3.61}$$

Hence, the voltage actuation of a piezoceramic can be simulated exactly using elastic elements with the thermal actuation rather than using piezoelectric elements. In the case of the commercially available MacroFiberComposites™ [131], the elongator type has negligible d_{31} and d_{32} components, bringing the analogy equation to its simplest form [170]:

$$d_{33}\frac{\Delta\phi}{t} = \alpha\Delta\Theta. \tag{3.62}$$

Arbitrarily setting the thermal expansion coefficient of the material to the value of the piezoelectric expansion coefficient, the applied temperature offset from the reference is then simply the applied voltage divided by the actuator thickness:

$$\Delta\Theta = \frac{\Delta\phi}{t} \quad (d_{33} = \alpha), \tag{3.63}$$

as long as unit systems are kept consistent.

There are some limitations of the thermal analogy [170, 171]. Piezoelectric elements can be model actuators but not sensors and it is not possible to simulate the behaviour of transducers using this method.

Thermal Analogy in MSC/NASTRAN

The thermal analogy method allows piezoelectric actuators to be modelled using classic FEM software like MSC NASTRAN. In this case, the MAT9 material properties card [161][p. 2002] completely describes a volumetric, anisotropic material as:

$$\left\{\begin{array}{c}\sigma_x\\ \sigma_y\\ \sigma_z\\ \tau_{xy}\\ \tau_{yz}\\ \tau_{zx}\end{array}\right\} = \begin{bmatrix} G_{11} & G_{12} & G_{13} & G_{14} & G_{15} & G_{16}\\ G_{12} & G_{22} & G_{23} & G_{24} & G_{25} & G_{26}\\ G_{13} & G_{23} & G_{33} & G_{34} & G_{35} & G_{36}\\ G_{14} & G_{24} & G_{34} & G_{44} & G_{45} & G_{46}\\ G_{15} & G_{25} & G_{35} & G_{45} & G_{55} & G_{56}\\ G_{16} & G_{26} & G_{36} & G_{46} & G_{56} & G_{66} \end{bmatrix} \left[\left\{\begin{array}{c}\varepsilon_x\\ \varepsilon_y\\ \varepsilon_z\\ \gamma_{xy}\\ \gamma_{yz}\\ \gamma_{zx}\end{array}\right\} - \left\{\begin{array}{c}A_1\\ A_2\\ A_3\\ A_4\\ A_5\\ A_6\end{array}\right\}(\Theta - \Theta_{REF})\right] \tag{3.64}$$

where Θ denotes the temperature excitation, Θ_{ref} is the reference temperature and A_i denote the thermal expansion coefficients and the usual symmetry constraints apply (eg. $G_{16} = G_{61}$). Alternatively, the MAT8 property can be used to define a two-dimensional material following the same pattern. Considering the material orthotropic, with equal in-plane components, the thermal expansion coefficients are simplified to:

$$A_1 = A_2 = \alpha_1, \quad A_3 = \alpha_3. \tag{3.65}$$

Therefore all properties can be expressed in terms available in NASTRAN:

$$\Theta_{ref} = 0 \quad \Theta = E_3 = \frac{\phi_3}{t}, \quad (A_1 = A_2 = d_{31}, \quad A_3 = d_{33}). \tag{3.66}$$

The piezoelectric actuators are driven by a voltage source. Assuming that the material is uniform, the electric field between two electrodes is constant and is given by:

$$E = \phi/t, \tag{3.67}$$

where E is the eletric field, ϕ is the potential difference between electrodes, and t is the distance between electrodes.

Active Twist Implementation

There are multiple ways to model the active twist motions for the beam and FE models. Volumetric finite element models can have their actuators directly modelled via the described thermal analogy method. In static cases, a single temperature difference needs to be defined, and in transient analysis types, a table of temperatures representing the voltage curve is needed. Generating sectional torsion directly via a thermal analogy is not supported for beam models. Instead, the

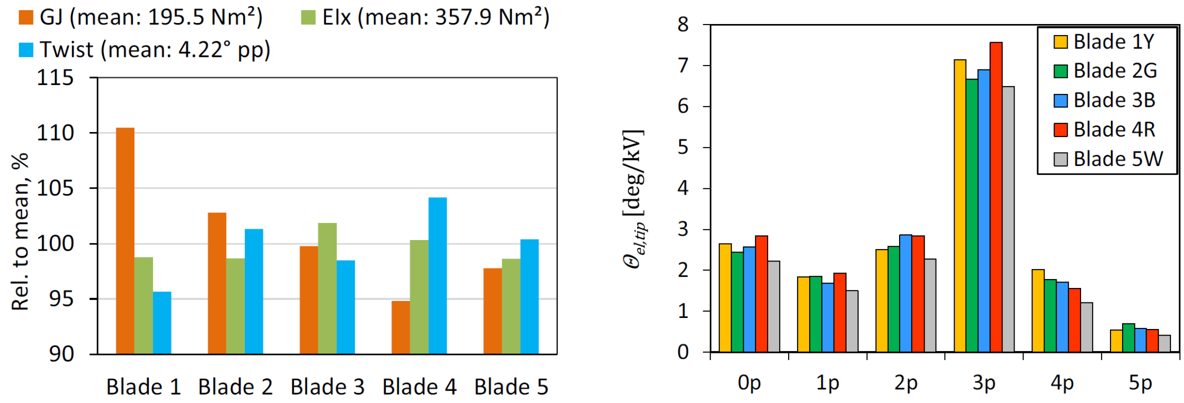

(a) Static blade properties

(b) Twist amplitudes at n/rev actuation

Figure 3.9: Measurements of static and dynamic twist amplitudes in the joint work at 80% peak-to-peak Voltage [13]. Figure (a) gives the mean measured properties in the header, and the relative deviations of each blade. Figure (b) shows the absolute twist response values.

twisting can be prescribed via an analytical, rigid mesh motion or by applying an analogous, expected torsion moment at the beams and nodes. A third option exists, where in a modal calculation, an additional torsion mode is superimposed, with a fixed, tabulated forcing function. However, this is practically indifferent from rigid mesh motions and has not been implemented in this study. Of course, the methods for the beam models can also be applied to the volumetric finite element model, with some caveats as to how the moments are applied.

At higher harmonic frequencies, the active twist system operates on a purely sinusoidal signal with a phase shift and a static offset defined as follows:

$$\theta = \theta_{\text{offset}} + \theta_{\text{active}} \cos(n\psi - \phi_n). \tag{3.68}$$

The resulting angle θ is the blade tip pitch-up torsion, n is the rotor frequency multiple of the active input, ψ is the rotor azimuth angle and ϕ_n is the active control phase shift. A 2/rev active input at a 210° phase, would then produce a tip pitch-up, meaning a reduction of blade twist, at 105° and 285° blade azimuth. For the STAR blades, the amplitude θ_{active} of the actuators at a 2/rev frequency was estimated to be 2.06 deg/kV, with 50% of the 2 kV peak-to-peak capability applied. This is close to the later measured 4.22° peak-to-peak at 2 kV as described in Figure 3.9 (b), taken from the collaboration paper [13]. The actuators are biased with θ_{offset} of 400 V, resulting in a 0.82° nose-up twist deformation when active. The simulations of this dissertation include this static offset as they were conducted as part of the pre-test prediction effort of the STAR project. They represent a practical use case of actuators, but they do not fully isolate the harmonic component of the twist. The static twist offset angle is also influenced by the changing actuator effectiveness under centrifugal and other forces, and is therefore not necessarily linearly additive with the harmonic component.

Chapter 4

CFD Meshing and FE Modelling for Helicopter Rotors

4.1 CFD Mesh generation

The meshes for this thesis have been set up as structured multiblock-grids in Ansys ICEM CFD, which allows a high grade of parallelisation in HMB3. All cells are therefore hexahedral. An overset-grid (chimera) method has been used to split the domain into a background and the blade-adjacent mesh. This allows for the blade to be freely articulated in the simulation domain without mesh deformation. In aeroelastic cases, overset grids enable mesh deformation methods which have little adverse effect on the volume ratios and cell skewness by deforming the chimera boundary with the surface. The background grids are unaffected by blade mesh deformations. The $k-\omega$ SST turbulence model with fully resolved boundary layers has been used for all test cases, and sets the grid scale for first surface layer height to $y^{+} \approx 1$. The blade geometries were detailed in Chapter 2, Sections 2.4.2 (ATR), 2.4.4 (STAR), and 2.7.1 (HVAB). After showing the blade meshes, the intermediate and far-field grids are presented.

4.1.1 Blade Meshes

With the straight trailing edge and the rounded leading edge, a C-H topology was chosen for the blocking around all rotor blades in this study. The blocking overhangs on both spanwise ends of the blade to capture the finite span's tip effects without interpolation between meshes. Different blade meshes were created for hover and forward flight of the STAR. The initial blade for the hover simulations was only modelled outboard of 22 %R. This allowed for a quicker set-up of the model and multiblock-grid. This geometry simplification caused minimal loss in accuracy, as the dynamic head in hover is quadratically dependent on the distance from the rotational axis. Therefore, the blade root contribution to lift and power is minimal. The forward flight mesh including the blade root had an increased number of blocks for better load balance on many cores. 384 blocks per blade were used instead of 118 blocks for the hover mesh. The increased number of blocks improved the boundary layer cell quality further, by smoothing the radial cell distribution and creating near-perfect surface normals via the spacing functions around the aerofoil's shape. This method was also applied to the HVAB hovering blade.

The blade meshes from Figures 4.1 and 4.2 have been used for all cases presented in this dissertation. They strike a balance between mesh density in regions of interest and computational cost. The spacing and geometries follow the experience and best practices to sufficiently resolve the aerodynamic phenomena in the RANS formulation of HMB3. Hover and forward flight validation and mesh studies were published by Jimenez-Garcia and Barakos [172, 173] and Fitzgibbon *et al.* [174]. A study on vortex wave breakdown in hover [175] showed that further mesh refinement did not affect the aerodynamic loads in hover. These practices are also validated by the obtained results of the HVAB blade in Section 5.2.3. Other comparable work by You, Jung and Kim [111] model an active twist rotor with similar geometry using 3.17 mio. cells for the four blades, and 12.5 million for the cartesian background, totalling 16.2 million cells for forward flight. A coarser background spacing of 0.15%c and a comparable time step of 0.2° were used. Some mesh and time-step studies have been conducted as part of this work, but not of the rigorous standard as would be required to be written up. One obstacle was that differing mesh resolutions required re-sizing of the chimera boundaries and time-step changes, to retain a suitable number and overlap between chimera interpolation cells. The meshes use a similar number of cells to higher Reynolds number cases of the aforementioned peer-reviewed works, meaning they are higher resolved, and the topology was improved for better cell quality and surface normal angles. The near-blade meshes and near-background was prioritised for mesh resolution, to enhance the performance prediction.

The k-ω-SST turbulence closing equations require a first layer cell height to satisfy the calculated $y^+ < 1$ above the no-slip boundary condition to accurately resolve the gradients in the flow laminar sublayer. The hover blades are modelled with a first layer height of $10^{-5}c$, which is within the y^+ requirement for almost all of the blade surface. However, y^+ values up to 1.7 were observed in limited areas of strong flow acceleration, only at regions of tip vortex interactions in maximum thrust hover. This is shown in the scenario of the STAR blade at a high incidence where stall is starting to occur (Figure 4.3). A symmetric colour scheme was chosen to emphasize values above and below $y^+ = 1$. Because of the validation of past cases, the good validation results in Section 5.2.3 and the prohibitive additional computational expense to re-run all cases, this was considered sufficiently resolved. Correct resolution and cell expansion ratios in the turbulent mixing layer, which is approximately between cell 10 and 40 from the surface, were emphasised.

The wall and the chordwise spacings were slightly reduced in the blade outboard region of the forward flight blade, in anticipation of more compressibility effects on the advancing side azimuthal station. The cell size requirements were relaxed in the root region. This avoids

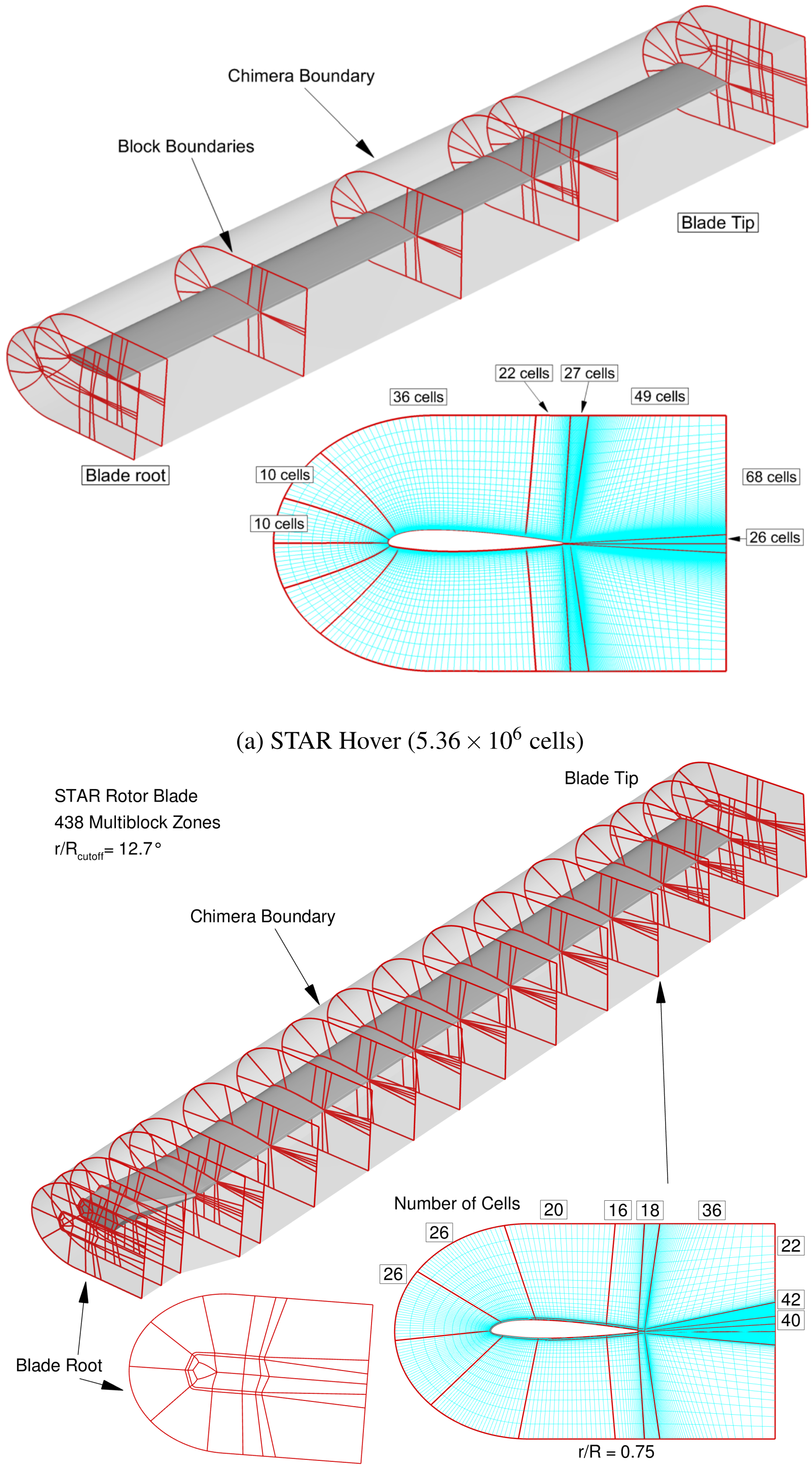

(a) STAR Hover (5.36×10^6 cells)

(b) STAR Forward flight, with root (4.95×10^6 cells)

Figure 4.1: Topology and mesh point distributions for the STAR blade.

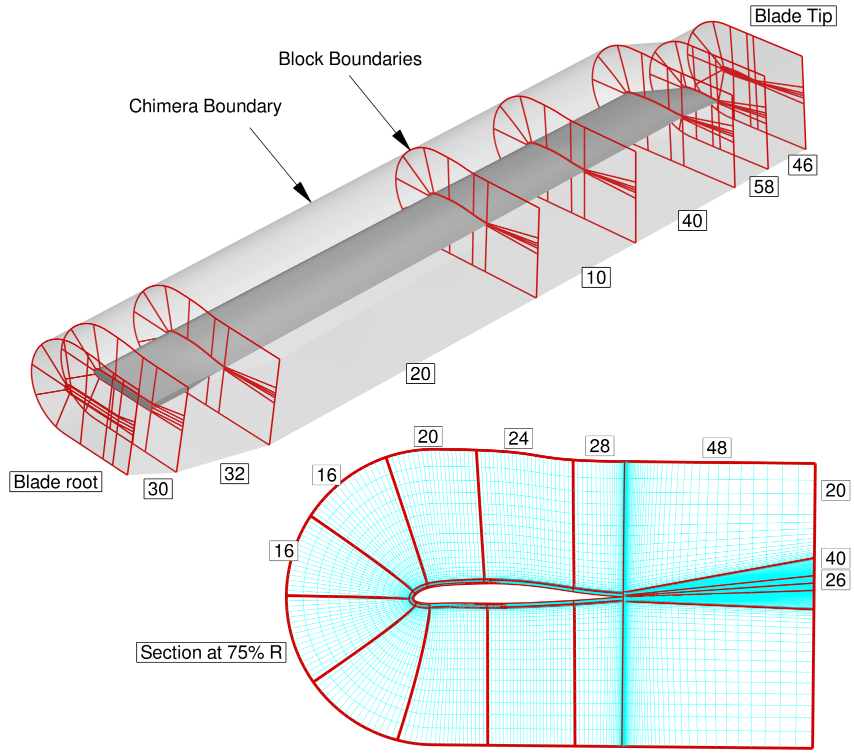

(c) HVAB Hover (4.73×10^6 cells)

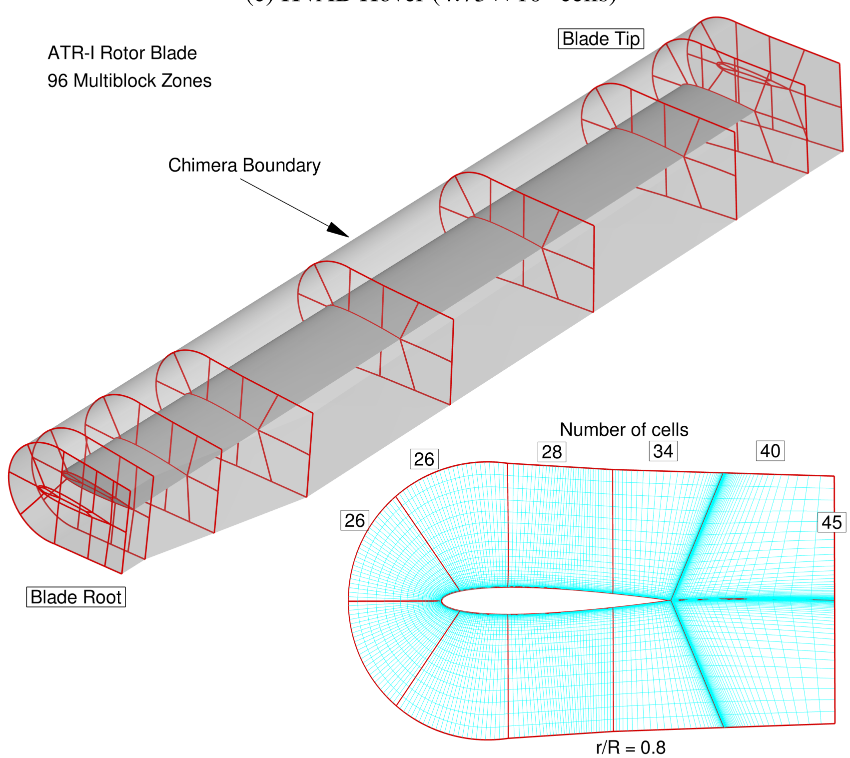

(d) ATR Hover (4.72×10^6 cells)

Figure 4.2: Topology and mesh point distributions for the HVAB and ATR blades.

overresolving the flow and aids convergence speed. The most difficult scenario of a maximum thrust forward flight in a dynamic stall is shown in Figure 4.4. With y^+ less than 1.4 in the worst areas of the presented case, this was considered sufficiently resolved. The blade root region of the forward flight blade is not streamlined and therefore shows higher flow gradients and much more turbulent and detached flows. While the y^+ is beyond the target on the advancing side, the trade-off was made to better resolve the turbulent wake of the blunt blade root shape. This area has an almost negligible effect on the integrated loads and the surface was considered sufficiently resolved for its importance. The HMB3 URANS flow solver, using the Menter k-ω SST turbulence model is validated for near blade Reynolds eddy turbulent viscosity ratios ($R_{et} = \mu_t/\mu$) values in the order of hundreds. Figure 4.5 shows the hovering STAR blade at less than 200 R_{et} in the near blade region. Most importantly, Figure 4.5 (b) and (c) specifically show a completely laminar sublayer in accordance with the fully resolved boundary layer model, and RET at the stagnation point is also ≤ 1, at around 0.25. These metrics have also been confirmed on the other hover and forward flight cases, at inboard, mid-span and outer locations, where no vortex interactions were occurring.

A hyperbolic distribution of nodes with an expansion ratio below 1.2 in the surface normal directions, sufficiently resolves the buffer layer flow. The outmost layer of the chimera boundaries on the foreground blade grids is sized to 0.08 chords for the STAR (due to the high aspect ratio), and 0.05 chords for the HVAB rotor. Hover cases where different linear blade twist distributions were compared, had the twist added in the meshing step by rotating the blade sections around the pitch axis. Changes due to the active twist system were instead applied via mesh deformation in the solver. This is explained in Chapter 3.2, Aero-servo-elastic Modelling in HMB3.

4.1.2 Hover Background Meshes

The blade background grid is similar for all hover cases with the domain size scaled by the rotor aspect ratio. The number of grid points is slightly adjusted to keep the background mesh spacing to 5% of the chord length in the near-blade region. The refined region includes the tip vortex path for at least three vortex passages. The boundary conditions and cell distributions are shown in Figure 4.6. The grid is circularly aligned, with a cylindrical inner wall, to simplify the blocking. This wall has little effect on the flow as the local air speed is almost zero, and it is not considered in the integrated loads.

The circumferential spacing at the blade tip region is slightly larger, at 8% c_{ref}, since much smaller flow gradients are expected in this direction. An effort was made to match the blade and background grid spacings, and an inverse distance weighted approach was used for the chimera interpolation. A Froude-boundary condition, based on a source-sink model, was applied to model the in and outflow of the domain. The cell spacings are gradually increased towards the domain boundaries, as a means to dissipate free turbulence, to accelerate convergence at no cost

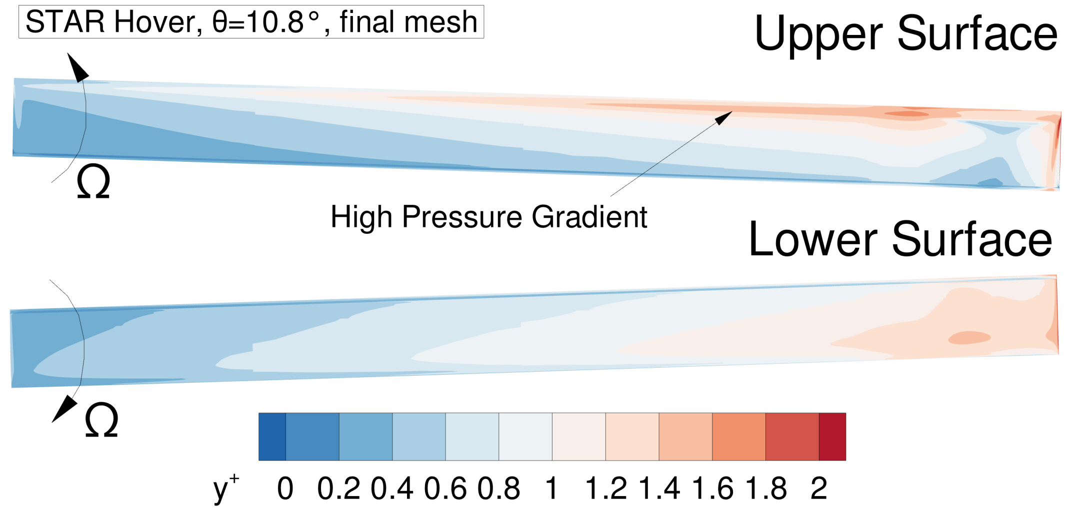

Figure 4.3: First layer cell height expressed in y^+ for the STAR blade in hover at 10.8° collective, in the finite element model coupled simulation.

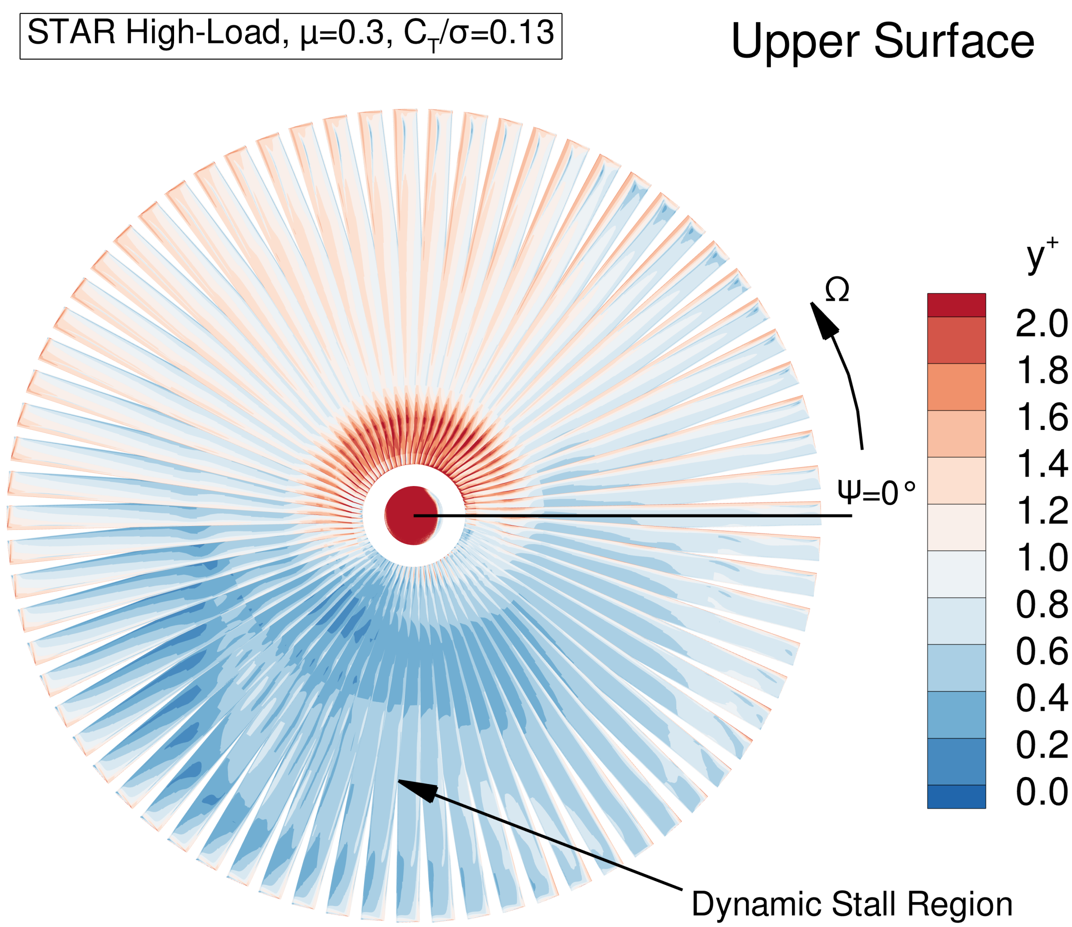

Figure 4.4: First layer cell y^+ at all azimuthal positions of a maximum thrust, dynamic stall forward flight simulation using the final mesh.

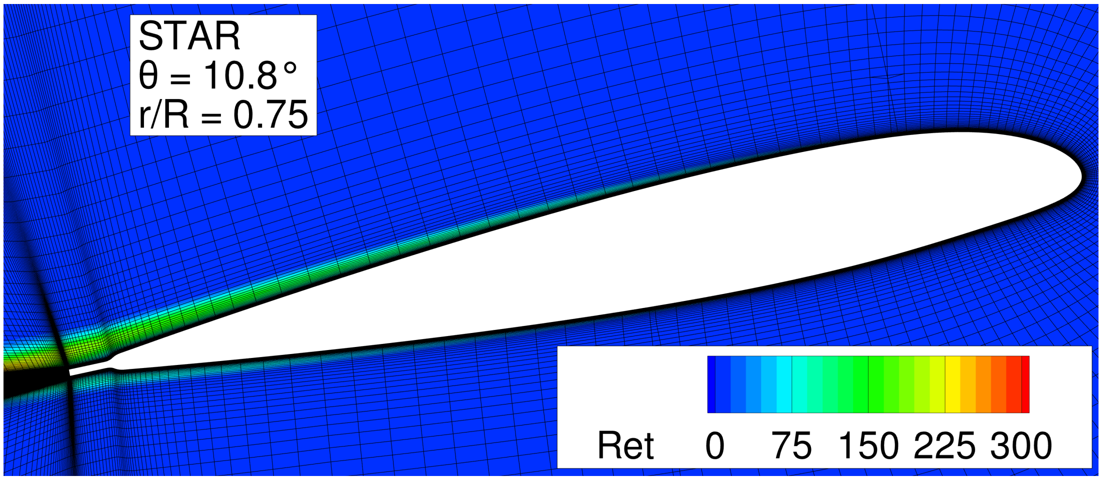

(a) With near blade grid

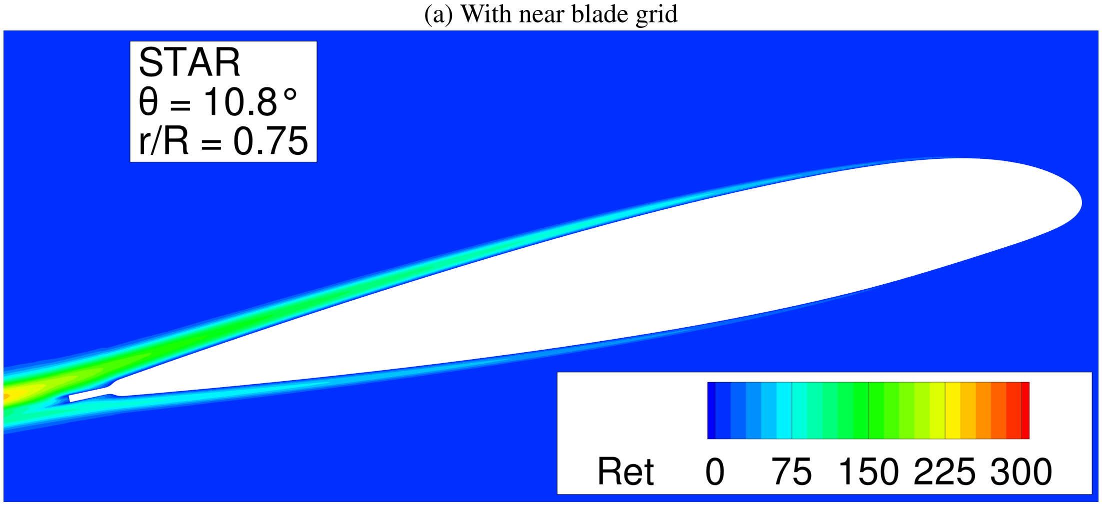

(b) Without near blade grid

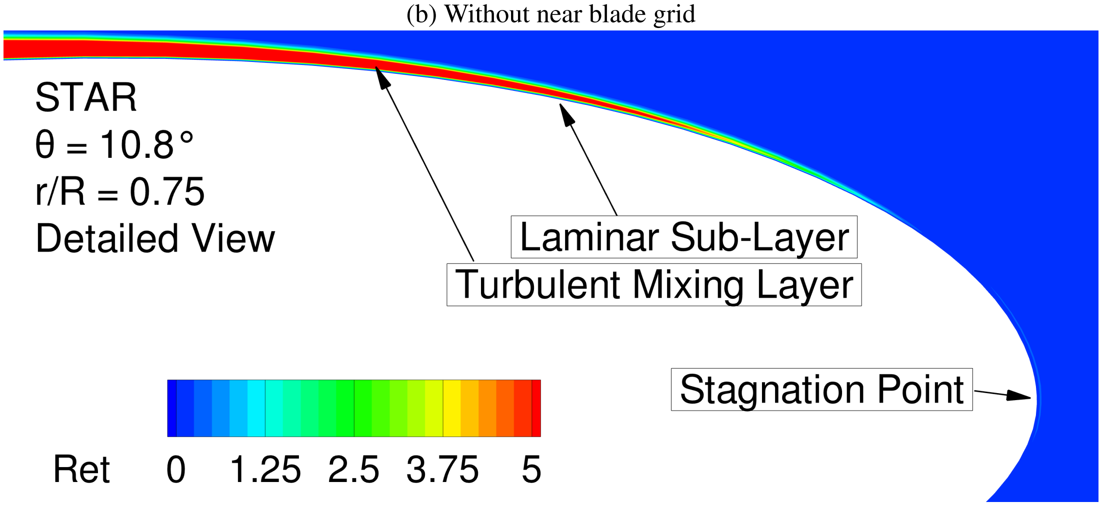

(c) Detail view without near blade grid

Figure 4.5: Reynolds eddy turbulent viscosity ratio (R_{et}) of the STAR blade in hover at 10.8° collective, at 75% radial station where no blade vortex interactions or shock occur.

in accuracy. This is analogous to the breakdown and viscous dissipation of the vortices and the wake of hovering rotors.

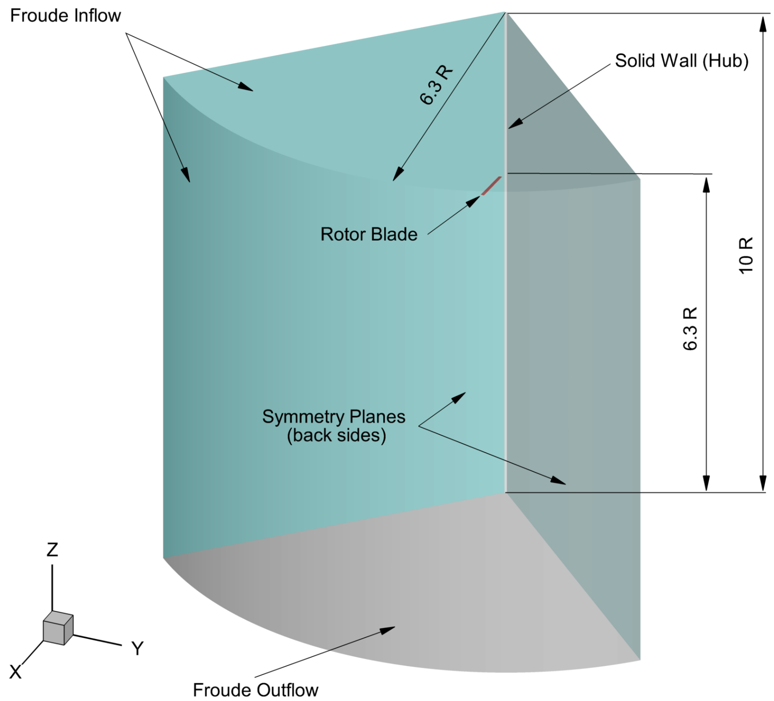

(a) Topology

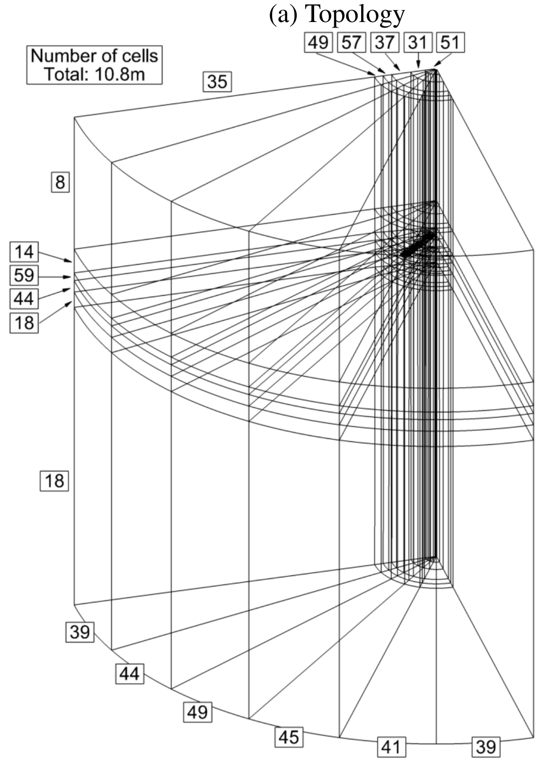

(b) Cell distribution

Figure 4.6: Topology, boundary conditions and cell distributions are shown for the 10.8m cell hover background mesh.

Table 4.1: Cell and block numbers of the CFD grids. The ratio of largest to mean block size is calculated as n_{max}/n_{avg}. Suffixes H: hover, F: forward flight

	Blade			Background			Total
Mesh	**Cells** $\times 10^6$	**Blocks**	**Ratio**	**Cells** $\times 10^6$	**Blocks**	**Ratio**	**Cells** $\times 10^6$
ATR-H	4.72	86	3.50	7.19	216	2.11	11.91
HVAB-H	4.73	204	3.48	7.19	216	2.11	11.92
STAR-H	5.36	120	5.15	10.8	216	3.29	16.16
STAR-F	4×4.95	4×438	5.35	11.42 + 2.09	448 + 816	3.15	33.31

4.1.3 Forward Flight Background Mesh

The background grid for the forward flight cases is shown in Figure 4.7. A three-level chimera method is used, with free stream conditions on the domain boundary. The rotor shaft angle is accounted for via the free stream velocity vector. The domain is a cylinder of 30 rotor radii in diameter, around the centre of rotation. The near-blade background grid is a disk, of which a quarter is shown in Figure 4.7 (b). This disk rotates with the rotor blades, which allows a wider range of possible time steps, avoiding interpolation issues. The disk is made of 11.4 million cells, which brings the full forward flight grid to 36.5 million cells. A small oblate sphere sits at the rotor centre to represent a simple hub. Near the blade tips, the disk spacing is 5% of the chord, and the radial resolution is 0.55 degrees per cell. This corresponds to a cell length of 15.8% c_{ref} at the rotor tip radius. The radius of the mesh disk is 1.3 times the rotor's radius.

Table 4.1 shows the number of cells and blocks for each grid. The ratio between the largest and average block size is also provided, to give an estimate of how well the grid could be load-balanced for highly parallelised computation. Most forward flight cases were computed on a range of 32 to 128 CPU cores and required approximately 128 GB of memory. The grids could be load-balanced even at 320 cores with an overhead of less than 3%, using a first-fit decreasing (FFD) algorithm. Alternatively, a load balancing script was created, using the graph optimisation tool METIS, which pre-ordered blocks into bins, equal to the number of computational nodes, before applying FFD. This reduced the communication overhead between the nodes, by finding a graph solution with the highest volume-to-surface ratio, within a constraint of 5% maximum to average ratio. The algorithm was more efficient for cases with at most one chimera interpolation level, as inter-mesh connectivity could not be considered, especially for moving meshes. At least approximately 100 blocks per node were needed for METIS to find an appropriate solution, due to the block size inhomogeneity in size and connectivity.

4.2 Structural Beam-Model and FE Mesh Generation

In this work, two structural modelling approaches for rotors in forward flight are compared for an active twist rotor. The first method is a 1D non-linear beam model, where the static

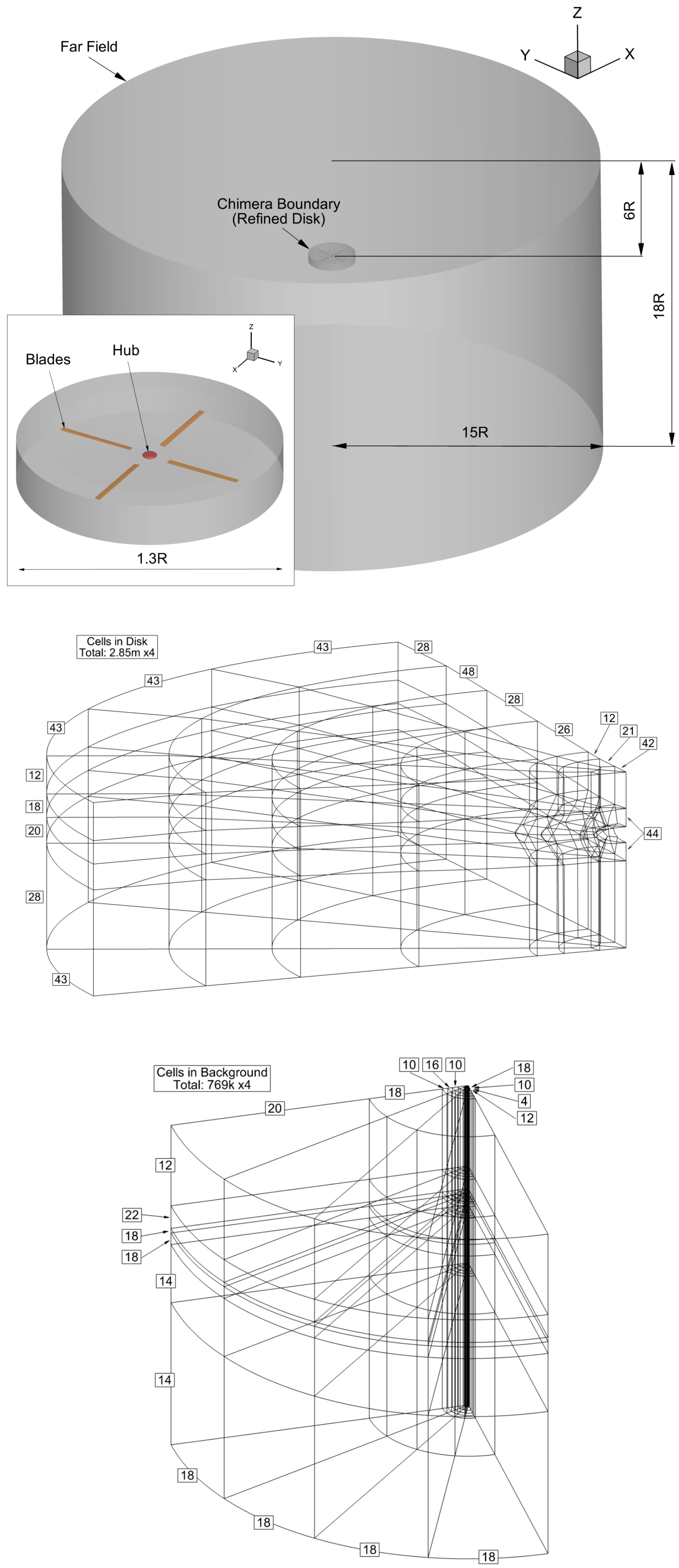

Figure 4.7: Forward flight mesh boundary conditions, topology, and domain cell counts noted at the block edges.

and dynamic twist is applied either via rigid rotations on the reference blade mesh, or applied moments at the nodes. The second method uses a medium-fidelity structural model made of 2D and 3D elements, where the active twist piezoelectric actuators are modelled via a thermal analogy method. The models are compared using loads extracted from the fluid dynamics solver HMB3.

1D beam finite element models are usually the easiest way to model the blade hub assembly using rotational spring/damper elements, and rigid, or elastic beams along the radius. Typically, ten or more beam sections are used in the aerodynamic region of the rotor blade. In some comprehensive rotor suites, the number of beam elements is equal to the number of aerodynamic panels.

Each beam element carries cross-sectional properties at the beam ends, which are interpolated along its length. The blade cross sections are simplified to their representative properties. These properties are explicitly related to blade motions, such that by changing one property value, the stiffness in the blade flapping direction can be manipulated. The large cross-section at the blade root or mounting region, made of strong materials such as carbon fibre and steel can often be simplified to rigid elements. The exception is the pitch horn and pitch link assembly, which is crucial for the prediction of blade torsion. Twist actuators can be modelled only by applying moments at beam cross-sections or by rigidly prescribed torsion.

2D/3D Finite element structural models consist of volumetric and/or surface elements, which carry the structural properties of the materials they are made of. The blade cross-section is resolved and usually consists of several elements. Depending on the available data for the blade volume, the blade can be accurately represented along the full span without interpolation. Pressure tapping locations and other structural details can also be included, in sufficiently resolved structural meshes. Active twist can be modelled as on the beams, or alternatively, by directly resolving the mechanism of the actuators. The piezo-actuators produce a strain because of a provided voltage differential, and one way to simulate the piezoelectric relation is by the Thermal Analogy Method (TAM). This is described in Section 3.2.4. Thermal-expansion coefficients are introduced to the actuator material, and prescribed component temperatures form an analogy to the reverse piezoelectric effect.

4.2.1 Analysis Conditions of Structural Models

All structural models were analysed with the commercial structural solver, as explained in the last chapter. Depending on the case, different loadings and boundary conditions were applied, which will be detailed. All structural models of the rotor blades consist of the $1/N_B$ rotational section, with the origin of the coordinate system representing the rotational axis. This simplification does not allow simulations of mechanically coupled blades, such as in teetering rotor heads, which are not considered in this study. This reduction of complexity has no negative consequences otherwise. The rotor head and region in-board of the hinges were considered rigid if no data was available. A fixed root boundary condition was applied by constraining the nodes in the analysis up to where the blade was clamped, and free-free modal analyses were computed by isolating the relevant sections from any nodes fixed to the origin coordinate system.

Where displacement outputs were desired, usually a single non-linear analysis step using the solution sequences *SOL 106* or *SOL 400* of MSC NASTRAN was sufficient. In difficult to converge conditions, such as the finite element model under centrifugal stress and hover load, two non-linear analysis steps were chained, to improve the convergence of the initial flap-hinge motion. The solver automatically calculates the total estimated load over all nodes, and then applies it with linearly increasing load-steps if specified. The centrifugal force, applied via the *RFORCE* keyword, is updated in non-linear iteration steps, as the structure deforms. Care was taken, to specify an appropriate minimum number of load-increments and inner iterations, to produce accurate convergence metrics, aiming for 2–7 inner updates per stiffness matrix update or load-increment, as recommended in the solver manual.

The structural eigenmodes were also directly extracted from the model inside the commercial solver. After an optional pre-stressing step, the eigenmode analysis is chained. Using the Lanzcos algorithm, the eigenvalues of the optionally pre-stressed stiffness matrix were obtained and normalised.

4.2.2 Beam-Models in MSC NASTRAN

STAR Beam-Model

For the STAR, both a beam- and a volumetric model were created. These structural models were then used with the HMB3 CFD solver. The rotor blade has a relatively stiff root section with cable housings mounted to the upper and lower sides. This complicated geometry causes large discontinuities in the beam properties in the hub and root area. The discontinuities are likely a small source of error in the beam-model, but due to the large stiffness and inboard position, this is negligibly small. The stiffnesses in this area are roughly up to four magnitudes larger than on the blade. On the lifting sections, the sectional properties are relatively linear in the spanwise directions. Some discontinuities exist, where the pressure sensors and other instruments are located in the blade skin. In these areas, the centre of gravity is ahead of the quarter chord. The discontinuities were smoothed out slightly, to allow for a working beam model. Some of the main blade properties are presented in Figure 4.8, without scales to comply with the non-disclosure agreement on the data. All sectional properties used for the beam models follow the metric kg-N-m-s system.

The 1D-beam model of the STAR is shown in Figure 4.9. The centre of rotation is at the origin (0,0). The blue sections between the green bars represent the cross-sectional beam elements (CBEAMs). The yellow underlining of the beams shows the spanwise sections, which include the active twist composites. The hinges are collocated at the radial position of 0.0375 R

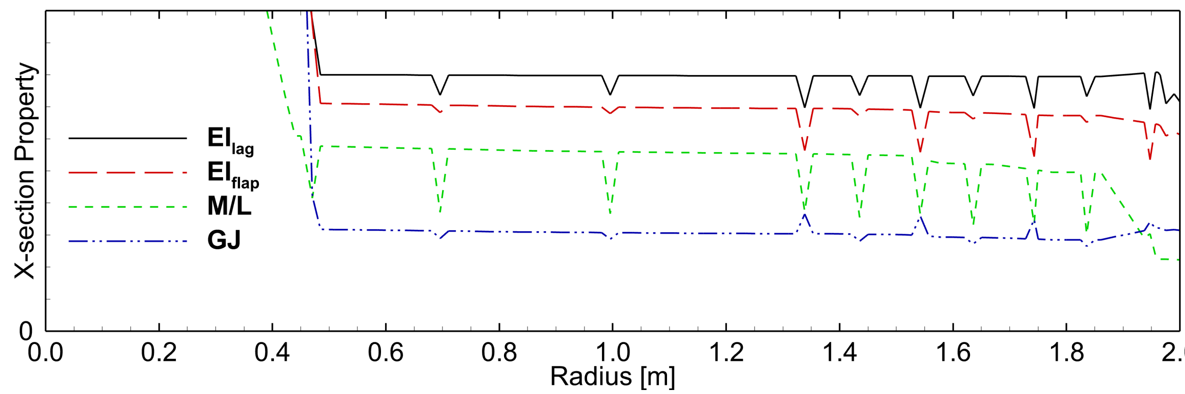

Figure 4.8: Radial distribution of the STAR blade properties over the aerofoil section. EI show the variation of flap and lag-bending stiffness, M/L is the sectional mass and GJ shows the torsional stiffness. The vertical axis is shown without scale according to the confidentiality of the data.

Table 4.2: NASTRAN elements used for the STAR rotor blade mode analysis.

Description	Abbreviation	Amount
Beam Element Connection	CBEAM	108
Rigid Bar	RBAR	218
Scalar Spring	CELAS2	2

and in flap-lag-pitch order. A lag-spring damper with a stiffness of 3013 Nm/rad is used. The total pitch link stiffness was measured as 3945 Nm/rad on the experiment, and replicated via a rotational spring in the model. Additionally, a spring in the flap direction with small stiffness (10 Nm/rad) is required for the NASTRAN model to converge the rigid blade mode component of the deformations. This minimum stiffness was determined in the worst-case condition at 120% of the rotational speed and a superimposed hover load. The assembly is considered to have a rigid single load-path inboard of the hinges. Modelling the dual load-path structure of the STAR provides no results benefits [176]. The model features 110 elastic beam elements, based on the number of available cross-sections in the data provided to STAR prediction partners. The number of total elements is listed in Table 4.2.

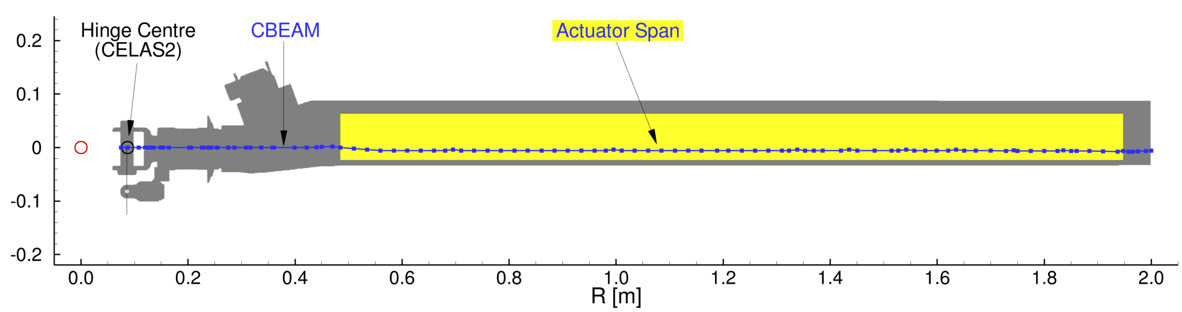

Figure 4.9: STAR blade beam model and silhouette. The rotational centre is at (0,0). The blue sections between the green bars represent the cross-sectional beam elements (CBEAMs). The yellow underlining of the beams represents the spanwise range, which includes the active twist composites.

The elastic axis of the beam elements is defined via the principal direction of the beam elements. For this reason, the nodes at which the properties are specified, are shifted by the elastic axis offset from the pitch axis line at (r/R, 0, 0). However, the properties used in the model were obtained in the normal plane of the pitching axis. When the beam elements were arranged at large angles of (more than 10 degrees) with respect to this axis, the properties got distorted. The large discontinuities in the properties produced sections with large element angle offsets, which needed to be simplified, to avoid distortion. With orders of magnitude stiffer parts inboard of 484.75 mm, and large cross-section discontinuities, the elastic axis is considered to be at the quarter chord location, to simplify the model to improve the accuracy of the method. Further outboard, the elastic axis offsets for sections which included the spar sensor cut-outs are reduced from the original dataset, to bring the angles to the quarter chord line to within less than 10°. The full extent of this simplification is shown in Figure 4.10.

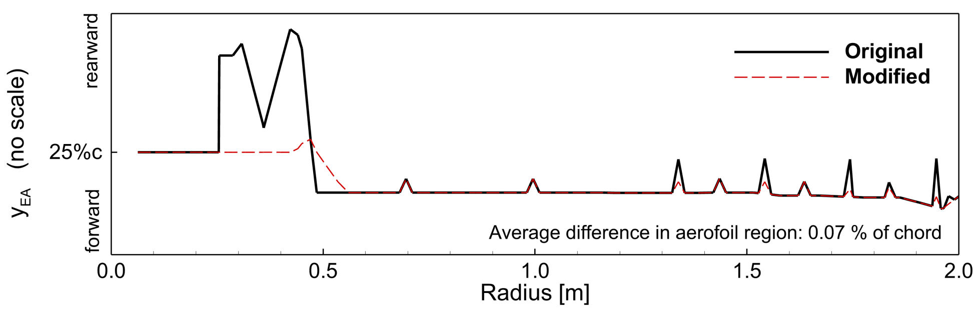

Figure 4.10: STAR blade elastic axis offset from quarter chord axis positive value (up) is toward trailing edge. The adjusted model, which reduces the angle offset of the beams w.r.t. 25%c line to be less than 10 deg is shown as dashed. The vertical axis scale was removed to comply with the data confidentiality.

HVAB Beam-Model

The same approach as in the STAR beam model was applied to the HVAB. The numerically obtained, cross-sectional properties for the HVAB rotor were provided in the technical memorandum by Overmeyer *et al.* [137]. An additional correction to the structural properties was published on the AIAA Hover Prediction Workshop (HPW) webpage [138]. The model in this work uses the properties for the blades SN001–005. The key spanwise parameters are given in Figure 4.11. Values from $r/R = 0.178$ (0.3 m) to $r/R = 0.98$ were provided, with multiple differing properties at some blade sections. Figure 4.12 shows the locations of the given cross sections on the skeleton model of the HVAB rotor blade in MSC NASTRAN. The sections between the rotational centre and the first given cross-section were modelled as rigid or quasi-rigid with high magnitudes of stiffness. No simplifications to the elastic axis positions were needed. Notably, the blade stiffness data shows a somewhat linear decreasing trend toward the blade tip, with a relatively constant mass. Therefore the blade torsion is expected to be non-linear with most bending in the outboard spanwise regions. All sectional properties were converted into a metric kg-N-m-s system.

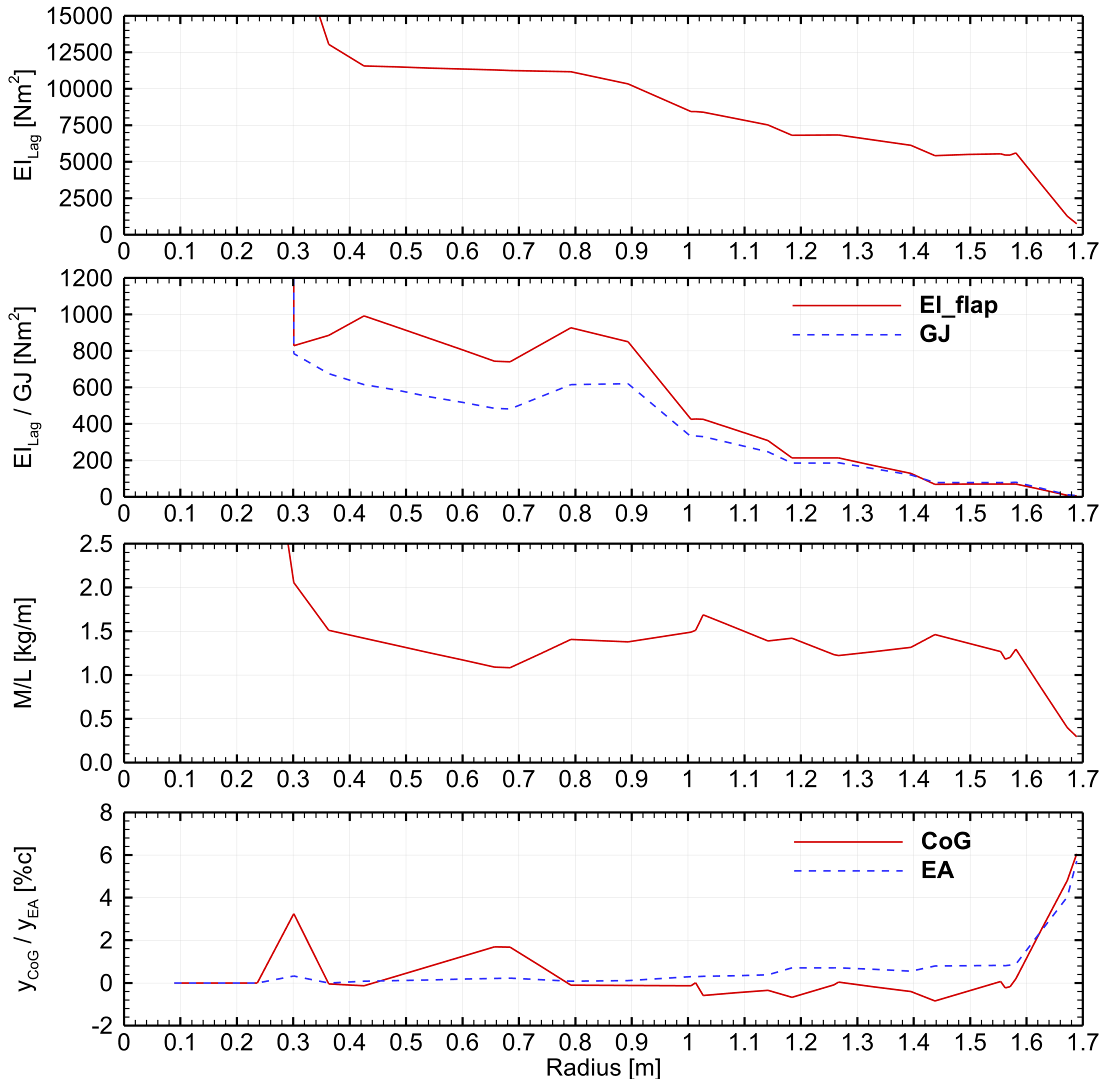

Figure 4.11: HVAB rotor spanwise distributions of key structural parameters from cross-sectional analysis [137, 138]. The root sections inboard of 0.3 m are considered rigid.

Based on the recommendations of the AIAA HPW, the hinges were not modelled, and instead, the recommended flap and lag angles were applied rigidly to the simulation. Therefore, the centrifugal force axis was not only adjusted for the blade pitch but also the lag and flap angles. Without any published structural validation data, the results are compared to the experiment in the aeroelastic hover validation case presented in Section 5.2.3.

ATR-I Rotor

The cross-sectional parameters for the ATR-I blade were only given between $r/R = 0.3$ to $r/R = 0.97$, corresponding to the regions containing the piezoelectric AFC actuators. The structural parameters chosen for this model and their source are described in Section 2.4.2. All available literature gives constant properties along this span. The properties from Shin (2001) [68] formed the basis of the model. No property data was available for the blade root region. Inboard the

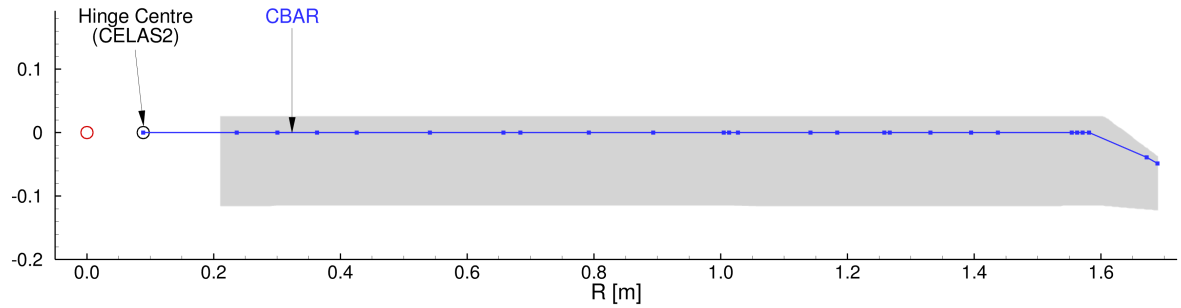

Figure 4.12: HVAB rotor blade beam model structure. The rotational centre is at (0,0). The blue sections represent the cross-sectional beam elements (CBEAMs). The silhouette of the full rotor blade assembly is in the background.

Table 4.3: NASTRAN elements used for the HVAB rotor blade mode analysis.

Description	Abbreviation	Amount
Beam Element Connection	CBEAM	23
Rigid Bar	RBAR	50
Scalar Spring	CELAS2	2

hinge centre, the rotor is considered rigid. A pitch spring of 100 Nm/rad and a lag spring of 5 Nm/rad were included to converge the rigid lag and flap modes. The model uses the same beam-approach as the previously shown STAR and HVAB structural models.

4.2.3 Finite Element Models

STAR FE model

The 3D-finite-element (FE) model created in this work approximates the shape of the STAR experimental rotor, based on [35], and with support from the STAR cooperation partners at DLR, KARI and Konkuk University. Some geometric and material assumptions were made, as are discussed in this section. The FEM model of UofG is built from both 2D and 3D elements. The blade's internal structure is made of volumetric prism elements. The rotor blade skin and actuator have been replaced with shell elements because the definition of the composite material coordinate system for volume elements is complex. The 2-D elements allow the use of the *PCOMP* statement, which can recreate any layup of materials. Moreso, these elements are less computationally demanding, while providing accurate results. The element types and their use cases are detailed in Section 3.2.1.

The rotor blade has 15 upper and 15 lower side actuator patches, spanning the majority of the chord length. The actuators build the outermost layer of the aerofoil shape, and the continuous blade skin is placed underneath these. The spanwise gaps between the actuators are filled with a second layer of the skin material and contain cut-outs for pressure sensors [35]. The rotor blade also features trailing edge spar strips.

The leading edge spar runs along the full rotor blade and starts at the mounting region of

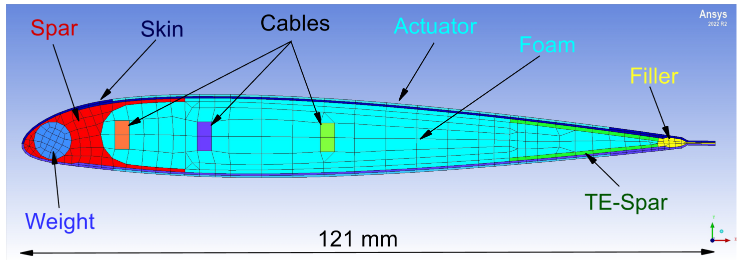

Figure 4.13: Approximate rotor 2D-section based on [35].

the root. It tapers until it reaches its final shape at 22% R, from where it is constant until the tip endplate is reached. The finite element mesh was extruded from the meshed 2-dimensional cross-section shown in Figure 4.13. The resulting prism elements keep the degrees of freedom as low as possible while maintaining good cell quality. Initially, just the spar and nose-weight were modelled for a mesh refinement study, shown in Section 4.2.4.

The 2D sections of the different components were separately meshed with similar sizing and then merged into a continuous meshed surface. The different materials were flagged in the cross-section, and spanwise variations were introduced similarly by changing the mesh part ID. This way, the actuators and nose weight could be discontinued at the relevant sections.

The blade model is made of 55640 CHEXA8, 7918 CPENTA6 and 20804 CQUAD4 elements, from radial stations 484.75 mm to 2000.0 mm. Each cross section consists of 297 elements which are extruded into 214 layers. The spanwise element size varies between 5 mm and 9 mm. At multiple stations along the span, where sensors are integrated, a nose weight is not fitted, and instead, the spar is extended to fill the gap. This is represented in the model. The nose weights of the blade are roughly 20 mm long tungsten carbide rod segments glued between the two halves of the spar. In the structural mesh, the weight and spar are extruded from the same cross-section and share mesh connectivity, due to limitations of the model fidelity and structural solver convergence when using separated meshes and contact boundary conditions. The modelled connectivity transfers loads and displacements as if the parts were perfectly joined. This is a potential error source, which is difficult to quantify, as exact data on the weight fitting tolerances, glue and load transfer capability were not available. However, an approximated Young's modulus of 50.2 GPa for the weights, as listed in the material property tables of [35,176], yielded an appropriate result for the bulk blade properties. Some properties, such as the density of the nose weight were corrected, compared to publications [35, 176]. The FE model in these studies assumed a uniform spanwise property distribution, where the alternating nose weight and spar sections were averaged to a mean compound density: $\rho = \frac{L_W \rho_W + L_{CFRP} \rho_{CFRP}}{L_W + L_{CFRP}}$, where subscripts $_W$ and $_CFRP$ denote tungsten and carbon fibre material, and L is the spanwise length where that material is used over the given cross-section.

The cable weights are uniform along the span in the current iteration, since their effect on the radial weight distribution is marginal. The approximate cross-section includes a simplification of the blade's internal cables. The cable bundles, as seen in the CT images, were simplified into three rectangular regions of lumped mass, at the same chordwise locations as in [35]. The stiffness properties of the cables were not considered for simplicity. From the materials and geometry suggested in [35], the weight of these cables was estimated as 0.459 kg, including the aerofoil section and the dense cabling of the blade root and connector housing. In this model, three foam sections at the chordwise station of the cable centre of mass are designated. The cable mass is distributed according to the number and thickness of the cables, for a good approximation of the centre of gravity. The pressure sensor cables were modelled as 0.183 kg, the actuator cables resulting mass was 0.044 kg and the strain gauge cables totalled 0.037 kg over the span of 484.75 mm to 1955 mm. The total cable mass in the aerofoil section then accounted for 0.264 kg.

The construction of the finite element models, including the spanwise discontinuities, are displayed in Figure 4.14. An x-ray image of a STAR blade cross section is shown for comparison in Figure 4.15, which highlights the sets of cables.

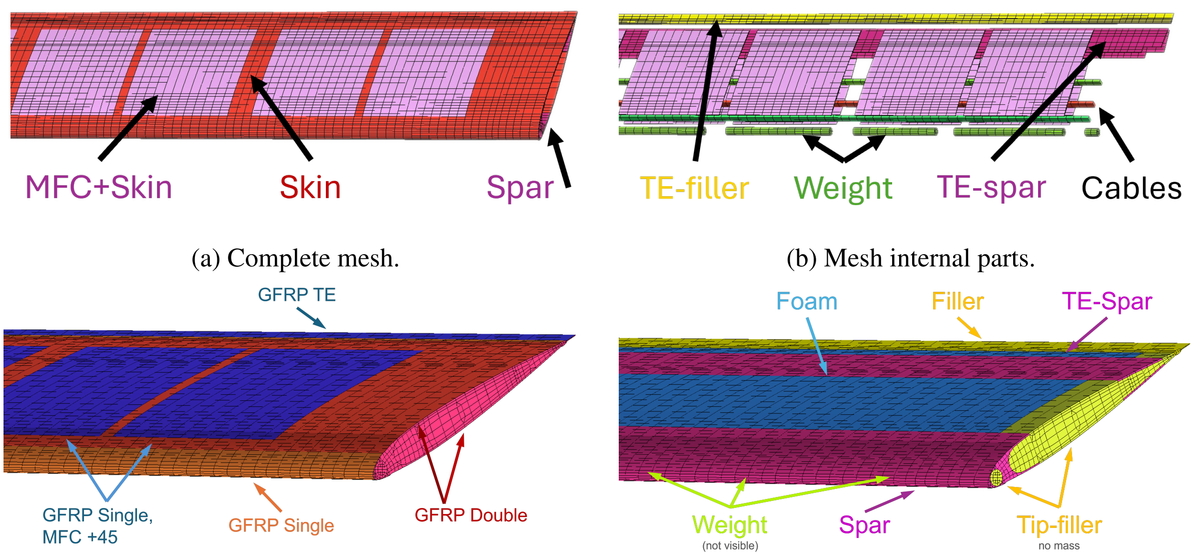

(a) Complete mesh. (b) Mesh internal parts. (c) Shell materials. (d) Volume materials including foam.

Figure 4.14: UofG mesh tip region of STAR II blade, with and without foam, spar and skin.

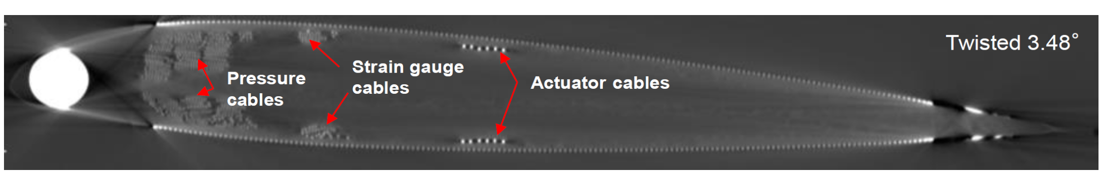

Figure 4.15: X-ray cross-section image of the STAR rotor blade [35].

Most of the material properties could be obtained from Ahn *et al.* [35]. The properties of the FE-model in this work are presented in Table 4.4. The orthotropic properties are shown, with direction 1 as the principal direction and directions 2 & 3 normal to that. The anisotropic stiffness matrix for the fibre-reinforced materials was calculated from the given material properties and rotated to the correct reference frame for the *MAT9* NASTRAN bulk data entry. The actuator is a MacroFiberComposite™ by Smart Material Corporation of P1 type. It is a d33-effect elongator and the full material property sheet is listed on the product webpage [131].

Additionally, a set of properties was created, featuring purely isotropic material properties, to show the effect of material anisotropic on the FE-model deflections. This is listed in Table 4.5. The strong anisotropy of the carbon fibre material of 0° layup direction causes a difference in overall stiffness, which is deemed acceptable for the comparison purposes of this chapter (Table 5.3).

Table 4.4: Materials of the STAR blade FE model, and their main properties [35, 176].

Material	E_1 [GPa]	$E_{2,3}$ [GPa]	ν_1	$\nu_{2,3}$	G_1 [GPa]	$G_{2,3}$ [GPa]	ρ [kg/m^3]
UD-Carbon (60%)	177	9.1	0.40	0.28	5.08	1.7	1580
UD-Glass (60%)	45.2	12.0	0.30	0.30	4.13	2.0	2008
Actuator	33.3	15.9	0.31	0.31	5.52	5.52	5440
Tungsten	50.2	50.2	0.34	0.34	18.7	18.7	19280
PU Foam	0.075	0.075	0.25	0.25	0.03	0.03	52
Resin Filler	3.15	3.15	0.30	0.30	1.21	1.21	1124

Table 4.5: Anisotropic variations of the materials of the STAR blade FE model.

Material	E_1 [GPa]	$E_{2,3}$ [GPa]	ν_1	$\nu_{2,3}$	G_1 [GPa]	$G_{2,3}$ [GPa]	ρ [kg/m^3]
UD-Carbon (60%)	120	120	0.30	0.30	–	–	1580
UD-Glass (60%)	45.2	45.2	0.30	0.30	–	–	2008
Actuator	33.3	33.3	0.31	0.31	–	–	5440

4.2.4 Mesh-refinement study

The spar and the nose weight have been produced in four mesh sizes, to estimate the computational performance and the impact on the result. A baseline two-dimensional shape with good cell quality was designed and then rotation-extruded along the length of the beam. The cell sizes in the 2D sections were between 0.5 and 2.5 mm edge length. The spanwise extrusion was done with 15 (coarse), 5 (medium), and 1 mm (fine) prism lengths. Another mesh with a roughly 4x coarsened 2D section was also tested with the coarsest spanwise spacing. The sections are shown in Figure 4.16. The degrees of freedom (DoF) for these cases were: 70k, 355k, and 1.77 mio. with a corresponding impact on computational time and memory requirement. The finest mesh required 15GB of memory for a non-linear static calculation of the spar, using SOL 400.

A testing load was applied to the beam with stresses and displacements calculated using the SOL 400 non-linear statics configuration. The loads are a centrifugal force and a spanwise-quadratically increasing body force, approximate to a light hover load. Figure 4.17 shows the results of the comparisons. The $2 \times 2 \times 2$ isoparametric integration shows increasing deflections with a peak bending up to 170 mm at the tip with mesh refinement. This suggests, that longer elements lead to an artificial stiffening of the structure. The analysis was repeated with the $2 \times 2 \times 2$ under-integration scheme, with the reduced shear formulation and the bubble function of NASTRAN. This scheme is the NASTRAN default for volume elements. All mesh levels showed the same result as the finest mesh in the isoparametric integration. The under-integration scheme required less CPU time for the same grid size. Therefore, the coarsest of all meshes was considered sufficiently resolved for the full rotor blade. The grid could not be coarsened further as the internal parts geometries can otherwise not be resolved at satisfactory element quality. More information on the formulation of the integration schemes and additional functions is provided in the NASTRAN manual [159].

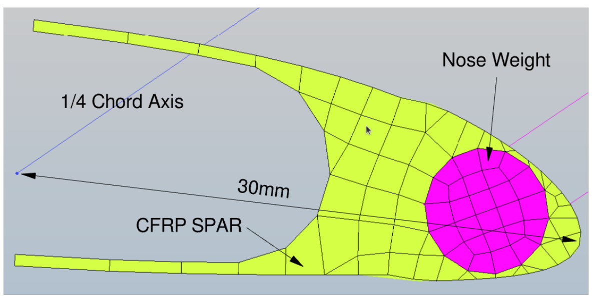

(a) Coarse (70k DoF, 15 mm extrusions)

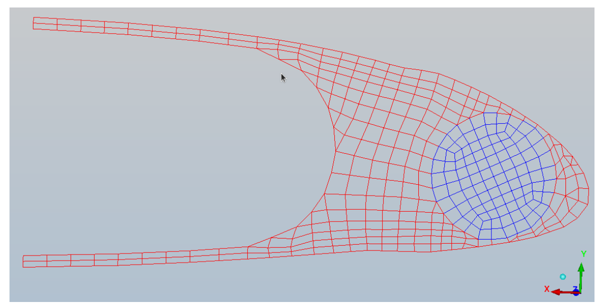

(b) Medium/Fine (355k/1.77 mio. DoF, 5 or 1 mm)

Figure 4.16: The FE mesh cross-sections (coarse, fine), used for the 3D spar approximation. The finer cross-section was tested at two spanwise spacings.

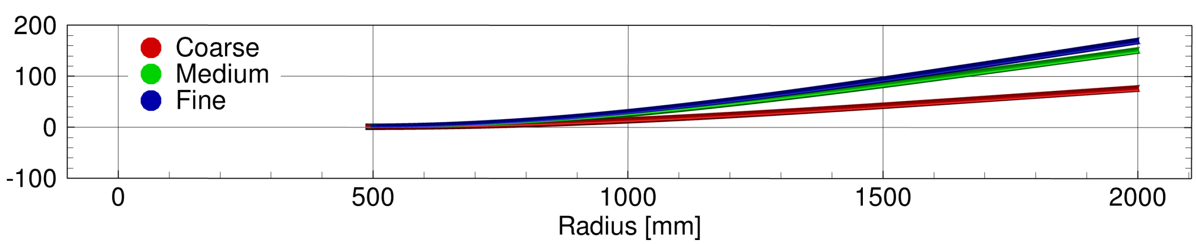

(a) Standard iso-parametric integration.

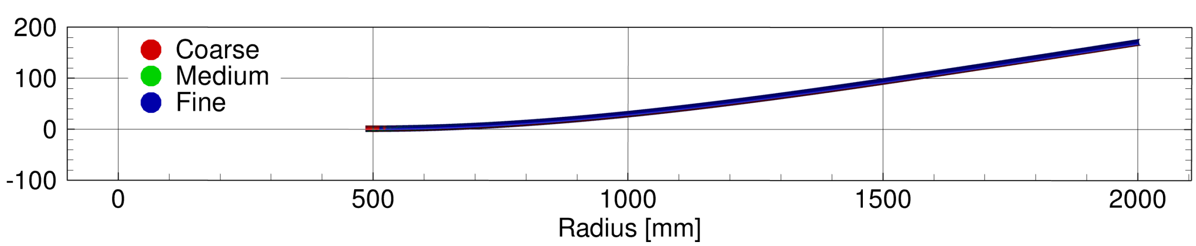

(b) Under-integration with reduced shear formulation.

Figure 4.17: Blade structural response obtained using different mesh refinements and integration methods.

Chapter 5

Results

5.1 Structural Results and Validation

5.1.1 BM 500 Piezoactuator Validation

Cote *et al.* [170] describe the implementation of the thermal analogy method in structural solvers such as MSC NASTRAN. A 19.05 mm×6.35 mm×0.508 mm rectangular cantilever beam with the properties of a BM 500 piezoceramic from Sensor Technology Limited was used as an example to compare the TAM implementations between MATLAB and MSC NASTRAN. The properties are listed in Table 5.1, where $G_{i,j}$ are the upper diagonal terms of the 6×6 symmetric stiffness matrix with row i and column j and α_i are the thermal expansion coefficients in coordinate i. The thermal expansion coefficients are the equivalent of the d_{11}, d_{22} and d_{33} piezoelectric coefficients.

Table 5.1: Structural properties of Sensor Technology Ltd. BM 500 [170].

Stiffness [GPa]				**Thermal Expansion** $[10^{-9}/\mathrm{K}]$	
$G_{1,1}$	121.0	$G_{3,3}$	111.0	α_1	−17.04
$G_{1,2}$	75.4	$G_{4,4}$	22.6	α_2	−17.04
$G_{1,3}$	75.2	$G_{5,5}$	22.6	α_3	37.32
$G_{2,2}$	121.0	$G_{6,6}$	21.1		
$G_{2,3}$	75.2				

An electric potential of 100 V between upper and lower surface was applied, for a longitudinal extension of the beam. From the simplified equivalence of the piezoelectric expansion and thermal expansion:

$$\frac{\Delta V}{t} * d_{33} \equiv \Delta\Theta * \alpha_3, \tag{5.1}$$

we obtain an equivalent temperature delta of $\Delta\Theta = 196\,850\,\mathrm{K}$, by setting $d_{33} \equiv \alpha_3$. This is not a real temperature, but an electric field analogue. The voltage differential ΔV divided by the

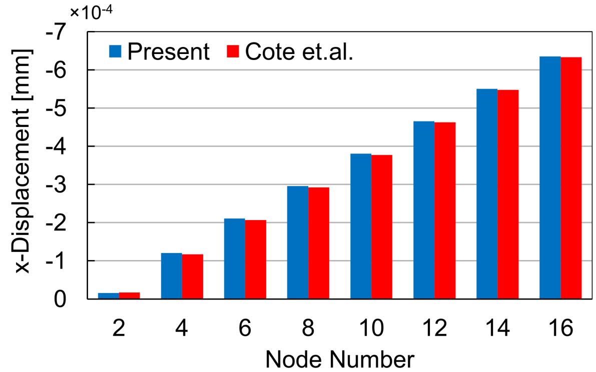

Figure 5.1: BM500 piezo actuator simulation results from MSC NASTRAN using the thermal analogy method. The same deformation as in [170] could be reproduced.

actuator thickness $t = 5.08 \times 10^{-4}$ m gives the electric field strength of the actuator, which is applied by the equivalent temperature difference in FEM.

A non-linear static analysis with the temperature load resulted in close reproduction of the BM 500 results in the literature. The final deformations are shown in Figure 5.1. The small difference in the result can be attributed to the different analysis types and integration schemes between the works.

5.1.2 STAR Structural Results and Comparison

First, static deflection results in different load and boundary conditions are compared between the structural models of the STAR. Then the static and rotating mode frequencies are plotted against the laboratory test results of DLR.

Section Properties and Static Results The elastic axis (SC) and neutral axis (TC) offsets for the FE-model were obtained by applying in-plane and out-of-plane forces, and interpolating the locations where the torsion or flap/chord bending was zero, as explained in [176]. For this, the blade root up to the start of the aerodynamic section was constrained. However, there was some additional structural coupling between the types of deformations. The centre-of-mass was simply obtained by evaluating the densities and locations of the surface and volume elements in MSC NASTRAN. The results are shown in (Figure 5.2), the bulk shear centre and tension centre are both ahead of the quarter chord and centre-of-gravity. The chordwise location of the elastic axis matches the 20% chord location of the experimental measurements cited in [35]. These structural properties are also located higher in the chord-normal direction, partially because more of the blade is pitch-up pre-twisted before 75% R. An un-twisted variant of the blade structural model was not created.

The static deformation responses in a vacuum are compared for a set of loads and the blade was at 0° of pitch. Tip-up force is applied at the quarter chord station when combined with centrifugal loading, the 50N up stand-alone force was best applied at the elastic axis chord

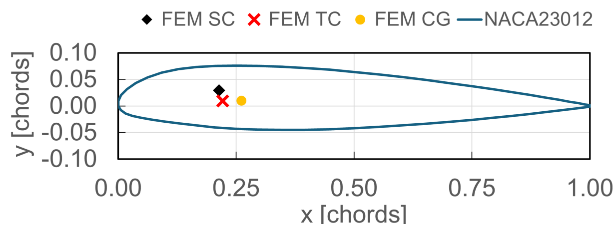

Figure 5.2: Sectional distribution of the shear-centre (SC), tension centre (TC) and centre of gravity (CG) on the UofG FEM model.

offset (6 mm ahead of pitch axis). The results are shown in Table 5.2. The torsion convention follows the twist distribution, negative values indicate tip pitch-down. With the centrifugal force applied to the cantilevered blade (Case 1), no torsion was observed on the beam model, as expected for a 1D model. However, the finite element model untwists by 0.42° as a product of the centrifugal force. Case 2, where only a small bending force was applied at the tip, finds reasonably good agreement between beam and FE-model in the non-rotating condition. Both cases exhibit no significant torsion, indicating that torsion-cross coupling is likely a product of the mass distribution. Comparing the torsion of the cases in 3 shows the effect of the actuator, and subtracting case 4 from 1 shows effectiveness at full rotor speed. At -400 V, both structural models are predicted to achieve approximately 0.94° of twist. This correlates well with the measured average, static active twist authority of 2.5 deg/kV [13]. Under centrifugal load, the "actuator model" on the beam shows a minimally reduced performance of 0.896°. In the 3D model, the actuator effectiveness is degraded significantly, down to 0.729° (-18%). The actuator patches are aligned at $\pm 45°$ and need to overcome the component centrifugal stiffening to induce torsion. Case 5 shows the maximum possible actuator voltage applied, to achieve 3.5° of blade untwisting (tip pitch up). Case 6 illustrates the strong cross-coupling of flap-bending and torsion in the FE model. At 70% of the flap-bending deflection, an additional 1.58° of pitch-up at the tip is produced, mostly due to the offsets of the structural axes. Little difference is observed between the clamped and the rigged condition, where only the structure up to the hinge station is considered. The rotor blade root and mounting mechanism are orders of magnitude stiffer than the aerodynamic region.

To confirm the cause of the torsion discrepancy between the beam and FE-models, two additional simulations using isotropic material properties were compared to the earlier results. Case 1a in Table 5.3 has all blade skin components exchanged for slightly stiffer anisotropic equivalents. Besides this, case 1b has the CFRP material of the spar and trailing edge straps replaced with a purely anisotropic material. Due to the extreme orthotropy of the original 0° material, increased chordwise bending stiffness is expected. Both tests under centrifugal load show a comparable blade bending and a similar or increased blade tip torsion coupling, compared to the earlier FE results. In the case without centrifugal load (2b) no significant torsion was observed, correlating similarly well with case 2. The results strongly indicate that the cross-

Table 5.2: Static structural deformations of the STAR blade under varying applied loads and boundary conditions. CF is Centrifugal force, clamped at 275 mm radius is a cantilevered boundary condition. Flapping and torsion (pitch-up) are given for the blade tip quarter chord point.

			Beam		FEM	
Case	**B.C.**	**Loads**	**Flap** [%c]	**Torsion** [°]	**Flap** [%c]	**Torsion** [°]
1	Clamped	CF	0.63	0.004	−0.40	0.420
2	Clamped	50N up (tip)	1.32	−0.026	1.625	−0.007
3	Clamped	-400V (-2.06 Nm)	0.11	−0.945	0.05	−0.939
4	Clamped	CF, -400V (-2.06 Nm)	0.86	−0.900	−0.51	−0.309
5	Clamped	1500V (7.72 Nm)	−0.42	3.542	−0.19	3.512
6	Clamped	CF, 500N up (tip)	54.75	0.174	37.25	1.751
7	Rigged	CF	0.23	0.035	−1.15	0.416
8	Rigged	CF, -400V (-2.06 Nm)	0.46	−0.909	−1.21	−0.318

coupling is induced mainly by the experienced offsets between the centre of gravity, elastic axis and neutral axis of the bulk blade properties. The discontinuous spanwise properties of the FE model, which could only be approximated in the beam model, interact with the centrifugal body force and cause torsion, which is additionally affected non-linearly by blade bending. It was not possible to apply the actuator voltage to the anisotropically modelled skin cases.

Table 5.3: Static structural deformations of the STAR blade FE-model with isoparametric skin-material properties of Table 4.5.

Case	**Isotropic Materials**	**B.C.**	**Loads**	**Flap** [%c]	**Torsion** [°]
1a	GFRP and Act.	Clamped	CF	−0.46	0.582
1b	CFRP, GFRP and Act.	Clamped	CF	−0.49	0.410
2b	CFRP, GFRP and Act.	Clamped	50N up (tip)	1.587	−0.014

Mode-Frequency Results The clamped blade frequencies are compared with experimentally measured values, published in [176]. The measured values were obtained by clamping the blade vertically in a vice, with the blade root up to approximately R=275 mm restricted in all degrees of freedom. The modes are split into flap-bending (F), lag-bending (L) and torsion (T) based on their primary shapes. Some heavily coupled modes with no identifiable primary mode are labelled as mixed (M). The beam model overpredicts the stiffness of the experimental blades (Figure 5.3). Especially, the second lag mode was found at a much higher frequency. Good agreement is found for the finite element model, which deviates slightly in torsion and lag modes. The mode shapes of the clamped modes are shown in Figure 5.4. Starting from the 1st flapping mode, which is lightly coupled to the 3rd flapping modes, increasing cross-coupling can be observed. The 2nd torsion mode particularly shows a significant lag-bending contribution, and the two modes can not be categorised easily. This also applies to other mode pairings at the nominal rotational speed.

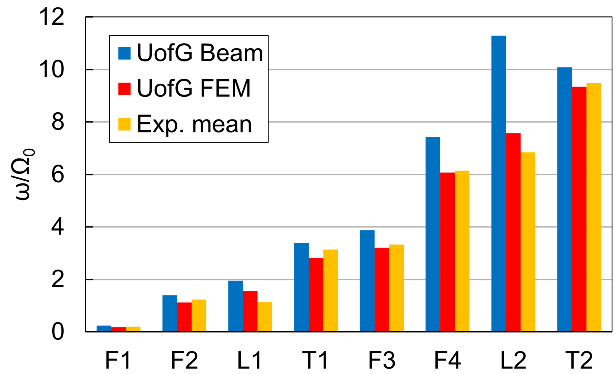

Figure 5.3: STAR blade resonant frequencies, clamped at 275 mm radius. The experimental data is the averaged blade structural response published in [176].

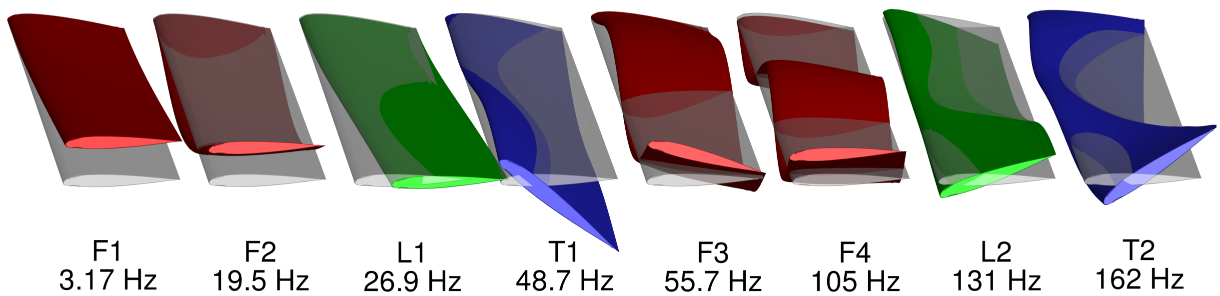

Figure 5.4: STAR blade mode shapes of the FE-model, clamped at 275 mm radius, with the undeformed shape shown semi-transparent.

Before the frequencies of the lag mode were made available, a parameter study was conducted on the STAR beam structural model. Changes in the flap-bending stiffness, torsional stiffness and pitch link stiffness were considered. To match the frequencies of the blade clamped at 275 mm radius, the torsional stiffness was reduced by 20%. The flap-bending stiffness had to be reduced by 28%. Figure 5.5 shows the resulting frequencies of the adjusted model. A multiplicative increase of stiffness by x % resulted in an approximately $\sqrt{x}$ % increase in the corresponding mode frequency. However, property changes like this do not guarantee correct results, as modes are a product of the stiffness and mass properties.

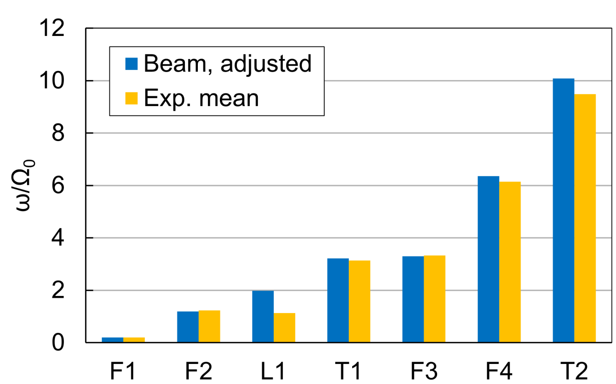

Figure 5.5: Beam-model clamped frequencies after property adjustments. The experimental data is the averaged blade structural response published in [176], no data for the lag mode was available.

The frequencies are also compared in the rigged, rotating condition, with measurements from [176]. The error bars show the highest and lowest measurements between the five tested rotor blades. The first flap and lag modes are dominated by the hinge stiffness and blade mass. Figure 5.6 (a) shows the results of the current beam model. The first flap modes are close to the measured frequencies. The first torsion mode and the following higher frequency modes are largely overpredicted in stiffness. The second lag mode is much closer to the experimentally determined value in the rigged boundary condition. The prediction frequencies of the finite element model correlate well with the measured values. The primarily flap-bending modes match the experiment. The blade torsional frequency is slightly underestimated, which has an influence on the 2nd torsion mode at the nominal rotor speed $\Omega_{rot}/\Omega_0 = 1$. For beam, FEM and experiment, the 2nd torsion and 5th flap-bending modes couple strongly and become indistinguishable in this region. Notably, some mixed modes exist for the FE model, which were not found with the beam-model. These modes have no primarily distinguishable mode shape and are likely a product of the strong cross-coupling terms and spanwise anisotropy. The structural amplitude of these modes is likely overshadowed by close-by pure modes, which makes such modes more difficult to identify in experimental measurements. The modal frequency chart gives a good indication of the validity of the FEM model. However the modes are always a product of inertia and stiffness properties, so more static blade deformation measurements would be needed for further validation.

For the STAR beam-model, the influence of the chosen structural solving scheme in NASTRAN was investigated for both static and rotating conditions. The results are shown in Table 5.4, where no discernable difference was found between mode extraction using *SOL 103* and *SOL 106*. Similarly, the finite element model was tested using the sequences *SOL 106* (explicit) and *SOL 400* (implicit), with no difference besides better convergence speed in the latter.

Table 5.4: Modal frequencies obtained using different solution strategies.

	ω/Ω_{ref} ($\Omega = 0$ Hz)		ω/Ω_{ref} ($\Omega = \Omega_{ref}$)		
SOL	**106**	**103**	**106**	**103**	**400**
F1	0.04	0.04	0.39	0.38	0.39
L1	0.27	0.27	1.01	1.01	1.01
F2	0.62	0.62	2.41	2.41	2.41
T1	1.92	1.92	3.62	3.62	3.62
F3	3.39	3.39	4.05	4.05	4.05

Computational Time The impact on CPU wall-clock time, running the structural solver was also evaluated. The software ran as a single-threaded process, on a 10-core, 20-thread Intel Xeon W-1290 @ 5200 MHz, with 32GB of DDR5 memory and a professional grade M2 NVMe solid state drive with 400 GB of free capacity. GPU acceleration using an NVIDIA Quadro RTX 4000 card with 8GB VRAM capacity provided a negligible speedup, as the models were

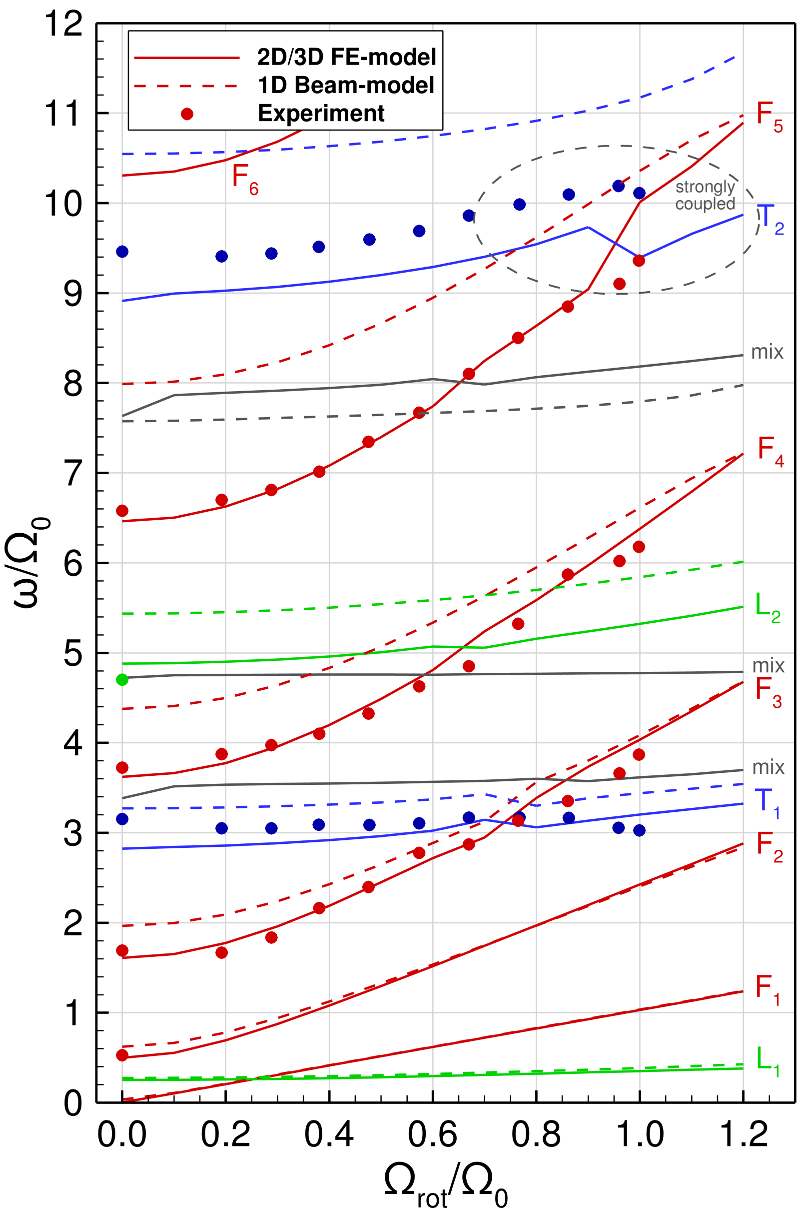

Figure 5.6: Comparison of the blade eigenfrequencies of the UofG beam and FEM model with the experimental STAR test [176]. Modes F1, F2, L1 and L2 have no or limited measurements available. The colours separate the modes by their primary nature of flap-bending (F), lag-bending (L) and torsion (T).

not optimised for this case. GPU utilisation was around 10% at energy-saving clock rates, indicating poor effectiveness.

The time to complete a SOL 106 non-linear static analysis for the 117k, 355k (3×), 1.77m (15×) DoF models of the mesh refinement were 38s, 124s (3.26×) and 824s (21.7×). The models were rigidly fixed in a cantilever position and centrifugal loads were applied. To determine the effect of the simulation complexity, the 315k DoF complete blade model was also measured in SOL 106. In the cantilevered and hinged configurations, the time to resolve the non-linear static deflection was 43 seconds for the non-rotating case. When the centrifugal loads were applied, the cantilevered case was finished in 160 seconds (3.7×). The rotating, hinged case took 1 hour, 10 minutes and 51 seconds to complete (≈ 100×). The computational effort increases non-linearly with the degrees of freedom in the model, in part due to increasing demands on memory and storage. A strong dependence between computational effort and problem non-linearity can also be observed, as the complex cases require many additional iterations and load-step increments. The final iteration of the 2D/3D FE model blade was significantly lower due to optimisations in terms of mesh quality, load stepping, boundary conditions and by using the SOL 400 implicit solver. The modal analysis of the full blade in the hinged, rotating boundary condition was reduced to a wall clock time of 1410 s (23.5 min).

5.1.3 ATR Eigenmode Analysis and Comparison

The eigenfrequency of the first 8 modes, including rigid lag and flap, were compared between UofG and the results in the works of Cesnik *et al.* [69] and Shin *et al.* [59,62] in Figure 5.7. The values at nominal rpm are compared in Table 5.5. The first five modes showed good frequency correlation, indicating correct mass and boundary conditions. However, the third flapping mode frequency showed a large difference. A small discrepancy of the first torsional frequency exists between the experimental measurements, where unexpectedly, the opposite of torsional stiffening was observed. This first torsion mode frequency is also relatively underpredicted by the beam-model of this work.

Because of the difficulties correlating the structural mode frequencies and the lack of aerodynamic performance data in the literature on the ATR, only a limited amount of analysis was conducted in the next sections.

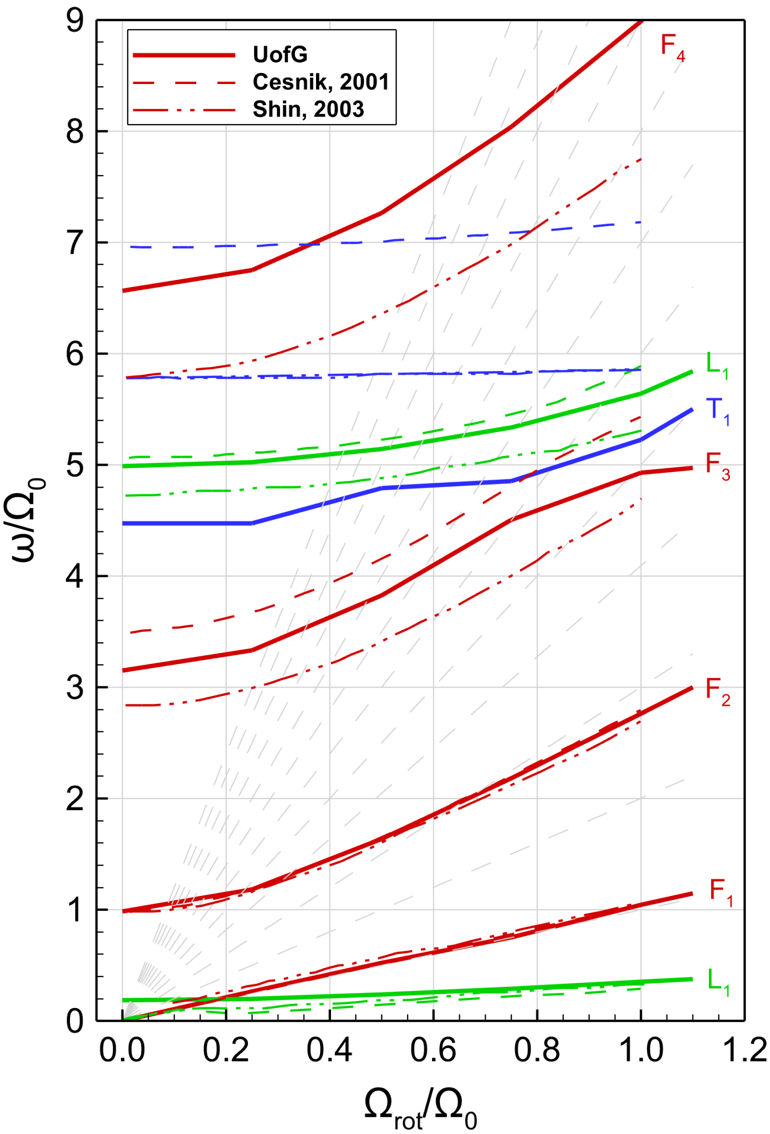

Figure 5.7: ATR rotor structural eigenmode-comparisons between University of Glasgow and published data by Cesnik [69] and Shin [59, 62]. The colours separate the modes by their primary nature of flap-bending (F), lag-bending (L) and torsion (T).

Table 5.5: ATR-I mode eigenfrequencies at 688 rpm.

Mode	**Frequ. UofG** [Hz]	**Frequ. Shin [62]** [Hz]	**Difference** [%]
Lag 0 (rigid)	4.03	3.7	8.92
Flap 0 (rigid)	11.9	11.9	0.00
Flap 1	31.7	30.8	2.92
Flap 2	56.5	53.8	5.02
Lag 1	60.3	60.9	−0.99
Torsion 1	64.7	67.2	−3.72
Flap 3	103.0	88.8	15.99

5.2 Effect of Twist on Hover Performance

As part of the work on active twist rotors, the effectiveness of rotor blade twist is analysed using aeroelastic numerical simulations. With sufficient twist authority, such rotor blades are predicted to show a significant increase in hovering efficiency and lifting capacity. The three simple planforms of the STAR, ATR and HVAB rotors at different aspect ratios and baseline twist levels were chosen, because the first two are active twist blades, and the latter has good data for validation. For each blade, a theoretical active twist version with 4° of additional twist is compared. Additionally, the baseline results of the HVAB rotor simulations are compared to the measured data of the most accurate hover experimental study as of today [139, 140].

The conditions of the hover simulations are summarised in Table 5.6 and sorted by increasing nominal twist angle. Fixed collective pitch angles were decided on for faster turn-around time. Five angles over the range of useful hovering thrust allow for accurate interpolation between the points. The coning angle was fixed for the rigid STAR and ATR simulations to avoid re-meshing the grid. The aeroelastic STAR cases used the elastic beam model including the hinges, where coning is a result of the hinge and the blade deformation. The HVAB rotor was also simulated before the release of any experimental data. Therefore, the cases use the hinge's cone and lag angles, provided as part of the AIAA hover prediction workshop [138] recommendations. The aeroelastic HVAB simulation cases additionally allow the blades to deform. Airloads and centrifugal stiffening are considered in all elastic blade cases. No elastic cases were simulated for the ATR, due to discrepancies in the structural response (Section 5.1.3), and the lack of hover validation data.

All force and moment coefficients use the US definitions, as shown in the nomenclature. Figure of merit (FM) changes are expressed in counts, where 1 count is an improvement by 0.01. In the aeroelastic STAR hover simulation, the blade hinges were included in the structural model, and the resulting flap and lag angles were a product of the airloads, centrifugal acceleration and the centre-of-gravity location of the beam model. Simulations were considered converged, when the loads average reached a clearly identifiable plateau, with residual values in HMB3 dropping 5 to 8 orders of magnitudes. The aerodynamic loads have been averaged over iterations where a quasi-steady state has been reached. Structural updates were applied every 15000 to 25000 steady iterations, depending on the convergence of the loads. The STAR elastic cases required roughly 10 deformation updates to reach a converged state out of an oscillatory behaviour, the HVAB required at least five. Due to the oscillatory nature of the structural updates, a variable under-relaxation factor is applied to reduce the structural deformation.

5.2.1 STAR Blade in Hover

In this section of the thesis, the STAR blade structural model used is the beam model described in Sectionr 5.1. Due to a modelling error, which is corrected in Section 5.3, this part of the

Table 5.6: Hover conditions for CFD computations.

Rotor	θ_{tw} [deg/R]	Elastic	θ_{75} [deg]	β [deg]
STAR	-8	no	5, 7, 9, 11, 12	2.5, 2.5, 2.5, 2.5, 2.5,
STAR	-12	no	5, 7, 9, 11, 12	2.5, 2.5, 2.5, 2.5, 2.5,
STAR	-8	yes	6.8, 7, 8.4, 9.9, 10.6, 11.6, 12	0.0, 0.0, 0.0, 0.0, 0.0, 0.0, 0.0
STAR	-12	yes	7, 8.4, 9.9, 10.8, 12	0.0, 0.0, 0.0, 0.0, 0.0
ATR	-10	no	8, 10, 12, 14	1.0, 1.0, 1.0, 1.0
ATR	-14	no	8, 10, 12, 14	1.0, 1.0, 1.0, 1.0
HVAB	-14	no	6, 8, 10, 12	0.4, 0.8, 1.3, 1.8
HVAB	-18	no	6, 8, 10, 12	0.4, 0.8, 1.3, 1.8
HVAB	-14	yes	6, 8, 10, 12, 14	0.4, 0.8, 1.3, 1.8, 2.3
HVAB	-18	yes	8, 10, 11, 12, 14	0.8, 1.3, 1.5, 1.8, 2.3

work uses a blade model, where the usually relatively small centroidal offsets of the elastic axis, neutral axis and centre of gravity are set so they are on the pitching axis. This has a minor effect on the results, as shown when compared to the updated simulation. Regardless, this data is still representative of the influence of changing twist on a rotor blade, therefore it is included in the discussion of this section.

The nominal STAR blade shows a peak figure of merit at just below 0.7 from the results of HMB3, shown in Figure 5.8 (a). The rigid rotor blade, compared with the elastic one, has a slightly lower figure of merit, as it does not aeroelastically twist the blade tip downwards. The mesh with increased twist achieves a 4-count improvement in FM over the baseline, which equates to 1 count per degree of twist change. The FM is improved by 3 counts, between high-twist and nominal blades when the blade structure is modelled. The blade thrust is marginally reduced due to the elastic deformations. At high pitch angles, however, the higher twisted blade produces more thrust than the baseline blade, as the rigid blade approaches a localised stall due to the thick aerofoil section used and the effect of the tip vortex. Some preliminary hover results, in ground effect, and with recirculation in the test chamber have been published in [105]. Because of this, the performance can not be compared to the results of this work.

Figure 5.8 (b) shows the integrated thrust and torque at the tested pitch angles. The blade torsion of the elastic blades lowers the values compared to the rigid blades. This torsion effect becomes less significant at higher pitch, which correlates to decreasing tip torsion in Figure 5.10. The higher twist mainly provided a reduction in torque, whereas thrust was less affected.

The radial distribution of the sectional thrust and torque components for two pitch angle settings are compared in Figure 5.9. Comparing the higher twist $\theta_{tw} = -12$ deg/R cases against the baseline $\theta_{tw} = -8$ deg/R cases, a clear trend of increased thrust on the inboard sections of the rotor blade can be observed — as expected. For all investigated pitch angles, the cross-over point of thrust and torque is at 75% R, where the nominal blade twist is zero. This section is marked by an additional gridline. In the outboard section, the blade is highly loaded, with a thrust

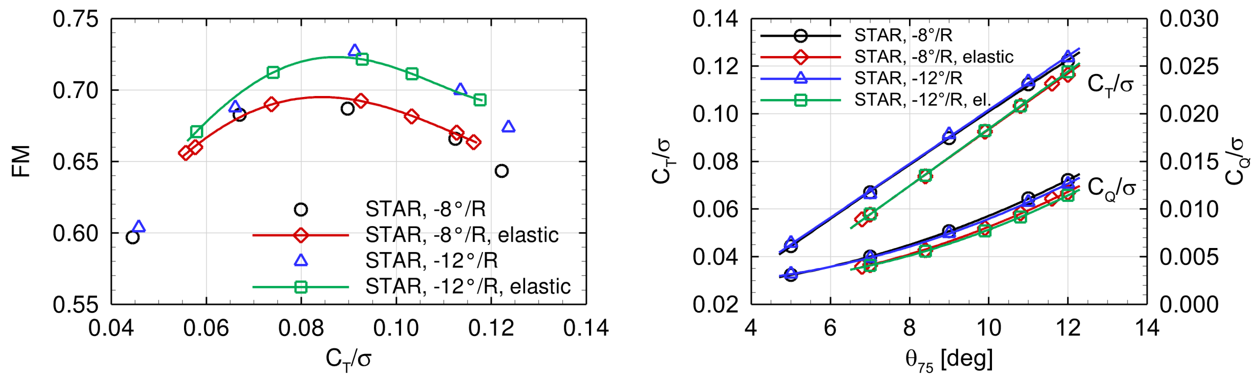

(a) Figure of Merit

(b) Thrust/Torque

Figure 5.8: Figure of merit over thrust coefficient and thrust coefficient vs collective of the STAR blade.

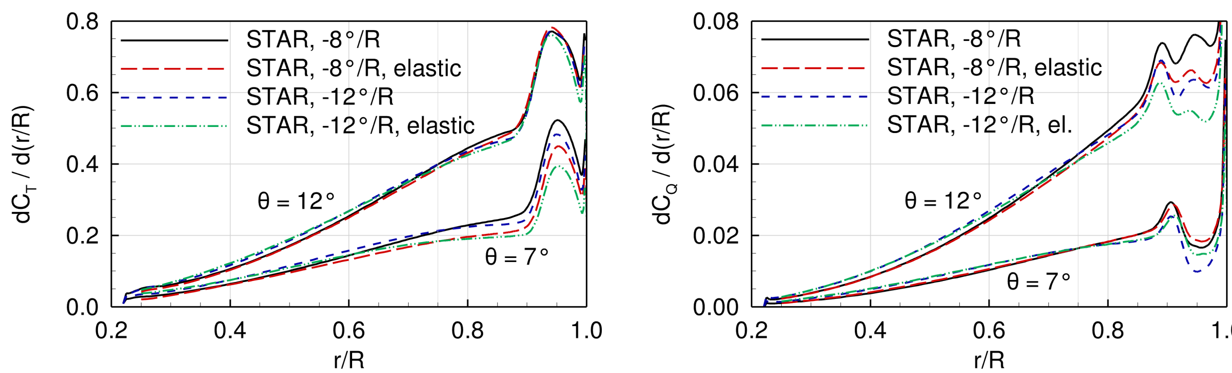

(a) Sectional coefficient of Thrust

(b) Sectional coefficient of Torque

Figure 5.9: Sectional coefficients of thrust and torque for selected collective angles of the STAR blade. The coefficients use the tip velocity for scaling.

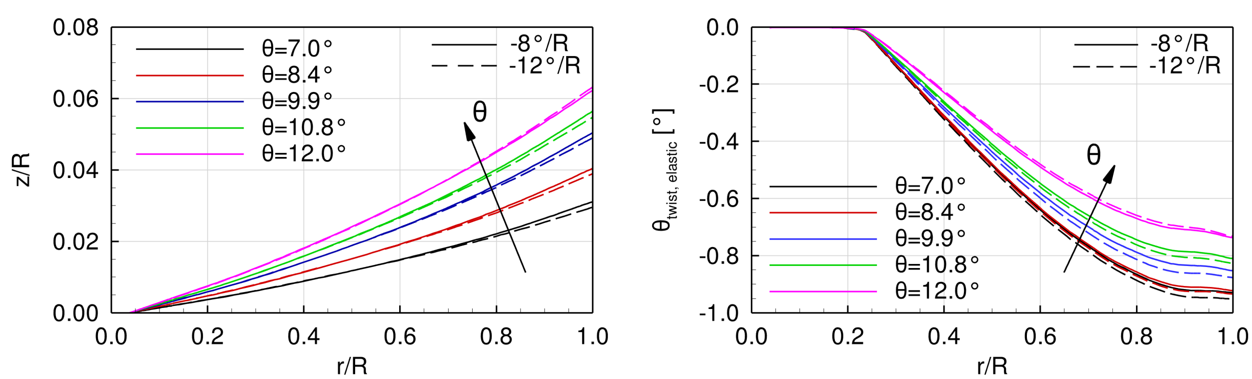

(a) Flap deformation

(b) Elastic pitch deformation

Figure 5.10: STAR blade deformations, the high-twist blade results are shown as dashed lines.

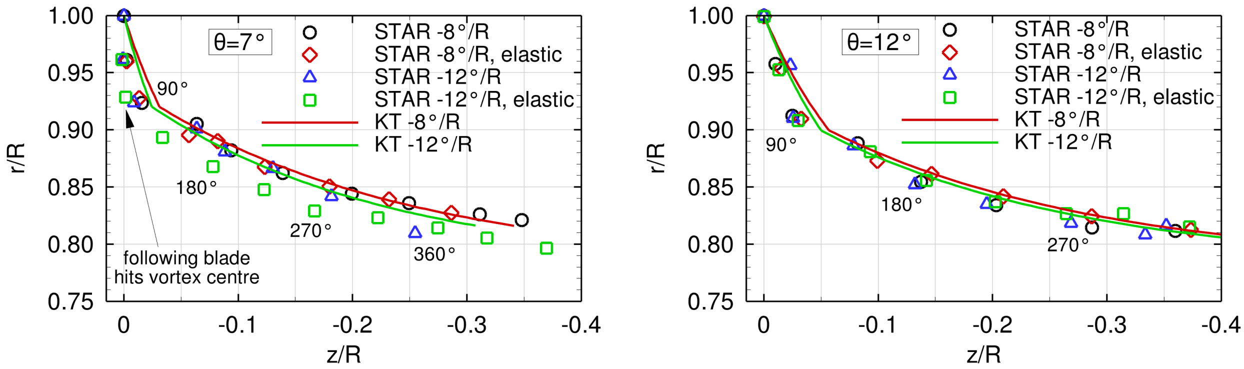

(a) $\theta_{75} = 7°$ (b) $\theta_{75} = 12°$

Figure 5.11: Tip vortex convection of the hovering STAR compared with the approximation of Kocurek and Tangler (KT) [177].

coefficient peak at 94%R. At the highest collective angle, the thrust peak is similarly limited for all blade configurations. This indicates, that the thick blade section is pitched too high outboard and experiences a thrust plateau due to an onset of flow separation. This benefits the higher-twist blades, which produce more thrust inboard. This is further discussed, in Section 5.3, where the FEM and beam model aeroelastic coupled simulations are compared.

The inboard torque coefficient is similar for both rigid and elastic baseline cases, while the higher local pitch of the high-twist case produces more drag. After 75% R, the trend flips again, with a significant torque reduction on the high-twist blade. At 12 degrees collective, a second torque peak forms at 95% R due to the increasingly transonic flow. At this location, the tip vortex of the previous blade produces an upwash, which further increases the aerodynamic angle of attack on the 12% chord thick aerofoil.

The aeroelastic deformations in hover for the STAR blade are shown in Figure 5.10. Nominal blade results and high-twist results are shown as full and dashed lines, respectively. A linear increase in blade flap with collective angle can be observed, reaching a peak value of 6.2% of radius at the blade tip on the highest thrust case. The majority contribution comes from the hinge flap angle. The blade flap of the high-twist blades is similar to the nominal blades and confirms that flapping mainly depends on the blade weight and overall thrust. The magnitudes of elastic blade twist are reduced with the blade collective setting. With increasing collective angle, the tip thrust reduced from 0.95 degrees to 0.72 degrees. The pitch-down moment reduces at higher blade pitch, partly due to the strong suction peak near the leading edge. This is partly because of the model blade's low Reynolds number in this compressible flow regime. The viscous friction component plays a large role at the low collective angles, contributing 42% of the blade torque at the lowest collective angle.

The tip vortex locations were identified from the simulation results by finding the peak in vorticity magnitude at intervals of 45 degrees of vortex age. The results are compared to the approximation of Kocurek and Tangler (KT) [177] in Figure 5.11. At low pitch settings and for the higher-twist blade, the tip vortex initially rises slightly above the following blade before being pushed downward. The elastic, high-twist case at 7 degrees collective has the following blade directly hit the tip vortex centre, which deflects the vortex inboard and is unsuitable for comparison. The higher twist case is observed to have less downward vortex displacement than the baseline, as the KT-model also predicts. The higher thrust results in Figure 5.11 (b) are less impeded by the following blades and match the empirical fit, confirming the validity of the simulation set-up.

5.2.2 ATR Blade in Hover

The ATR rotor is simulated between 8 to 14 degrees collective control angle for rigid blades of nominal and increased twist. The experimental conditions were replicated, in a heavy gas atmosphere with a speed of sound $a = 167.8$ m/s and the ratio of specific heats $\gamma = 1.116$, at the full Mach number of 0.65. The peak figure of merit in Figure 5.12 (a) is predicted to be 0.658 and the 4 degree increased twist blade shows an improvement of 2 counts over the high-efficiency region. The thrust over collective angle curve matches between nominal and high-twist blades. Figure 5.12 (b) confirms the 75% R section as the ideal radial position for zero twist, where any linear twist distributions produce comparable thrust. Expectedly, the sectional thrust curves for the nominal and high-twist ATR blades intersect at 75% radius (Figure 5.13). While the sectional thrust inboard of 75% R increases linearly with the collective angle, diminishing increases can be observed near the peak at 93% R. The tip vortex formation produces a sharp thrust spike at the blade tip. Two characteristic peaks in torque coefficient, comparable to the STAR at a higher collective angle are formed. Similarly to the STAR, the second peak at 93–95% R diminishes at lower pitch angles. This region also shows the most significant improvement in rotor torque when the twist is increased. However, the 14-degree collective angle shows a larger-than-expected increase in torque at this location, indicating a loss of efficiency for the nominal blade.

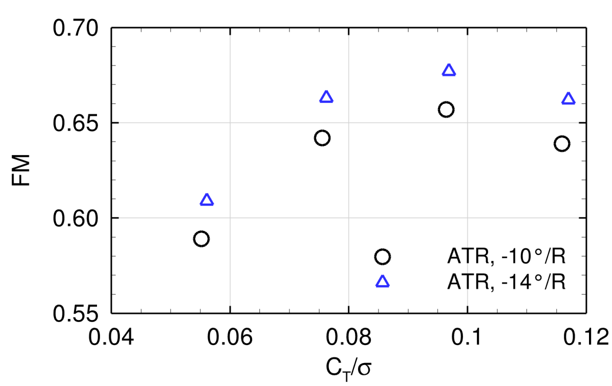

(a) Figure of Merit

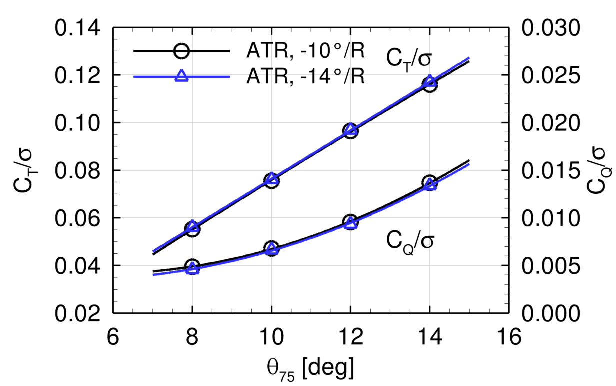

(b) Thrust/Torque

Figure 5.12: Figure of merit over thrust coefficient and thrust coefficient vs collective of the ATR blade.

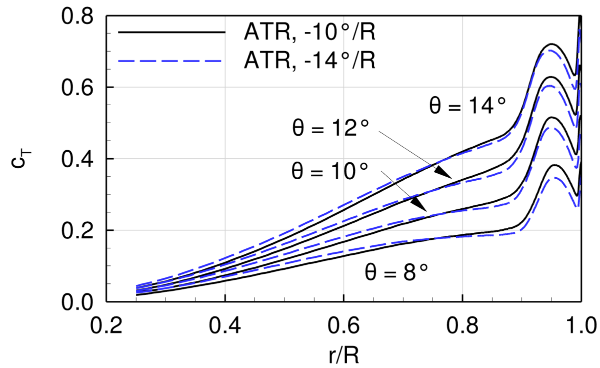

(a) Coefficient of Thrust

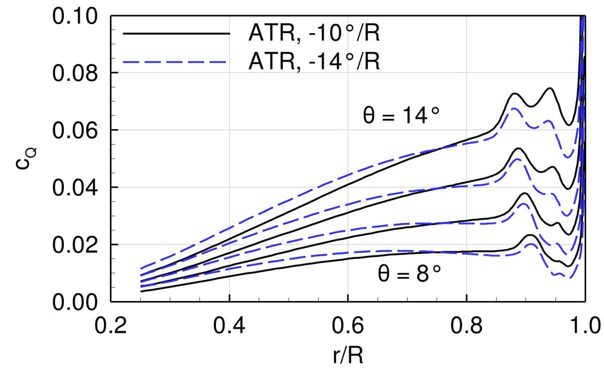

(b) Coefficient of Torque

Figure 5.13: Sectional coefficients of thrust and torque for selected collective angles of the ATR blade. The coefficients use the tip velocity for scaling.

5.2.3 HVAB Blade in Hover and Experimental Comparison

The prediction results from HMB3 are compared to the published experimental data - first published by Norman *et al.* [140] in 2023, then fully available on the AIAA hover prediction workshop page of NASA [139]. The experiment features performance measurements with an estimated error of only $\pm 0.005FM$. Some performance data is available for the cases where both upper and lower blade surfaces were tripped, which correlates to the fully-turbulent model in the prediction work.

The figure of merit curves and the thrust produced for each simulated pitch angle are shown in Figure 5.14 (a). It includes the experimental measurements, where the flow is tripped on both surfaces. This corresponds to the fully turbulent model chosen for the CFD simulation, due to the otherwise low Reynolds number. A peak figure of merit of 0.71 is predicted in the rigid simulation. The elastic blade indicates two counts higher hover efficiency obtained at a higher thrust than the rigid blade. The experiment with tripped flow on both surfaces, at a peak FM of 0.715, is between the rigid and elastic results. At low and high thrust, the experimental result matches best with the elastic blade simulations. The blade with -18 degrees/R in twist shows the highest figure of merit, increasing the FM of the original blade by two counts. The additional pitch-down deformation on the aeroelastic simulation of the high-twist HVAB blade brings a further two-count improvement in figure of merit at an also higher thrust value.

The thrust and torque coefficients are shown in Figure 5.14 (b). The elastic blade prediction shows less thrust at any root collective due to the pitch-down deformation over the blade span. The thrust and torque measurements of the experiment match very well, but indicate slightly higher thrust at peak figure of merit and slightly less power at low collective angles. The rigid simulations clearly overpredict the rotor loads, because of the higher blade incidence on average at the blade tip region.

In Figure 5.15, the sectional thrust coefficients show loading peaks at 94% R. The influence of the tip vortex interaction is visible, with a thrust maximum at around 94% R. Inboard of this,

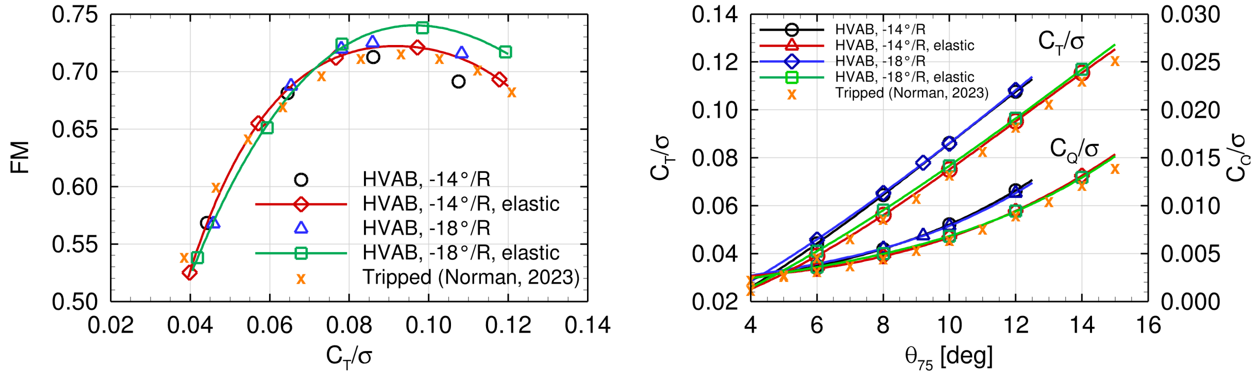

(a) Figure of Merit (b) Thrust & Torque Coefficients

Figure 5.14: Figure of merit over thrust coefficient, compared with tripped flow experiment [139, 140] and thrust coefficient at blade pitch of the HVAB rotor blade.

the small relief through this vortex is visible. At the lower collective angle, the weaker tip vortex creates a less intense effect in the spanwise range of 85–95% *R*. This is also particularly visible in (b). Because of the swept tip, a significant blade torsion difference arises between rigid and aeroelastic simulations. The HVAB blade also has sharp thrust and torque peaks at 100% R as a product of the tip vortex formation. The high-twist cases produce a similar thrust when compared to the nominal blades, with more loading inboard of 75% R, but less outboard. The sectional torque coefficient peaks at 87.5% R, just inboard of the thrust plateau at the high pitch condition, before both cases show a peak torque at the location of peak sectional thrust. The torque then sharply falls towards the rotor tip, with a further peak at the tip vortex formation at 100% R. The elastic rotor blades produce less thrust and torque, than the rigid counterparts.

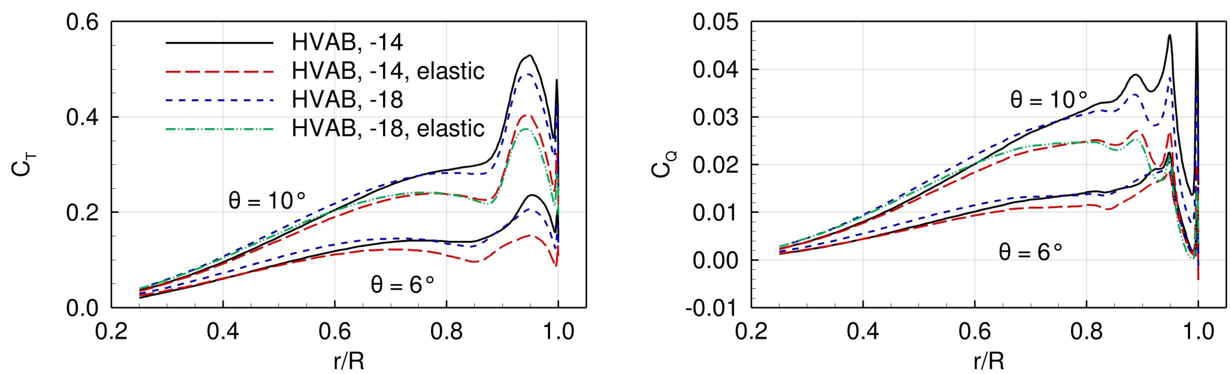

(a) Coefficient of Thrust (b) Coefficient of Torque

Figure 5.15: Sectional coefficients of thrust and torque for selected collective angles of the HVAB rotor blade.

The overall bending moment is dominated by the normal force component on the swept tip and blade sectional moments match well between experiment and simulation, as shown in Figure 5.16 for the 10° collective pitch case.

In addition to Figure 5.15, the results of all simulated collective angles for validation are shown in Figure 5.17. The normal force coefficient is analogous to the thrust coefficient in

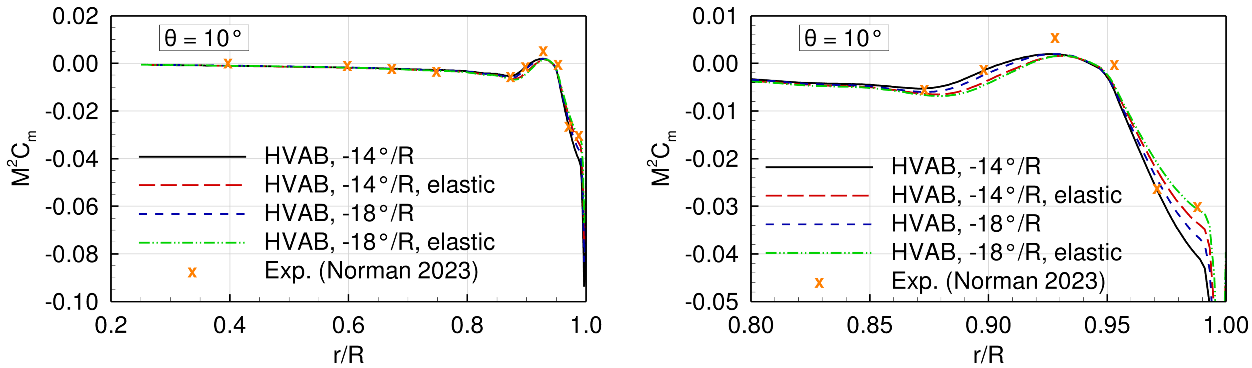

(a) Whole blade.

(b) Tip region detail view.

Figure 5.16: HVAB sectional moment coefficient around the pitching axis (0/0). The experimental data with natural transition (Run 77) [139, 140] compares to the elastic, $14°/R$ baseline aeroelastic result (red, long-dashed lines).

this case, due to the small angle differences, but was chosen to match the experimental data representation. In Figure 5.17 (a), the sectional normal force coefficients are compared to the integrated pressure from the natural transition experiment. Satisfactory agreement is found, which is comparable to other numerical predictions from the AIAA HPW. The sectional pitching moment coefficient in Figure 5.17 (b) is shown around the pitching axis (0,0). The trends of the experiment were predicted correctly, with small deviations near the blade tip.

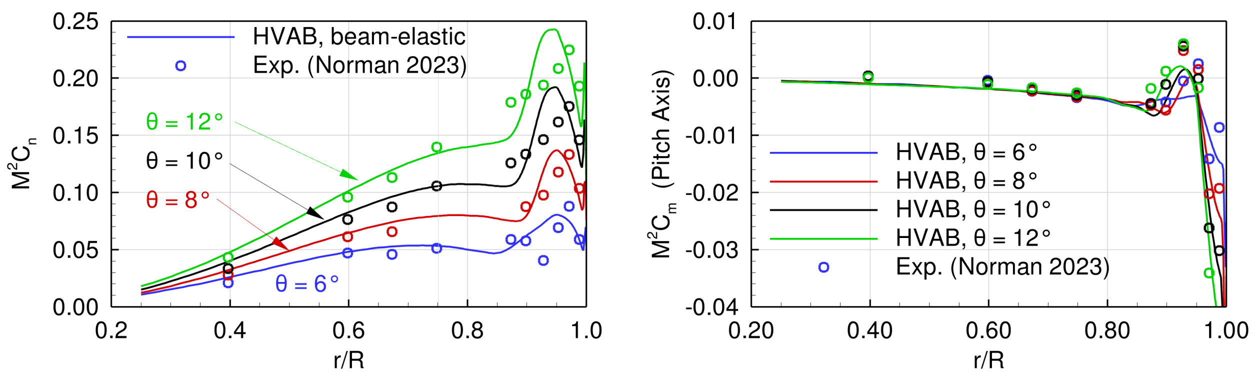

(a) Coefficient of Normal Force

(b) Coefficient of Pitching Moment

Figure 5.17: Sectional coefficients of normal force and pitching moment around the pitch axis for the HVAB rotor blade. The coefficients use the tip velocity for scaling and are compared with the free-transition experimental data (Run 77) [139, 140].

The blade deformations are compared to the experimentally obtained results of run 77 (natural transition) in Figure 5.18. The flap displacements are indistinguishable between the twist levels and match the experimental results, as the normal force coefficients do. The blade torsions of the 10 and 12-degree collective angle cases are close to the experimental results and match very well in the most significant blade part. The low-thrust cases show less deformation than the free-transition experiment.

The differences could be partially caused by what seems a discrepancy between the pub-

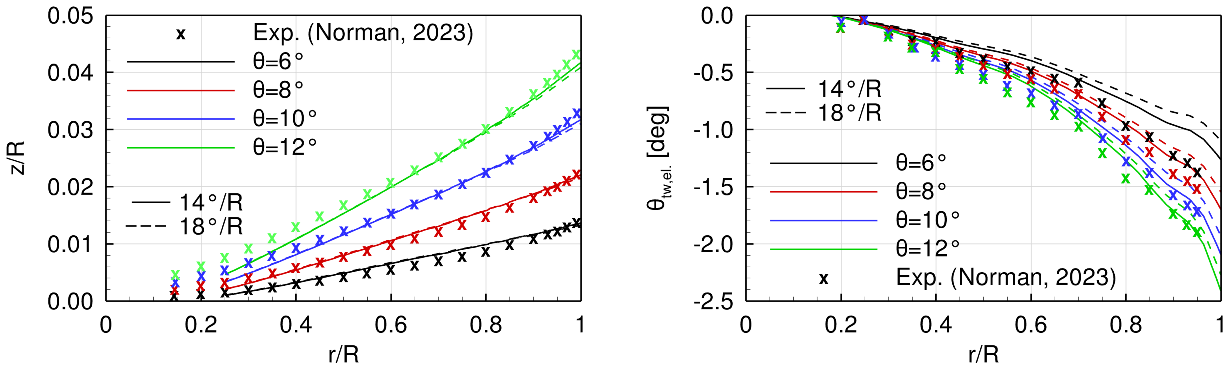

(a) Flap deformation (b) Elastic pitch deformation

Figure 5.18: HVAB blade deformations, the high-twist blade results are shown as dashed lines.

lished structural beam properties and the real blade stiffnesses and sectional offsets. Such differences can arise for example due to temperature effects on the materials, which undergo repetitive stress-cycles in the experiment. This hypothesis of mismatched beam properties is supported by the deformation predictions of Jain [178], whose results show a comparable torsion increase from the blade midpoint and a similarly wide spread between the collective settings. Less significant factors for this error could be the fixed blade coning assumption, the chosen CFD and turbulence modelling of this study, the experimental testing conditions and the accuracy of measurement tools. Unfortunately, no further data for validation of the structural model is available.

There could also be some amount of flap-torsion cross-coupling in the experimental blades causing this difference. But, as opposed to the STAR blade, the HVAB blade has its structural axes closely aligned with the pitching axis, which generally avoids strong cross-coupling under centrifugal load.

5.3 Hover Results of FE and Beam Structural Models

In this section, the differences between the finite-element and beam structural models are compared. The RANS fluid simulation is combined with the servo-elastic structural model and actuator model as a novel method. The differences between the currently popular beam model approach and the finite-element active twist model are quantified. This section follows a similar course as the previous comparisons in Section 5.2.1. Because of further progress with NASTRAN during the development of the FE model, and the useful discussions with other project partners, the structural beam model in this section includes the elastic axis, neutral axis and centre-of-gravity offsets from the quarter chord line as described in Section 4.2.2. This beam model better reflects the true properties of the experimental STAR rotor blades, but some differences persist as shown by the structural eigenmode results of Section 5.1.2. The finite element model is the best representation of the real rotor blade, based on the property dataset and experimental measurements, which is reflected in the results of this section.

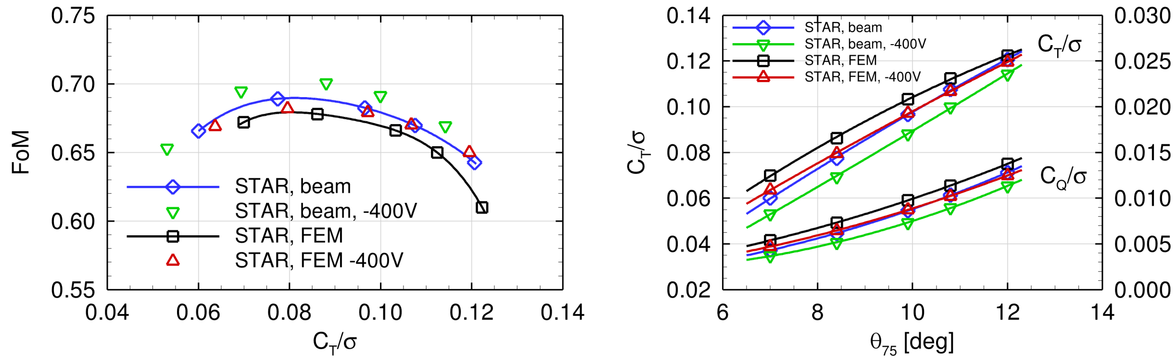

(a) Figure of Merit. (b) Thrust and Torque Coefficients.

Figure 5.19: Hover performance of the STAR rotor, estimated using the beam and FEM elastic models with and without actuation.

5.3.1 Test condition

The STAR rotor was simulated in hover to test the aeroelastic response and actuator modelling. For five collective angles, the beam-model and the FE-model are compared. The same angles as in Table 5.6 were selected. At the time of writing, the experimental model rotor has yet to be tested in representative hover conditions. However, in 2023 it was successfully tested in the DLR whirl tower. Wilke *et al.* [105] investigated this difficult recirculating flow with large amounts of turbulence. To show the effect of the actuators, a $-400\,\mathrm{V}$ tip-down twist actuation was applied. This represents 80% of the actuator capability. It was determined, that the actuators at this voltage produce a 2.06 Nm distributed moment between their start and end stations of approximately 26% R and 95% R. During bench testing, this translates to approx. 1.05° of additional twist through torsion.

5.3.2 Performance and Deformations

The beam-model and FE-model of the STAR have been compared in the coupled hovering simulation. First, the hovering performance in terms of figure of merit (FM), thrust and torque are shown in Figure 5.19. An efficiency difference of 1 count in figure of merit was found between the beam and FE-model simulations, throughout the performance range. Applying the 2.06 Nm torsion over the actuator span of the beam-model resulted in a performance improvement of 1.5 counts at the peak. Conversely, the FE-structural model, with the $-400\,\mathrm{V}$ applied through the thermal analogy showed a smaller improvement of just 0.5 counts. At high thrust coefficients, the active twist actuator is more effective. Figure 5.19 (b) is consistent with figure (a). Through increased tip-down torsion deformation, the beam model cases produce less thrust at a given collective angle. The torsion improves the rotor power, matching with theory.

The normal force distribution shown in Figure 5.20 (a) follows a similar trend to the HVAB blade, with a tip vortex-induced loading peak between 93% and 95% R. At the highest collective, this peak reaches a saturation point, due to the onset of stall. This is not the case in the

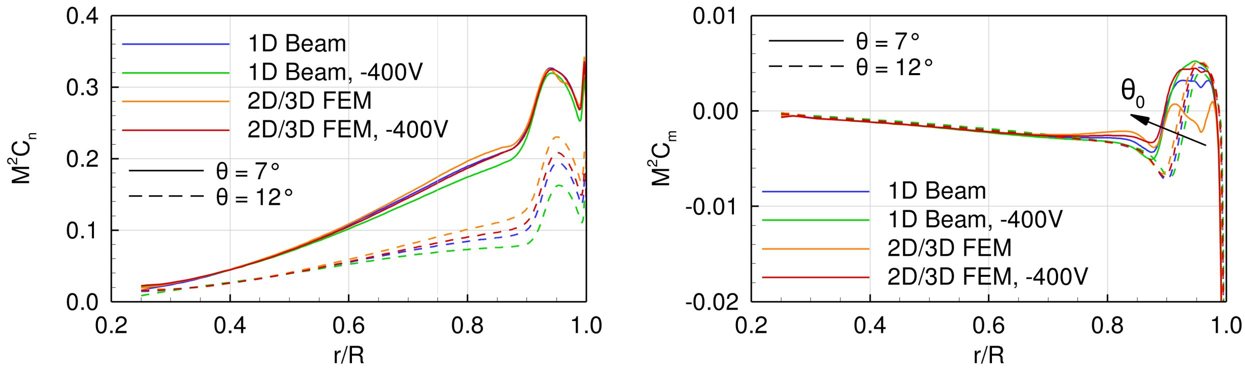

(a) Coefficient of Thrust

(b) Coefficient of Pitching Moment

Figure 5.20: Sectional coefficients of normal force and pitching moment around for selected collective angles of the STAR blade.

intermediate collective settings, which are not pictured for better legibility. The FE-model case, shows the most severe stall, as this case has the highest effective tip pitch-up angle. With a fixed blade root angle, the actuator-on cases produce less overall twist, mainly in the outboard section, as expected. The severity of the stall is visible in the sectional moment coefficient of Figure 5.20 (b). In the lower collective cases, the blade aerodynamic pitching moment differs little between the structural models, but some effects can be seen due to the different strength and location of the first passing blade tip vortex. Especially from 75% to 85% R, the pitching moment characteristic of the modified NACA 23012 aerofoil shows, which tends to produce an increasing pitch-up moment at higher incidence angles.

The blade deformations of Figures 5.21 are split into four subfigures for legibility. The slightly reduced thrust with the actuators engaged is reflected in the flap angle of the blade. Beam-model (a) and FE-model (c) show matching flap deflection around the hinge up to half of the radius. The lower flap-bending near the blade tip of the FE-model is because it has a more uniform mass distribution, while the beam-model mass is less near the tip. This part of the structural model may be addressed in future follow-up work, however, should have a smaller effect on the hover performance of the rotor. Some larger differences can be observed in the radial torsion plots (b) and (d).

The torsion is not just a direct result of the aerodynamic pitching moment of Figure 5.20 (b), which has been demonstrated as similar between the structural models. Instead, it is partially driven by the centrifugal force in combination with the offsets of structural axes, and partially by the 3-dimensional coupling of the layups and materials for the FE-model. Also, high-flapping cases have been shown to induce structural pitch-down torsion (Table 5.2). The actuator adds 1.1° of torsion to the beam model, 0.9° at $\theta = 12^\circ$. In the simulations of the FE-model, the added torsion is 1.0° at the lowest collective and 0.7° at $\theta = 12^\circ$. The blade torsion saturates at 1.0°, as the rotor blade tip enters stall. The spread of torsion between the collective angles of the FEM is larger than for the beam-model, due to the larger offset between the elastic axis and neutral axis.

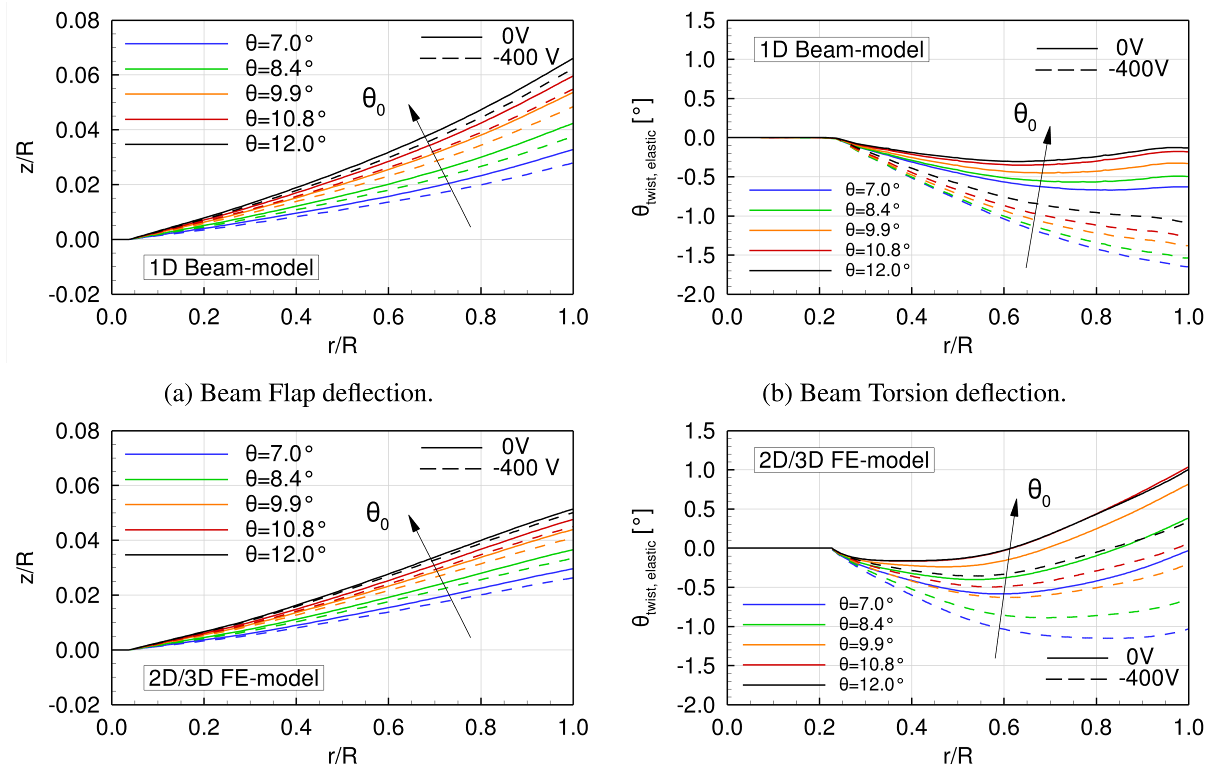

(a) Beam Flap deflection.

(b) Beam Torsion deflection.

(c) FEM Flap deflection.

(d) FEM Torsion deflection.

Figure 5.21: Comparison of the blade deflections of beam-model and FEM in the aeroelastic coupled simulation.

The torsion values also differ slightly from the static bench-test results in Section 5.1.2, due to the changed boundary conditions and loading. The actuator is slightly more effective at lower collective angles.

Figure 5.22 compares the flow solution of the two highest chosen collective angles of the simulation using the 2D/3D FE structural model. Near the stall limit, a separation bubble can be seen outboard of 95% R. This relatively low stall angle is caused by the tip vortex downwash exacerbating the drawbacks of the 12% c thick aerofoil. At the highest collective, and without using the torsion actuators a clear region of separated flow can be observed. This region coincides with the downward-rotating section of the Q-criterion visualised vortex tube. The tip vortex is also split by the blade surface. The shedded shear layer from the previous blade-passings is also visible in (a) and (b). The start of the separation bubble in (c) and the separation region in (d) is accompanied by a sharp drop in pressure coefficient, indicating the formation of a weak shock. This is present in both structural models, but more pronounced for the FE-models with higher pitch-up torsion. The active twist at $-400\,\mathrm{V}$ alleviates this, but no adjustment to the collective was made to match the thrust.

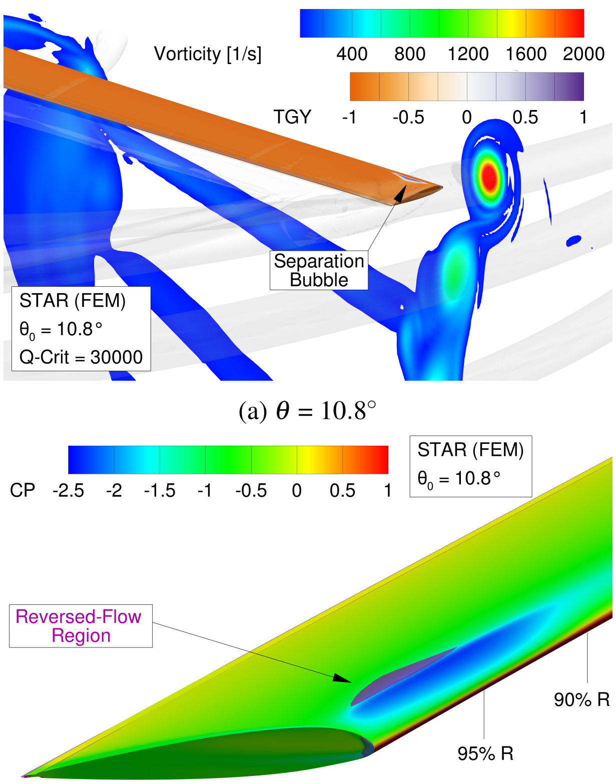

(a) θ = 10.8° (b) θ = 12.0°

(c) Detail θ = 10.8° (d) Detail θ = 12.0°

Figure 5.22: Rotor blade tip reversed flow regions of STAR FE-model hover cases. The top two figures show the surface flow-direction tensor and the detailed figures show the volumetric region of reversed flow.

5.4 Effect of Passive and Active Twist in Forward Flight

5.4.1 Flight Conditions and Trim

In forward flight, a high-speed and a high-load cruise condition are considered for the STAR. In these cases, the STAR with the original blade geometry (also called "baseline blade") is compared to a variant with higher twist 12 degrees/R blades, referred to as "high-twist" for short. This twist increase is the same as in the hover section, quantifying the effect of twist. The third compared condition is the STAR using 2/rev active twist at 80% of its amplitude and with the offset voltage of the material. This condition is called "active twist" for brevity. The trim goals in all cases are a set target thrust at a fixed rotor shaft angle, and zero aerodynamic pitching and rolling moments.

The first condition, high-speed level flight, is simulated at tip speed ratio $\lambda = 0.349$, at a shaft tilt of -11.11 degrees (rotor disk tilted forwards). The target thrust coefficient is moderate at $C_T/\sigma = 0.0639$. The second condition, high-load, uses a lower advance ratio of 0.303, no shaft tilt and a high thrust coefficient $C_T/\sigma = 0.13$ at the full Mach number. This thrust coefficient is near the rotor power divergence point of the half-speed condition presented in [13]. Due to the higher Mach numbers, and stronger BVI, it may not be possible to trim to zero aerodynamic rolling moment, in which case the residual moments are compared to make a statement on the effect of blade twist. The rotor rotor shaft angle is purposefully chosen to induce a dynamic stall on the retreating rotor blades under high-load. This approach has previously been used in the GOAHEAD (Generation of advanced helicopter experimental aerodynamic database for CFD code validation) European project test case 5a to induce dynamic stall on the 7AD rotor [179, 180]. Both active twist cases copy the actuator deployment envisaged for the wind tunnel test. The actuators operate at a 400 V nose-up bias, with a $\pm$500 V periodic voltage, which is estimated to achieve a 2.06° peak-to-peak torsion deflection at that frequency. The bias accounts for 0.82° active twist nose-up tip deflection. This offset is included to model the true, current-day capabilities of the actuator technology, as applied to the STAR blades. This however does not fully isolate the harmonic component. Further computations without the offset were omitted as the available computational time was too large to add more trimmed forward flight calculations. The correlation between voltage and elastic torsion was made in [13]. The high-speed condition active twist phase is $\phi_2 = 210$ deg, which corresponds to pitch-up at $\Psi = 105$ and 295 deg azimuth. In previous studies, such as [13, 111] this phase was found to be the most promising for power and vibration reduction using 2/rev actuation. The most promising phase of the higher-load condition was chosen, which is $\phi_2 = 0$ deg. This is based on previously published work [13]. This leads to nose-up tip twist maxima at $\Psi = 0$ deg and at 180 deg rotor azimuth, and to nose-down minima at 90 and 270 deg azimuth.

In forward flight, the unsteady residuals of the CFD were resolved to at least 2.5 orders of magnitude with a variable number of inner iterations in the dual time-stepping approach. A simulation was considered completed when the trim goal was reached and the loads settled into a periodic motion, which resulted in a constant vibration index.

5.4.2 Vibration and Performance Results

The vortex structures of the forward flight cases are shown in Figure 5.23. The higher-twist (b) and active twist (c) are compared to the passive rotor (a). Some of the blunt trailing edge vortex shedding and interactions with the previous blade are visible, mainly on the advancing blade side. The twist had a stronger effect on the high-load condition. In all three snapshots, complex dynamic stall vortex structures can be seen at III, due to the 0 deg shaft angle. Secondary and tertiary interactions occur on the retreating side (IV & V). The active twist blade (f) has a less pronounced initial BVI at station III. BVI is also clearly visible at the advancing blade, and at the front of the rotor disk (I & II). The blade tips on the retreating sides produced lower vorticity magnitude in the high load case when compared to the high-speed condition.

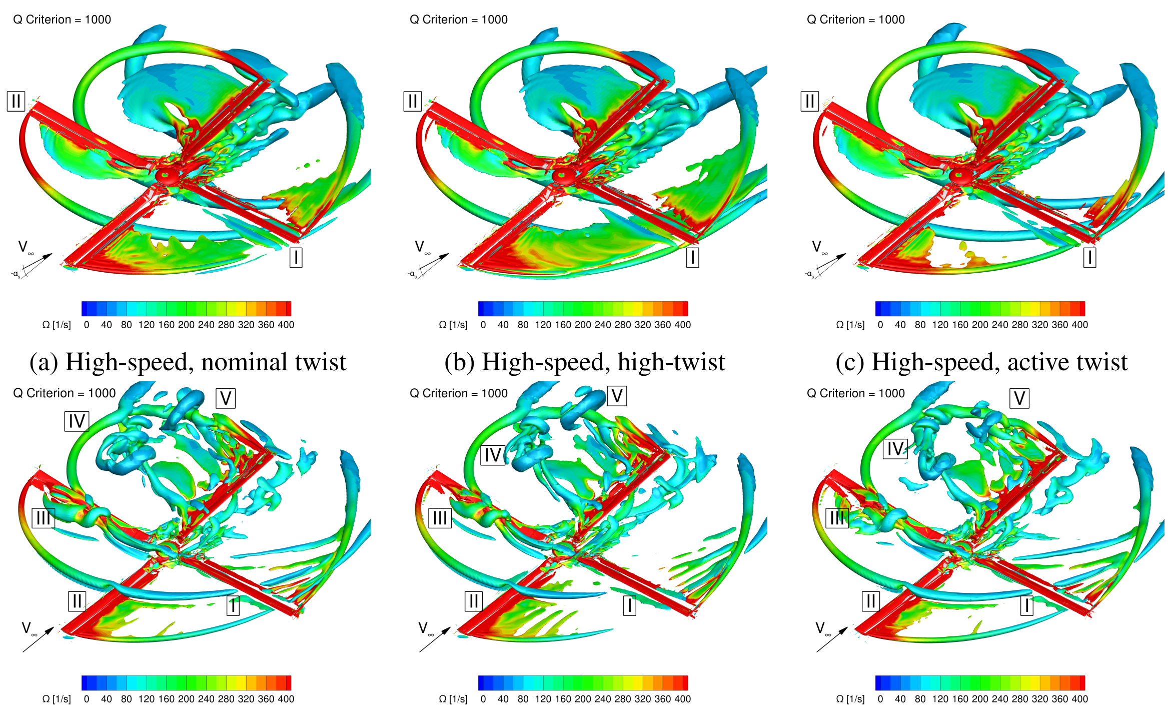

(a) High-speed, nominal twist (b) High-speed, high-twist (c) High-speed, active twist

(d) High-load, Nominal twist (e) High load, high-twist (f) High load, active twist

Figure 5.23: Instantaneous Q-criterion vortex structures for the high-speed and high-load flight at 0 degrees azimuth, coloured using vorticity magnitude. The rotor travels toward the bottom-left of the image and rotates clockwise as seen. The dynamic stall vortex on the high-load blade is marked as DSV.

The vibration intrusion index (VI) and lift-to-drag equivalent ratio L/D_e are defined in Section 1.2.2. The 4/rev component amplitudes generally outweighed the 8/rev by more than an order of magnitude in all cases presented here.

The performance and low-frequency vibrations of the high-speed case are shown in Figure 5.24. The change in rotor efficiency is negligible. However, the high-twist rotor suffers an

18% vibration index penalty. This confirms the trend observed in a similar case by You, Jung and Kim [111]. The active twist with $\phi_2 = 210$ deg reduces the vibration index by 22% instead. The vibration components are broken down in Figure 5.24 (c). The sum of the amplitude variations of the 4/rev and 8/rev are shown. The 4/rev amplitude in the z-direction (thrust variation) contributes significantly. The moment values are normalised by the rotor radius in the VI metric, so they are less significant than their amplitudes in Nm shown in the figure. Distributing the thrust more evenly over the quarter revolution of the rotor makes the active twist effective at reducing the vibration index. The presented flight conditions both have significantly higher thrust than propulsive force, hence the thrust variations are much more significant, than in-plane forces. Propulsive and side force 4/rev variations are near zero due to the trimmed, level flight condition and the 4-bladed symmetry of opposing forces. The rolling and pitching moment contribute to VI due to the difficulty to achieve trim in the high-speed and high-load cases. While the integrated moments are trimmed around the whole revolution of the blade, individual azimuth stations of the rotor can have large deviations from the average hub moments. The active twist shifts between rolling and pitching moment variations by improving the local pitch angle of the blade. The thrust vibration is reduced with the decreased blade twist on the advancing and retreating sides. The average blade collective is effectively increased there, and decreased front and back. This reduces the thrust and rolling moment variations over a quarter revolution.

Table 5.7: Trim states of the high-speed cases.

	Baseline	**High-twist**	**Active-twist**
θ_{75} [degrees]	11.12	10.88	10.46
θ_{1s} [degrees]	6.37	6.15	6.70
θ_{1c} [degrees]	-1.06	-0.95	-1.34
$C_M,x/\sigma$	-2.41×10^{-3}	-2.43×10^{-3}	-3.20×10^{-3}
$C_M,y/\sigma$	-3.46×10^{-3}	-6.55×10^{-3}	-2.47×10^{-3}
VI (eqn. 1.10)	0.103	0.122	0.081

At both flight conditions, the collective and cyclic pitch angles show differences of 0.3 degrees or less between nominal and high-twist, as seen in Tables 5.7 and 5.8. The local blade pitch is defined as $\theta_{loc}(r,\psi) = \theta_{tw}(r/R - 0.75) + \theta_{75} - \theta_c \cos(\psi) - \theta_s \sin(\psi)$, and does not account for the additional twist from the actuators. Due to the offset voltage, the active-twist cases require less collective angle, equivalent to approximately 75% of the offset twist change. The differences are largest for the high-load flight, and the best approximate trim states are listed in Table 5.8. Due to the retreating side dynamic stall in this case, a large increase in lateral cyclic is required, compared to the high-speed flight. The high-load dynamic-stall case is just beyond a trimable thrust. All forward flight cases were trimmed using the HMB trimming algorithm, based on 2-D aerodynamics. CFD and trimming were alternated until the desired trim state was achieved, or in this case, until the rolling moment could not be further reduced. The resid-

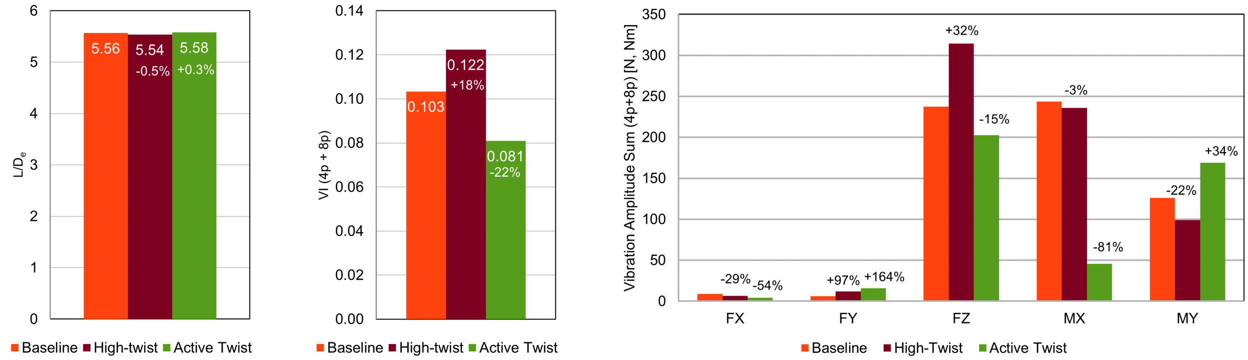

(a) L/D_e (b) VI (c) Vibration components

Figure 5.24: High-speed case performance metrics. The vibration components in (c) are the square of the amplitude, to represent their contribution to the overall vibration intrusion index.

ual rolling moment is comparable between the baseline and the increased twist simulations, and high collective and lateral cyclic inputs are required. The residual rolling moment of the baseline case is 190 Nm, which corresponds to an offset of the thrust vector by 2.6 cm to the advancing side. The active twist is closest to the required rolling moment trim. The active component increases the blade pitch angle at the front and back of the rotor disk, by reducing the twist. This alleviates the advancing and retreating sides, allowing for better rolling moment trim. Since increasing thrust and advance ratio at this point is limited by the rolling moment imbalance, it can be deduced that the active twist system increases the operating envelope in this flight condition.

The performance and vibration breakdown in Figure 5.25 shows that the higher blade twist slightly improves performance, but causes increased vibration. The main vibration component is a variation of the rotor pitching moment at the blade passing frequency. The vibration index is reduced by 8%, and the pitching moment vibration is shifted more towards the rolling moment axis. The 4/rev thrust component is reduced, and more significant to the VI, than the rolling moment variations in Nm.

Table 5.8: Trim states of the high-load cases.

	Baseline	**High-twist**	**Active-twist**
θ_{75} [degrees]	12.18	11.81	11.00
θ_{1s} [degrees]	10.71	10.23	9.88
θ_{1c} [degrees]	-2.83	-3.02	-2.60
$C_M, x^{US}/\sigma$	-1.85×10^{-3}	-1.88×10^{-3}	-1.16×10^{-3}
VI (eqn. 1.10)	0.335	0.348	0.315

The plots of Figures 5.26 and 5.28, show the STAR as clockwise spinning with the free stream inflow from the left. The forces are in the blade frame of reference, with M^2C_T being upwards in the shaft axis direction, and M^2C_Q is the torque coefficient about the shaft axis. The moment coefficient is negative for pitch-down moments. The columns show the results obtained

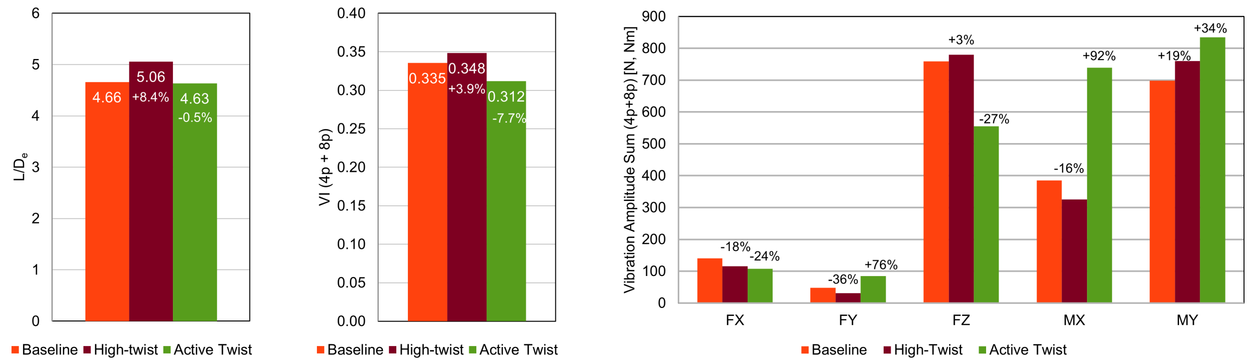

(a) L/D_e (b) VI (c) Vibration components

Figure 5.25: High-load case performance metrics. The vibration components in (c) are the square of the amplitude, to represent their contribution to the overall vibration intrusion index.

from simulations using the baseline, the +4 degrees/R higher-twisted and the active-twist STAR blades. In Figure 5.26, the rotor tip on the advancing side is generally offloaded due to pitch-down moment-induced deformations. A further reduction of lift in the outboard, advancing regions, is visible on the high-twist rotor. However, this is compensated by more lift inboard on the advancing side, which reduces the required lateral cyclic. This limits the thrust peak at the back of the rotor disk, affecting the rotor torque. This region experiences a large reduction in rotor torque, and generally, the lower tip sectional pitch can be observed in the torque difference in Figure 5.26 (b), compared to (a). The active twist case has a lower collective due to the elastic torsion offset from the actuator, so the advancing tip is also offloaded more than in the baseline configuration. It is more equally distributed around the whole azimuth. All cases are trimmed to a comparative and low rotor pitching moment. Overall, the L/D_e changes between the cases are negligibly small. The changes in the section pitching moment coefficient between the cases are small, with an increased pitch-down moment at the offloaded advancing blade tip on the higher twist blade compared to the reference. The back of the disk, where the thrust is reduced also showed a reduced pitch-down moment. Figure 5.27, shows the rotor blade deformations. The large amount of thrust at the front and back of the rotor causes a 2/rev flapping motion in the simulation. The disk tilt is negligibly small. The pitch-up deformation when using the active twist system is clearly visible in Figure 5.27 (c), due to the pitch-up bias of the actuators, and the active phasing.

The vortex shedding phenomenon, was also investigated in the high-speed flight case. Because of the shaft angle, the effect of passing blade vortices is not noticeable on the integrated airloads of a single rotor blade, shown in Figure 5.30. The majority of the blade thrust loading occurs in the front and back of the rotor disk, matching with Figure 5.26 (a). The resolved boundary layer simulation shows a trailing edge vortex shedding of approximately 8.3 kHz behind the blade of the high-speed flight simulation, made visible through the detailed view of the thrust.

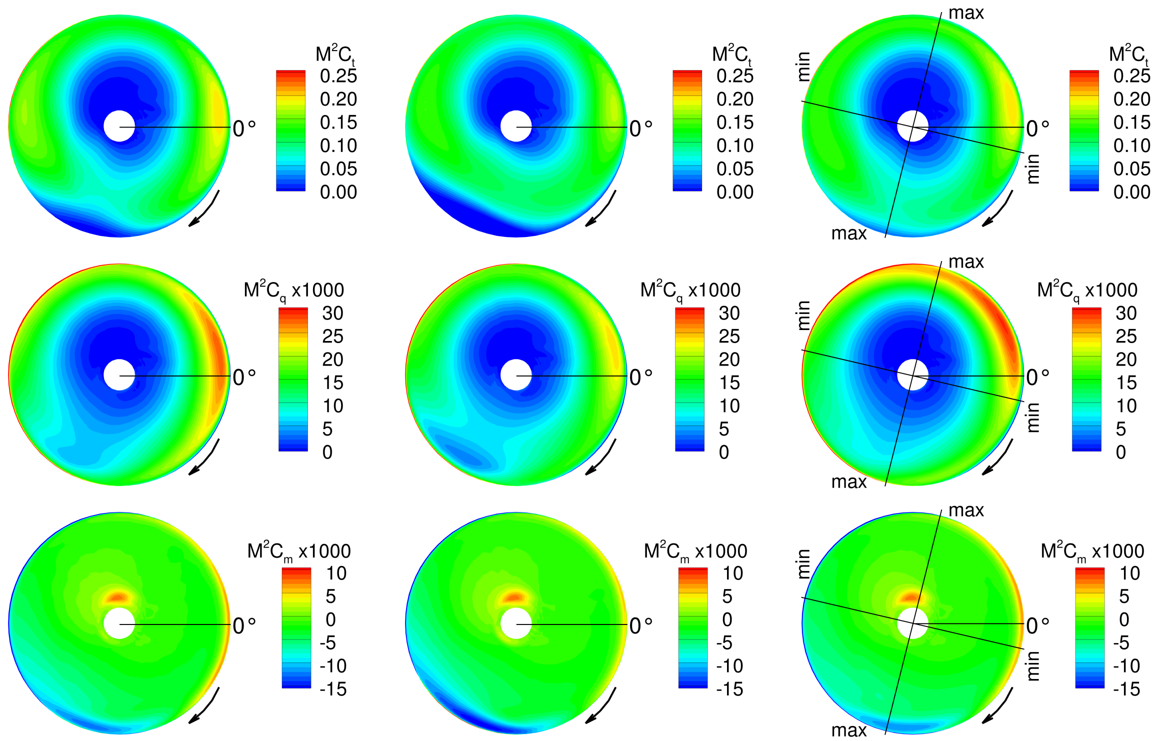

(a) nominal (b) high-twist (c) active-twist

Figure 5.26: High-speed case M^2 sectional thrust, torque and moment coefficients.

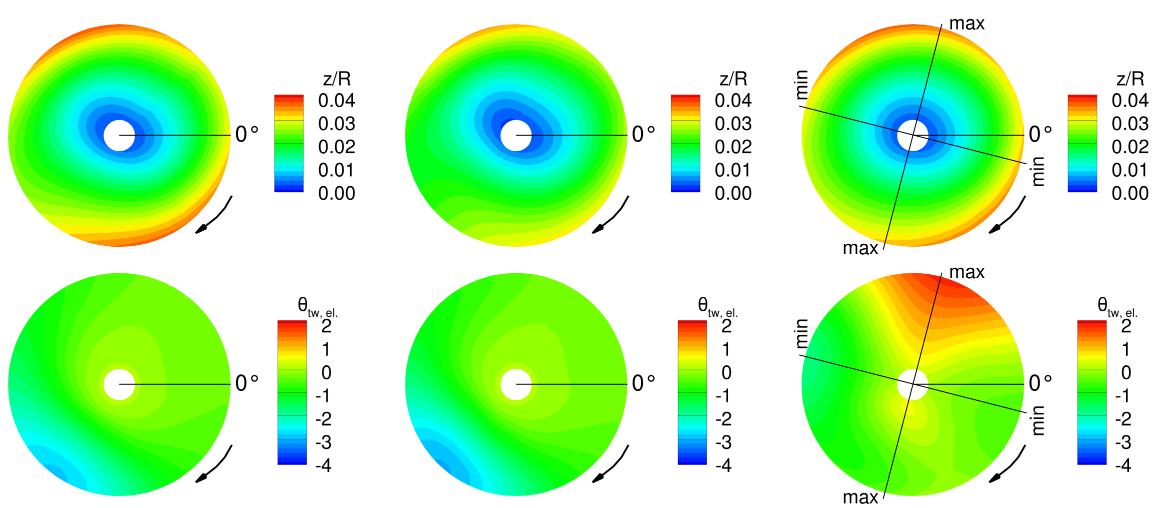

(a) nominal (b) high-twist (c) active-twist

Figure 5.27: High-speed case. Flap and torsion deformations.

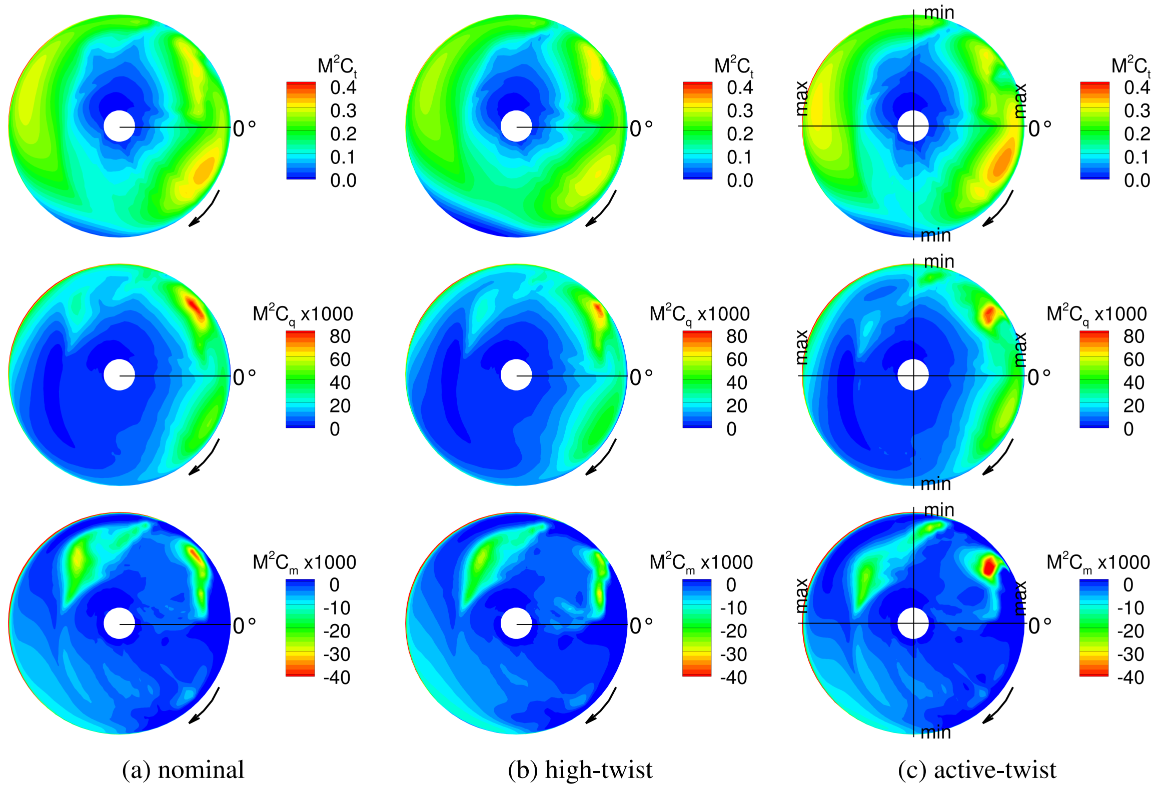

Figure 5.28: High load case M^2 sectional thrust, torque and moment coefficients.

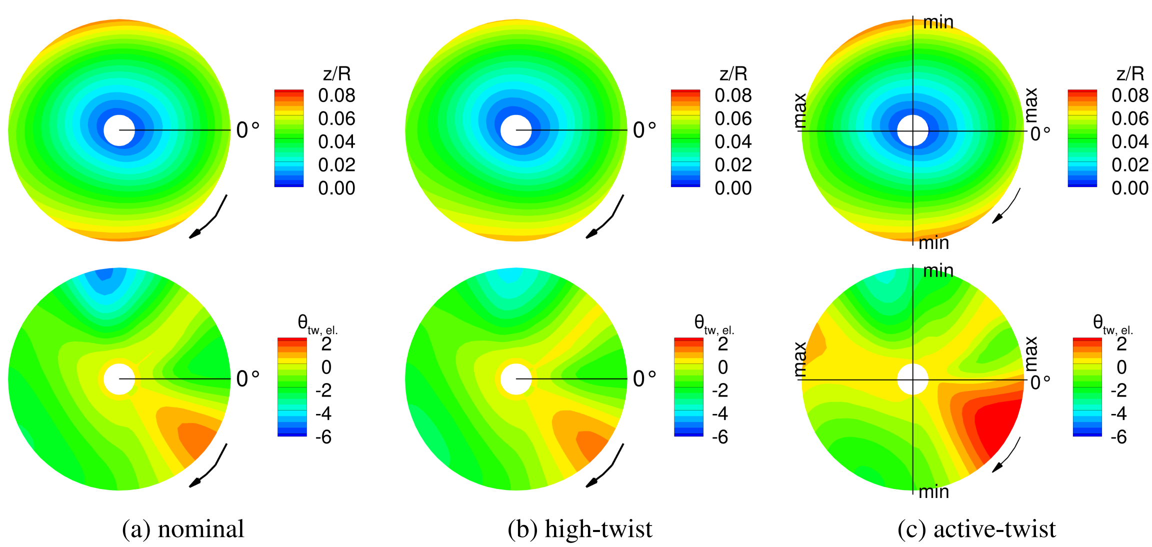

Figure 5.29: High load case. Flap and torsion deformations.

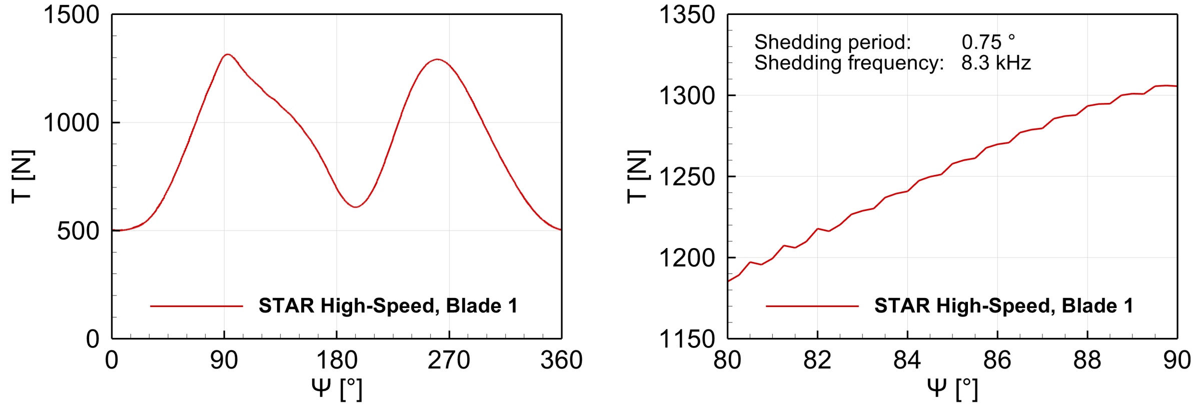

(a) Full blade revolution

(b) Detail sample

Figure 5.30: High-speed case integrated thrust history of Blade 1, starting at the back of the disk.

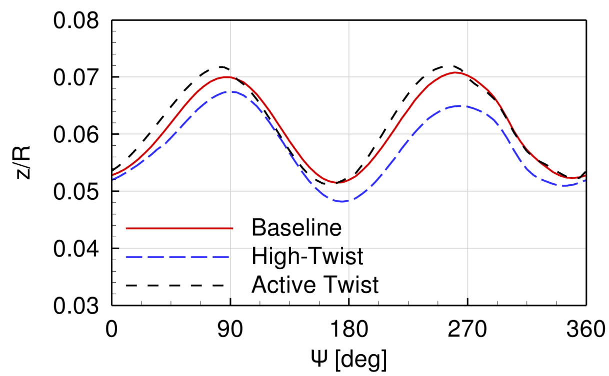

Figure 5.31: High load case tip flapping.

The high-load results of Figure 5.28 show that mainly the retreating side blade tip and rear of the rotor disk are loaded. The advancing side tip is less offloaded than in the high-speed case, due to the generally higher thrust coefficient. The higher twist blade (b) carries less loading than the baseline (a) at the advancing tip, which tends to be beneficial for performance in this dynamic stall condition. The thrust reduction follows a similar profile as for the high-speed case. BVI effects can be clearly seen in all plots between 90 and 270 degrees azimuth. The moment coefficient plot shows BVI-induced stall on the retreating blade, and BVI in the advancing side region, with attached flow. The sectional pitch-down moment is less, overall, at the turbulent rear part of the rotor disk for the high-load case, but is stronger on the retreating side. The higher-twist blade shows a slightly reduced area of dynamic stall. The front and back of the rotor disk produce a similar thrust as the baseline rotor. With active twist, the rotor produces much more thrust forward and aft, which helps achieve rolling moment trim. The torque at the back and front is increased. This condition also shows dynamic stall in a large region. The lower torque and the bending moment indicate a lower intensity of this BVI, compared with the other two high-load conditions. The flapping is dominated by 1/rev content for the baseline and high-twist case. The more equal load distribution with active twist causes a more pronounced flap-up on the retreating side. The increased thrust causes larger torsion deformations on the rotor blades than in the high-speed case. The active twist is visible with some phase delay in Figure 5.29, but the torsion also seems affected by the BVI-induced loads. Figure 5.31 isolates the blade tip location from the previous plots. The z/R axis is zoomed to fit the data. It shows that the active twist case has slightly increased longitudinal flapping over the baseline, due to its increased front and back loading. The high-twist has less tip flapping and shows a disk tilt toward the front and the retreating sides because sufficient rolling moment balance could not be established at this thrust. This is further evidence, that higher blade twist reduces the maximum trimable thrust.

Chapter 6

Conclusions and Future Steps

This thesis investigated the aero-servo-elastic performance of active twisting rotors in hover and forward flight. The novel approach of this work combined the high-fidelity fluid dynamics simulation with a combined structural and actuator modelling via the thermal analogy method. The aeroelastic coupling code was first validated against the experiment of the HVAB rotor blade. Static structural responses and eigenmodes were compared between models and to experimental data where available. For three rotor blades, the hovering performance of differing twist levels was compared. In high-speed and high-load forward flight, the effect of passive twist change and active twist was evaluated, using performance and vibration metrics.

6.1 Conclusions

Compared to other forms of individual blade control, validation data of active twist rotor blades is very limited. Through participation in the STAR project, high-quality structural models could be created. The HVAB experiment of the AIAA Hover Prediction Workshop was identified as suitable for passive blade validation. Good performance agreement was found between the aeroelastic coupled simulation and the experimental run with tripped flow on both surfaces. The integrated sectional loads of normal force and pitching moment coefficient correlated well with the experimental runs. The blade elastic deformations in flap-bending and torsion were suitably accurate. From the available sectional properties of the blade, and results in this work and literature, it was concluded that the provided structural data of the HVAB may have been a main source for the small discrepancies found in blade torsion.

A thermal analogy method is described and implemented in the commercial solver, which equates piezoelectric strain to thermal strain. The thermal analogy method was first validated against published simulation results for the simple BM 500 piezo-actuator.

Then finite element models were created to represent the rotor blades, made of either 1D beam elements or 2D/3D finite elements. It was found that tweaking the beam model sectional parameters was relatively easy to obtain correct structural frequencies, as they are representative of bulk model properties, such as bending stiffness. This, however, does not guarantee correct results. The volumetric structural model of the STAR blade demonstrated the feasibility of going beyond beam models for rotor analysis, and its main advantages for modelling spanwise to in-plane strain coupling. One main difficulty was identified for 3D modelling, which also affects sectional property extraction for beams. Glued-in segments of high stiffness, such as the nose weight rod segments contributed significantly to the bending, torsion and cross-coupling terms. However, the employed manufacturing technique made it difficult to estimate how much stress and strain is transferred through the semi-rigid glue-contact boundaries. Modelling such contact is possible in 3D FE, but was avoided in this work due to the already high complexity and difficulty finding convergence in the structural solver. However, the chordwise elastic axis position could be confirmed against published results. The hinge required a small spring stiffness to converge the otherwise rigid body motion inside the structural solver.

The STAR beam model from the provided properties overestimated the modal eigenfrequencies of the experiment in both clamped and rigged boundary conditions. In clamped and rigged conditions without centrifugal force, the differences were most pronounced in the higher frequency modes. However, near the nominal rotational frequency, all frequencies besides the second torsion and fifth flapping modes were considered sufficiently close to experiments for use in aeroelastic prediction. The volumetric structural model of the STAR has mode eigenfrequencies, which are close to the measured values. However, the model also predicts a small number of additional mixed, cross-coupled modes without any dominant component and such mixed modes have not been recorded in the published experimental results. All STAR structural models showed a strong coupling between 5$^{\text{th}}$ flap-bending and 2$^{\text{nd}}$ torsion modes, which are indistinguishable beyond $0.7\Omega_r ef$. The 2$^{\text{nd}}$ torsion mode was found to be strongly dependent on the pitch link stiffness in the model.

The 1D beam model showed a linear and predictable torsion behaviour when a torque, representative of active twist, was externally applied. The torsion was mostly unaffected by centrifugal stiffening. In static deformation simulations, a strong cross-coupling between torsion and flap-bending was observed in the 3D FE model. It was concluded that this was largely caused by the offsets of the elastic and neutral axes. Exchanging the composite parts with isotropic materials did not eliminate the observed coupling. When a force was applied to bend the blade, no excessive torsion was noted, confirming the torsion was induced only by the centrifugal body force. The active twist capability of the volumetric model was also affected by the centrifugal stiffening effect. For the same input voltage, the active twist response was reduced by approximately 19% at the nominal rotor speed. The effect of blade-bending on this could not be eliminated, but is expected to be relatively small. In addition to regular centrifugal stiffening, the torsion induced by the centrifugal forces puts significant strain on the actuators. While no non-linearities were modelled in the actuator, the torsional strain likely acts in a non-linearly relation to the overall blade torsion, and therefore where actuators reduced blade torsion, the opposing centrifugal cross-coupling increased, offsetting the actuators effect.

The model made of 110 beam elements could be quickly generated by a script after the data was pre-processed, and it converged within seconds. The volumetric models required significantly more modelling effort, material properties and internal geometry data. It was found that models with increasing degrees of freedom disproportionately increased computational time, due to constraints on the required file-io. A 15$\times$ increase in DoF increased computational time by 21.7$\times$. Significant increases in computational time were found in the more complex boundary conditions. CPU time increased 100$\times$ from cantilevered force deflection to the rigged, rotating case. A pre-stressed modal analysis in the latter condition required about 23 minutes after some further modelling and solver parameter optimisations.

Initially, the effect of rotor blade twist as a parameter was investigated for ATR, HVAB and STAR model scale rotors. The geometric linear blade twist was increased by 4°/R, which resulted in a more efficient hovering performance. The least twisted blades benefitted the most at up to 4 counts FM in the case of the rigid STAR blade simulation. The rigid ATR results and the aeroelastic STAR results showed 3 counts of improvement. The highly twisted HVAB rotor blade confirmed the diminishing improvements of increasingly twisted blades with only 2 counts FM improvement. This conclusion matched well with the analytical solution of the ideal hover-induced velocity profile.

From all three model scale rotor blades, thrust peaks near 94% R could be observed, as a product of the tip vortex interaction. At the highest simulated thrust levels, flow separations started to occur at this section, and the sectional thrust coefficient stagnated, while torque increased. At a fixed 75% R collective setting, increasing twist produced an equal amount of additional inboard thrust as was lost outboard of that location. The tip vortex locations of the hover simulation matched well with the experimental fit by Kocurek and Tangler for rectangular planform blades with linear twists. Only at high twist and low incidence, where no downward tip vortex convection occurred, significant differences were found, as the tip vortex was hit by the following rotor blade. Therefore, it was concluded that higher blade twist, while more aerodynamically efficient can be a cause of BVI vibrations and noise at low-load hover.

With an increased twist, only a minuscule change in rotor blade flap-bending was observed, with the higher twist bending the tip slightly less as the tip gets off-loaded. Small differences were found for the blade torsion, with $\approx 0.1°$ more tip-down torsion on the STAR, and $\approx 0.15°$ tip-up on the HVAB. Increasing twist reduced the effect aerodynamic pitch angle of the swept tip of the HVAB, largely reducing the pitch-down moment from the sweep lever arm, explaining this difference. It was also demonstrated, that the 75% R station's pitch angle correlated well with the expected thrust when torsional deformations such as through active twist were considered.

The effect of rotor blade twist was also investigated in aeroelastic coupled forward flight simulations. A modal coupling approach was employed, where the blade deformations were a result of a superposition of the first 7 blade mode's contributions. A vibration intrusion index was used, to quantify the amplitudes of the aerodynamic loads occurring at the single and double blade-passing frequencies.

First, a high-speed flight condition at $\lambda = 0.349$, at moderate thrust was investigated on the STAR rotor. The rotor shaft angle was set to $-11.11°$, where fuselage weight, drag and rotor thrust were assumed to be in balance. The nominal blade was compared to one with $4°/R$ increased twist and a $210°$ phase active twist at 50% of the actuator voltage range. The active twist phase corresponded to a blade-tip pitch-up at $\psi = 105°$ and $\psi = 295°$ azimuth. The active twist system has a mean tip-pitch up bias of $1.0°$, which slightly changes the effective linear blade twist distribution.

With increasing blade twist, a lesser collective and lateral cyclic input was required to trim the high-speed case. With active twist, the collective was reduced significantly by 0.66°, but accounting for the actuator bias, the effective change at 75%R was minor 0.09°. The high-speed flight prediction found insignificant differences between the cases in terms of lift-to-drag ratio. However, the higher blade twist significantly increased the shaft-direction contribution of vibratory hub forces, leading to an 18% increase in the vibration index. The active twist instead reduced this vibration index by 22%, by distributing the loading more evenly over the whole azimuth. At the simulated harmonic input, the rolling moment contribution was reduced by more than 80%, at the cost of slightly increased pitching moment vibration. With increased twist, the rotor blade tip sectional thrust was shown to get increasingly negative, while with active twist, the advancing side blade tip was loaded more. Because of the still relatively moderate angle, no shock was identified. The mean rotor coning was reduced at higher twist, as the thrust was generated further inboard. The active twist case showed little difference in the blade flapping behaviour, but the range of blade torsion values was shifted closer to zero. The additional torsion from the actuator could clearly be identified.

Additionally, a high-load forward flight case at $\lambda = 0.3$ and maximum rotor thrust were chosen to demonstrate the active-twist systems improved load-carrying capacity. This condition also displayed strong blade vortex interaction, due to the chosen 0° shaft angle. These strong blade vortex interactions were seen throughout the whole rotor blade disk, but most significantly on the retreating side and at the back.

The nominal STAR rotor could not be trimmed at this thrust, with a small residual rolling moment of $C_{M,x}/\sigma = 1.85 \times 10^{-3}$. Further lateral cycling input at this condition caused increasing blade pitching moment and flapping responses, which in turn increased the residual rolling moment when the trimming algorithm was applied again. The higher twisted blades showed a lift-to-drag ratio improvement of 8%, however, it could not overcome the trim problem to produce the targeted thrust. A small vibration increase was also found. A higher-harmonic active twist input at 0° phase (tip pitch-up at 0° and 180°), showed a large reduction of the residual rolling moment at this thrust, at significantly lower cyclic angles. Knowing that at higher advance ratios and thrust in forward flight, the rolling moment becomes more difficult to trim, this inversely shows the potential of the active twist system to increase the rotor speed or load-carrying capacity at speed. Additionally, the vibration was shown to be lowered by nearly 8%. This was mainly due to a decrease in thrust force variations, but large rolling moment vibrations counteract much of the gains. The in-plane vibration contributions were found to be small in both forward flight cases. This is likely due to the methodology in the work, where mechanical forces absorbed by the lag damper were not considered. Retreating blade vortex interactions were clearly visible in this flight condition, and the active twist system reduced those as it was visible in the sectional moment coefficients. The blade deformation showed a similar trend as in the high-speed condition.

Finally, the STAR 1D beam and 2D/3D finite element structural models were compared in the aeroelastic hover simulation. Instead of a rigidly changed twist, the actuators were modelled, by applying a moment on the beam elements, or by the thermal analogy method.

The beam model showed about a 1 count higher figure of merit than the equivalent simulation using the FE model. While using the beam model, the active twist provided an expectedly constant efficiency improvement over the useful thrust range, the gains were lower using the FE thermal analogy method. Only near the maximum thrust, was where the active twist system worked effectively at increasing the performance. The better performance of the beam model simulations was caused by the difference in torsion. The finite element model aeroelastic simulation also tended towards a pitch-down blade torsion at the mid-span, but the centrifugal/torsion and flap/torsion cross-coupling caused the blade to pitch up at the tip. A saturation of torsion was found at 10.8° collective, where further increases did not affect the blade torsion. At all collective settings, the beam model showed constant effectiveness of approximately 1.1° additional tip-torsion. The coupled simulation of the volumetric structural model instead showed varying actuator effectiveness with thrust. The STAR rotor blade also formed a local stall bubble at 94% R in the aeroelastic simulations. When the pitch was further increased, the section completely stalled due to the tip-vortex interaction. This phenomenon was expected due to the large induced velocity from the blade tip vortex, in combination with the thick aerofoil, accelerating the flow to locally transonic speeds.

The presented results show a future potential for such active twist actuators. However, larger efficiency gains in forward flight need to be demonstrated to overcome the power demand of the actuators and the associated cost in manufacturing and maintenance. The L/D_e improvements in the range of 2%–6% reported from IBC tests could not be reproduced in the active twist simulations. The need for high-fidelity tools for fluid dynamics and servo-structural dynamics has been proven by the employed novel simulation method and the significant differences found between 1D beam and volumetric finite element structural and actuator modelling.

6.2 Next Steps

For future work on the topic of active twist helicopter rotors exploration of the following topics is recommended:

- Significance of active twist on modern rotor planforms. The STAR was chosen in this work, due to the ongoing experimental testing campaign in the international cooperation. The rotor is based on the simple BO-105, but modern helicopters overcome vibration with advanced rotor tip shapes and by using 5 or more rotor blades. The feasibility of active twist needs to be demonstrated for such rotor blades to become widely adopted.

- Full-scale simulations and tests. Where aeroelastic validation data and the blade's internal CAD and materials data are available, a high-fidelity coupled simulation of a modified, active twist version of such blade may give valuable insights to calculate the actuator's effectiveness. As of now, such studies have usually been conducted with either purely structural calculations or simplified beam properties for comprehensive analysis.

- Acoustic impact of active twist rotor blades. As a powerful tool to reduce vibration and manipulate the downwash and blade vortex locations, active twist also has been demonstrated to alter the noise emissions of the rotor. Further numerical and experimental work is needed to show the benefits of the system, and how they can be exploited in conjunction with other targets.

- Aero-servo-elastic coupling in forward flight. The computational cost of strongly coupled aeroelastic simulations, using volumetric finite element structural models, is higher than currently used models. However, such models are needed to further assess the effectiveness of active twist rotors in transient flight and to validate the results of simpler beam methods. In such simulations, the mechanically transmitted forces through the pitch link and lag dampers should also be integrated into the vibration analysis.

- Active twist schedule optimisation. The high computational cost of the simulations in this work prohibited a more thorough study of active twist phases and non-sinusoidal input schedules. In the future, it may be possible to integrate lower fidelity rotor analysis tools into the coupled CFD/CSD solver to optimise the active twist to the flight condition at a reduced computational cost.

Bibliography

[1] A. R. S. Bramwell, G. Done, and D. Balmford. *Bramwell's Helicopter Dynamics (2nd Edition)*. Butterworth-Heinemann, 2001.

[2] W. Johnson. *Helictoper Theory*. Dover Publications, New York, NY, USA, 1994.

[3] A. Gessow. Effect of rotor-blade twist and plan-form taper on helicopter hovering performance. Technical Report NACA-TN-1542, 1948.

[4] A. F. Jones, R. Markiewicz, and M. R. J. An experimental investigation into the effect of twist on a berp type helicopter rotor in forward flight. Technical report, 1999. (Unpublished).

[5] W. Johnson. Performance and loads data from a wind tunnel test of a full-scale rotor with four blade tip planforms. NASA TM–81229, September 1980.

[6] J. G. Leishman. *Principles of Helicopter Aerodynamics*. Cambridge Aerospace Series, 2nd ed., 2006.

[7] G. Reichert. Helicopter vibration control - a survey. *Vertica*, 5:1–20, 1981.

[8] D. E. Kakaley, M. R. Jolly, and G. D. Buckner. An offset hub active vibration control system for mitigating helicopter vibrations during power loss: Simulation and experimental demonstration. *Aerospace Science and Technology*, 77:610–625, 2018.

[9] E. Breitbach and A. Büter. The main sources of helicopter vibration and noise emissions and adaptive concepts to reduce them. *Journal of structural control*, 3(1-2):21–32, 1996.

[10] U. T. Arnold and D. Fürst. Closed loop IBC results from CH-53G flight tests. *Aerospace Science and Technology*, 9(5):421–435, 2005. Rotorcraft Research. `doi:/10.1016/j.ast.2005.01.014`.

[11] A. Bauknecht, B. Ewers, O. Schneider, and M. Raffel. Blade tip vortex measurements on actively twisted rotor blades. *Experiments in Fluids*, 58(49), 2017. `doi:10.1007/s00348-017-2312-3`.

[12] J. W. Lim, D. D. Boyd Jr., F. Hoffmann, B. G. Van Der Wall, D.-H. Kim, S. N. Jung, Y. H. You, Y. Tanabe, J. Bailly, C. Lienard, and Y. Delrieux. Aeromechanical evaluation of Smart-Twisting Active Rotor. In *40th European Rotorcraft Forum 2014*, volume 1, pages 558–575. Royal Aeronautical Society, 2014.

[13] B. G. van der Wall, J. W. Lim, J. Riemenschneider, S. Kalow, G. A. Wilke, D. D. Boyd Jr., J. Bailly, Y. Delrieux, I. Cafarelli, Y. Tanabe, H. Sugawara, S. N. Jung, S. H. Hong, D.-H. Kim, H. J. Kang, G. N. Barakos, and R. Steininger. New smart twisting active rotor (STAR) - pretest predictions. *CEAS Aeronautical Journal*, 2024. `doi:10.1007/s13272-024-00731-z`.

[14] A. Brocklehurst and G. Barakos. A review of helicopter rotor blade tip shapes. *Progress in Aerospace Sciences*, 56:35–74, 2013. `doi:10.1016/j.paerosci.2012.06.003`.

[15] R. JanakiRam, R. Smith, B. Charles, and A. Hassan. Aerodynamic design of a new affordable main rotor for the Apache helicopter. In *American Helicopter Society 59th Annual Forum*, Phoenix, USA, 2003.

[16] T. Fitzgibbon. *Advanced Rotor Blade Design based on High-Fidelity Computational Fluid Dynamics*. PhD thesis, University of Glasgow, January 2021.

[17] D. Alfano, P. Cranga, V. Gareton, F. Guntzer, and J. Hirsch. The Blue Edge^{TM} blade continuation. In *Vertical Flight Society's 75th Annual Forum & Technology Display*, Philadelphia, PA, USA, 2019.

[18] M. Imiela. High-fidelity optimization framework for helicopter rotors. *Aerospace Science and Technology*, 23(1):2–16, 2012.

[19] P. Rauch, M. Gervais, P. Cranga, A. Baud, J. Hirsch, A. Walter, and P. Beaumier. Blue Edge^{TM}: the design, development and testing of a new blade concept. In *67th Annual Forum of the American Helicopter Society*, Virginia Beach, VA, USA, 2011.

[20] G. Wilke. Variable-fidelity methodology for the aerodynamic optimization of helicopter rotors. *AIAA Journal*, 57(8):3145–3158, 2019.

[21] G. Wilke. Quieter and greener rotorcraft: concurrent aerodynamic and acoustic optimization. *CEAS Aeronautical Journal*, 12:495–508, 2021. `doi:10.1007/s13272-021-00513-x`.

[22] E. P. N. Duque. A numerical analysis of the british experimental rotor program blade. In *45th Annual Forum of the American Helicopter Society*, Boston, MA, USA, 1989.

[23] F. Perry. Aerodynamics of the world speed record. In *43rd Annual Forum of the American Helicopter Society*, St. Louis, MO, USA, 1987.

[24] R. Hansford. Rotor load correlation with the british experimental rotor program blade. In *42nd Annual Forum of the American Helicopter Society*, Washington, D. C., USA, 1986.

[25] P. P. Friedmann. On-blade control of rotor vibration, noise, and performance: Just around the corner? the 33rd Alexander Nikolsky honorary lecture. *Journal of the American Helicopter Society*, 59(4):1–37, 2014.

[26] K. Nguyen. Higher harmonic control analysis for vibration reduction of helicopter rotor systems. Technical Report NASA-TM-103855, NASA, 1995.

[27] R. Cheng, C. Theodore, and R. Celi. Effects of higher harmonic control on rotor performance. In *50th Annual Forum of the American Helicopter Society*, 2000.

[28] C. Kessler. Active rotor control for helicopters: individual blade control and swashplateless rotor designs. *CEAS aeronautical journal*, 1(1-4):23–54, 2011.

[29] P. M. Küfmann, R. Bartels, B. G. van der Wall, O. Schneider, H. Holthusen, and J. Postma. The second wind-tunnel test of DLR's multiple swashplate system. *CEAS Aeronautical Journal*, pages 385–402, 2019. `doi:10.1007/s13272-018-0323-2`.

[30] Y. Yu, B. Gmelin, W. Splettstoesser, J. Philippe, J. Prieur, and T. Brooks. Reduction of helicopter blade-vortex interaction noise by active rotor control technology. *Progress in Aerospace Sciences*, 33(9-10):647–687, 1997. `doi:10.1016/S0376-0421(97)00006-7`.

[31] C. Kessler. Active rotor control for helicopters: Motivation and survey on higher harmonic control. *CEAS Aeronautical Journal*, 1(1-4):3–22, 2011. `doi:10.1007/s13272-011-0005-9`.

[32] B. G. van der Wall, C. L. Burley, Y. Yu, H. Richard, K. Pengel, and P. Beaumier. The hart ii test – measurement of helicopter rotor wakes. *Aerospace Science and Technology*, 8(4):273–284, 2004. `doi:10.1016/j.ast.2004.01.001`.

[33] B. van der Wall, J. W. Lim, M. J. Smith, S. N. Jung, J. D. Baeder, and D. D. Boyd Jr. The HART II international workshop: an assessment of the state of the art in CFD/CSD prediction. *CEAS Aeronautical Journal*, 4:223–252, 2013.

[34] S. N. Jung, M. K. Dhadwal, Y. W. Kim, J. H. Kim, and J. Riemenschneider. Cross-sectional constants of composite blades using computed tomography technique and finite element analysis. *Composite Structures*, 129:132–142, 2015. `doi:10.1016/j.compstruct.2015.03.074`.

[35] J. H. Ahn, H. J. Hwang, S. Chang, S. N. Jung, S. Kalow, and R. Keimer. X-ray computed tomography method for macroscopic structural property evaluation of active twist composite blades. *Aerospace*, 8(12), 2021. doi:10.3390/aerospace8120370.

[36] T. Millott and P. Friedmann. Vibration reduction in helicopter rotors using an actively controlled partial span trailing edge flap located on the blade. Technical Report NASA-CR-4611, NASA, 6 1994.

[37] F. Dehaeze, K. Baverstock, and G. Barakos. CFD simulation of flapped rotors. *Aeronautical Journal*, 119(1222):1561–1583, 2015. doi:10.1017/S0001924000011404.

[38] F. Straub, V. Anand, T. Birchette, and B. Lau. SMART rotor development and wind tunnel test. In *35th European Rotorcraft Forum 2009, ERF 2009*, volume 1, pages 413–430, 2009.

[39] F. K. Straub, V. R. Anand, B. H. Lau, and T. S. Birchette. Wind tunnel test of the SMART active flap rotor. *Journal of the American Helicopter Society*, 63(1), 2018. doi:10.4050/JAHS.63.012002.

[40] M. Mistry, F. Gandhi, M. Nagelsmit, and Z. Gurdal. Actuation requirements of a warp-induced variable twist rotor blade. *Journal of Intelligent Material Systems and Structures*, 22(9):919–933, 2011.

[41] M. Mistry and F. Gandhi. Design, fabrication, and benchtop testing of a helicopter rotor blade section with warp-induced spanwise camber variation. *Journal of Intelligent Material Systems and Structures*, 26(10):1272–1289, 2015.

[42] M. A. Woodgate, V. A. Pastrikakis, and G. N. Barakos. Method for calculating rotors with active Gurney flaps. *Journal of Aircraft*, 53(3):605–626, 2016. doi:10.2514/1.C032773.

[43] V. Pastrikakis, R. Steijl, and G. Barakos. Computational analysis of the W3 Sokol rotor with gurney flaps. In *39th European Rotorcraft Forum 2013, ERF 2013*, pages 75–76, 2013.

[44] V. Pastrikakis, R. Steijl, and G. Barakos. *Performance enhancement of rotors in hover using fixed Gurney flaps*, pages 51–67. 2017. doi:10.1007/978-3-319-50568-8_3.

[45] V. Pastrikakis, R. Steijl, and G. Barakos. Alleviation of retreating side stall using active elements for helicopter rotors. In *40th European Rotorcraft Forum 2014*, volume 1, pages 219–239, 2014.

[46] V. Pastrikakis, R. Steijl, and G. Barakos. *Alleviation of retreating side stall using active Gurney flaps*, pages 69–86. 2017. `doi:10.1007/978-3-319-50568-8_4`.

[47] A. P. F. Bernhard and I. Chopra. Hover testing of active rotor blade-tips using a piezo-induced bending-torsion coupled beam. *Journal of intelligent material systems and structures*, 9(12):963–974, 1998.

[48] A. P. F. Bernhard and I. Chopra. Analysis of a bending-torsion coupled actuator for a smart rotor with active blade tips. *Smart Materials and Structures*, 10(1):35–52, 2001.

[49] A. P. F. Bernhard and I. Chopra. Hover test of Mach-scale active twist rotor using piezo-bending-torsion actuators. *Journal of Aircraft*, 39(4):678–688, 2002. `arXiv:10.2514/2.2981`, `doi:10.2514/2.2981`.

[50] M. R. Amoozgar, A. D. Shaw, J. Zhang, and M. I. Friswell. Composite blade twist modification by using a moving mass and stiffness tailoring. *AIAA Journal*, 57(10):4218–4225, 2019. `arXiv:10.2514/1.J057591`, `doi:10.2514/1.J057591`.

[51] R. G. Loewy. Recent developments in smart structures with aeronautical applications. *Smart materials and structures*, 6(5):R11–R42, 1997.

[52] M. L. Wilbur, M. P. Mistry, P. F. Lorber, R. Blackwell, S. Barbarino, T. H. Lawrence, and U. T. Arnold. Chapter 24 - rotary wings morphing technologies: State of the art and perspectives. In A. Concilio, I. Dimino, L. Lecce, and R. Pecora, editors, *Morphing Wing Technologies*, pages 759–797. Butterworth-Heinemann, 2018. `doi:10.1016/B978-0-08-100964-2.00024-1`.

[53] P. Shivashankar and S. Gopalakrishnan. Review on the use of piezoelectric materials for active vibration, noise, and flow control. *Smart Materials and Structures*, 29(5), 2020.

[54] R. Derham, D. Weems, B. Matthew, and R. Bussom. The design evolution of an active materials rotor. In *Proceedings of the 57th American Helicopter Society Annual Forum*, volume 57-00049, Washington, DC, USA, 2001.

[55] V. K. Wickramasinghe and N. W. Hagood. Durability characterization of active fiber composite actuators for helicopter rotor blade applications. *Journal of Aircraft*, 41(4):931–937, 2004. `doi:10.2514/1.988`.

[56] D. B. Weems, D. M. Anderson, M. B. Mathew, and R. C. Bussom. A large-scale active-twist rotor. In *60th American Helicopter Society Annual Forum*, Baltimore, MD, USA, June 2004.

[57] P. C. Chen and I. Chopra. Induced strain actuation of composite beams and rotor blades with embedded piezoceramic elements. *Smart materials and structures*, 5(1):35–48, 1996.

[58] P. C. Chen and I. Chopra. Wind tunnel test of a smart rotor model with individual blade twist control. *Journal of intelligent material systems and structures*, 8(5):414–425, 1997.

[59] S. Shin and C. Cesnik. Helicopter performance and vibration enhancement by twist-actuated blades. In *44th AIAA/ASME/ASCE/AHS/ASC Structures, Structural Dynamics, and Materials Conference*, 2003. `doi:10.2514/6.2003-1818`.

[60] M. Wilbur, W. Yeager, W. Wilkie, C. Cesnik, and S. Shin. Hover testing of the NASA/Army/MIT active twist rotor prototype blade. In *American Helicopter Society 56th Annual Forum*, Virginia Beach, VA, USA, 01 2000.

[61] M. Wilbur, W. T. J. Yeager, T. William, and M. Sekula. Further examination of the vibratory loads reduction results from the NASA/ARMY/MIT Active Twist Rotor test. *58th American Helicopter Society Annual Forum*, 02 2002.

[62] S. Shin, C. Cesnik, and S. Hall. Closed-loop control test of the NASA/Army/MIT Active Twist Rotor for vibration reduction. *Journal of the American Helicopter Society*, 50(2):178–194, 2005. `doi:10.4050/1.3092854`.

[63] A. Bauknecht, B. Ewers, O. Schneider, and M. Raffel. Aerodynamic results from the STAR hover test: An examination of active twist actuation. In *41st European Rotorcraft Forum 2015, ERF 2015*, volume 1, pages 92–107, 2015.

[64] P. C. Chen. *Development of a Smart Rotor with Induced-Strain Actuation of Blade Twist*. PhD thesis, University of Maryland, 1996.

[65] J. Rodgers, N. Hagood, and D. Weems. Design and manufacture of an integral twist-actuated rotor blade. In *38th Structures, Structural Dynamics, and Materials Conference*, Kissimmee, FL, USA, 4 1997. `doi:10.2514/6.1997-1264`.

[66] C. E. Cesnik, S. Shin, W. Wilkie, M. L. Wilbur, and P. H. Mirick. Modeling, design, and testing of the NASA/Army/MIT Active Twist Rotor prototype blade. In *American Helicopter Society 55th Annual Forum*, volume 1, pages 533–544, Montréal, Québec, Canada, 1999.

[67] S. Shin. Design, manufacturing, and testing of an active twist rotor. Master's thesis, Massachusetts Institute of Technology, Dept. of Aeronautics and Astronautics, 1999.

[68] S. Shin. *Integral Twist Actuation of Helicopter Rotor Blades for Vibration Reduction*. PhD thesis, Massachusetts Institute of Technology, 8 2001.

[69] C. E. S. Cesnik, S. Shin, and M. L. Wilbur. Dynamic response of active twist rotor blades. *Smart materials and structures*, 10(1):62–76, 2001.

[70] S. J. Shin, C. E. S. Cesnik, W. K. Wilkie, and M. L. Wilbur. Design and manufacturing of a model-scale Active Twist Rotor prototype blade. *Journal of intelligent material systems and structures*, 19(12):1443–1456, 2008.

[71] A. R. H. Goodwin and M. R. Moldover. Thermophysical properties of gaseous refrigerants from speed of sound measurements. i. apparatus, model, and results for 1,1,1,2-tetrafluoroethane R134a. *The Journal of Chemical Physics*, 93(4):2741–2753, 1990. doi:10.1063/1.458913.

[72] M. L. Wilbur, P. H. Mirick, W. T. Yeager, C. W. Langston, C. E. S. Cesnik, and S. Shin. Vibratory loads reduction testing of the NASA/Army/MIT Active Twist Rotor. *Journal of the American Helicopter Society*, 47(2):123–133, 2002.

[73] G. Fleming, H. Soto, and B. W. South. Projection moire interferometry for rotorcraft applications: Deformation measurements of active twist rotor blades. 2002.

[74] E. R. Booth and M. L. Wilbur. Acoustic aspects of active-twist rotor control. *Journal of the American Helicopter Society*, 49(1):3–10, 2004.

[75] P. Wierach, J. Riemenschneider, S. Optiz, and F. Hoffmann. Experimental investigation of an active twist model rotor blade under centrifugal loads. In *33rd European Rotorcraft Forum 2007, ERF33*, volume 3, pages 1653–1665, 2007.

[76] J. Riemenschneider and S. Opitz. Measurement of twist deflection in Active Twist Rotor. *Aerospace Science and Technology*, 15(3):216–223, 2011.

[77] J. Riemenschneider, S. Keye, P. Wierach, and H. M. des Rochettes. Overview of the common DLR/ONERA project active twist blade. In *30th European Rotorcraft Forum*, Marseille, France, 9 2004.

[78] P. Masarati, M. Morandini, J. Riemenschneider, P. Wierach, S. Gluhih, and E. Barkanov. Optimal design of an active twist 1:2.5 scale rotor blade. In *31st European Rotorcraft Forum*, volume 2005, pages 37.1–37.14, 2005.

[79] A. Ballauer and P. F. Sheridan. *VertiFlite*, volume 15. American Helicopter Society, August 1969.

[80] P. Wierach, S. Opitz, and S. Kalow. Experimental investigation of an active twist model rotor blade with a low voltage actuation system. *The Aeronautical Journal*, 119(1222):1499–1512, 2015. doi:10.1017/S0001924000011374.

[81] S. Kalow, B. van de Kamp, C. Balzarek, and J. Riemenschneider. Manufacturing of a next generation active twist helicopter rotor blade and experimental results of functionality test. In *74th American Helicopter Society Annual Forum*, Phoenix, AZ, USA, 5 2018.

[82] S. Kalow, B. van de Kamp, R. Keimer, and J. Riemenschneider. Next generation active twist helicopter rotor blade - simulated results validated by experimental investigation. In *45th European Rotorcraft Forum 2019, ERF 2019*, volume 2, pages 1378 – 1386, Warsaw, Poland, 2019.

[83] M. Schulz, S. Opitz, and J. Riemenschneider. A new concept to determine the mass distribution of an active twist rotor blade. *CEAS aeronautical journal*, 3(2-4):117–123, 2012.

[84] C. E. S. Cesnik, D. G. Opoku, F. Nitzsche, and T. Cheng. Active twist rotor blade modelling using particle-wake aerodynamics and geometrically exact beam structural dynamics. *Journal of fluids and structures*, 19(5):651–668, 2004.

[85] M. L. Wilbur and M. K. Sekula. The effect of tip geometry on active-twist rotor response. In *American Helicopter Sociert 61st Annual Forum*, 6 2005.

[86] J. Park and J. Kim. Design and aeroelastic analysis of active twist rotor blades incorporating single crystal macro fiber composite actuators. *Composites Part B: Engineering*, 39(6):1011–1025, 2008.

[87] J. Mok. *Design Optimization for Active Twist Rotor Blades*. PhD thesis, University of Michigan, Horace H. Rackham School of Graduate Studies, 2010.

[88] D. E. Fogarty, M. L. Wilbur, M. K. Sekula, and D. D. Boyd Jr. CFD/CSD investigation of BVI noise reduction using harmonic active twist control. In *38th European Rotorcraft Forum 2012, ERF 2012*, volume 1, pages 682–697, 2012.

[89] D. Kumar and C. E. S. Cesnik. New optimization strategy for design of active twist rotor. *AIAA Journal*, 53(2):436–448, 2015. `doi:10.2514/1.J053195`.

[90] S. Massey, A. Kreshock, and M. Sekula. Coupled CFD/CSD analysis of rotor blade structural loads with experimental validation. In *31st AIAA Applied Aerodynamics Conference*. American Institute of Aeronautics and Astronautics Inc., 2013. `doi:10.2514/6.2013-3158`.

[91] S. J. Massey, A. R. Kreshock, and M. K. Sekula. Coupled cfd/csd analysis of an active-twist rotor in a wind tunnel with experimental validation. volume 2, page 1207 – 1232, 2015.

[92] C. Tung, F. X. Caradonna, and W. R. Johnson. The prediction of transonic flows on an advancing rotor. *Journal of the American Helicopter Society*, 31(3):4–9, 1986. doi:10.4050/JAHS.31.3.4.

[93] M. Potsdam, H. Yeo, and W. Johnson. Rotor airloads prediction using loose aerodynamic/structural coupling. *Journal of Aircraft*, 43(3):732 – 742, 2006. doi:10.2514/1.14006.

[94] F. Hoffmann, R. Keimer, and J. Riemenschneider. Structural modeling and validation of an active twist model rotor blade. *CEAS aeronautical journal*, 7(1):43–55, 2015;2016;.

[95] S. Glukhikh, E. Barkanov, A. Kovalev, P. Masarati, M. Morandini, J. Riemenschneider, and P. Wierach. Design of helicopter rotor blades with actuators made of a piezomacrofiber composite. *Mechanics of composite materials*, 44(1):57–64, 2008.

[96] A. Kovalovs, E. Barkanov, and S. Gluhihs. Active twist of model rotor blades with D-Spar design. *Transport (Vilnius, Lithuania)*, 22(1):38–44, 2007.

[97] A. Kovalovs, E. Barkanov, S. Ruchevskis, and M. Wesolowski. Modeling and design of a full-scale rotor blade with embedded piezocomposite actuators. *Mechanics of composite materials*, 53(2):179–192, 2017.

[98] A. Kovalovs, E. Barkanov, S. Ruchevskis, and M. Wesolowski. Optimisation methodology of a full-scale Active Twist Rotor blade. In *Procedia Engineering*, volume 178, pages 85–95, 2017.

[99] E. Barkanov, A. Kovalov, P. Wierach, and J. Riemenschneider. Optimized comparative analysis of an active twist for helicopter rotor blades with C- and D-Spar designs. *Mechanics of composite materials*, 54(5):553–566, 2018.

[100] B. G. van der Wall, J. W. Lim, J. Riemenschneider, S. Kalow, G. A. Wilke, D. D. Boyd Jr., J. Bailly, Y. Delrieux, I. Cafarelli, Y. Tanabe, H. Sugawara, S. N. Jung, S. H. Hong, D.-H. Kim, H. J. Kang, G. Barakos, and R. Steininger. Smart twisting active rotor (STAR) - pre-test predictions. In *48th European Rotorcraft Forum*, Winterthur, Switzerland, 9 2022.

[101] G. A. Wilke, B. G. van der Wall, Y. Tanabe, H. Sugawara, D.-H. Kim, H. J. Kang, S. N. Jung, S. H. Hong, J. Bailly, G. Barakos, R. Steininger, and J. W. Lim. Vortex-induced stall on an actively twisted highly loaded model rotor blade. In A. Dillmann, G. Heller, E. Krämer, C. Wagner, and J. Weiss, editors, *New Results in Numerical and Experimental Fluid Mechanics XIV*, pages 623–633, Cham, 2024. Springer Nature Switzerland. doi:10.1007/978-3-031-40482-5_59.

[102] J. Raddatz and J. K. Fassbender. Block structured navier-stokes solver flower. In N. Kroll and J. K. Fassbender, editors, *MEGAFLOW - Numerical Flow Simulation for Aircraft Design*, pages 27–44, Berlin, Heidelberg, 2005. Springer Berlin Heidelberg.

[103] B. Benoit, A.-M. Dequin, K. Kampa, w. von Grünhagen, P.-M. Basset, and B. Gimonet. Host, a general helicopter simulation tool for germany and france. In *56th Annual Forum of the American Helicopters Society*, Virginia Beach, VA, USA, 2000.

[104] Y. Tanabe, S. Saito, and I. Otani. Validation of computational results of rotor/fuselage interaction analysis using rFlow3D code. Technical report, 2010.

[105] G. Wilke, H. Sugawara, T. Yasutada, O. Schneider, and B. G. van der Wall. Investigations of a boxed rotor: The STAR II rotor in DLR's test hall. In *49th European Rotorcraft Forum, ERF 2023*, Buckeburg, Germany, 9 2023.

[106] D. Han, V. Pastrikakis, and G. N. Barakos. Helicopter flight performance improvement by dynamic blade twist. *Aerospace Science and Technology*, 58:445–452, 2016.

[107] D. Thakkar and R. Ganguli. Use of single crystal and soft piezoceramics for alleviation of flow separation induced vibration in a smart helicopter rotor. *Smart materials and structures*, 15(2):331–341, 2006.

[108] D. Thakkar and R. Ganguli. Induced shear actuation of helicopter rotor blade for active twist control. *Thin-walled structures*, 45(1):111–121, 2007.

[109] P. M. Pawar and S. N. Jung. Active twist control methodology for vibration reduction of a helicopter with dissimilar rotor system. *Smart materials and structures*, 18(3):035013, 2009.

[110] C. Brillante, M. Morandini, and P. Mantegazza. Periodic controllers for vibration reduction using actively twisted blades. *Aeronautical Journal*, 120(1233):1763–1784, 2016.

[111] Y. H. You, S. N. Jung, and C. J. Kim. Optimal deployment schedule of an active twist rotor for performance enhancement and vibration reduction in high-speed flights. *Chinese Journal of Aeronautics*, 30(4):1427–1440, 2017.

[112] Y. You and S. N. Jung. Optimum active twist input scenario for performance improvement and vibration reduction of a helicopter rotor. *Aerospace Science and Technology*, 63:18–32, 2017.

[113] M. K. Sekula and M. L. Wilbur. Optimization of an Active Twist Rotor blade planform for improved active response and forward flight performance. *Journal of the American Helicopter Society*, 62(3):1–12, 2017. doi:doi:10.4050/JAHS.62.032002.

[114] S. Vouros, N. D. Polyzos, I. Goulos, and V. Pachidis. Impact of optimized variable rotor speed and active blade twist control on helicopter blade-vortex interaction noise and environmental impact. *Journal of fluids and structures*, 104:103285, 2021.

[115] G. Servera, P. Beaumier, and M. Costes. A weak coupling method between the dynamics code HOST and the 3d unsteady Euler code WAVES. *Aerospace Science and Technology*, 5(6):397–408, 2001. doi:10.1016/S1270-9638(01)01120-8.

[116] K. Pahlke and B. G. van der Wall. Calculation of multibladed rotors in high-speed forward flight with weak fluid-structure coupling. In *27th European Rotorcraft Forum, ERF*, Moscow, Russia, 9 2001.

[117] A. Datta, M. Nixon, and I. Chopra. Review of rotor loads prediction with the emergence of rotorcraft CFD. *Journal of the American Helicopter Society*, 52(4):287–317, 2007. doi:10.4050/JAHS.52.287.

[118] A. Datta, M. Nixon, and I. Chopra. X3D — a 3-D solid finite element multibody dynamic analysis for rotorcraft. In *AHS Aeromechanics Specialists Conference on Aeromechanics Design for Vertical Lift*, pages 529–557, San Francisco, CA, USA, 1 2016.

[119] W. Staruk, A. Datta, I. Chopra, and B. Jayaraman. An integrated three-dimensional aeromechanics analysis of the nasa tilt rotor aeroacoustic model. *Journal of the American Helicopter Society*, 63(3):1–12, 2018.

[120] M. Patil and A. Datta. A scalable time-parallel solution of periodic rotor dynamics in x3d. *Journal of the American Helicopter Society*, 66(4):1–16, 2021. doi:10.4050/JAHS.66.042007.

[121] M. Patil, R. Lumba, B. Jayaraman, and A. Datta. An integrated three-dimensional aeromechanical analysis for the prediction of stresses on modern coaxial rotors. *The International Journal of High Performance Computing Applications*, 38(4):356–376, 2024. doi:10.1177/10943420241255089.

[122] M. Patil, R. Lumba, and A. Datta. X3D v2.0 - A parallel 3D finite element multibody dynamic analysis for rotorcraft. In *Proceedings of the Transformative Vertical Flight - Sixth Decennial VFS Aeromechanics Specialists' Conference,*, Santa Clara, CA, USA, 2024.

[123] M. S. Sicim and M. O. Kaya. Optimization of vibration reduction in a helicopter blade with 2 way fluid-structure interaction. In *Smart Materials, Adaptive Structures and Intelligent Systems*, volume 1, page V001T03A009, 09 2018. doi:10.1115/SMASIS2018-8017.

[124] F.-K. Benra, H. J. Dohmen, J. Pei, S. Schuster, and B. Wan. A comparison of one-way and two-way coupling methods for numerical analysis of fluid-structure interactions. *Journal of Applied Mathematics*, 2011(1):853560, 2011. doi:10.1155/2011/853560.

[125] R. Haehnel, J. Lim, Y. Wenren, S. Tain, and W. Yu. Structural analysis of a rotorcraft blade design using iVABS. In *Vertical Flight Society, Forum 79*, West Palm Beach, FL, USA, 2023.

[126] I. Chopra. Review of state of art of smart structures and integrated systems. *AIAA Journal*, 40(11):2145–2187, 2002. doi:10.2514/2.1561.

[127] A. Büter and E. Breitbach. Adaptive blade twist - calculations and experimental results. *Aerospace Science and Technology*, 4(5):309–319, 2000. doi:10.1016/S1270-9638(00)00134-6.

[128] D. Thakkar and R. Ganguli. Active twist control of smart helicopter rotor - a survey. *Journal of Aerospace Sciences and Technologies*, 57, 01 2005.

[129] A. Bent and N. Hagood. Piezoelectric fiber composites with interdigitated electrodes. *Journal of Intelligent Material Systems and Structures*, 8(11):903–919, 1997. doi:10.1177/1045389X9700801101.

[130] W. K. Wilkie, R. G. Bryant, J. W. High, R. L. Fox, R. F. Hellbaum, A. J. Jalink, B. D. Little, and P. H. Mirick. Low-cost piezocomposite actuator for structural control applications. In J. H. Jacobs, editor, *Smart Structures and Materials 2000: Industrial and Commercial Applications of Smart Structures Technologies*, volume 3991, pages 323 – 334. International Society for Optics and Photonics, SPIE, 2000. doi:10.1117/12.388175.

[131] MacroFiberComposite™ properties. https://www.smart-material.com/MFC-product-propertiesV2.html. Accessed: 2024-11-27.

[132] H. Prahlad and I. Chopra. Design of a variable twist tilt-rotor blade using shape memory alloy (SMA) actuators. In L. P. Davis, editor, *Smart Structures and Materials 2001: Smart Structures and Integrated Systems*, volume 4327, pages 46 – 59. International Society for Optics and Photonics, SPIE, 2001. doi:10.1117/12.436559.

[133] J. . Park, S. . Kim, and S. N. Jung. Optimal design of a variable-twist proprotor incorporating shape memory alloy hybrid composites. *Composite Structures*, 93(9):2288–2298, 2011.

[134] S. Ameduri and A. Concilio. A shape memory alloy torsion actuator for static blade twist. *Journal of Intelligent Material Systems and Structures*, 30(17):2605–2626, 2019.

[135] S. Ameduri, A. Concilio, B. Galasso, and A. Gianvito. Development of a conceptual demonstrator of a SMA-based rotorcraft blade twist system. In *Proceedings of SPIE - The International Society for Optical Engineering*, volume 10965, 2019.

[136] S. Ameduri, M. Ciminello, A. Concilio, I. Dimino, B. Galasso, M. Guida, G. Bruno, and M. F. Miceli. Modelling of a sma blade twist system suited for demonstration in wind tunnel and whirl tower plants. *Applied Sciences*, 13(21), 2023. `doi:10.3390/app132112039`.

[137] D. Overmeyer, P. Copp, and N. Schaeffler. Hover validation and acoustic baseline blade set. Technical Report NASA-TM-2020-5002153, AIAA, NASA, May 2020.

[138] Rotorcraft hover prediction workshop (HPW). `https://www.aiaa-hpw.org/hvab-rotor`, 2020. Accessed: 2022-09-13.

[139] Hover validation and acoustic baseline rotor test. `https://rotorcraft.arc.nasa.gov/HVAB/`. Accessed: 2023-10-19.

[140] T. R. Norman, J. T. Heineck, E. T. Chairer, L. N. Wagner, G. K. Yamauchi, M. Dominguez, A. L. Sheikman, N. W. Schaeffler, A. D. Overmeyer, M. Ramasamy, and C. C. Cameron. Fundamental test of a hovering rotor: Comprehensive measurements for cfd validation. In *Vertical Flight Society Forum 79*, West Palm Beach, FL, USA, 5 2023. `doi:10.4050/F-0079-2023-17983`.

[141] R. Steijl, G. N. Barakos, and K. Badcock. A framework for CFD analysis of helicopter rotors in hover and forward flight. *International Journal for Numerical Methods in Fluids*, 51(8):819–847, 2006. `doi:10.1002/d.1086`.

[142] R. Steijl and G. N. Barakos. Sliding mesh algorithm for CFD analysis of helicopter rotor-fuselage aerodynamics. *International Journal for Numerical Methods in Fluids*, 58(5):527–549, 2008. `doi:10.1002/d.1757`.

[143] P. Spalart and S. Allmaras. One-equation turbulence model for aerodynamic flows. *Recherche aerospatiale*, (1):5–21, 1994.

[144] ANSYS. *ANSYS ICEMCFD 2019 Help Manual*. 2019.

[145] C. Hirsch. *Numerical Computation of Internal and External Flows (Second Edition)*. Butterworth-Heinemann, Oxford, second edition edition, 2007. `doi:10.1016/B978-075066594-0/50040-0`.

[146] W. Sutherland. 1893.

[147] O. Reynolds. On the dynamical theory of incompressible viscous fluids and the determination of the criterion. *Philosophical Transactions of the Royal Society of London. A*, 186:123–164, 1895. doi:10.1098/rsta.1895.0004.

[148] A. Favre. The equations of compressible turbulent gases. In *Problems of Hydrodynamics and Continuum Mechanics*, pages 104–113, Paris, 1965. CNRS. Originally published in French as "Équations des gaz turbulents compressibles".

[149] J. Boussinesq. *Essai sur la théorie des eaux courantes*, volume 23 of *Mémoires présentés par divers savants à l'Académie des Sciences*. Imprimerie Nationale, Paris, 1878.

[150] F. R. Menter. Two-equation eddy-viscosity turbulence models for engineering applications. *AIAA Journal*, 32(8):1598–1605, 1994. doi:10.2514/3.12149.

[151] B. Launder and D. Spalding. The numerical computation of turbulent flows. *Computer Methods in Applied Mechanics and Engineering*, 3(2):269–289, 1974. doi:10.1016/0045-7825(74)90029-2.

[152] D. Wilcox. Reassessment of the scale-determining equation for advanced turbulence models. *AIAA Journal*, 28(11):1299–1310, 1988. doi:10.2514/3.10041.

[153] S. Osher and S. Chakravarthy. Upwind schemes and boundary conditions with applications to Euler equations in general geometries. *Journal of Computational Physics*, 50(3):447–481, 1983. doi:10.1016/0021-9991(83)90106-7.

[154] B. van Leer. Towards the ultimate conservative difference scheme. V.A second-order sequel to Godunov's method. *Journal of Computational Physics*, 32(1):101–136, 1979. doi:10.1016/0021-9991(79)90145-1.

[155] G. D. van Albada, B. van Leer, and W. W. Roberts. A comparative study of computational methods in cosmic gas dynamics. *Astronomy and Astrophysics*, 108(1):76–84, 1982. doi:10.1007/978-3-642-60543-7.

[156] A. Jameson. Time-dependent calculations using multigrid, with applications to unsteady flows past airfoils and wings. In *AIAA 10th Computational Fluid Dynamics Conference*, Honolulu, HI, USA, 1991. doi:10.2514/6.1991-1596.

[157] J. Steger, F. Dougherty, and J. Benek. Chimera grid scheme. In *ASME Mini-Symposium on Advances in Grid Generation*, Houston, TX, USA, 1983.

[158] M. Jarkowski, M. Woodgate, G. N. Barakos, and J. Rokicki. Towards consistent hybrid overset mesh methods for rotorcraft CFD. *International Journal for Numerical Methods in Fluids*, 74(8):543–576, 2014. doi:10.1002/fld.3861.

[159] MSC Software. *MSC Nastran 2024 Reference Guide Manual*. 2024.

[160] R. Steininger. Structural modelling and thermal analogy in MSC NASTRAN. Technical report, 2024. (Unpublished).

[161] MSC Software. *MSC Nastran 2024 Quick Reference Guide*. 2024.

[162] A. R. M. Altmikus, S. Wagner, P. Beaumier, and G. Servera. A comparison: Weak versus strong modular coupling for trimmed aeroelastic rotor simulations. In *American Helicopter Society 58th Annual Forum*, Montreal, Canada, 6 2002.

[163] S. Babu, G. Loupy, F. Dehaeze, G. Barakos, and N. Taylor. Aeroelastic simulations of stores in weapon bays using detached-eddy simulation. *Journal of Fluids and Structures*, 66:207–228, 2016. doi:10.1016/j.jfluidstructs.2016.07.014.

[164] F. Dehaeze, G. Barakos, and L. Garipova. Coupled CFD/CSD simulation of the helicopter main rotor in high-speed forward flight. *Russ. Aeronaut.*, 60:198–205, 2017. doi:10.3103/S1068799817020064.

[165] P. Lancaster and K. Salkauskas. Surfaces generated by moving least squares methods. *Mathematics of computation*, 37(155):141–158, 1981.

[166] E. Luke, E. Collins, and E. Blades. A fast mesh deformation method using explicit interpolation. *Journal of Computational Physics*, 231(2):586–601, 2012. doi:10.1016/j.jcp.2011.09.021.

[167] E. Balmès, D. Chapelle, J. M. Leclère, and M. Vidrascu. OpenFEM: an open source finite element toolbox. http://www.utc.fr/lrm/giens05/CDROM/CDROM/lo01.pdf, 2005.

[168] IEEE standard on piezoelectricity, 1987.

[169] X.-J. Dong and G. Meng. Dynamic analysis of structures with piezoelectric actuators based on thermal analogy method. *The International Journal of Advanced Manufacturing Technology*, 27(9):841–844, Feb 2006.

[170] F. Côté, P. Masson, N. Mrad, and V. Cotoni. Dynamic and static modelling of piezoelectric composite structures using a thermal analogy with MSC/NASTRAN. *Composite Structures*, 65(3):471 – 484, 2004.

[171] M. Staworko and U. Tadeusz. Modeling and simulation of piezoelectric elements – comparison of available methods and tools. *Mechanics*, 27(5):161–171, 2008.

[172] A. Jimenez Garcia and G. N. Barakos. Accurate predictions of rotor hover performance at low and high disc loadings. *Journal of Aircraft*, 55(1):89–110, 2018. doi:10.2514/1.C034144.

[173] A. Jimenez-Garcia and G. Barakos. Numerical simulations on the PSP rotor using HMB3. In *AIAA Aerospace Sciences Meeting, 2018*, number 210059, Kissimmee, FL, USA, 2018. doi:10.2514/6.2018-0306.

[174] T. A. Fitzgibbon, M. A. Woodgate, A. Jimenez-Garcia, and G. N. Barakos. Validation of the steady-state hover formulation for accurate performance predictions. *AIAA Journal*, 57(12):5293–5308, 2019. doi:10.2514/1.J058408.

[175] T. Fitzgibbon and G. Barakos. Investigation of wake breakdown in hover using the hmb3 solver. In *AIAA SciTech Forum 2022*, San Diego, CA, USA, 2022. doi:10.2514/6.2022-1320.

[176] S. H. Chang, S. H. Hong, S. N. Jung, D.-H. Kim, F. Becker, S. Kalow, and R. Steininger. Experimental-cum-numerical evaluation of structural properties and vibrational spectra of new smart twisting active rotor blades. In *50th European Rotorcraft Forum, ERF 2024*, Marseille, France, 9 2024.

[177] J. Kocurek and J. Tangler. A prescribed wake lifting surface hover performance analysis. *Journal of The American Helicopter Society*, 22:24–35, 1977.

[178] R. Jain. CFD-CSD pre-test hover predictions validation for the HVAB rotor. In *AIAA SCITECH 2024 Forum*, Orlando, FL, USA, 1 2024. doi:10.2514/6.2024-0893.

[179] O. Boelens, G. Barakos, M. Biava, A. Brocklehurst, M. Costes, A. D'Alascio, M. Dietz, D. Drikakis, J. Ekaterinaris, I. Humby, W. Khier, B. Knutzen, J. Kok, F. LeChuiton, K. Pahlke, T. Renaud, T. Schwarz, R. Steijl, L. Sudre, H. Van Der Ven, L. Vigevano, and B. Zhong. The blind-test activity of the GOAHEAD project. In *33rd European Rotorcraft Forum*, volume 2, pages 759–794, 2007.

[180] R. Steijl and G. Barakos. Cfd analysis of complete helicopter configurations – lessons learnt from the GOAHEAD project. *Aerospace Science and Technology*, 19(1):58–71, 2012. doi:10.1016/j.ast.2011.01.007.